Molecules interacting with short and intense laser pulses: Simulations of correlated ultrafast dynamics

Marie Labeye

SORBONNE UNIVERSITÉ

Thèse de Doctorat de Physique

École Doctorale de Physique en Île de France (ED 564)

Présentée par :

Marie Labeye

En vue d'obtenir le grade de :

Docteure de SORBONNE UNIVERSITÉ

Sujet de thèse :

Molecules interacting with short and intense laser pulses: Simulations of correlated ultrafast dynamics.

Présentée le 19 juillet 2018

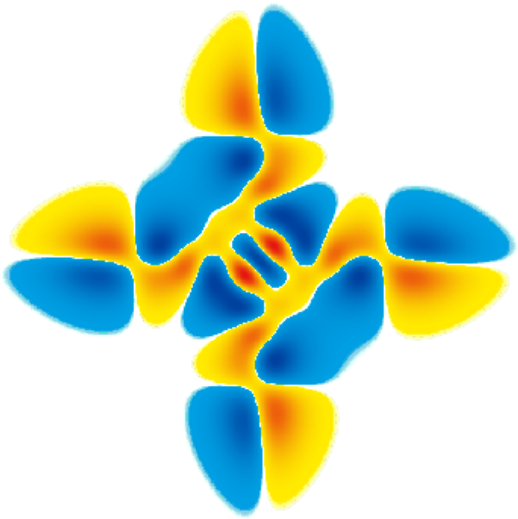

Composition du jury :

M. Jan-Michael Rost	Professeur	Rapporteur
M. Henri Bachau	Directeur de Recherches	Rapporteur
Mme Emily Lamour	Professeure	Examinatrice
Mme Federica Agostini	Maître de Conférences	Examinatrice
M. Thierry Ruchon	Ingénieur CEA	Examinateur
M. Richard Taïeb	Directeur de Recherches	Directeur de thèse

Contents

Acknowledgements

Ce manuscrit, et plus généralement cette thèse, ont profité de l'aide et du soutien d'un grand nombre de personnes. Je vais essayer d'en remercier le plus possible ici, mais il est bien évident que je vais en oublier certain·e·s, et je m'en excuse par avance.

Tout d'abord merci à mes deux encadrants Richard et Jérémie pour m'avoir laissé la liberté de travailler à ma façon et sur les sujets qui me plaisaient le plus, mais tout en restant attentifs à ce que je faisais, et disponibles pour des discussions scientifiques parfois animées mais toujours intéressantes. Merci bien sur à François pour m'avoir initiée au C++, et pour m'avoir laissé ses codes, mais surtout pour m'avoir laissé des questions scientifiques ouvertes et intéressantes sur lesquelles me lancer. Une très gros merci à Sévan pour les mille déjeuners passés ensemble, pour la course à la rédaction, pour les soirées en musique, pour l'oreille attentive très efficace en débuggage, et bien sur pour la gestion bancaire. Merci à la fine équipe du bureau 103 : Anthony, Anthony, Quentin, Antoine, Lucia, Jia Ping, Liu Hang, ainsi que Valentin et Christopher, pour le bureau le plus animé et le mieux équipé de tout le laboratoire. Merci à tous les autres doctorant·e·s, post docs et stagiaires du labo pour la super ambiance, les sorties, les restos et tout les moments passés au labo : Mehdi, Basile, Solène, Selma, Alessandra, Aicha, Gildas, Bastien, Aoqiu, Sylvain, Moustafa, Aladdine, Farzad, Alter, Carla, Dimitris, Junwen, Jessica, Xuan, Meiyi, Jiatai mais aussi Tsveta qui compte parmis les vieux du labo maintenant. Un énorme merci à David Massot pour le soutien administratif et surtout pour les chocolats ! Merci à Emmanuelle pour tous les gâteaux et à Rabah pour les discussions politiques et les soirées Jazz. Merci aussi aux vieux du labo : Loïc, Jérôme, Marc, Boris pour les repas à la cantine et les pauses café.

Je ne sais pas comment remercier assez Antoine Fermé pour le soutien moral, scientifique et technique tout au long de ces six dernières années. Merci pour m'avoir écoutée râler des heures durant quand j'étais bloquée. Merci d'avoir toujours été disponible pour parler de sciences : des morceaux entiers de cette thèse sont sortis de discussions avec toi. Merci pour m'avoir trouvé les références de Maths qu'il fallait quand je trouvais certaines approches pas assez rigoureuses et pour m'avoir aidé à les comprendre. Merci de m'avoir donné le courage de me lancer dans des gros calculs que j'aurais cru impossibles ou beaucoup trop longs. Merci d'avoir relu ma thèse, si je peux me vanter d'avoir aussi peu de fautes d'anglais c'est grâce à toi. Et j'en passe...

Merci beaucoup à tous mes coloc : ceux du Père Co, Matthieu, Amiel, Oscar et Cyril pour la vie bordélique et animée qu'on a menée pendant trois ans, et à ceux de l'Ivryade, Valentin, Marine, encore Amiel, Romain, et plus récemment Alix et Maguelone pour ces deux ans de vie commune, pour les soirées, pour les bouffes, pour les discussions militantes (et non militantes), pour le bricolage et le jardinage, pour les aprem projections, pour les

week end jeux, pour les vacances à la montagne et jusqu'à la gestion de mon pot de thèse. Ça aura été deux ans incroyables.

Merci à Pablo pour les moments passés ensemble. Merci à Axelle Percyfion qui est toujours là pour organiser les petits verres qui se terminent en grosses soirées. Merci à tou·te·s les copains et les copines que j'ai croisé·e·s pendant toutes ces années à Paris, pour n'oublier personne je ne mets pas de nom mais vous vous reconnaitrez.

Merci aussi aux copains et aux copines de Grenoble qui sont toujours là après toutes ces années. Merci à Timothée toujours motivé pour tout, et à Aline qui nous a organisé des supers vacances dans toute l'Europe, en Sicile, et en Bretagne. Merci à Alexandra pour t'occuper de ma Maman quand je ne suis pas là, merci à Jago pour les ballades aux Saillants, merci à Stéphane pour les journées aux Monteynard et les soirées jeux au Tipi, merci à Bastruite pour sa jovialité, Dorine, Fufu, Bastounet, Carlos, Baptiste, Gabi, Gabi et Robin, Simon, et tous les autres.

Merci à toute la famille qui est montée à Paris pour la soutenance, ça m'a fait très plaisir.

Et le meilleur pour la fin, une attention particulière à mon grand-père Germain pour m'avoir initiée à la science et surtout pour m'avoir donné le goût de la recherche et l'amour de la physique.

Abbreviations

2PT	Second order Perturbation Theory
ADK	Ammosov, Delone and Krainov tunnel ionization formula
Mo-ADK	Molecular ADK tunnel ionization formula
ATI	Above Threshold Ionization
BO	Born-Oppenheimer (approximation)
BS	Bond-Softening
c.c.	complex conjugate
CEP	Carrier Envelope Phase
CI	Configuration Interaction
CIS	Configuration Interaction with Single excitations
CISD	Configuration Interaction with Single and Double excitations
CN	Crank Nicolson algorithm
CPA	Chirped Pulse Amplification
DPT	Degenerate Perturbation Theory
EGS	Electronic Ground State
EM	ElectroMagnetic (field)
EWP	Electron Wave Packet
FFT	Fast Fourier Transform
FFTW	Fastest Fourier Transform in the West library (FFTW) http://fftw.org/
HF	Hartree-Fock
HHG	High order Harmonic Generation
HHS	High order Harmonic generation Spectroscopy
HOMO	Highest Occupied Molecular Orbital
IR	InfraRed (radiation)
LCAO	Linear Combination of Atomic Orbitals
LF	Lochfraß

LL	Landau and Lifshitz
NWP	Nuclear Wave Packet
PES	Potential Energy Surface
PPT	Perelomov, Popov and Terent'ev tunnel ionization formula
PWA	Plane Wave Approximation
REMPI	Resonance-Enhanced MultiPhoton Ionization
RK4	Fourth order Runge-Kutta
SAE	Single Active Electron (approximation)
SC	Smirnov and Chibisov
SCF	Self Consistent Field
fs	femtosecond 1 fs $= 10^{-15}$ s
as	attosecond 1 as $= 10^{-18}$ s
SFA	Strong Field Approximation
SI	International System of units (Système International)
SPA	Saddle Point Approximation
STFT	Short Time Fourier Transform
TDCI	Time-Dependent Configuration Interaction
TDDFT	Time-Dependent Density Functional Theory
TDSE	Time-Dependent Schrödinger Equation
Ti:Sa	Titanium-Sapphire
TISE	Time-Independent Schrödinger Equation
arb. unit	arbitrary unit
a.u.	atomic units
XUV	Extreme UltraViolet (radiation)

Nomenclature

Atomic quantities

p Electron momentum.
r Electron position.
$\hat{H}_0$ Field-free Hamiltonian.
E_i Bound energies of $\hat{H}_0$.
$|\varphi_i\rangle$ Bound eigenstates of $\hat{H}_0$.
E_0 Groundstate energy of $\hat{H}_0$.
$|\varphi_0\rangle$ Groundstate of $\hat{H}_0$.
$|\varphi_E\rangle$ Continuum eigenstates of energy E of $\hat{H}_0$.
ϕ_a Atomic orbital for the LCAO approximation of $|\varphi_0\rangle$.
I_p Ionization potential.
μ Nuclei reduced mass.
R Internuclear vector.
V_0 Atomic or molecular potential.
a Regularization parameter of the Soft Coulomb potential.
V_ee Interelectronic repulsion.
V_NN Internuclear repulsion.

Laser quantities

$\mathbf{A}_\mathrm{L}$ Vector potential of the laser field.
V_L Electric potential of the laser field.
ϕ_cep Carrier envelop phase.
F_0 Peak amplitude of the laser electric field.
$\mathbf{F}_\mathrm{L}$ Laser electric field.
I_L Peak intensity of the laser pulse.
λ_L Central wavelength of the laser field.
N_c Number of optical cycles in the pulse.
T_L Laser pulse period.
τ_L Laser pulse duration.
U_p Ponderomotive potential.
ω_L Central frequency of the laser field.

SFA quantities

d_ion Ionization dipole matrix element.
$\mathbf{d}_\mathrm{rec}$ Recombination dipole matrix element.
D Dipole. General notation for the position, velocity or acceleration dipole.

M Molecular ionization dipole matrix element.
$\mathbf{L}$ Molecular recombination dipole matrix element.
$\mathbf{p}_{\text{at}}$ Atomic stationary momentum, solution of (I.104).
t'_{at} Atomic ionization time, solution of (I.104).
t_{at} Atomic recombination time, solution of (I.104).
$\mathbf{p}_{\alpha\beta}$ Molecular stationary momentum, solution of (I.120).
$t'_{\alpha\beta}$ Molecular ionization time, solution of (I.120).
$t_{\alpha\beta}$ Molecular recombination time, solution of (I.120).
t' Ionization time.
t Recombination time.

Other quantities

$\mathbf{j}$ Flux of electronic density.
$\hat{H}$ Time-dependent Hamiltonian.
$\hat{H}_{\text{l}}$ Length gauge Hamiltonian.
$\hat{H}_{\text{v}}$ Velocity gauge Hamiltonian.
Γ Ionization rate.
Γ_{SC} Ionization rate of Smirnov ad Chibisov (III.1).
$\widetilde{\Gamma}_{\text{SC}}$ Corrected ionization rate (III.20).
γ Keldysh parameter.
ψ_{l} Length gauge time-dependent wave function.
ψ_{v} Velocity gauge time-dependent wave function.
E_{S} Stark shift.
$\widetilde{I_{\text{p}}}$ Corrected ionization potential.
t_{i} Initial time in the semi-classical model.
t_{r} 1^{st} Return time in the semi-classical model.
ω_{c} Cutoff frequency.
x_α Limit distance between short and long trajectories: the short trajectories never go beyond x_α, while the long trajectories always do..

Simulation parameters

L_{sep} End of the absorber used for trajectory separation.
h_{abs} Absorber width.
h_{sep} Width of the absorber used for trajectory separation.
ζ Absorber exponent.
Δt Simulation time step.
n_t Number of time steps per laser cycle.
Δx Simulation grid space step.
L Size of the simulation box.
N_x Number of grid points.
L_W Size of the box used for the window analysis.
γ_W Half width of the window operator.

Introduction

Light and matter are amongst the physicist's favorite objects. They may interact in such an immense variety of ways that they open virtually infinite possibilities. This gives rise, not only to one of the richest and most active fields of physics, but also to an ever growing number of practical tools to design new physical experiments. To give just an example, the fundamental process of *stimulated emission*, which is induced by the interaction between a photon and an atom, allowed to develop the laser (for Light Amplification by Stimulated Emission of Radiation) that one can nowadays find in every laboratory, from the optical table to the conference room.

The uncontested success of the laser as a universal tool for a wide panel of applications comes from its remarkable properties. It emits a monochromatic, intense, but most important of all, *coherent* radiation. This last attribute makes it the perfect tool to study the quantum nature of matter, and thus to question its most fundamental properties. Since the pioneer invention of the maser (Microwave Amplification by Stimulated Emission of Radiation) in the 50s and the subsequent development of the laser in the 60s, tremendous efforts have been made to improve all the characteristics of this celebrated light source. New wavelength bands have been made available, and some lasers now even have the possibility to tune their wavelength over given spectral ranges. The intensity of the emitted light was increased by several orders of magnitude, opening the way for the development of strong field physics [1]. In particular, the invention of the revolutionary Chirped Pulse Amplification (CPA) [2] was a real breakthrough for the generation of laser pulses of much higher intensities. For pulsed lasers, the duration of the pulse could be reduced to the Fourier limit of one optical cycle, reaching pulses of only a few femtoseconds (1 fs $= 10^{-15}$ s). This incredible achievement was at the origin of the *femtochemistry* experiments pioneered by Zewail [3, 4], that could explore molecular dynamics, i.e. chemical reactions, at such short time scales.

These improvements of the laser, and in particular the possibility to reach very high intensities (from 10^{14} W.cm^{-2} to 10^{22} W.cm^{-2}), led to the discovery of highly non-linear processes like Above Threshold Ionization (ATI) in 1979 [5], non-sequential multiple ionization in 1982 [6], or High order Harmonic Generation (HHG) by two different groups in 1987 [7] and 1988 [8]. These findings initiated extensive theoretical works in order to unveil the mechanisms behind such non-linear processes [9–11], which even today remains an active field of research. But beyond its intrinsic fundamental interest, the discovery of HHG originated a real revolution. It enabled the generation of coherent light pulses in the Extreme UltraViolet (XUV) regime, which is still impossible nowadays for optical lasers, with the shortest time durations ever produced. These pulses can last only a few tens of attoseconds (1 as $= 10^{-18}$ s) [12–14], the current world record being of 43 as [15],

and thus offer the possibility to study *electronic* dynamics at its natural time scale.

This new light source gave birth to a whole new field of science: attosecond physics [16–19]. It was used to measure attosecond photoionization time delays in rare gases like Neon [20] and Argon [21], but also in more complex systems like chiral molecules [22] and solids [23, 24]. The dynamics of fundamental processes like Auger decay [25], or tunnel ionization [26] could be assessed experimentally. Electron dynamics could be reconstructed with attosecond resolution in atoms [27], molecules [28] and solids [29–31]. Dynamical electronic correlations were observed through the attosecond dynamics of a Fano resonance in Helium [32, 33]. Sub-femtosecond nuclear dynamics could be measured in molecules [34]. Attosecond physics now also extends to nanoscale structures [35–37] for which the near fields that originates from light interaction with nanostructures may be used to assess and control attosecond electron dynamics and scattering [38–40].

Besides its prodigious properties, which have made it a now widespread light source, the light that is emitted in HHG also contains a lot of structural and dynamical information on the emitting system itself. This has contributed to the development of a new type of spectroscopy that relies on HHG as a *self-probe* [41]. This new technique allows to measure attosecond nuclear dynamics [42–44], to image time-dependent electron wave packets [45], to reconstruct the orbitals of the system through tomography [46–48], to follow multielectron dynamics in atoms [49], molecules [50] and solids [51], to discriminate enantiomers of chiral molecules [52–54] and resolve chiral dynamics in molecules [55], or to reveal dynamical symmetries in atoms and molecules [56].

All these exciting new achievements urge the need for advanced theoretical and numerical methods to analyze, explain and design all these experiments. Indeed the interaction between atoms and photons is often understood by means of the powerful time-dependent perturbation theory. Yet this theory is only adequate to model the linear, or moderately non-linear, processes that arise in moderately intense laser fields. In the case of HHG and other highly non-linear processes, the intensity of the laser electric field is comparable with the interaction between the electron and the nuclei, so that it cannot be considered as a perturbation. The theoretical description of the electron dynamics in such strong fields thus supposes to solve the Time-Dependent Schrödinger Equation (TDSE):

$$\mathrm{i}\hbar\frac{\mathrm{d}\,|\Psi(t)\rangle}{\mathrm{d}t} = \hat{H}(t)\,|\Psi(t)\rangle$$

which involves the time-dependent wave function $|\Psi(t)\rangle$ that entirely describes the state of the system, and the time-dependent Hamiltonian $\hat{H}(t)$ that governs its dynamics. However this approach gives, in itself, very little insight on the physical processes affecting the system. Indeed, since the wave function is not a physical observable, it is not directly measurable and hence remains very difficult to interpret as such.

During my PhD, I relied on two different strategies to extract physical interpretation on strong field processes. On the one hand, I considered simplified model systems in low dimensions for which I could perform extensive numerical simulations. This allowed me to explicitly solved the TDSE for many different field and system parameters, and to subsequently carry out various analyses on the obtained time-dependent wave function. On the other hand I built approximate analytical models to describe the system dynamics. The two approaches are highly complementary, and their confrontation enables a deep assessment of the different approximations that are at the basis of the models.

The aim of this thesis is to explore the different aspects of the dynamics of atoms and molecules triggered by strong laser fields. In a first chapter I review the different methods that are commonly invoked to understand the interaction between light and matter. In particular I will present the celebrated three-step model that is at the basis of most of the physical intuition we now have on strong field processes. Then I present the different model systems for which I solved the TDSE, and I detail the numerical methods that I used to simulate and analyze their dynamics in a laser field. In chapters III, IV and V, I present my results on tunnel ionization, two-center interferences in diatomic molecules revealed by HHG, and on the electron-nuclei correlations observed in the vibronic dynamics of H_2. In a last chapter, for the main part realized in collaboration with Felipe Zapata Abellán, Emanuele Coccia, Julien Toulouse, Valérie Véniard and Eleonora Luppi from the Laboratoire de Chimie Théorique at Sorbonne Université, I explore the possibility of solving the TDSE for larger and more complex systems, and thus simulate correlated dynamics in multielectronic molecules.

Chapter I

Atoms and molecules in strong fields

This chapter is intended to be a roadmap in the vast and flourishing field of light-matter interaction. For experimental reasons, this field is central in atomic and molecular physics. Indeed, light is a remarkably versatile tool to study matter at the atomic level, be it at the atomic length scale, from one Ångström to several nanometers, or at the atomic time scale, from one attosecond to several seconds. In particular, the coherent nature of laser light is very powerful to reveal the quantum nature of matter, which is at the source of a rich variety of physical phenomena. Among them one finds linear processes such as emission, absorption and diffusion, moderately non linear processes such as multiple photons transitions, Raman diffusion, Resonance-Enhanced MultiPhoton Ionization (REMPI), and highly non linear processes such as HHG, ATI, and tunnel ionization. Using these phenomena as a toolbox, one can use photons to prepare and measure quantum states of atoms and molecules [57, 58], laser pulses to initiate, control, and track atomic and molecular dynamics over time [59, 50, 60, 32, 61], and synchrotron or free electron laser sources to visualize systems at different length scales [62–66]. One may also use counter-propagating laser beams to create optical lattices and trap cold atoms or ions and investigate fundamental questions of quantum mechanics [67, 68]. The list of utilizations of photons to control and measure atoms and molecules is interminable [69].

From another point of view, one may also see atoms as an effective tool to analyze and manipulate photons. In non linear optics, where the Holy Grail is to make photons interact with photons, atoms are promising candidates to mediate such interactions [70]. Atoms may also be used to prepare and measure photons in a given quantum state and question the fundamental quantum properties of light [71]. Ensembles of atoms are used to drastically slow and even trap light pulses [72–74]. Often used in strong field physics, the photoionization of an atom converts a photon into a photoelectron and allows to retrieve all information on the incoming photons by the detection of the outcoming electron [75–77, 12].

In this chapter we do not pretend to be exhaustive, but rather to introduce the theoretical models and pictures that allow oneself to get a physical intuition in this field. We will start by the description of a mono-electronic atom in an ElectroMagnetic (EM) field. We will remain in the so-called semi-classical description of the atom-field interaction, which means that the atom will be described by quantum mechanics but the EM field will be classical. In this framework we will derive the time-dependent Schrödinger equation that is the core of the theoretical description of light-matter interaction. Atomic

units (a.u.) are used throughout this thesis, unless otherwise stated.

Objectives

- Derive the TDSE in the two commonly used gauges (length and velocity), and discuss their relative properties.
- Find approximate solutions of the TDSE in the multi-photon regime with the time-dependent perturbation theory.
- Describe the new extremely non-linear processes that appear in the tunnel regime.
- Find interpretative models to explain the mechanisms behind these non-linear processes.

I.1 Time-Dependent Schrödinger Equation

We present the case of a single atom, ion, or molecule, with only one electron, e.g. the H atom or H_2^+ molecular ion, but most of the conclusions we draw are general and also hold for multielectronic systems. Our approach is largely inspired from the lecture notes of Jean Michel Raimond *Atoms and Photons* [78].

Our system is defined by its field-free Hamiltonian, which reads, in atomic units:

$$\hat{H}_0 = \frac{\hat{\mathbf{p}}^2}{2} + V_0(\hat{\mathbf{r}}), \tag{I.1}$$

where $\hat{\mathbf{r}}$ and $\hat{\mathbf{p}}$ are the position and momentum operators, and V_0 is the atomic potential generated by the nuclei and the possible remaining electrons. Since this Hamiltonian is time-independent, the dynamics can be deduced from solutions of the Time-Independent Schrödinger Equation (TISE):

$$\hat{H}_0 \left|\varphi\right\rangle = E \left|\varphi\right\rangle . \tag{I.2}$$

The solutions of this equation, i.e. the eigenstates and eigenvalues of $\hat{H}_0$, will be labelled $|\varphi_i\rangle$ and E_i for the bound states. In particular we will write $|\varphi_0\rangle$ for the ground state of energy E_0. The continuum states $|\varphi_{E,\beta}\rangle$ are in general infinitely degenerated so that the state is not solely determined by its energy E, but by a set of quantum numbers that we will denote as β. This label β can e.g. contain the orbital quantum numbers ℓ and m for an atom, or the electron momentum components k_x,k_y for a free electron. To alleviate the notation we will explicitly specify β only when required, and the degenerate continuum states of energy E will be denoted by $|\varphi_E\rangle$.

In the presence of an EM field, the Hamiltonian $\hat{H}$ becomes time-dependent, so that the evolution of the system is described by the TDSE:

$$\mathrm{i}\frac{\mathrm{d}}{\mathrm{d}t}|\psi(t)\rangle = \hat{H}|\psi(t)\rangle, \tag{I.3}$$

where ψ is the time-dependent wave function. The Hamiltonian $\hat{H}$ is exactly the same as the Hamiltonian of a classical electron in a classical EM field, but with the position $\mathbf{r}$ and momentum $\mathbf{p}$ replaced by their operator counterparts:

$$\hat{H} = \frac{1}{2}\left[\hat{\mathbf{p}} + \mathbf{A}_\mathrm{L}(\hat{\mathbf{r}}, t)\right]^2 + V_0(\hat{\mathbf{r}}) - V_\mathrm{L}(\hat{\mathbf{r}}, t), \tag{I.4}$$

where $\mathbf{A}_\mathrm{L}$ is the vector potential and V_L the scalar electric potential of the field[1]. In the following, the EM field will almost always be generated by a laser, thus we will use the subscript L for the related quantities. Note that in this expression we have neglected the effect of the magnetic field on the system, and particularly on the spins of the system. This approximation will hold as long as the field intensity I_L is not too high, typically $I_\mathrm{L} \lesssim 10^{16}$ W.cm^{-2}. For higher intensity regimes, one would have to use a relativistic description of the electron.

In classical electrodynamics [79], only the electric and magnetic fields are physical observables. The vector and scalar potentials are thus defined up to a choice of gauge:

$$\begin{pmatrix} \mathbf{A}_\mathrm{L} \\ V_\mathrm{L} \end{pmatrix} \rightarrow \begin{pmatrix} \mathbf{A}'_\mathrm{L} = \mathbf{A}_\mathrm{L} + \boldsymbol{\nabla}\chi(\mathbf{r},t) \\ V'_\mathrm{L} = V_\mathrm{L} - \dfrac{\partial\chi}{\partial t}(\mathbf{r},t) \end{pmatrix}, \tag{I.5}$$

which has no incidence on the value of the observables. In quantum mechanics, the wave function will be gauge dependent, but not the observables. Among all the possible gauge choices, only two are commonly used in strong field physics: the so-called *velocity* gauge and *length* gauge.

I.1.1 Velocity gauge

This first choice of gauge, usually called *velocity* gauge or AP gauge, is actually based on the well-known Coulomb gauge [79]:

$$\boldsymbol{\nabla}\cdot\mathbf{A}_\mathrm{L} = 0. \tag{I.6}$$

One of the advantages of this choice is that, since there are no source generating the fields (which are *external* fields), we have $V_\mathrm{L} = 0$ [79]. As a consequence, the electric field:

$$\mathbf{F}_\mathrm{L} = -\frac{\partial\mathbf{A}_\mathrm{L}}{\partial t} - \boldsymbol{\nabla}V_\mathrm{L} = -\frac{\partial\mathbf{A}_\mathrm{L}}{\partial t} \tag{I.7}$$

is simply deduced from the vector potential.

To obtain the expression of the TDSE in this gauge, we expand the quadratic term in (I.4). In doing so, we have to be careful because, since the individual coordinates of $\hat{\mathbf{p}}$ and $\hat{\mathbf{r}}$ do not commute, the coordinates of $\hat{\mathbf{p}}$ and $\mathbf{A}_\mathrm{L}(\hat{\mathbf{r}},t)$ do not commute either. Nevertheless we can show that, in the Coulomb gauge:

$$\hat{\mathbf{p}}\cdot\hat{\mathbf{A}}_\mathrm{L} = \hat{\mathbf{A}}_\mathrm{L}\cdot\hat{\mathbf{p}}. \tag{I.8}$$

For this we use the relation

$$\left[\hat{p}^{(i)}, f(\hat{r}^{(i)})\right] = -\mathrm{i}\hbar\frac{\partial f}{\partial\hat{r}^{(i)}}, \tag{I.9}$$

where i stands for any of the three space directions x, y and z. It directly follows that

$$\sum_i \left[\hat{p}^{(i)}, \hat{A}_\mathrm{L}{}^{(i)}\right] = -\mathrm{i}\hbar\boldsymbol{\nabla}\cdot\hat{\mathbf{A}}_\mathrm{L}. \tag{I.10}$$

[1] We use the SI convention for the Maxwell equations. Note that in the gaussian (or cgs) conventon one would have $\hat{H} = \frac{1}{2}\left[\hat{\mathbf{p}} + \frac{1}{c}\mathbf{A}_\mathrm{L}(\hat{\mathbf{r}},t)\right]^2 + V_0(\hat{\mathbf{r}}) - V_\mathrm{L}(\hat{\mathbf{r}},t)$, and $\mathbf{F}_\mathrm{L} = -\frac{1}{c}\frac{\partial\mathbf{A}_\mathrm{L}}{\partial t} - \boldsymbol{\nabla}V_\mathrm{L}$ where c is the speed of light.

And thus

$$\hat{\mathbf{p}} \cdot \hat{\mathbf{A}}_\mathrm{L} = \sum_i \hat{p}^{(i)} \hat{A}_\mathrm{L}{}^{(i)} = \hat{\mathbf{A}}_\mathrm{L} \cdot \hat{\mathbf{p}} + \mathrm{i}\hbar \boldsymbol{\nabla} \cdot \hat{\mathbf{A}}_\mathrm{L}, \tag{I.11}$$

which, using (I.6), gives directly (I.8). In the Coulomb gauge, the time-dependent Hamiltonian finally reads:

$$\hat{H} = \hat{H}_0 + \hat{\mathbf{p}} \cdot \mathbf{A}_\mathrm{L}(\hat{\mathbf{r}}, t) + \frac{1}{2} A_\mathrm{L}(\hat{\mathbf{r}}, t)^2. \tag{I.12}$$

This expression is actually quite difficult to handle, and we will need to make two last steps to get the commonly used velocity gauge Hamiltonian. First we perform the so-called *dipole* approximation: we assume that the wavelength λ_L of the laser is much larger than the typical size of the atom i.e. $\lambda_\mathrm{L} \ll 1$ Å. This allows to neglect the $\mathbf{r}$ dependency in all field quantities by taking their value at $\mathbf{r} = 0$. Second we get rid of the quadratic term in $\mathbf{A}_\mathrm{L}$ by performing the unitary transform:

$$|\psi(t)\rangle \to \mathrm{e}^{-\frac{\mathrm{i}}{2}\int A_\mathrm{L}(\tau)^2 \mathrm{d}\tau} \tag{I.13}$$

Eventually, we get the velocity gauge time-dependent Hamiltonian as:

$$\boxed{\hat{H}_\mathrm{v} = \hat{H}_0 + \hat{\mathbf{p}} \cdot \mathbf{A}_\mathrm{L}(t)}, \tag{I.14}$$

where we have dropped the $\hat{\mathbf{r}}$ dependency in $\mathbf{A}_\mathrm{L}$ for clarity.

I.1.2 Length gauge

The other commonly used choice of gauge is called *length* or ER gauge. To derive the TDSE in that case, we will start with the Hamiltonian (I.4) and expand the quadratic term with care regarding the non-commutativity of $\hat{\mathbf{p}}$ and $\mathbf{A}_\mathrm{L}$:

$$\hat{H} = \hat{H}_0 - V_\mathrm{L}(\hat{\mathbf{r}}, t) + \frac{1}{2}\hat{\mathbf{p}} \cdot \mathbf{A}_\mathrm{L}(\hat{\mathbf{r}}, t) + \frac{1}{2}\mathbf{A}_\mathrm{L}(\hat{\mathbf{r}}, t) \cdot \hat{\mathbf{p}} + \frac{1}{2} A_\mathrm{L}(\hat{\mathbf{r}}, t)^2. \tag{I.15}$$

First we make the same approximation we did in the previous section, i.e. we neglect the term quadratic in $\mathbf{A}_\mathrm{L}$. Second, we also make the dipole approximation, but this time keeping the first order in $\hat{\mathbf{r}}$ in the development of V_L:

$$V_\mathrm{L}(\hat{\mathbf{r}}, t) = V_\mathrm{L}(0, t) + \hat{\mathbf{r}} \cdot \boldsymbol{\nabla} V_\mathrm{L}(0, t). \tag{I.16}$$

The scalar $V_\mathrm{L}(0, t)$ can be dropped since it will only induce a time-dependent global phase on the wave function. We obtain:

$$\hat{H} = \hat{H}_0 - \hat{\mathbf{r}} \cdot \boldsymbol{\nabla} V_\mathrm{L}(0, t) + \frac{1}{2}\hat{\mathbf{p}} \cdot \mathbf{A}_\mathrm{L}(0, t) + \frac{1}{2}\mathbf{A}_\mathrm{L}(0, t) \cdot \hat{\mathbf{p}}. \tag{I.17}$$

We then chose a gauge function χ so that the new vector potential $\mathbf{A}'_\mathrm{L}(0, t) = 0$ cancels at the origin at all times t, e.g.:

$$\chi(\mathbf{r}, t) = -\mathbf{r} \cdot \mathbf{A}_\mathrm{L}(0, t). \tag{I.18}$$

The gradient of this function is equal to $-\mathbf{A}_\mathrm{L}(0,t)$. It is thus easy to see from (I.5) that this gauge function fulfils our condition $\mathbf{A}'_\mathrm{L}(0,t) = 0$. The new scalar potential reads:

$$V'_\mathrm{L}(\mathbf{r},t) = V_\mathrm{L}(\mathbf{r},t) + \mathbf{r}\cdot\frac{\partial \mathbf{A}_\mathrm{L}}{\partial t}(0,t). \tag{I.19}$$

By taking its gradient at $\mathbf{r} = 0$, we obtain:

$$\boldsymbol{\nabla} V'_\mathrm{L}(0,t) = \boldsymbol{\nabla} V_\mathrm{L}(0,t) + \frac{\partial \mathbf{A}_\mathrm{L}}{\partial t}(0,t) = -\mathbf{F}_\mathrm{L}(0,t), \tag{I.20}$$

which is exactly the expression of the electric field at the origin. This gives the final expression for the Hamiltonian in length gauge:

$$\boxed{\hat{H}_\mathrm{l} = \hat{H}_0 + \hat{\mathbf{r}}\cdot\mathbf{F}_\mathrm{L}(t),} \tag{I.21}$$

where, again for clarity, we have dropped the $\hat{\mathbf{r}}$ dependency in $\mathbf{F}_\mathrm{L}$. Note that in this expression, the atom-field interaction Hamiltonian has exactly the same form $-\mathbf{d}\cdot\mathbf{F}$ as the one of a classical electric dipole $\mathbf{d}$ in a classical electric field $\mathbf{F}$. This is quite satisfactory since it is common to think of the atom as an electric dipole $\mathbf{d}$ with instantaneous value $\mathbf{d}(t) = -\mathbf{r}$ the position of the electron relative to the nucleus. It is also more intuitive to think in the $\mathbf{r}$ representation than in the $\mathbf{p}$ representation. For these reasons, this is the form that we mainly use in analytic developments.

I.1.3 Relation between length and velocity gauges

The two gauges we just described are equivalent for observables. However wave functions, and populations in the different bound $|\varphi_i\rangle$ and continuum $|\varphi_E\rangle$ states will be gauge dependent in presence of the field. We can show that the velocity and length gauges are actually related by a unitary transform, i.e. there exists a unitary operator $U(t)$ ($U^\dagger U = \mathbb{1}$) exchanging the length ψ_l and velocity ψ_v gauge wave functions:

$$|\psi_\mathrm{l}(t)\rangle = U(t)\,|\psi_\mathrm{v}(t)\rangle\,. \tag{I.22}$$

To find $U(t)$, we start by the Hamiltonian (I.4), in the Coulomb gauge i.e. with $V_\mathrm{L} = 0$, with the dipole approximation:

$$\hat{H} = \frac{1}{2}\left[\hat{\mathbf{p}} + \mathbf{A}_\mathrm{L}(0,t)\right]^2 + V_0(\hat{\mathbf{r}}). \tag{I.23}$$

The velocity gauge wave function ψ_v evolves under this Hamiltonian, therefore the transformed wave function ψ_l evolves under the transformed Hamiltonian:

$$\hat{H}_\mathrm{l} = U\hat{H}U^\dagger + \mathrm{i}\frac{\mathrm{d}U}{\mathrm{d}t}U^\dagger. \tag{I.24}$$

If we now choose

$$U(t) = \mathrm{e}^{\mathrm{i}\hat{\mathbf{r}}\cdot\mathbf{A}_\mathrm{L}(0,t)}, \tag{I.25}$$

then we have

$$U\left(\hat{\mathbf{p}} + \mathbf{A}_\mathrm{L}(0,t)\right)^2 U^\dagger = \hat{\mathbf{p}}^2 \tag{I.26}$$

and

$$\mathrm{i}\frac{\mathrm{d}U}{\mathrm{d}t}U^\dagger = -\mathbf{r}\cdot\frac{\partial \mathbf{A}_\mathrm{L}}{\partial t}(0,t) = \mathbf{r}\cdot\mathbf{F}_\mathrm{L}(0,t), \tag{I.27}$$

since $V_\mathrm{L} = 0$ in the Coulomb gauge. The atomic potential V_0 is unchanged by the transformation $UV_0U^\dagger = V_0$ because the two operators commute. Thus we get:

$$\hat{H}_\mathrm{l} = \hat{H}_0 + \hat{\mathbf{r}}\cdot\mathbf{F}_\mathrm{L}(t), \tag{I.28}$$

which is exactly the Hamiltonian in length gauge I.21. The relation between the length and velocity gauge wave functions finally reads:

$$\boxed{|\psi_\mathrm{l}(t)\rangle = \mathrm{e}^{\mathrm{i}\hat{\mathbf{r}}\cdot\mathbf{A}_\mathrm{L}(0,t)}\,|\psi_\mathrm{v}(t)\rangle\,.} \tag{I.29}$$

Note that the operators that do not commute with $\hat{\mathbf{r}}$ are thus gauge dependent:

$$\hat{O}_l = \mathrm{e}^{\mathrm{i}\hat{\mathbf{r}}\cdot\mathbf{A}_\mathrm{L}(0,t)}\,\hat{O}_v\,\mathrm{e}^{-\mathrm{i}\hat{\mathbf{r}}\cdot\mathbf{A}_\mathrm{L}(0,t)}, \tag{I.30}$$

but their expectation values are not:

$$\begin{aligned}
\langle\psi_\mathrm{l}|\hat{O}_l|\psi_\mathrm{l}\rangle &= \langle\psi_\mathrm{v}|\mathrm{e}^{-\mathrm{i}\hat{\mathbf{r}}\cdot\mathbf{A}_\mathrm{L}(0,t)}\,\hat{O}_l\,\mathrm{e}^{\mathrm{i}\hat{\mathbf{r}}\cdot\mathbf{A}_\mathrm{L}(0,t)}|\psi_\mathrm{v}\rangle && \text{(I.31)}\\
&= \langle\psi_\mathrm{v}|\mathrm{e}^{-\mathrm{i}\hat{\mathbf{r}}\cdot\mathbf{A}_\mathrm{L}(0,t)}\,\mathrm{e}^{\mathrm{i}\hat{\mathbf{r}}\cdot\mathbf{A}_\mathrm{L}(0,t)}\,\hat{O}_v\,\mathrm{e}^{-\mathrm{i}\hat{\mathbf{r}}\cdot\mathbf{A}_\mathrm{L}(0,t)}\,\mathrm{e}^{\mathrm{i}\hat{\mathbf{r}}\cdot\mathbf{A}_\mathrm{L}(0,t)}|\psi_\mathrm{v}\rangle && \text{(I.32)}\\
&= \langle\psi_\mathrm{v}|\hat{O}_v|\psi_\mathrm{v}\rangle\,. && \text{(I.33)}
\end{aligned}$$

Besides the projection of $|\psi_\mathrm{l}\rangle$ and $|\psi_\mathrm{v}\rangle$ on the different eigenstates of $\hat{H}_0$ may also differ. However, if the EM field takes the form of a laser pulse with a finite time duration, then the two wave functions coincide as soon as the laser is switched off, and so do the operators.

I.1.4 Comparison between length and velocity gauges

As we have seen, the two exposed gauges are perfectly equivalent in the sense that they describe the same physics. However, when we look for approximate solution of the TDSE, the results may be dependent of the choice of gauge. In particular if we numerically solve the TDSE, then the different gauges may have different numerical properties, i.e. different accuracies, or different convergence behaviors. In general the velocity gauge has better numerical performance than the length gauge [80, 81] for the description of ionization. This can be intuitively interpreted by the following consideration: an electron ionized by an EM field has generally a bound velocity, i.e. a bound $\mathbf{p}$, so that the AP interaction Hamiltonian is bounded, while its position $\mathbf{r}$ can go to infinity, and so can the ER interaction Hamiltonian. To give an illustrative example, we numerically solved the TDSE in the two gauges for a model system which is a one dimensional analogue of H_2^+ (see sections VI.1 and II.1.1 for details). We exposed this 1D H_2^+ at its fixed equilibrium internuclear distance $R = 1$ Å to a short laser pulse of central wavelength $\lambda_\mathrm{L} = 800$ nm, intensity $I_\mathrm{L} = 10^{14}$ W.cm^{-2}, and with a trapezoidal envelope of total duration τ_L of 10 optical cycles, i.e. $\tau_\mathrm{L} = 27$ fs, with linear ramps of 1 optical cycle. The energy distribution of the wave function at the end of the pulse is plotted in Figure I.1 for the

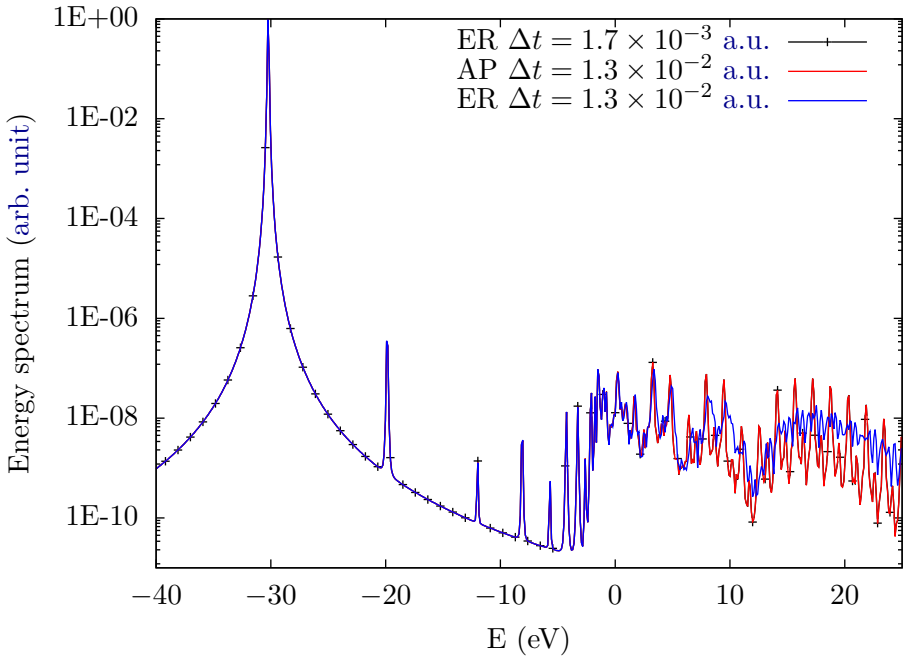

Figure I.1 *Energy distribution of the 1D* H_2^+ *at the end of the laser pulse computed with the window method [82] (see section II.3.4).*

two different gauges and for different values of the time step Δt. We see on the figure that for $\Delta t = 1.3 \times 10^{-2}$ a.u. the results obtained in the velocity (in red) and length (in blue) gauge do not coincide in the positive energy region (the continuum). It seems that the final population in the continuum states $|\varphi_E\rangle$ is gauge dependent. However we saw in the previous section that as soon as the laser is switched off, i.e. at the end of the pulse, then the length and velocity wave functions should coincide. The problem here is that the length gauge simulation is not converged at a time step $\Delta t = 1.3 \times 10^{-2}$ a.u., i.e. that the error induced by the propagation algorithm is not negligible. If we perform the same simulation, in length gauge, but at a smaller time step $\Delta t = 1.7 \times 10^{-3}$ a.u. (in black on Figure I.1), then the results perfectly agree with the velocity gauge and the two curves are indistinguishable for the naked eye. This means that, indeed, the numerical solution in each gauge are equivalent as long as the calculation is converged. However the length gauge has a slower convergence than the velocity gauge. We just mention that this observation is actually restricted to Δt, the convergence properties with respect to Δx are very simillar for the two gauges.

We may intuitively think that this is related to numerical accuracy (or inaccuracy) problems, i.e. because of the finite precision of real numbers representation in a computer. We investigated this issue by comparing our numerical results where the wave function is represented on a spatial grid, to numerical simulations performed by Felipe Zapata Abellán during his PhD at the Laboratoire de Chimie Théorique where the wave function is represented on a B-splines basis set (see section VI.1.2). In both cases, the same propagation algorithm is used: a Crank Nicolson (CN) algorithm [83] (see section II.1.2 b)). It is remarkable in Figure I.2 that the results obtained in the grid (in blue) and B-splines

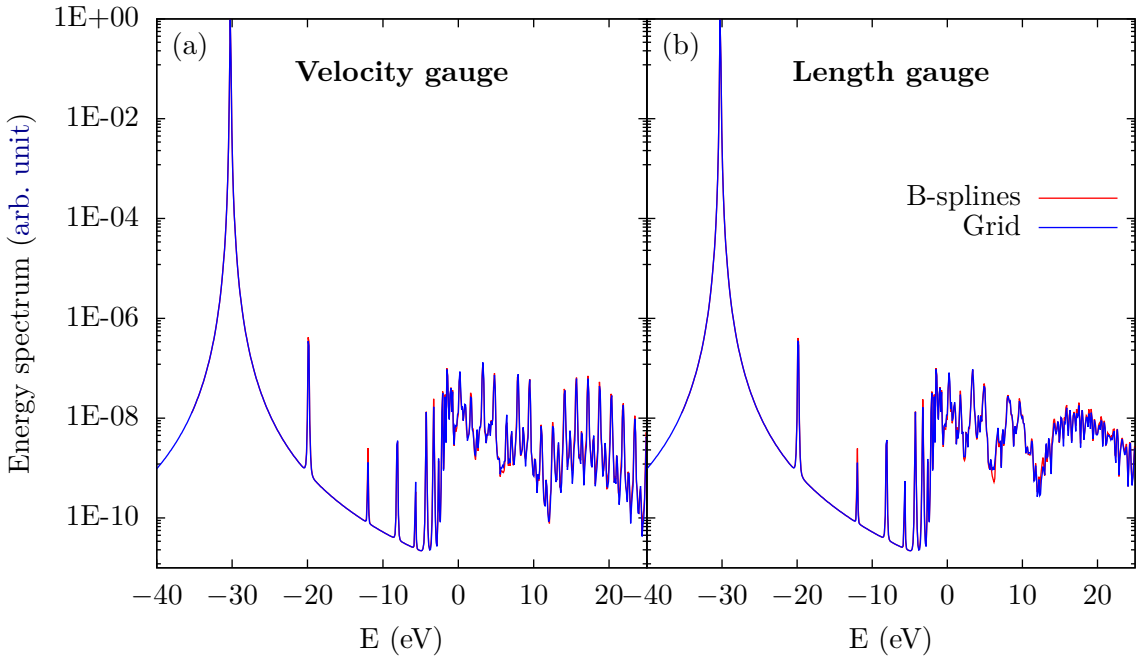

Figure I.2 *Energy distribution of the 1D* H_2^+ *at the end of the laser pulse computed with a Grid and a B-splines representation and in (a) velocity or (b) length gauge. In both cases* $\Delta t = 1.3 \times 10^{-2}$ a.u..

(in red) basis sets are identical. The slow convergence of the length gauge numerical simulation that we just pointed out with the grid is also observed with B-splines. We can therefore conclude that is is a general feature of the CN propagation algorithm.

These disparities between the two gauges are not restricted to numerical computations, they will also come out when we seek approximate solutions of the TDSE. For example in the Strong Field Approximation (SFA) framework (see section I.3.3), the results we obtain are actually gauge dependent. The physical interpretation of these approximate methods can thus be complex, since, as we will see, one of the two gauges may give unphysical results in some cases [84]. To overcome these difficulties a gauge independent formulation of the SFA has recently been developped in [85], however we will not discuss it in more detail in this thesis.

I.2 Time-dependent perturbation theory

When we think of an atom or a molecule interacting with light, in particular in spectroscopy, we like to think in terms of absorption and emission of one or several photons by the atom or the molecule. This intuitive picture of light-matter interaction is rooted in the Time-Dependent Perturbation Theory. No need to say how central this theory is, not only for the treatment of light-matter interaction, but for any quantum problem involving a small time-dependent perturbation to a system. The derivation that we present here is greatly inspired from the well-known book of Cohen-Tannoudji, Diu and Laloë [86].

I.2.1 General time-dependent perturbation

a) Time-dependent Schrödinger equation in the stationary states basis

In this method we suppose that we know exactly the solutions of a time-independent problem, i.e. that we know all the eigenstates and eigenvalues of a Hamiltonian $\hat{H}_0$. In our case it will be the field-free atomic (or molecular) Hamiltonian for the electron. We will consider that, for times $t < 0$, the perturbation $\hat{W}(t)$ is zero, so that the initial state of the system is in an eigenstate $|\varphi_i\rangle$ of $\hat{H}_0$. At time $t = 0$ the perturbation is switched on and the *perturbed* Hamiltonian reads:

$$\hat{H}(t) = \hat{H}_0 + \lambda \hat{W}(t), \tag{I.34}$$

where $\lambda \ll 1$ and $\hat{W}$ is comparable to $\hat{H}_0$. In our case this perturbation $\lambda\hat{W}(t)$ will be the interaction Hamiltonian $\hat{\mathbf{p}} \cdot \mathbf{A}_{\mathrm{L}}(t)$ or $\hat{\mathbf{r}} \cdot \mathbf{F}_{\mathrm{L}}(t)$ depending on the choice of gauge.

The initial state $|\varphi_i\rangle$ is no longer a stationary state of the system and the wave function starts to evolve under the Hamiltonian (I.34). The point of this section is to describe the dynamics of the perturbed system. We will then be interested in the probability $\mathcal{P}_{if}(t)$ to have a transition from the initial state to a final state $|\varphi_f\rangle$ after a time t.

The set of all eigenstates of $\hat{H}_0$ provides a natural basis on which to develop the time-dependent wave function:

$$|\psi(t)\rangle = \sum_j |\varphi_j\rangle \langle\varphi_j|\psi(t)\rangle = \sum_j c_j(t) |\varphi_j\rangle , \tag{I.35}$$

and the perturbation:

$$\hat{W}(t) = \sum_{j,k} |\varphi_j\rangle \langle\varphi_j| \hat{W}(t) |\varphi_k\rangle \langle\varphi_k| = \sum_{j,k} W_{jk}(t) |\varphi_j\rangle \langle\varphi_k| . \tag{I.36}$$

The unperturbed Hamiltonian $\hat{H}_0$ is diagonal in the $\{|\varphi_j\rangle\}$ basis:

$$\hat{H}_0 = \sum_j E_j |\varphi_j\rangle \langle\varphi_j| . \tag{I.37}$$

Inserting (I.35), (I.36) and (I.37) in the TDSE, we get a system of coupled linear differential equations for the coefficients $c_j(t)$:

$$\mathrm{i}\frac{\mathrm{d}c_j}{\mathrm{d}t}(t) = E_j c_j(t) + \lambda \sum_k W_{jk}(t) c_k(t). \tag{I.38}$$

We can get rid of the $\hat{H}_0$ contribution to the dynamics by moving to the interaction representation with respect to $\hat{H}_0$, i.e. by performing the unitary transform

$$|\widetilde{\psi}(t)\rangle = \mathrm{e}^{\mathrm{i}\hat{H}_0 t} |\psi(t)\rangle . \tag{I.39}$$

In this representation, the coefficients become:

$$\widetilde{c}_j(t) = \mathrm{e}^{\mathrm{i}E_j t} c_j(t). \tag{I.40}$$

Introducing the Bohr angular frequency:

$$\omega_{jk} = E_j - E_k, \tag{I.41}$$

we get the final system of coupled differential equations:

$$\mathrm{i}\frac{\mathrm{d}\widetilde{c}_j}{\mathrm{d}t}(t) = \lambda \sum_k W_{jk}(t)\, \mathrm{e}^{\mathrm{i}\omega_{jk}t}\, \widetilde{c}_k(t), \tag{I.42}$$

that we need to solve to access the dynamics of the perturbed system.

Up to now we haven't made any approximations on the perturbation $\hat{W}$. However, there is in general no direct solution to the *exact* system of equations (I.42). Time-dependent perturbation theory is one way to get an *approximate* solution to (I.42). The principle is to consider that, since $\lambda \ll 1$, $\lambda\hat{W}$ can be considered small with respect to the unperturbed Hamiltonian $\hat{H}_0$. In that case we can suppose that the coefficient $\widetilde{c}_j(t)$ are close to their value $\widetilde{c}_j^{(0)}(t)$ without the perturbation. We can thus, in analogy with a Taylor expansion, expand them in powers of λ:

$$\widetilde{c}_j(t) = \widetilde{c}_j^{(0)}(t) + \lambda\widetilde{c}_j^{(1)}(t) + \lambda^2\widetilde{c}_j^{(2)}(t) + \dots. \tag{I.43}$$

When we insert this in (I.42), we get

$$0 = \mathrm{i}\frac{\mathrm{d}\widetilde{c}_j^{(0)}}{\mathrm{d}t}(t) + \sum_{n\geq 1} \lambda^n \underbrace{\left(\mathrm{i}\frac{\mathrm{d}\widetilde{c}_j^{(n)}}{\mathrm{d}t}(t) - \sum_k W_{jk}(t)\, \mathrm{e}^{\mathrm{i}\omega_{jk}t}\, \widetilde{c}_k^{(n-1)}(t) \right)}_{\mathcal{Z}_n(t)}. \tag{I.44}$$

Since this has to be true for any value of λ (provided that λ remains small enough), then each individual term $\mathcal{Z}_n(t)$ has to be equal to zero:

$$\mathrm{i}\frac{\mathrm{d}\widetilde{c}_j^{(n)}}{\mathrm{d}t}(t) = \sum_k W_{jk}(t)\, \mathrm{e}^{\mathrm{i}\omega_{jk}t}\, \widetilde{c}_k^{(n-1)}(t), \quad n \geq 1. \tag{I.45}$$

We can therefore compute the $\widetilde{c}_j^{(n)}(t)$ recursively, starting from the unperturbed coefficients computed when $\lambda = 0$:

$$\widetilde{c}_j^{(0)}(t) = \delta_{ij}. \tag{I.46}$$

b) First order solution

The first order coefficients $\widetilde{c}_j^{(1)}(t)$ are solutions of the differential equation:

$$\mathrm{i}\frac{\mathrm{d}\widetilde{c}_j^{(1)}}{\mathrm{d}t}(t) = W_{ji}(t)\, \mathrm{e}^{\mathrm{i}\omega_{ji}t}, \tag{I.47}$$

which can be integrated as

$$\widetilde{c}_j^{(1)}(t) = -\mathrm{i}\int_0^t W_{ji}(t')\, \mathrm{e}^{\mathrm{i}\omega_{ji}t'}\, \mathrm{d}t'\,. \tag{I.48}$$

After a time t, the transition probability $\mathcal{P}_{if}(t)$ is equal to the population in state $|\varphi_f\rangle$. To first order, we get

$$\mathcal{P}_{if}^{(1)}(t) = \left|\lambda c_f^{(1)}(t)\right|^2 = \left|\lambda \widetilde{c}_f^{(1)}(t)\right|^2 \tag{I.49}$$

$$= |\lambda|^2 \left| \int_0^t W_{ji}(t')\, \mathrm{e}^{\mathrm{i}\omega_{ji}t'}\, \mathrm{d}t' \right|^2 . \tag{I.50}$$

c) Higher orders solution

The higher order solutions are then deduced recursively. The second order reads

$$\widetilde{c}_j^{(2)}(t) = -\sum_k \int_0^t \mathrm{d}t_2\, W_{jk}(t_2)\, \mathrm{e}^{\mathrm{i}\omega_{jk}t_2} \int_0^{t_2} \mathrm{d}t_1\, W_{ki}(t_1)\, \mathrm{e}^{\mathrm{i}\omega_{ki}t_1}, \tag{I.51}$$

which can be written in another form:

$$\begin{aligned} c_j^{(2)}(t) = -\sum_k \int_0^t \mathrm{d}t_2 \int_0^{t_2} \mathrm{d}t_1\, \mathrm{e}^{-\mathrm{i}E_j(t-t_2)} \left\langle \varphi_j \right| \hat{W}(t_2) \left| \varphi_k \right\rangle \mathrm{e}^{-\mathrm{i}E_k(t_2-t_1)} \\ \times \left\langle \varphi_k \right| \hat{W}(t_1) \left| \varphi_i \right\rangle \mathrm{e}^{-\mathrm{i}E_i t_1}, \end{aligned} \tag{I.52}$$

where we have used (I.40). It is actually possible to find a physical interpretation of this formula in terms of quantum paths. This interpretation assumes that the states evolve freely i.e. without the perturbation, except at times t_1 and t_2 for which *transitions* between states occur, and the integrations sum up over all the possible transition times.

For a given set of values of k, t_1 and t_2, with obviously $0 < t_1 < t_2 < t$, we look at the integrand, and we read it from right to left. We are initially at time $t = 0$ in state $|\varphi_i\rangle$, and evolve in that state until $t = t_1$. This evolution without any perturbation only involves a phase factor $\mathrm{e}^{-\mathrm{i}E_i t_1}$. Then, at time $t = t_1$, state $|\varphi_i\rangle$ experiences an instantaneous transition to state $|\varphi_k\rangle$ through the perturbation $\hat{W}(t_1)$. This involves the *transition* matrix element $\langle\varphi_k| \hat{W}(t_1) |\varphi_i\rangle$. We are then in state $|\varphi_k\rangle$ from time $t = t_1$ to time $t = t_2$, this adds a phase factor $\mathrm{e}^{-\mathrm{i}E_k(t_2-t_1)}$. There is then a second transition at time $t = t_2$ from state $|\varphi_k\rangle$ to the final state $|\varphi_j\rangle$ with transition matrix element $\langle\varphi_j| \hat{W}(t_2) |\varphi_k\rangle$. Finally, state $|\varphi_j\rangle$ evolves freely from $t = t_2$ to the final time t, adding a phase factor $\mathrm{e}^{-\mathrm{i}E_j(t-t_2)}$. We get the contribution for this precise quantum path. To get the final result, we need to sum the contributions of all possible quantum paths, i.e. we need to integrate over all possible values of t_1 and t_2 and sum over all possible intermediate states k. We eventually recover (I.52).

This general interpretation remains valid for higher orders of perturbation theory. For an arbitrary order n, we get

$$\begin{aligned} c_j^{(n)}(t) = (-\mathrm{i})^n \sum_{k_1,\cdots,k_{n-1}} \int_0^t \mathrm{d}t_n \int_0^{t_n} \mathrm{d}t_{n-1} \cdots \int_0^{t_2} \mathrm{d}t_1\, \mathrm{e}^{-\mathrm{i}E_j(t-t_n)} \left\langle \varphi_j \right| \hat{W}(t_n) \left| \varphi_{k_{n-1}} \right\rangle \\ \times\, \mathrm{e}^{-\mathrm{i}E_{k_{n-1}}(t_n-t_{n-1})} \left\langle \varphi_{k_{n-1}} \right| \hat{W}(t_{n-1}) \left| \varphi_{k_{n-2}} \right\rangle \cdots \left\langle \varphi_{k_1} \right| \hat{W}(t_1) \left| \varphi_i \right\rangle \mathrm{e}^{-\mathrm{i}E_i t_1} . \end{aligned} \tag{I.53}$$

I.2.2 Perturbation by an electromagnetic field

a) n-photons transitions

When the time-dependent perturbation is an EM field, then each *transition* that we just described is interpreted as an *absorption* or *emission* of one photon. Note that this is only an interpretation. Indeed the notion of photon emerges from the quantification of the EM field. Since we treat the EM field classically, our model does not account for photons.

As we said in section I.1.2, the lenth gauge Hamiltonian is more intuitive and hence often preferred for analytic development and interpretative reasoning. We thus express the transition matrix elements in this gauge:

$$\lambda W_{ji} = \mathbf{F}_\mathrm{L} \cdot \langle \varphi_j | \, \hat{\mathbf{r}} \, | \varphi_i \rangle \tag{I.54}$$

$$= \mathbf{F}_\mathrm{L} \cdot \mathbf{d}_{ji}, \tag{I.55}$$

where $\mathbf{d}_{ji}$ is the transition dipole moment. If the field is linearly polarized, i.e.:

$$\mathbf{F}_\mathrm{L} = F_\mathrm{L}(t)\mathbf{u}_z, \tag{I.56}$$

then we have:

$$\lambda W_{ji} = F_\mathrm{L}(t) d_{ji}^{(z)}. \tag{I.57}$$

The transition probability from a state $|\varphi_i\rangle$ to another state $|\varphi_f\rangle$ upon absorption or emission of one photon will thus be proportional to $\left|d_{fi}^{(z)}\right|^2$. This imposes strict conditions on the relative symmetry of $|\varphi_i\rangle$ and $|\varphi_f\rangle$ for which $d_{fi}^{(z)}$ does not vanish, that are called *selection rules*. In the case of an atom, to satisfy these selection rules, the initial and final orbitals of the electron have to differ in orbital angular momentum by exactly $\Delta\ell = \pm 1$.

We can go a little bit further in the case of a sinusoidal electric field:

$$F_\mathrm{L}(t) = F_0 \sin(\omega_\mathrm{L} t). \tag{I.58}$$

The first order coefficient (I.48) can be computed exactly in that case:

$$\lambda \tilde{c}_j^{(1)}(t) = -\frac{\mathrm{i} F_0 d_{ji}^{(z)}}{2} \left(\frac{1 - \mathrm{e}^{\mathrm{i}(\omega_{ji} + \omega_\mathrm{L})t}}{\omega_{ji} + \omega_\mathrm{L}} - \frac{1 - \mathrm{e}^{\mathrm{i}(\omega_{ji} - \omega_\mathrm{L})t}}{\omega_{ji} - \omega_\mathrm{L}} \right). \tag{I.59}$$

We can easily deduce the transition probability:

$$\mathcal{P}_{if}^{(1)}(t) = \frac{F_0^2 \left| d_{fi}^{(z)} \right|^2}{4} \left| \frac{1 - \mathrm{e}^{\mathrm{i}(\omega_{fi} + \omega_\mathrm{L})t}}{\omega_{fi} + \omega_\mathrm{L}} - \frac{1 - \mathrm{e}^{\mathrm{i}(\omega_{fi} - \omega_\mathrm{L})t}}{\omega_{fi} - \omega_\mathrm{L}} \right|^2. \tag{I.60}$$

We point out two observations: first there is an obvious resonance at the laser frequency:

$$\omega_\mathrm{L} = |E_f - E_i|. \tag{I.61}$$

This is the manifestation of energy conservation: upon absorption or emission of a photon, the system either gains or loses an amount of energy equal to the energy of that photon.

Second, this transition probability is proportional to F_0^2, i.e. proportional to the intensity of the laser I_L. We will see that this is characteristic of one-photon transitions.

For the second order, we get:

$$\lambda^2 \tilde{c}_j^{(2)}(t) = -\frac{F_0^2}{4} \sum_k d_{jk}^{(z)} d_{ki}^{(z)} \sum_{\alpha,\beta=\pm 1} \alpha\beta \left[\frac{1 - \mathrm{e}^{\mathrm{i}(\omega_{jk}+\alpha\omega_\mathrm{L})t}}{(\omega_{jk}+\alpha\omega_\mathrm{L})(\omega_{ki}+\beta\omega_\mathrm{L})} - \frac{1 - \mathrm{e}^{\mathrm{i}[\omega_{ji}+(\alpha+\beta)\omega_\mathrm{L}]t}}{[\omega_{ji}+(\alpha+\beta)\omega_\mathrm{L}](\omega_{ki}+\beta\omega_\mathrm{L})} \right]. \tag{I.62}$$

Here again we can make a few comments. First we see that we have a resonance at $E_j - E_i = \pm 2\omega_\mathrm{L}$. This is again characteristic of energy conservation: upon absorption or emission of two photons, the systems gains or loses twice the energy of one photon. It is important to notice that this resonance is present whether or not an actual intermediate state $|\varphi_k\rangle$ exists halfway in between the initial $|\varphi_i\rangle$ and final states $|\varphi_j\rangle$. However, in the presence of such an intermediate state the transition amplitude is greatly enhanced. This configuration is called a resonant multiphoton transition and is the basis of the widespread REMPI technique [87–89].

Note that the associated two-photon transition probability is proportional to F_0^4, i.e. to the square I_L^2 of the laser intensity. This is characteristic of two-photon transitions. This power law can be generalized to the n-photon case. We can easily see from (I.53) that

$$\lambda^n \tilde{c}_j^{(n)}(t) \propto F_0^n. \tag{I.63}$$

The associated n-photon transition probability will thus be proportional to the n^th power I_L^n of the laser intensity.

b) Fermi's Golden rule

If the final state $|\varphi_{E,\beta}\rangle$ belongs to the continuum, characterized by its energy E and possibly a set of other parameters β (note that β can contain both continuous and/or discrete parameters), then all the previous statements remain valid, except that we get probability density functions. To recover probabilities, we need to integrate over a neighbourhood of E and β, that we denote respectively δE and $\delta\beta$. We get:

$$\delta\mathcal{P}(E,\beta,t) = \int_{E\in\delta E,\,\beta\in\delta\beta} \mathrm{d}E\,\mathrm{d}\beta\,\rho(E)|\langle\varphi_{E,\beta}|\psi(t)\rangle|^2. \tag{I.64}$$

In the near-resonant case, i.e. when $E - E_i \simeq \omega_\mathrm{L}$, the first order transition probability (I.60) becomes:

$$\delta\mathcal{P}(E,\beta,t) = F_0^2 \int_{E\in\delta E,\,\beta\in\delta\beta} \mathrm{d}E\,\mathrm{d}\beta\,\rho(E)|\langle\varphi_{E,\beta}|\,\hat{z}\,|\varphi_i\rangle|^2 \frac{\sin^2[(E-E_i-\omega_\mathrm{L})t]}{(E-E_i-\omega_\mathrm{L})^2}. \tag{I.65}$$

If the interaction time t is long enough, we can make the approximation:

$$\frac{\sin^2[(E-E_i-\omega_\mathrm{L})t]}{(E-E_i-\omega_\mathrm{L})^2} \underset{t\to\infty}{\longrightarrow} 2\pi t\delta(E-E_i-\omega_\mathrm{L}), \tag{I.66}$$

and if $\delta\beta$ is small enough, we get:

$$\delta\mathcal{P}(E,\beta,t) = \begin{cases} F_0^2 \delta\beta |\langle \varphi_{E_i+\omega_\mathrm{L},\beta}| \hat{z} |\varphi_i\rangle|^2 \rho(E_i+\omega_\mathrm{L}) t & \text{if } E_i+\omega_\mathrm{L} \in \delta E \\ 0 & \text{if } E_i+\omega_\mathrm{L} \notin \delta E \end{cases} \tag{I.67}$$

Differentiating this expression with respect to time, we recover the well known Fermi's Golden rule.

c) Illustrative example

To show the characteristic features of n-photon transitions, we consider a very simple system: an electron trapped in a one dimensional Gaussian potential well:

$$V_0(x) = -\mathrm{e}^{\frac{x^2}{2}}. \tag{I.68}$$

This system has only two bound states: the ground state of energy $E_0 = -16.2$ eV, and an excited state $E_1 = -1.03$ eV. It is initially in the ground state, and is then exposed to laser pulses of various central wavelengths and peak intensities. We can observe two different kinds of excitations: from the ground state to the first excited state; and from the ground state to a continuum state, i.e. ionization of the "atom". Note that, from (I.67), only a continuum state satisfying the energy conservation relation can be populated.

We plot on Figure I.3 the population in the first excited states and in the continuum states at the end of the laser pulse as a function of the incident photon energy. The transition probability to the first excited state (in green) has sharp peaks at $\omega_\mathrm{L} = (E_1 - E_0)/n$, for $n = 1$, $n = 3$ and $n = 5$. These correspond to the one, three and five photon excitations. The even-photon transitions towards this excited state are not observed because of the selection rules. In one dimension these selection rules imposes conditions on the parity of the wave function, which can be seen as an analogue of the orbital angular momentum ℓ. They state that the absorption of an even number of photons keeps the parity unchanged, and that the absorption of an odd number of photons induces a change of parity. Since the ground and excited state have opposite parities, only odd-photons transitions are allowed.

The ionization probability (in red) has a stair-like shape: we observe thresholds at $\omega_\mathrm{L} = -E_0/n$ and in between them the ionization probability is almost constant. These thresholds correspond to n-photon ionization. For each value of the continuum energy, there is always an odd and an even continuum states, so the selection rules can always be fulfilled. This is why we observe ionization with odd number of photons, as well as even number of photons. However the final states will be different because the populated continuum wave function will have the same parity as the number of absorbed photons.

Finally, we observe resonances in the ionization probability at $\omega_\mathrm{L} = (E_1 - E_0)/n$, with $n = 1$, $n = 3$ and $n = 5$. These correspond to the REMPI processes we described above. At photon energy $\omega_\mathrm{L} = E_1 - E_0$, we observe a resonant 2-photon ionization: one photon to get to the first excited state, and one additional photon to ionize the electron. This is denoted as a $(1+1)$ REMPI process. We also observe the $(3+1)$ and $(5+1)$ REMPI processes corresponding respectively to 3 or 5 photon transitions from the ground to the excited states, and one additional photon to ionize the electron. Note that, because of the selection rules, we do not observe $(n+1)$ REMPI processes when n is even.

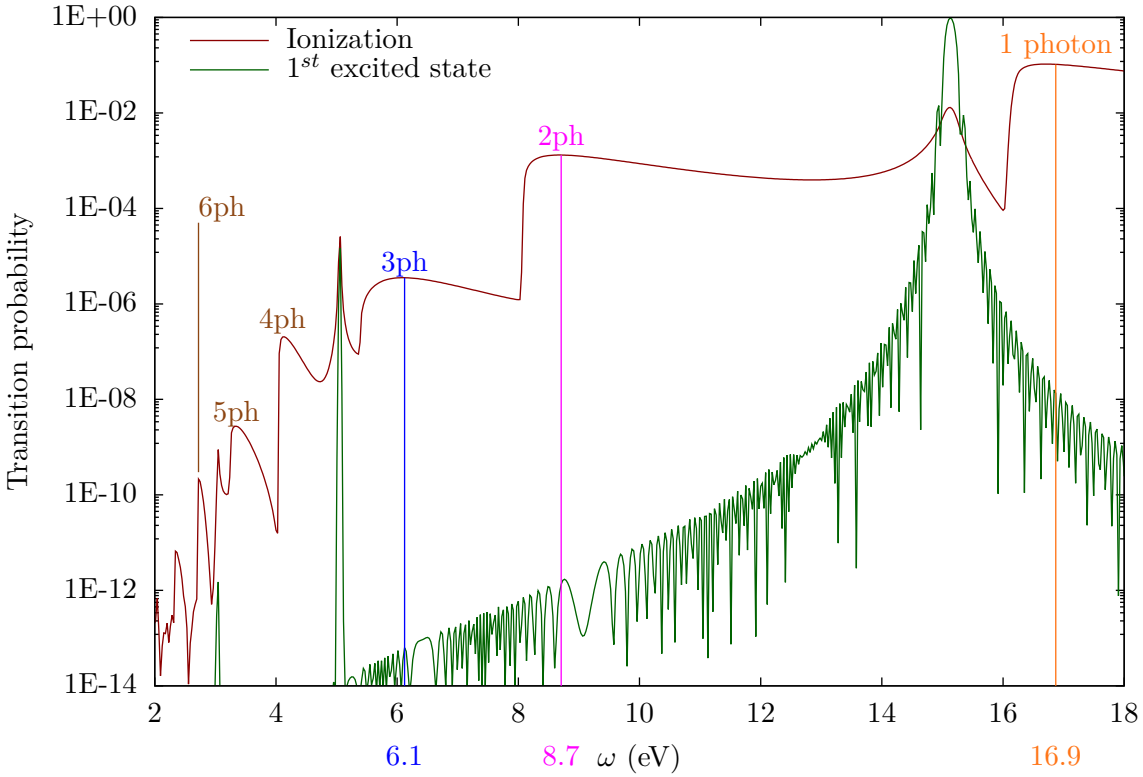

Figure I.3 *Absorption spectrum of an electron in a Gaussian potential well (I.68), exposed to a sine square envelope laser pulse of 200 optical cycles and of peak intensity* $I_L = 3.5 \times 10^{12}$ W.cm^{-2} *computed by solving the TDSE (see section II.1.1). In red the ionization probability at the end of the pulse, in green the population in the first excited state at the end of the pulse. The number of photons for each ionization threshold is displayed.*

We also investigated the dependence of ionization probability as a function of the laser intensity. As we said before, n-photon transition probabilities are proportional to I_L^n. To observe more clearly this feature, we plotted the ionization probability on a log-log scale in Figure I.4. We observe that, as expected, the ionization probability at $\omega_L = 16.9$ eV (orange crosses), is perfectly fitted by a linear law $f(x) = ax$; the ionization probability at $\omega_L = 8.7$ eV (purple x's) is perfectly fitted by a quadratic law $f(x) = ax^2$; and the ionization probability at $\omega_L = 6.1$ eV (blue stars) is perfectly fitted by a cubic law $f(x) = ax^3$. This corroborates our attribution of one, two and three-photons ionization threshold in Figure I.3.

I.3 High Harmonic Generation and Strong Field Approximation

In the previous section, we have reviewed the basics of light-matter interaction through the very powerful time-dependent perturbation theory. However, as its name indicates, this method is relevant only in situations where the EM field represents a small perturbation to the atomic or molecular system. This restricts its range of applicability to low intensity

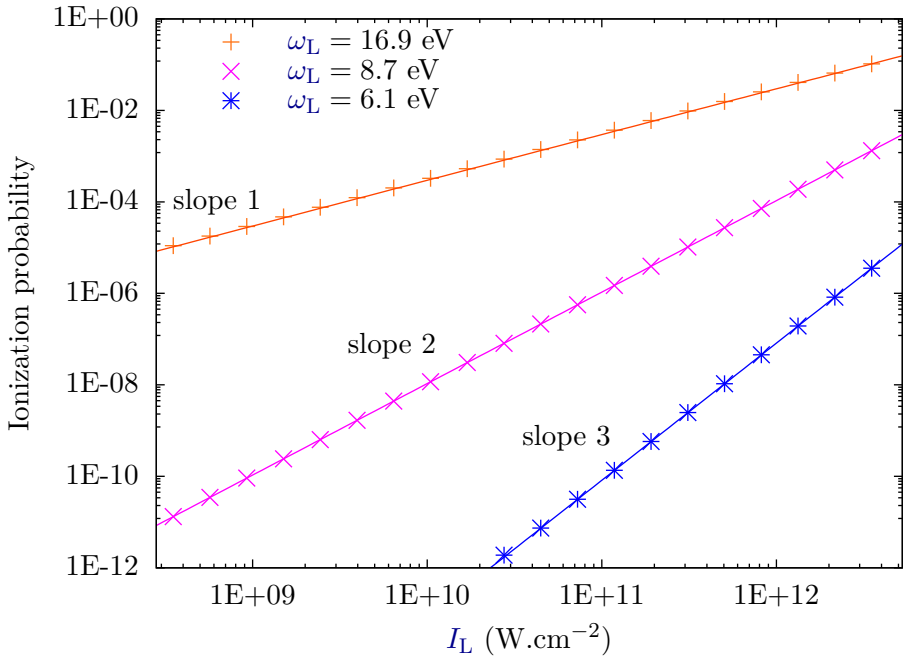

Figure I.4 *Ionization probability as a function of the laser pulse intensity for three different photon energies (indicated in Figure I.3) computed by solving the TDSE (see section II.1.1). The system and laser pulse are the same as in Figure I.3. The dots are the results of the numerical simulations, and the lines are power law fits.*

and high frequency laser fields. When the laser intensity is too high, compared to the strengh of the electron-nuclei interaction, then the electric field substantially distorts the atomic potential so that the electron may escape through tunnel effect. This highly non-linear effect, called tunnel ionization, is the first step of many strong field processes such as HHG [90, 91], ATI [92, 93] or non-sequential multiple ionization [94].

The distinctive feature of these strong field processes is their extreme non-linearity, which is inherited from their common first step, i.e. tunnel ionization. This first step cannot be accounted for by perturbation theory, i.e. by the description in terms of one or several photon transitions. This strong field regime, or tunnel regime, is the source of completely different physical phenomena. The description, analysis, and interpretation of these new phenomena thus relies on specific tools, and specific physical models.

In this thesis we are mainly interested in HHG, which is the subject of the present section. This particular process present many different aspects, both experimental and theoretical. It is, together with the XRay free electron lasers (XFEL), one of the only source of attosecond coherent light pulses [95–97], and is therefore at the heart of many attosecond-resolution time resolved experiments [32, 33, 50, 22, 27, 29]. It is also a powerful self-probe of the chemical species that generate the harmonics. Indeed, it allows to reconstruct the dynamics of the emitting system both temporally and spatially with Ångström and attosecond resolution [59, 98, 99, 45, 41]. This multiplicity of experiments requires advanced theory, not only in the form of numerical simulations that are necessary

for the quantitative analysis of experimental results, but also in the form of analytic intuitive physical models that are valuable for the description, interpretation and design of experiments.

In this section, we first present a phenomenological approach to HHG, then we detail a very powerful model that describes HHG in the Strong Field Approximation (SFA): the so-called Lewenstein model [11]. Though HHG has also been observed and used in solids [100–102], nanoscale strucures [103, 104] and liquids [105], in this thesis we focus on the gas phase. We will describe the process at a single atom (or molecule) level. The physical models that we can construct at this level of description constitute the ground for all the qualitative physical pictures and interpretations we have of HHG. To get more quantitative results it is then necessary to include macroscopic collective effects [106, 90, 96, 107, 108], such as phase matching between the different emitters, inhomogeneity in the gas, or spatial dependency of the laser intensity close to the focus area. However, the accurate quantitative computation of HHG still remains a challenge for theoreticians. We will therefore concentrate on physical insight, rather than on quantitative accuracy as such.

I.3.1 What is High order Harmonic Generation ?

When a short laser pulse of a few tens of fs, with Infrared (IR) or mid-IR central wavelength, and high intensity $I_L \sim 10^{14} - 10^{15}$ W.cm^{-2}, is focused on a gas jet, then we observe that this gas re-emits a radiation [7, 8, 109–111]. This radiation has very peculiar characteristics, as can be seen from the typical spectrum in Figure I.5. This spectrum was computed with the numerical methods detailed in sections II.1.1 and II.3.2. First it is very large, spreading from the IR to the XUV domain, which enlightens the non-linearity of the process. Second, it is shaped as a train of very short pulses of a few tens of as [95, 112]. Third, its spectrum is only composed of the odd harmonics $(2p+1)\omega_L$ of the incident laser frequency. All these odd harmonics have almost the same intensity, from harmonic 1 to a *cut-off* value that is generally around a few tens but than can go up to a few hundreds in some conditions. Above this *cut-off* energy (around harmonic 52 on Figure I.5, indicated by an arrow) the harmonic intensity sharply decreases. The last characteristic is that this radiation is coherent [107].

From all those very promising characteristics, it is quite easy to understand the popularity of HHG as a light source. However it is not so easy at first sight to understand the mechanism creating this radiation. We can first observe that, in the conditions cited above, we are in the tunnel regime and not in the perturbative regime. Or, said otherwise, ionization is dominated by tunnel ionization rather than multiphoton ionization. The limit between these two regimes is in practice measured by the Keldysh parameter γ [113]. It is defined as the ratio of the so-called "tunnelling time", i.e. the time the electron takes to tunnel out of the potential barrier, to half a laser period. From this definition we see that we will be in the tunnel regime if $\gamma \ll 1$, i.e. if the electron has enough time in half a laser period to tunnel out. On the contrary, for $\gamma \gg 1$ we will be in the multi-photon regime. The formal expression of the Keldysh parameter reads

$$\gamma = \sqrt{\frac{I_p}{2U_p}}, \tag{I.69}$$

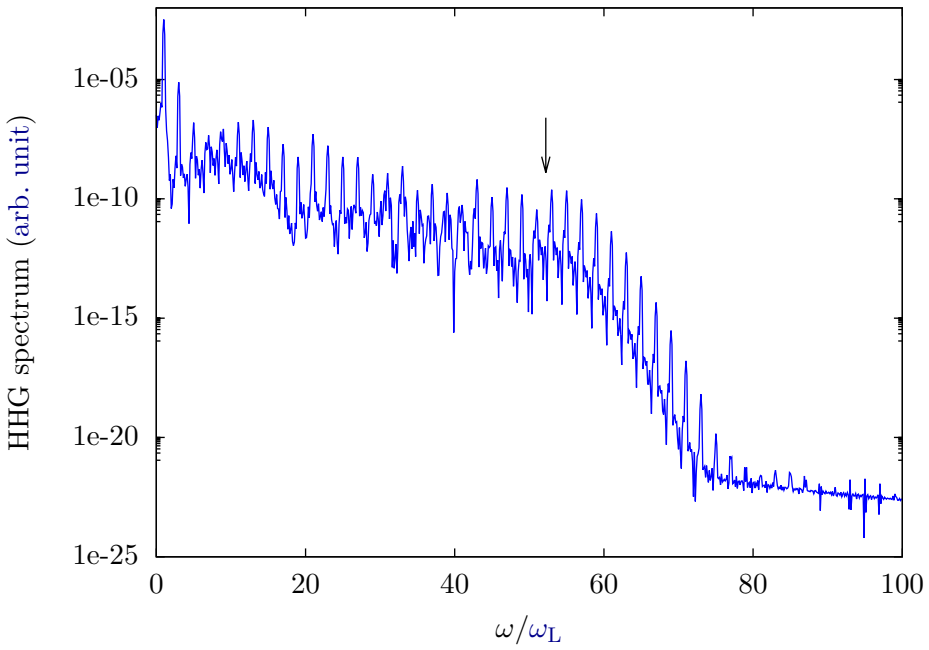

Figure I.5 *Example of an HHG spectrum emitted by a 1D Helium atom defined by a Soft-Coulomb potential (II.1) with regularization parameter $a = 0.707$ a.u. computed by solving the TDSE (see section II.1.1). The incident laser pulse is a Ti:Sa $\lambda_L = 800$ nm pulse with a trapezoidal envelope of 10 optical cycles with linear ramps of one optical cycle, and of intensity $I_L = 3 \times 10^{14}$ W.cm^{-2}. The position of the cut-off, predicted by (I.78), is indicated by an arrow.*

where $U_p = {F_0}^2/(4{\omega_L}^2)$ is the ponderomotive energy of the electron in the EM field. For example, if we take the case of a Helium atom, $I_p = 24.6$ eV, and a Titanium-Sapphire (Ti:Sa) laser with $\lambda_L = 800$ nm, then the tunnel regime is reached for intensities higher than 2×10^{14} W.cm^{-2}. In this regime, we can actually consider that the field oscillations are very slow compared to the electron dynamics, so that the electron instantaneously adapts to the value of the laser electric field. This is very different from multi-photon ionization where the electron is sensitive to the electric field integrated over several periods.

To emphasize the difference between the two regimes, we can look at the time-dependent wave function during the laser pulse. We show on Figure I.6 snapshots of the absolute value of the wave function at different times in the case of a 1D Helium atom exposed to a laser of $\omega_L = 27$ eV and $I_L = 3.5 \times 10^{12}$ W.cm^{-2}. The Keldysh parameter is $\gamma = 67$ so we are in the multi-photon regime, and more precisely in the one-photon regime since the photon energy is sufficient to ionize the "atom". We see on Figure I.6 that the ionized electron gradually forms two symmetric and unstructured bell-shaped wave packets that leave the nucleus. During the laser pulse, their growth is mostly sensitive to the laser envelope, and not so much to the instantaneous value of the electric field. In particular it is almost insensitive to the so-called Carrier Envelope Phase (CEP), i.e. to the phase between the field oscillations and its envelope. The electron that leaves the nucleus, called a *photoelectron*, behaves almost like a classical free electron with kinetic

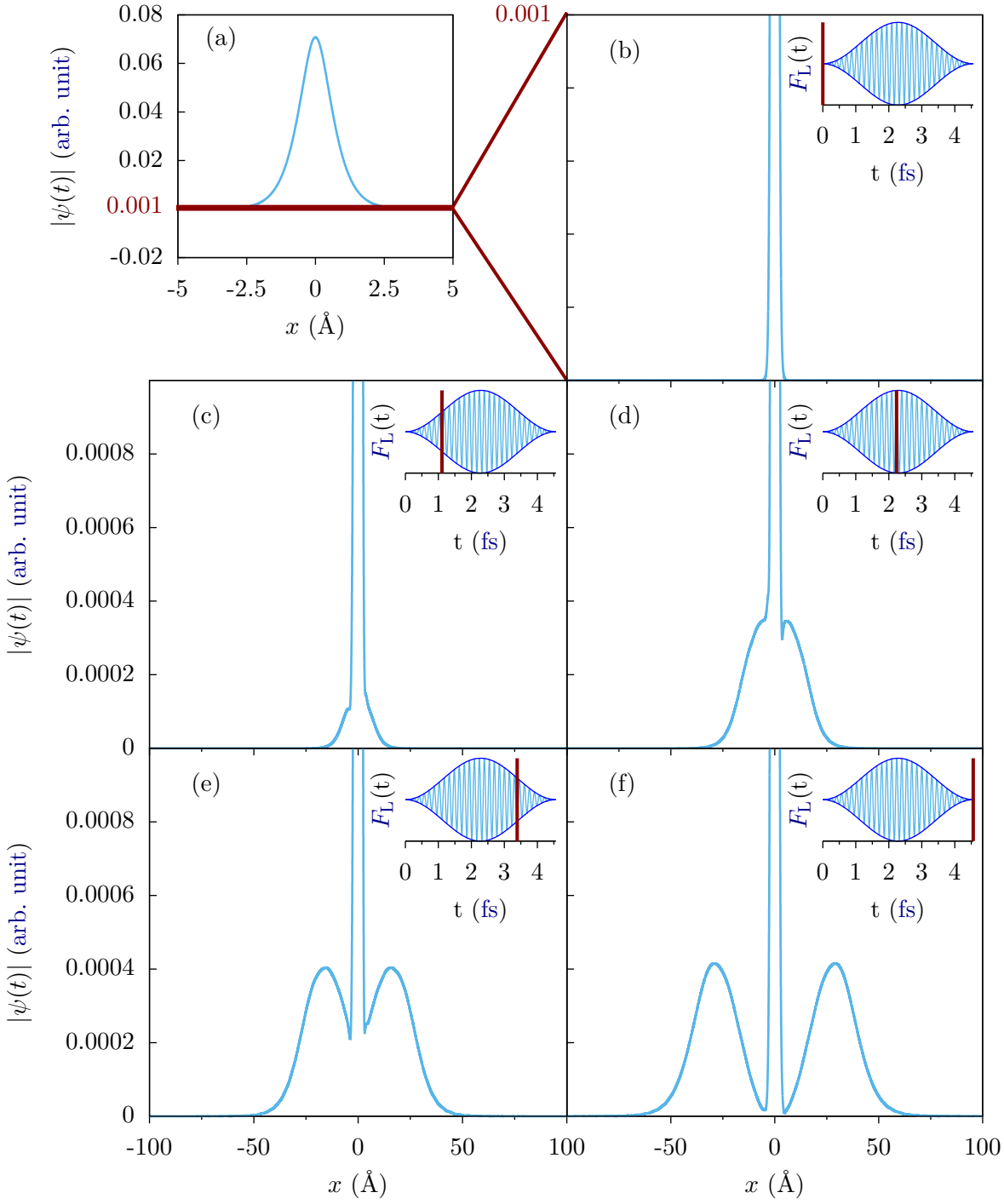

Figure I.6 *One photon ionization $\gamma = 67$ of a 1D Helium atom exposed to a sine square laser pulse of* 4.6 fs, *i.e. 30 optical cycles, with* $\lambda_L = 46$ *nm, i.e.* $\omega_L = 27$ eV, *and* $I_L = 3.5 \times 10^{12}$ W.cm^{-2}. *Panel (a) shows the modulus of the initial wave function and panel (b) is a zoom on small modulus values. Panels (c)-(f) are zoomed snapshots of the modulus of the wave function during the laser pulse respectively at* $t_c = 1.1$ fs, $t_d = 2.2$ fs, $t_e = 3.4$ fs *and* $t_f = 4.6$ fs.

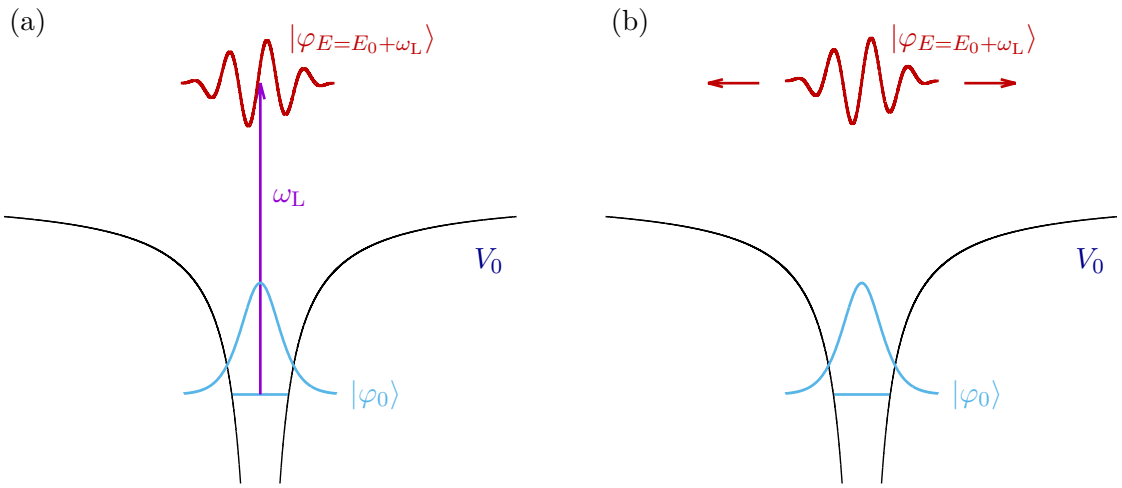

Figure I.7 *Schematic representation of one-photon ionization. Panel (a): instantaneous absorption of one photon, panel (b): isotropic diffusion of the photoelectron away from the nucleus.*

energy $\omega_L - I_p$. This one-photon ionization process is schematized in Figure I.7: panel (a) depicts the transition from the ground state $|\varphi_0\rangle$ to a continuous state of energy $E_0 + \omega_L$ through the absorption of a laser photon, and panel (b) the isotropic diffusion of the photoelectron away from the nucleus.

In the tunnel regime, we observe on Figure I.8 a radically different behaviour. We observe again the birth of Electron Wave Packets (EWPs), corresponding to the ionized electron. However in this case the growth of these wave packets follows the instantaneous value of the electric field, and will therefore be highly sensitive to the CEP. At each half cycle of the electric field, we observe the birth of a new EWP that leaves the nucleus in the direction opposite to the electric field, i.e. towards the right on panels (c) and (d) and towards the left on panels (e) and (f).

The major difference with the multiphotonic regime, and that we want to point out, is that the EWPs do not leave the nucleus with a constant kinetic energy $\omega_L - I_p$. In the half cycle that follows the one of its birth, each EWP *changes* its direction of propagation and is brought back close to the nucleus by the electric field that changes sign. It is noticeable on Figure I.8: on panel (c) and (d) a continuum EWP is created and leaves the nucleus towards the right, on panel (e) it now propagates towards the left, and on panel (f) it has been brought back to the nucleus.

This has several consequences. First the EWPs that were initially born in different directions are not "completely" independent as was the case in the multiphotonic regime. They may now interfere with each other [114], creating the structures that are visible on panel (f) of Figure I.8. Second, the electron that has been brought back to the nucleus can now recombine with the ionic core, liberating its kinetic energy through the emission of a photon. This process is the time reversed equivalent of the photoionization process that we have seen on Figure I.6, and is at the origin of the HHG radiation.

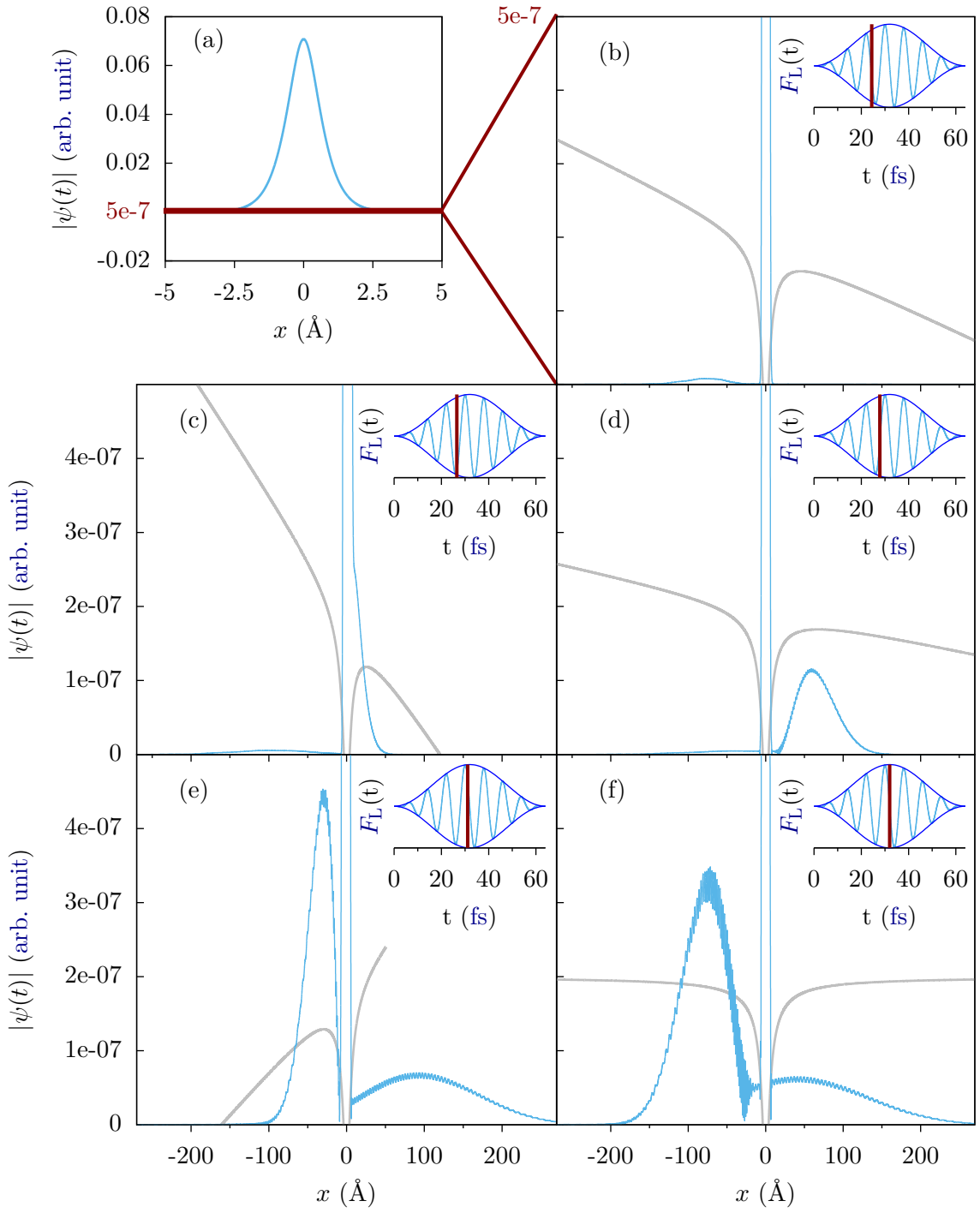

Figure I.8 *Tunnel ionization* $\gamma = 0.51$ *of a 1D Helium atom exposed to a sine square laser pulse of* 64 fs, *i.e. 8 optical cycles, with* $\lambda_L = 2.4$ µm, *i.e.* $\omega_L = 0.52$ eV, *and* $I_L = 8.8 \times 10^{13}$ W.cm^{-2}. *In blue: panel (a) shows the modulus of the initial wave function, panels (b)-(f) are zoomed snaphots of the modulus of the wave function during the fourth optical cycle of the laser pulse respectively at* $t_b = 24.4$ fs, $t_c = 26.6$ fs, $t_d = 27.8$ fs, $t_e = 31.1$ fs *and* $t_f = 32$ fs. *The effective potential* $V_0(x) + xF_L(t)$ *is schematically drawn in gray.*

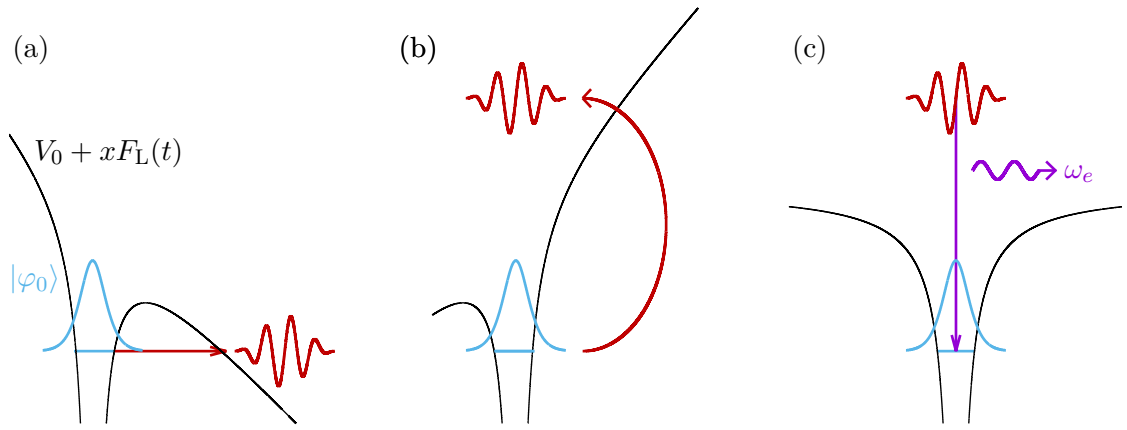

Figure I.9 *Schematic representation of the three step model. Panel (a): tunnel ionization, panel (b): acceleration by the field and rescattering towards the nucleus, panel (c): recombination to the ground state and emission of a photon.*

We thus saw that we can decompose the HHG process into three successive steps that are repeated at each half cycle of the laser electric field: tunnel ionization, propagation in the continuum under the unfluence of the electric field, and recombination with the ionic core. This is the celebrated three-step model [9, 10] that is at the basis of all the intuitive models about HHG. We sketch these three steps on Figure I.9: on panel (a) we see the electron wave packet that tunnel out of the potential energy barrier formed by the atomic potential and the electric field, on panel (b) this electron is accelerated and rescattered toward the ionic core and on panel (c) it recombines to the ground state and liberates its kinetic energy by emitting a photon. Note that the first of these three steps, tunnel ionization, is the central topic of Chapter III.

From the time-dependent wave function depicted in Figure I.8, we can compute quantitatively all the relevant observables. In particular if we extract the spectrum of the emitted light, we get the HHG spectrum like the one shown in Figure I.5. Nevertheless, it is difficult to grasp any more physical insight about the process. To better understand the mechanisms behind HHG, and to rationalize its main characteristics enumerated above, it is very useful to construct approximate analytic models. Since the interaction with the field can be considered large with respect to the nuclei influence, we will, in first approximation, neglect the influence of the nuclei during the second step of the process: the propagation. We will first detail the properties of a free classical electron in an oscillating electric field. Then we will develop one of the most widespread model for the theoretical description of HHG: the so-called "Lewenstein model" that allows the quantum description of the three-step model.

I.3.2 Semi-classical model

We present here the semi-classical model developed in [91, 92]. We consider that after the first step, i.e. tunnel ionization, the electron behaves classically and under the influence of the electric field only. We suppose that the electron is born at time t_i at the

origin $\mathbf{r}(t_\mathrm{i}) = 0$, with no kinetic energy $\dot{\mathbf{r}}(t_\mathrm{i}) = 0$. We neglect the influence of the laser pulse envelope, so that the electric field reads:

$$F_\mathrm{L}(t) = -F_0 \cos(\omega_\mathrm{L} t). \tag{I.70}$$

The x component of the electron position follows Newton's equation:

$$\ddot{x}(t) = -F_\mathrm{L}(t). \tag{I.71}$$

Which can easily be integrated to get the electron velocity:

$$\dot{x}(t) = \frac{F_0}{\omega_\mathrm{L}} \big[\sin(\omega_\mathrm{L} t_\mathrm{i}) - \sin(\omega_\mathrm{L} t)\big], \tag{I.72}$$

and position:

$$x(t) = \frac{F_0}{{\omega_\mathrm{L}}^2} \big[\omega_\mathrm{L}(t - t_\mathrm{i}) \sin(\omega_\mathrm{L} t_\mathrm{i}) + \cos(\omega_\mathrm{L} t) - \cos(\omega_\mathrm{L} t_\mathrm{i})\big]. \tag{I.73}$$

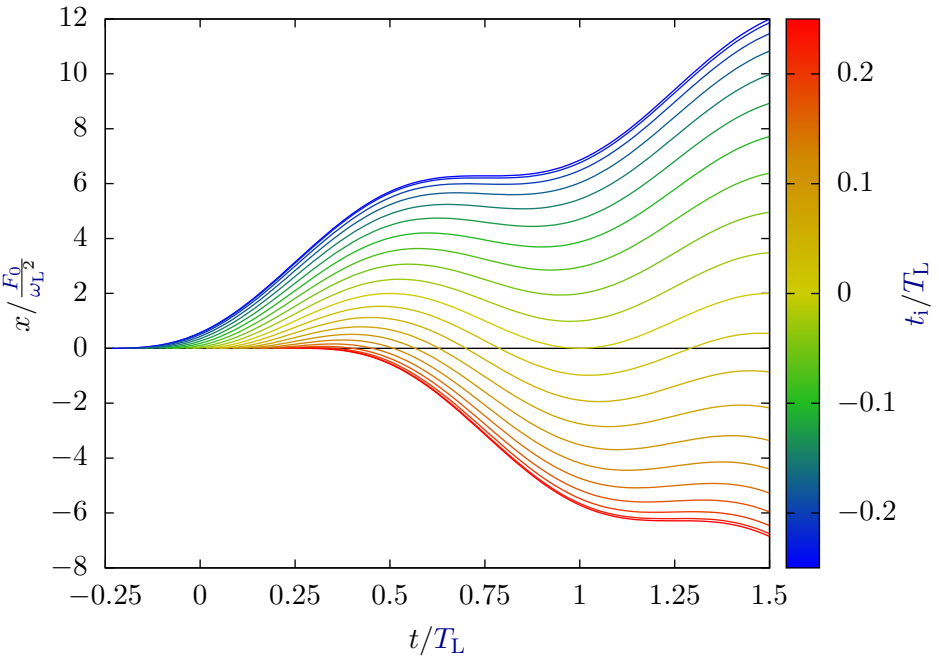

Figure I.10 *Trajectories of a classical electron in an oscillatory electric field.*

For different values of t_i the electron will thus follow different trajectories, that are plotted on Figure I.10. In order to make the third step, i.e. the recombination step, possible we need the electron to go back to the origin at some return time t_r. We see on Figure I.10 that this condition imposes some restriction on the ionization time t_i. We can compute that only the trajectories that starts at $t_\mathrm{i} \in [0; T_\mathrm{L}/4]$ will return to the origin at least once (modulo $T_\mathrm{L}/2$ of course). The return time t_r is solution of the equation

$$\omega_\mathrm{L}(t_\mathrm{r} - t_\mathrm{i}) \sin(\omega_\mathrm{L} t_\mathrm{i}) - \cos \omega_\mathrm{L} t_\mathrm{i} = -\cos \omega_\mathrm{L} t_\mathrm{r}, \tag{I.74}$$

which can be rewritten

$$\dot{F}_{\mathrm{L}}(t_{\mathrm{i}})(t_{\mathrm{r}} - t_{\mathrm{i}}) + F_{\mathrm{L}}(t_{\mathrm{i}}) = F_{\mathrm{L}}(t_{\mathrm{r}}). \tag{I.75}$$

The left-hand side of (I.75) is the equation of the tangent to F_{L} at time t_{i}. The graphical meaning of (I.75) is thus that the tangent of F_{L} at t_{i} crosses F_{L} at time t_{r}. We can therefore look at the solutions of (I.75) graphically. As we can see on Figure I.11, a given

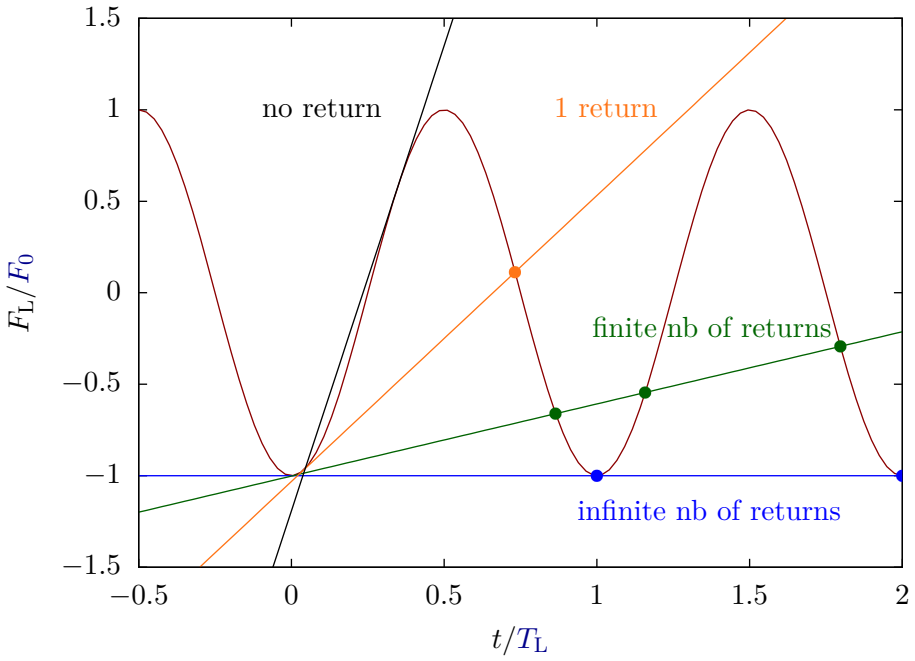

Figure I.11 *Graphical solutions of equation (I.75). Electric field $F_{\mathrm{L}}(t)$ in red, and its tangents at $t_{\mathrm{i}} = 0.35\ T_{\mathrm{L}}$ in black, at $t_{\mathrm{i}} = 0$ in blue, at $t_{\mathrm{i}} = 0.01\ T_{\mathrm{L}}$ in green, at $t_{\mathrm{i}} = 0.04\ T_{\mathrm{L}}$ in orange.*

trajectory may either never return to the origin, or it may have an infinite number of returns, or any finite number of them, depending on the ionization time t_{i}.

As we have said, we will concentrate on the trajectories that return at least once to the origin, and more precisely we will concentrate on the first return of these trajectories. Indeed, in quantum dynamics the EWP behaves almost classically, except that it has a finite spatial width. Upon propagation, this width will increase, not only in the x direction, but also in the transverse y and z directions. The height of the EWP will thus decrease, out of probability conservation, so that the probability that the ionized electron hits the ionic core at its return is therefore lower for subsequent returns, and we can consider that, in practice, only the first of them will participate to HHG [115].

Since the recombination step is the time reversed equivalent of photoionization, the energy ω_{e} of the emitted photon will obey a relation of energy conservation equivalent to (I.61):

$$\omega_{\mathrm{e}} = E - E_0 = E + I_{\mathrm{p}}, \tag{I.76}$$

where E is the energy of the rescattering electron before recombination. Since we neglect the influence of the nuclei, this energy E is simply equal to its kinetic energy E_{k} at its

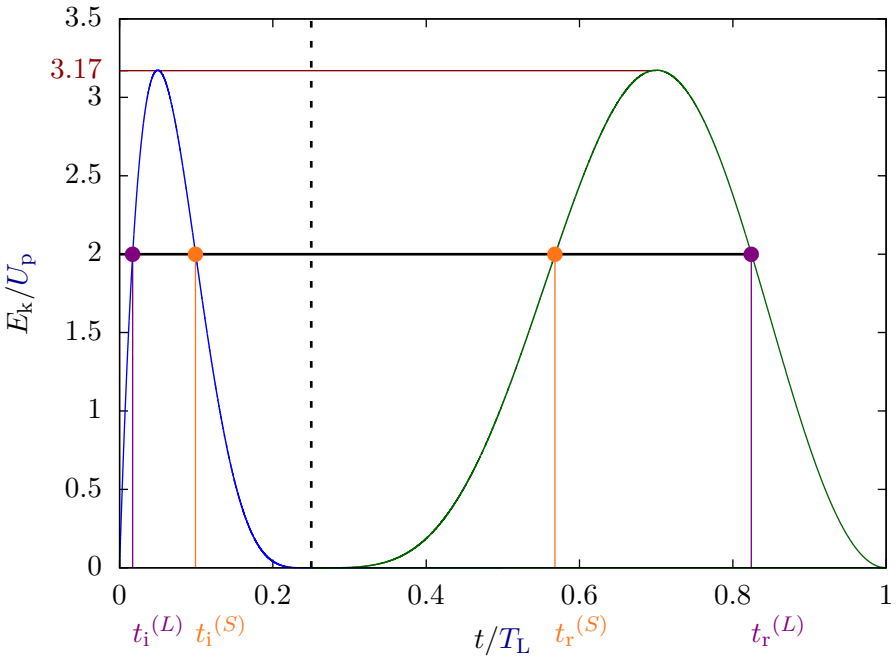

Figure I.12 *Kinetic energy of the ionized electron at its first return as a function of t_i in blue, and a function of t_r in green.*

return time t_r:

$$E = E_k = \frac{1}{2}\dot{x}(t_r)^2. \tag{I.77}$$

We can compute numerically this kinetic energy for each trajectory, by solving (I.74) with a bisection algorithm. This is shown on Figure I.12. Since each trajectory can be labelled by its ionization time t_i, but also by its first return time t_r, we can consider the kinetic energy (I.77) to be either a function of t_i (in blue) or of t_r (in green).

There are several important points to notice on Figure I.12. First we see quite clearly that the kinetic energy has a maximum at $E_c \simeq 3.17\ U_p$, indicating that the electron can never return to the nucleus with an energy higher than this value $3.17\ U_p$. The energy that the electron can transfer to the emitted photon upon recombination can thus never be larger than:

$$\boxed{\omega_c = I_p + 3.17\ U_p.} \tag{I.78}$$

This directly explains the abrupt cutoff in the HHG spectrum that is observed in HHG experiments and can be seen in the illustrative Figure I.5. Indeed, for the Helium atom, and for the laser pulse considered in Figure I.5, we can compute that $\omega_c \simeq 52\ \omega_L$, which is the value indicated by the arrow.

We also notice that to each value of the kinetic energy $E_k \in [0; 3.17\ U_p[$ corresponds two different trajectories, i.e. two different pairs of values (t_i, t_r). This is illustrated on Figure I.12 for an arbitrary kinetic energy of $E_k = 2\ U_p$. There are thus two different families of trajectories, called *long* and *short* trajectories and labelled with the

subscripts (L) and (S) on Figure I.12. The short trajectories corresponds to electrons that are always ionized after, and that always recombine before the electrons of the long trajectories, hence their respective names. These two trajectories correspond to two different quantum paths that have the same initial and final state. This makes it possible to have quantum interferences between those two paths [29] that are partly encoded in the EWPs structures that we have seen on Figure I.8 (f).

We can actually show [91] that the two families of trajectories are spatially separated by:

$$x_\alpha = \frac{F_0}{\omega_{\mathrm{L}}^2}. \tag{I.79}$$

Meaning that the short trajectories will never go beyond this limit, while all the long trajectories cross it. We can also show that the longest of the long trajectories leaves the origin at $t_{\mathrm{i}} = 0$. Using the trajectory formula (I.73), we see that in this case, the electron never go beyond $2x_\alpha$. The electron trajectories that will participate to the HHG process are thus all located in a definite region of space $r \in [0, 2x_\alpha]$ around the origin. If we define $x_{\max}$, the maximal excursion between ionization and first return of a given trajectory, we see that this region of space is itself separated into two distinct areas. The maximal excursion $x_{\max}$ of the short trajectories lies in $[0, x_\alpha]$ while for the long trajectories $x_{\max}$ lies in $[x_\alpha, 2x_\alpha]$. This can be used to separate the contributions of the two families of trajectories to the HHG emission, as we will see in section II.3.3.

Note that, since these two trajectories propagate for different amounts of time, the EWP accumulates a different phase during the propagation, and the emitted photon corresponding to each trajectory will carry a different phase. This have important consequences on the phase matching conditions for the collective emission of an ensemble of atoms and therefore on the temporal shape of the emitted bursts of XUV light [106, 90, 96, 108]. The emission corresponding to each trajectory will have different phase matching conditions, and will therefore have different propagation properties in the generating medium. This also can be used, for example, to spatially separate the contribution of the two families of trajectories [116, 117].

From the shape of the kinetic energy in Figure I.12, we deduce that the HHG spectrum is continuous over the range $\omega \in [I_{\mathrm{p}}, I_{\mathrm{p}} + 3.17\ U_{\mathrm{p}}]$, and this is actually what we get if the incident laser pulse contains only one generating cycle. We can estimate its temporal duration from the Fourier transform relation

$$\Delta\omega_{\mathrm{e}}\Delta\tau_{\mathrm{e}} = 3.17\ U_{\mathrm{p}}\Delta\tau_{\mathrm{e}} \geq 2\pi. \tag{I.80}$$

We get that, for a Ti:Sa laser $\lambda_{\mathrm{L}} = 800$ nm with intensity $I_{\mathrm{L}} = 10^{14}$ W.cm^{-2} (which are typical values for HHG), the time duration of the harmonic emission verify $\Delta\tau_{\mathrm{e}} \geq 250$ as. This is the typical time duration of the harmonic emission, also called atto-burst for obvious reasons. This time can also be interpreted as a *recollision duration* τ_{r}:

$$\tau_{\mathrm{r}} = \frac{d}{v} \simeq 25 \text{ as}, \tag{I.81}$$

where $d \simeq 1$ a.u. is the typical size of the atom and $v \simeq 1$ a.u. is the speed of the rescattering electron.

For laser pulses that contain several optical cycles, we will have emission of such an atto-burst at each half cycle of the incident laser. The temporal profile of the harmonic emission is thus composed of a train of short pulses, synchronized with the incident laser electric field. For atoms that have a central symmetry, all those pulses are identical, except that two consecutive pulses have opposite signs. The emitted electric field $F_\mathrm{e}(t)$ thus takes the general form:

$$F_\mathrm{e}(t) = \sum_j G\left(t - \frac{2j\pi}{\omega_\mathrm{L}}\right) - G\left(t - \frac{(2j+1)\pi}{\omega_\mathrm{L}}\right), \tag{I.82}$$

where $G(t)$ is the electric field of one pulse of the train. This is schematically represented on Figure I.13.

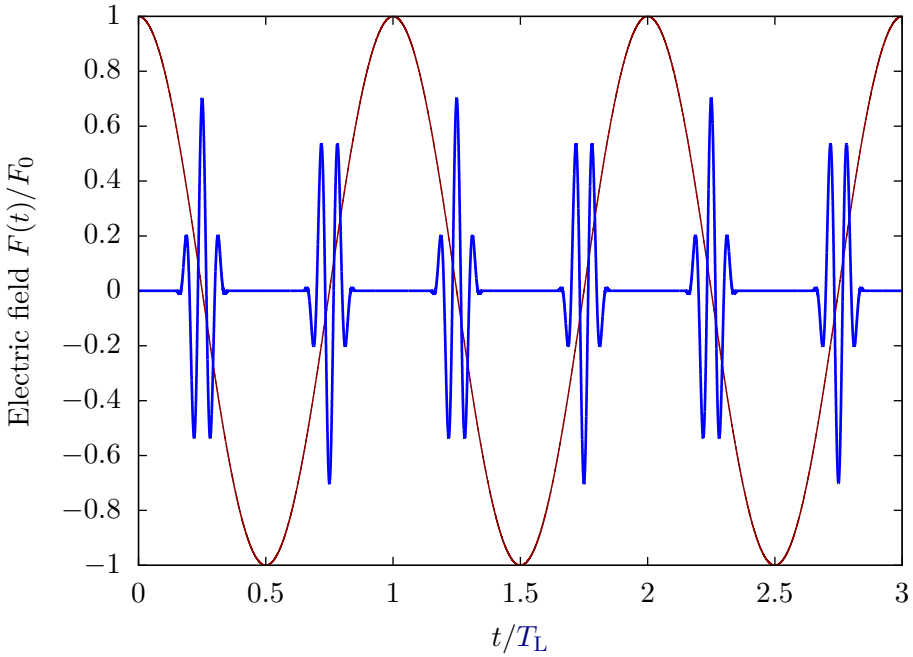

Figure I.13 *Schematic view of the temporal profile of the HHG radiation (in blue). The laser electric field is showed in red.*

If we take the Fourier transform of such a train of pulses, we find a Dirac comb:

$$\widetilde{F}_\mathrm{e}(\omega) = \sum_n \int_{-\infty}^{\infty} \mathrm{d}t\, \mathrm{e}^{-\mathrm{i}\omega t}\left[G\left(t - \frac{2n\pi}{\omega_\mathrm{L}}\right) - G\left(t - \frac{(2n+1)\pi}{\omega_\mathrm{L}}\right)\right] \tag{I.83}$$

$$= \sum_n \int_{-\infty}^{\infty} \mathrm{d}t\, G(t)\left\{\exp\left[-\mathrm{i}\omega\left(t + \frac{2n\pi}{\omega_\mathrm{L}}\right)\right] - \exp\left[-\mathrm{i}\omega\left(t + \frac{(2n+1)\pi}{\omega_\mathrm{L}}\right)\right]\right\} \tag{I.84}$$

$$= \widetilde{G}(\omega)\left(1 - \mathrm{e}^{-\mathrm{i}\pi\omega/\omega_\mathrm{L}}\right)\sum_n \mathrm{e}^{-\mathrm{i}2n\pi\omega/\omega_\mathrm{L}} \tag{I.85}$$

$$= \widetilde{G}(\omega)\left(1 - \mathrm{e}^{-\mathrm{i}\pi\omega/\omega_\mathrm{L}}\right)\sum_n \delta\left(\frac{\omega}{\omega_\mathrm{L}} - n\right). \tag{I.86}$$

This Dirac comb directly explains why we only see harmonics of the incident laser field in the HHG spectrum. The continuous Fourier transform of one atto-burst $\widetilde{G}(\omega)$ will act as an envelope over this Dirac comb. Moreover we see that the $\left(1 - \mathrm{e}^{-\mathrm{i}\pi\omega/\omega_\mathrm{L}}\right)$ factor vanishes for even harmonics. This elucidates why we only see the *odd* harmonics of the incident laser field in the HHG spectrum. Of course this is strongly related to the symmetry of the system. In anisotropic media such as oriented or aligned molecules [98] or with other laser polarizations [118–121] even harmonics are observed in HHG spectra.

I.3.3 Strong field approximation

We saw that we could explain most of the features of the HHG process with the semi-classical model. We will now go a little further in our description by invoking the Strong Field Approximation (SFA). This approximation allows to develop an interpretative quantum model for HHG: the Lewenstein model [11]. This widely used model justifies, in the quantum framework, all the results and interpretations that we just obtained with the semi-classical model, hence its immense success.

a) Assumptions

Let us start by summarizing all the approximations of this model, keeping in mind that, of course, these approximations have limitations, as will be discussed later in this thesis. We want to solve the TDSE in the length gauge (I.21), so we first list all the assumptions we made to obtain this Hamiltonian:

Semi-classical approximation: the atom is treated with quantum mechanics, but the EM field is classical.

Non relativistic electron: verified for $I_\mathrm{L} \leq 10^{16}$ W.cm^{-2}, this allowed us to neglect the influence of the magnetic field on the electron.

Dipole approximation: verified for large wavelength with respect to the atom size $\lambda_\mathrm{L} \gg r$, this allowed to neglect the $\mathbf{r}$ dependency in the field quantities.

To these, we add new assumptions for the description of our system:

Frozen nuclei: we drop the dependency in the position of the nuclei. This is justified by the large difference of masses between the electron and the nuclei. Since the nuclei are much heavier, their dynamics evolves at much longer time scales. We can therefore neglect their motion for very short laser pulses of a few tens of fs.

Single Active Electron (SAE): the only active electron evolves under the action of an effective potential V_0 that represents its averaged interaction with the whole ionic core.

In this framework, the SFA assumptions read [11]:

(a) The contributions of the excited bound states $|\varphi_i\rangle$, with $i \geq 1$, are neglected. The wave function can thus be decomposed on the ground state $|\varphi_0\rangle$ and on the continuum states $|\varphi_E\rangle$ only.

(b) The depletion of the ground state $|\varphi_0\rangle$ is neglected, the population in the ground state is considered to be equal to one.

(c) Plane Wave Approximation (PWA): The influence of the potential V_0 on the ionized electron is neglected, i.e. the continuum states $|\varphi_E\rangle$ are approximated by plane waves $|\mathbf{k}\rangle$, where $\langle\mathbf{r}|\mathbf{k}\rangle = \mathrm{e}^{i\mathbf{k}\cdot\mathbf{r}}$. Note that we also made this approximation for the classical analysis made in the previous section.

Assumption **(a)** implies that we are out of any resonance, which is generally the case for the photon energies used in HHG. Assumption **(b)** is valid for intensities that are below the saturation intensity. Assumption **(c)** is systematically valid for short-range potentials. For Coulomb-like potential, it is justified under two conditions: when the electron is far from the nucleus, it requires that the electric field is large enough, i.e. that the Keldysh parameter is small $\gamma \leq 1$, and when the electron returns close to the nucleus, it requires that this electron has a sufficiently high kinetic energy so that it does not feel the potential V_0. This approximation will thus only hold for the high energy part of the emitted spectrum. The low energy part $\omega_\mathrm{e} \leq I_\mathrm{p}$ cannot be accurately computed in this model.

b) Dipole expression

From assumptions **(a)** and **(c)** we get the following ansatz for the wave function

$$|\psi(t)\rangle = \mathrm{e}^{iI_\mathrm{p}t}\left(a_0(t)\,|\varphi_0\rangle + \int \mathrm{d}\mathbf{k}\, c(\mathbf{k},t)\,|\mathbf{k}\rangle\right), \tag{I.87}$$

with

$$\left(\frac{\hat{p}^2}{2} + V_0(\hat{\mathbf{r}})\right)|\mathbf{k}\rangle \simeq \frac{\hat{p}^2}{2}\,|\mathbf{k}\rangle = \frac{k^2}{2}\,|\mathbf{k}\rangle\,, \tag{I.88}$$

and with assumption **(b)**, we get $a_0(t) \simeq 1$. Inserting (I.87) in the TDSE and projecting over $|\mathbf{k}\rangle$, we get the following differential equation for the time-dependent coefficients:

$$\dot{c}(\mathbf{k},t) = -\mathrm{i}\left(I_\mathrm{p} + \frac{k^2}{2}\right)c(\mathbf{k},t) - \mathrm{i}F_\mathrm{L}(t)\left(\langle\mathbf{k}|\,x\,|\varphi_0\rangle + \int \mathrm{d}\mathbf{k}'\, c(\mathbf{k}',t)\,\langle\mathbf{k}|\,x\,|\mathbf{k}'\rangle\right), \tag{I.89}$$

where we assumed that the laser field is linearly polarized along the x direction. The last term can be integrated by parts:

$$-\,\mathrm{i}\int \mathrm{d}\mathbf{k}'\, c(\mathbf{k}',t)\,\langle\mathbf{k}|\,x\,|\mathbf{k}'\rangle = \int \mathrm{d}\mathbf{k}'\,\frac{\partial c}{\partial p_x}(\mathbf{k}',t)\,\langle\mathbf{k}|\mathbf{k}'\rangle = \frac{\partial c}{\partial k_x}(\mathbf{k},t). \tag{I.90}$$

We define d_ion the ionization dipole matrix element:

$$d_\mathrm{ion}(\mathbf{k},t) = F_\mathrm{L}(t)\,\langle\mathbf{k}|\,x\,|\varphi_0\rangle\,, \tag{I.91}$$

so that (I.89) finally reads

$$\dot{c}(\mathbf{k},t) = -\mathrm{i}\left(I_\mathrm{p} + \frac{k^2}{2}\right)c(\mathbf{k},t) - \mathrm{i}d_\mathrm{ion}(\mathbf{k},t) + F_\mathrm{L}(t)\frac{\partial c}{\partial k_x}(\mathbf{k},t). \tag{I.92}$$

This equation integrates to:

$$c(\mathbf{k},t) = \int_0^t \mathrm{d}t' d_{\mathrm{ion}}(\mathbf{k} - \mathbf{A}_{\mathrm{L}}(t) + \mathbf{A}_{\mathrm{L}}(t'), t') \times \exp\left[-\mathrm{i}\int_{t'}^t \mathrm{d}\tau \left(\frac{(\mathbf{k} - \mathbf{A}_{\mathrm{L}}(t) + \mathbf{A}_{\mathrm{L}}(\tau))^2}{2} + I_{\mathrm{p}}\right)\right], \tag{I.93}$$

where the vector potential $\mathbf{A}_{\mathrm{L}}$ is defined in the Coulomb gauge by (I.7).

We are interested in the radiation emitted by the system, which is proportional to the average value of the dipole operator:

$$\mathbf{D}(t) = \langle\psi(t)|\,\hat{\mathbf{D}}\,|\psi(t)\rangle\,. \tag{I.94}$$

Depending on the chosen representation, $\hat{\mathbf{D}}$ may either be the position $\hat{\mathbf{D}}_{\mathrm{d}}$, velocity $\hat{\mathbf{D}}_{\mathrm{v}}$ or acceleration $\hat{\mathbf{D}}_{\mathrm{a}}$ operator defined in (II.77). The three representations are actually equivalent. In fact, it is easy to show by integration by part that they are simply related to one another by factors of ω, see section II.3.2 for more details.

Using the approximate ansatz (I.87), we get:

$$\mathbf{D}(t) = \langle\varphi_0|\,\hat{\mathbf{D}}\,|\varphi_0\rangle + \int \mathrm{d}\mathbf{k}\, c(\mathbf{k},t)\,\langle\varphi_0|\,\hat{\mathbf{D}}\,|\mathbf{k}\rangle + \int \mathrm{d}\mathbf{k}\, c^*(\mathbf{k},t)\,\langle\mathbf{k}|\,\hat{\mathbf{D}}\,|\varphi_0\rangle + \iint \mathrm{d}\mathbf{k}\,\mathrm{d}\mathbf{k}'\, c^*(\mathbf{k}',t)c(\mathbf{k},t)\,\langle\mathbf{k}'|\,\hat{\mathbf{D}}\,|\mathbf{k}\rangle\,. \tag{I.95}$$

We neglect the continuum-continuum contributions [11, 122], and drop the ground state contribution since it cancels for apolar systems and only adds a constant component to the spectrum for polar molecules. We also perform the substitution $\mathbf{p} = \mathbf{k} - \mathbf{A}_{\mathrm{L}}(t)$, and get

$$\mathbf{D}(t) = \int_0^t \mathrm{d}t' \int \mathrm{d}\mathbf{p}\, \mathbf{d}_{\mathrm{rec}}(\mathbf{p} + \mathbf{A}_{\mathrm{L}}(t)) d_{\mathrm{ion}}(\mathbf{p} + \mathbf{A}_{\mathrm{L}}(t'), t')\, \mathrm{e}^{-\mathrm{i}S(\mathbf{p},t,t')} + \mathrm{c.c.}, \tag{I.96}$$

where $\mathbf{d}_{\mathrm{rec}}$ is the recombination dipole matrix element:

$$\mathbf{d}_{\mathrm{rec}}(\mathbf{p}) = \langle\varphi_0|\,\hat{\mathbf{D}}\,|\mathbf{p}\rangle\,, \tag{I.97}$$

and S the quasiclassical action:

$$S(\mathbf{p},t,t') = \int_{t'}^t \mathrm{d}\tau \left(\frac{[\mathbf{p} + \mathbf{A}_{\mathrm{L}}(\tau)]^2}{2} + I_{\mathrm{p}}\right). \tag{I.98}$$

We can interpret (I.96) in the same spirit as in time-dependent perturbation theory in section I.2.1 c): at $t = 0$ the system is in state $|\varphi_0\rangle$, and it accumulates a phase $\mathrm{e}^{\mathrm{i}I_{\mathrm{p}}t'}$ until time t' where it is transferred to state $|\mathbf{p}\rangle$ with transition matrix element $d_{\mathrm{ion}}(\mathbf{p} + \mathbf{A}_{\mathrm{L}}(t'), t')$. Afterwards it evolves in that state under the influence of the field only, accumulating a phase $\int_{t'}^t \mathrm{d}\tau\,[\mathbf{p} + \mathbf{A}_{\mathrm{L}}(\tau)]^2/2$, and it finally recombines to the ground state $|\varphi_0\rangle$ at time t with transition matrix element $\mathbf{d}_{\mathrm{rec}}(\mathbf{p} + \mathbf{A}_{\mathrm{L}}(t))$. The last $\mathrm{e}^{\mathrm{i}I_{\mathrm{p}}t}$ factor comes from (I.87). It is remarkable that we recognize the three steps mentioned before: ionization, propagation in the continuum and recombination to the ground state.

To get the spectrum of the emitted radiation we need to compute the Fourier transform of the dipole:

$$\widetilde{\mathbf{D}}(\omega) = \widetilde{\mathbf{D}}_+(\omega) + \widetilde{\mathbf{D}}_-(\omega), \tag{I.99}$$

with

$$\widetilde{\mathbf{D}}_+(\omega) = \int \mathrm{d}t \int_0^t \mathrm{d}t' \int \mathrm{d}\mathbf{p}\, \mathbf{d}_{\mathrm{rec}}(\mathbf{p} + \mathbf{A}_{\mathrm{L}}(t)) d_{\mathrm{ion}}(\mathbf{p} + \mathbf{A}_{\mathrm{L}}(t'), t')\, \mathrm{e}^{-\mathrm{i}[S(\mathbf{p},t,t')+\omega t]}, \tag{I.100}$$

and $\widetilde{\mathbf{D}}_-(\omega) = \widetilde{\mathbf{D}}_+^*(-\omega)$.

Note that within SFA the two gauges described in sections I.1.2 and I.1.1 are not equivalent anymore. Here we made all the calculations in the length gauge, i.e. with the ER expression of the Hamiltonian (I.21). If we make the same derivation in the velocity gauge, i.e. with the AP expression of Hamiltonian (I.14), we obtain [84]

$$\widetilde{\mathbf{D}}_+(\omega) = \int \mathrm{d}t \int_0^t \mathrm{d}t' \int \mathrm{d}\mathbf{p}\, \mathbf{d}_{\mathrm{rec}}(\mathbf{p}) d_{\mathrm{ion}}(\mathbf{p}, t')\, \mathrm{e}^{-\mathrm{i}[S(\mathbf{p},t,t')+\omega t]}, \tag{I.101}$$

where the ionization dipole element reads:

$$d_{\mathrm{ion}}(\mathbf{p}, t') = A_{\mathrm{L}}(t') \left\langle \mathbf{p} \middle| -\mathrm{i}\frac{\partial}{\partial p_x} + \frac{{A_{\mathrm{L}}}^2(t')}{2} \middle| \varphi_0 \right\rangle. \tag{I.102}$$

These differences between the results obtained in each of the two gauges can actually be used to test the validity of the SFA approximations.

c) Saddle point approximation

The triple integral (I.100) cannot be computed analytically in the general case, and its numerical evaluation is very costly. Nevertheless we can get an approximate, and intuitive, evaluation of it by performing the Saddle Point Approximation (SPA). Since $I_{\mathrm{p}}/\omega_{\mathrm{L}}$ is very large, the quasiclassical action has very large variations, and the exponential term in (I.100) oscillates very fast. If it oscillates much faster than the preexponential term, then the main contribution to the integral comes from the points where the phase is stationary:

$$\boldsymbol{\nabla}(S(\mathbf{p}, t, t') \pm \omega t) = 0, \tag{I.103}$$

where the $\boldsymbol{\nabla}$ operator contains here the derivatives with respect to all the variables of S. The sign in front of ω is a $+$ for $\widetilde{\mathbf{D}}_+(\omega)$ and a $-$ for $\widetilde{\mathbf{D}}_-(\omega)$. This evaluation of the integral relies on the method of stationary phase [123, 124], that allows to compute the asymptotic form of generalized Fourier transform integrals. More details are given in Appendix A.

The evaluation of (I.100) in the SPA reduces to solving (I.103). For the term $\widetilde{\mathbf{D}}_-(\omega)$ this gives

$$\int_{t'}^{t} [\mathbf{p} + \mathbf{A}_{\mathrm{L}}(\tau)]\, \mathrm{d}\tau = 0 \tag{I.104a}$$

$$\frac{[\mathbf{p} + \mathbf{A}_{\mathrm{L}}(t)]^2}{2} + I_{\mathrm{p}} - \omega = 0 \tag{I.104b}$$

$$\frac{[\mathbf{p} + \mathbf{A}_{\mathrm{L}}(t')]^2}{2} + I_{\mathrm{p}} = 0. \tag{I.104c}$$

These three equations actually encode the three step model. The first of them involves the classical velocity $\mathbf{p}+\mathbf{A}_\mathrm{L}$ of the free electron in the laser field. The integral of this velocity is equal to the difference between the positions at recombination and at ionization [11]:

$$\int_{t'}^{t} [\mathbf{p} + \mathbf{A}_\mathrm{L}(\tau)]\,\mathrm{d}\tau = \mathbf{r}(t) - \mathbf{r}(t') \tag{I.105}$$

The solutions of (I.104a) are thus quantum paths where the electron is ionized at position $\mathbf{r}(t')$ at time t' and then returns to this same position a later time t. This is what we intuitively expect of an electron being ionized at the nucleus and later returning to this nucleus to recombine.

The second equation encodes the energy conservation at the recombination time t. Indeed $[\mathbf{p}+\mathbf{A}_\mathrm{L}]^2/2$ is the kinetic energy of the electron in the continuum, (I.104b) thus states that the energy ω of the emitted photon is equal to the energy difference between the electron in the continuum and the ground state. We retrieve the energy conservation (I.76).

Finally, the third saddle point equation (I.104c) represents the energy conservation at ionization time t'. Note that this equation does not have any solution for real values of $\mathbf{p}$ and t'. The solutions of (I.104) thus involves complex stationary points for the phase. This is related to the intrinsic quantum nature of tunnel ionization, which has no classical counterpart. The imaginary part of t' may be interpreted as the tunnel ionzation time [11]. Observe that this ionization time is the time when the electron starts its trajectory in the continuum, but cannot be related to a tunnel ionization *duration*. It is actually impossible to define such an ionization duration rigorously and without any ambiguity in the framework of quantum mechanics [125, 126].

If we compute numerically the solutions of (I.104) we find two families of solutions, which are the analogues of the *short* and *long* trajectories described in the previous section. In conclusion the quantum paths that are solutions of (I.104), i.e. the paths that give the largest contribution to HHG, are actually the quantum equivalents of the trajectories of the classical three step model.

Note that for the term $\widetilde{\mathbf{D}}_+(\omega)$ the saddle point equations (I.104) are identical, except for (I.104b), where there is a change of sign in front of ω:

$$\frac{[\mathbf{p}+\mathbf{A}_\mathrm{L}(t)]^2}{2} + I_\mathrm{p} + \omega = 0. \tag{I.106}$$

Since this equation does not satisfy energy conservation, the contribution of the $\widetilde{\mathbf{D}}_+(\omega)$ term will actually be negligible in (I.99), and we will only keep $\widetilde{\mathbf{D}}_-(\omega)$ in the following.

We note $(\mathbf{p}_\mathrm{at}, t_\mathrm{at}, t'_\mathrm{at})$ the solutions of the *atomic* equations (I.104) to distinguish them from the solutions of the *molecular* equations that we will detail in the following section. The Fourier transform of the dipole (I.100) finally writes:

$$\widetilde{\mathbf{D}}_\mathrm{at}(\omega) = \sum_{j=S,L} C({t_\mathrm{at}}^{(j)}, {t'^{(j)}_\mathrm{at}})\mathbf{d}_\mathrm{rec}({\mathbf{p}_\mathrm{at}}^{(j)} + \mathbf{A}_\mathrm{L}({t_\mathrm{at}}^{(j)}))d_\mathrm{ion}({\mathbf{p}_\mathrm{at}}^{(j)} + \mathbf{A}_\mathrm{L}(t'^{(j)}_\mathrm{at}), t'^{(j)}_\mathrm{at})\,\mathrm{e}^{-\mathrm{i}S_\mathrm{at}}, \tag{I.107}$$

where S and L stands for the short and long trajectories respectively and S_at is the quasiclassical action evaluated at the stationary point:

$$S_\mathrm{at} = S(\mathbf{p}_\mathrm{at}, t_\mathrm{at}, t'_\mathrm{at}) - \omega t_\mathrm{at} \tag{I.108}$$

The saddle point prefactor C reads [127]:

$$C(t,t') = \left(\frac{2\pi}{\mathrm{i}(t-t')}\right)^{\frac{3}{2}} \frac{\pi}{\sqrt{\det \mathcal{H}_{S_p}(t,t')}}, \tag{I.109}$$

where $\mathcal{H}_{S_p}$ is the Hessian matrix of $S_p(t,t') = S(\mathbf{p}_{\mathrm{at}}(t,t'),t,t') - \omega t$, where $\mathbf{p}_{\mathrm{at}}(t,t')$ is the solution of (I.104a):

$$\det \mathcal{H}_{S_p}(t,t') = \frac{\partial^2 S_p}{\partial t^2}\frac{\partial^2 S_p}{\partial t'^2} - \left(\frac{\partial^2 S_p}{\partial t \partial t'}\right)^2. \tag{I.110}$$

d) Molecular saddle point approximation

In principle the development that we just made can be applied to atoms or molecules. Indeed the unperturbed ground state $|\varphi_0\rangle$ and the ionization potential I_{p} that enters the final result (I.107) could either belong to an atom or a molecule. However in practice this formulation gives very bad results even for the smallest molecule that comprises only two nuclei.

The reason is that the SPA that we used to compute the integral in (I.100) assumes that the preexponential term $\mathbf{d}_{\mathrm{rec}} d_{\mathrm{ion}}$ varies slowly with respect to the quasiclassical action. For atoms this will almost always be the case and we can use (I.107). On the contrary, in the case of molecules this preexponential factor may cancel for values of $(\mathbf{p},t,t')$ that reflects the molecular orbital structure. If this zero is close to the stationary point, i.e. the solution of (I.104), then the SPA fails to predict the correct value of the integral. We thus need to take this zero into account when looking for stationary points. Said otherwise, we need to take the molecular structure into account in our description.

The method that we present here for homonuclear diatomic molecules has been introduced in [84], and then developed in [128, 129] and will be investigated in more details in Chapter IV. It relies on the Linear Combination of Atomic Orbitals (LCAO) approximation, which adds to all the assumptions listed before in section I.3.3 a). It amounts to write the ground state $|\varphi_0\rangle$ as a sum of two shifted functions ϕ_{a}:

$$\varphi_0(\mathbf{r}) = \frac{1}{\sqrt{2(1+w(\mathbf{R}))}}\left[\phi_{\mathrm{a}}\left(\mathbf{r}-\frac{\mathbf{R}}{2}\right) + \phi_{\mathrm{a}}\left(\mathbf{r}+\frac{\mathbf{R}}{2}\right)\right], \tag{I.111}$$

where $w(\mathbf{R})$ is the overlap between the two shifted ϕ_{a} orbitals, and $\mathbf{R}$ is the internuclear vector. We choose the center of the molecule as origin of the coordinate system, so that nucleus 1 is located at $-\mathbf{R}/2$ and nucleus 2 at $+\mathbf{R}/2$. Inserting (I.111) in the expression

of d_{ion} (I.91) gives:

$$\begin{aligned}
d_{\text{ion}}(\mathbf{p},t) &= F_{\text{L}}(t)\,\langle\mathbf{p}|\,x\,|\varphi_0\rangle \\
&= \frac{F_{\text{L}}(t)}{\sqrt{2(1+w(\mathbf{R}))}}\int \mathrm{d}\mathbf{r}\left[\phi_{\text{a}}\left(\mathbf{r}-\frac{\mathbf{R}}{2}\right)+\phi_{\text{a}}\left(\mathbf{r}+\frac{\mathbf{R}}{2}\right)\right] x\,\mathrm{e}^{\mathrm{i}\mathbf{p}\cdot\mathbf{r}} \\
&= \frac{F_{\text{L}}(t)}{\sqrt{2(1+w(\mathbf{R}))}}\int \mathrm{d}\mathbf{r}\,\phi_{\text{a}}(\mathbf{r})\,\mathrm{e}^{\mathrm{i}\mathbf{p}\cdot\mathbf{r}}\left[\left(x+\frac{R_x}{2}\right)\mathrm{e}^{\mathrm{i}\mathbf{p}\cdot\frac{\mathbf{R}}{2}}+\left(x-\frac{R_x}{2}\right)\mathrm{e}^{-\mathrm{i}\mathbf{p}\cdot\frac{\mathbf{R}}{2}}\right] \\
&= \frac{F_{\text{L}}(t)}{\sqrt{2(1+w(\mathbf{R}))}}\left[-\mathrm{i}\frac{\partial\widetilde{\phi}_{\text{a}}}{\partial p_x}(\mathbf{p})\left(\mathrm{e}^{\mathrm{i}\mathbf{p}\cdot\frac{\mathbf{R}}{2}}+\mathrm{e}^{-\mathrm{i}\mathbf{p}\cdot\frac{\mathbf{R}}{2}}\right)+\frac{R_x}{2}\widetilde{\phi}_{\text{a}}(\mathbf{p})\left(\mathrm{e}^{\mathrm{i}\mathbf{p}\cdot\frac{\mathbf{R}}{2}}-\mathrm{e}^{-\mathrm{i}\mathbf{p}\cdot\frac{\mathbf{R}}{2}}\right)\right] \\
&= M_1(\mathbf{p},t)\,\mathrm{e}^{\mathrm{i}\mathbf{p}\cdot\frac{\mathbf{R}}{2}}+M_2(\mathbf{p},t)\,\mathrm{e}^{-\mathrm{i}\mathbf{p}\cdot\frac{\mathbf{R}}{2}},
\end{aligned} \tag{I.112}$$

where we noted $M_\alpha(\mathbf{p},t)$ the molecular ionization dipole element:

$$M_\alpha(\mathbf{p},t) = -\frac{F_{\text{L}}(t)}{\sqrt{2(1+w(\mathbf{R}))}}\left[\mathrm{i}\frac{\partial\widetilde{\phi}_{\text{a}}}{\partial p_x}+(-1)^\alpha\frac{R_x}{2}\widetilde{\phi}_{\text{a}}(\mathbf{p})\right]. \tag{I.113}$$

The expression of the recombination dipole $\mathbf{d}_{\text{rec}}$ (I.97) in the LCAO approximation strongly depends on the chosen dipole representation [130]. Following the argumentation in [131], and [130], we take the velocity form of the dipole $\hat{\mathbf{D}} = -\mathrm{i}\boldsymbol{\nabla}$, which gives:

$$\begin{aligned}
\mathbf{d}_{\text{rec}}(\mathbf{p}) &= \langle\varphi_0|-\mathrm{i}\boldsymbol{\nabla}\,|\mathbf{p}\rangle \\
&= \frac{1}{\sqrt{2(1+w(\mathbf{R}))}}\int \mathrm{d}\mathbf{r}\left[\phi_{\text{a}}\left(\mathbf{r}-\frac{\mathbf{R}}{2}\right)+\phi_{\text{a}}\left(\mathbf{r}+\frac{\mathbf{R}}{2}\right)\right]\mathbf{p}\,\mathrm{e}^{\mathrm{i}\mathbf{p}\cdot\mathbf{r}} \\
&= \frac{\mathbf{p}}{\sqrt{2(1+w(\mathbf{R}))}}\widetilde{\phi}_{\text{a}}(\mathbf{p})\left(\mathrm{e}^{\mathrm{i}\mathbf{p}\cdot\frac{\mathbf{R}}{2}}+\mathrm{e}^{-\mathrm{i}\mathbf{p}\cdot\frac{\mathbf{R}}{2}}\right) \\
&= \mathbf{L}(\mathbf{p})\left(\mathrm{e}^{\mathrm{i}\mathbf{p}\cdot\frac{\mathbf{R}}{2}}+\mathrm{e}^{-\mathrm{i}\mathbf{p}\cdot\frac{\mathbf{R}}{2}}\right),
\end{aligned} \tag{I.114}$$

where $\mathbf{L}(\mathbf{p})$ is the molecular recombination dipole:

$$\mathbf{L}(\mathbf{p}) = \frac{\mathbf{p}}{\sqrt{2(1+w(\mathbf{R}))}}\widetilde{\phi}_{\text{a}}(\mathbf{p}). \tag{I.115}$$

Since both recombination and ionization dipole elements are composed of two terms, the preexponential factor is composed of four terms:

$$\mathbf{d}_{\text{rec}}(\mathbf{p}+\mathbf{A}_{\text{L}}(t))d_{\text{ion}}(\mathbf{p}+\mathbf{A}_{\text{L}}(t'),t') = \sum_{\alpha,\beta=1}^{2}\mathbf{L}(\mathbf{p}+\mathbf{A}_{\text{L}}(t))M_\alpha(\mathbf{p}+\mathbf{A}_{\text{L}}(t'),t')\,\mathrm{e}^{-\mathrm{i}\Phi_{\alpha,\beta}}, \tag{I.116}$$

where the phase $\Phi_{\alpha,\beta}$ reads:

$$\Phi_{\alpha,\beta}(\mathbf{p},t,t') = (-1)^\alpha\left[\mathbf{p}+\mathbf{A}_{\text{L}}(t')\right]\cdot\frac{\mathbf{R}}{2}-(-1)^\beta\left[\mathbf{p}+\mathbf{A}_{\text{L}}(t)\right]\cdot\frac{\mathbf{R}}{2}. \tag{I.117}$$

There are thus four contributions to the dipole spectrum (I.96):

$$\widetilde{\mathbf{D}}(\omega) = \sum_{\alpha,\beta=1}^{2} \int \mathrm{d}t \int_0^t \mathrm{d}t' \int \mathrm{d}\mathbf{p}\, \mathbf{L}(\mathbf{p} + \mathbf{A}_\mathrm{L}(t)) M_\alpha(\mathbf{p} + \mathbf{A}_\mathrm{L}(t'), t')\, \mathrm{e}^{-\mathrm{i}S_{\alpha,\beta}(\mathbf{p},t,t')}, \tag{I.118}$$

where we defined a *modified* action $S_{\alpha,\beta}$:

$$S_{\alpha,\beta}(\mathbf{p}, t, t') = S(\mathbf{p}, t, t') + \Phi_{\alpha,\beta}(\mathbf{p}, t, t') - \omega t. \tag{I.119}$$

As in the atomic case, we compute these four integrals using the SPA. We thus need to find the stationary points of $S_{\alpha,\beta}$, i.e. solve $\boldsymbol{\nabla} S_{\alpha,\beta} = 0$. Since each of the four integrals in (I.118) have a different expression for the phase $S_{\alpha,\beta}$, we have four sets of saddle point equations for each values of α and β [128]:

$$\int_{t'}^{t} [\mathbf{p} + \mathbf{A}_\mathrm{L}(\tau)]\, \mathrm{d}\tau + \left[(-1)^\alpha - (-1)^\beta\right] \frac{\mathbf{R}}{2} = 0 \tag{I.120a}$$

$$\frac{[\mathbf{p} + \mathbf{A}_\mathrm{L}(t)]^2}{2} + I_\mathrm{p} + (-1)^\beta \mathbf{F}_\mathrm{L}(t) \cdot \frac{\mathbf{R}}{2} - \omega = 0 \tag{I.120b}$$

$$\frac{[\mathbf{p} + \mathbf{A}_\mathrm{L}(t')]^2}{2} + I_\mathrm{p} + (-1)^\alpha \mathbf{F}_\mathrm{L}(t') \cdot \frac{\mathbf{R}}{2} = 0 \tag{I.120c}$$

and thus four families of stationary solutions, that correspond to four families of quantum paths.

As we have said in the previous section the first equation (I.120a) is related to the trajectory of the free electron. Indeed, as we already said $\mathbf{p} + \mathbf{A}_\mathrm{L}$ is the classical velocity of the ionized electron, and its integral is equal to the difference between the positions at recombination and at ionization times. Therefore the cases where $\alpha = \beta$ correspond to trajectories where the electron is ionized and recombines at the *same* position. On the contrary, in the cases where $\alpha \neq \beta$ the electron is ionized at a point $\mathbf{r}(t')$ and recombines at a *different* position $\mathbf{r}(t)$, and these two positions are separated by $\pm\mathbf{R}$. This has a clear interpretation: at ionization, the electron may leave the molecule from either one of its two nuclei, and likewise when it returns to the molecule it may recombine to either one of the nuclei. The four different families of equations, labelled by α, β, thus correspond to trajectories where the electron leaves the molecules from nucleus α and returns to nucleus β.

The two remaining equations, which represent energy conservation at ionization and recombination, are also modified. This is a consequence of the fact that the saddle point equations are not translationaly invariant [84]. The energy of the electron in the continuum, which was only equal to its kinetic energy $[\mathbf{p} + \mathbf{A}_\mathrm{L}]^2/2$ in the atomic case (I.104), get an additional term arising from its interaction with the electric field $\mathbf{r} \cdot \mathbf{F}_\mathrm{L}$. If the free electron is located on nucleus α, i.e. at $\mathbf{r} = (-1)^\alpha \mathbf{R}/2$, this interaction is thus equal to $(-1)^\alpha \mathbf{F}_\mathrm{L}(t') \cdot \mathbf{R}/2$, which is the additional term in (I.120b) and (I.120c).

Note that both the *long* and *short* trajectories contributions are thus written as a sum of the four terms corresponding to the four situations we just mentioned. Nevertheless, to alleviate the notations, we do not explicitly write the sum over the long and short

trajectories in the final expression of the dipole spectrum, which reads

$$\widetilde{\mathbf{D}}_{\alpha,\beta}(\omega) = \sum_{\alpha,\beta=1}^{2} C_{\alpha,\beta}(t_{\alpha\beta}, t'_{\alpha\beta})\mathbf{L}(\mathbf{p}_{\alpha\beta} + \mathbf{A}_{\mathrm{L}}(t_{\alpha\beta}))M_{\alpha}(\mathbf{p}_{\alpha\beta} + \mathbf{A}_{\mathrm{L}}(t'_{\alpha\beta}), t'_{\alpha\beta})\,\mathrm{e}^{-\mathrm{i}S_{\alpha,\beta}}, \quad \text{(I.121)}$$

where $(\mathbf{p}_{\alpha\beta}, t_{\alpha\beta}, t'_{\alpha\beta})$ are the molecular stationary points, and $C_{\alpha,\beta}$ is the saddle point prefactor (I.109).

Chapter II
Numerical methods

During my PhD, I studied diverse systems with different dimensionality and complexity. For all these systems, we want to solve the same equation, namely the Schrödinger equation. But in practice we use distinct methods suited to the specificity of each system and each physical phenomenon we are interested in. All the results presented in this thesis were computed with numerical programs written by myself, unless explicitly stated otherwise. In this chapter are presented the numerical methods and algorithms underlying these programs. In each case, we choose the numerical method as a compromise between a reasonable computational cost, and a controllable numerical error. For the relatively small systems considered here, limitations usually come from the number of operations rather than memory. We will thus define our computational cost by the complexity of the algorithms used in the different numerical methods.

Numerical error originates from two sources: numerical precision, and algorithm precision. Indeed, since our computers have a *finite* memory, each number is stored on a definite number of bytes. For example, here we use 16 bytes to store each *real* number, which is the so-called *double precision*. This defines our machine accuracy. All the numerical arithmetic is thus performed on *truncated* numbers. Consequently each arithmetic operation is performed with a finite precision which depends on the type of operation and on the relative value of the numbers involved in the operation. In general the numerical error is particularly important when summing two numbers that have very different orders of magnitude, or when subtracting two numbers that are very close. In general, it is actually quite tricky to control this numerical error. Besides, even with an infinite computer memory the algorithm error remains. The latter arises from both the discretization of the Hilbert space and the discretization of time. This algorithm error can in general be controlled by raising the number of points in each of these discretizations, until we reach what we call convergence i.e. the numerical machine accuracy.

The convergence properties of an algorithm are of crucial importance. A faster convergence allows to save some computational time and thus to describe larger or more complex systems. We will be highly concerned by these convergence properties, i.e. by the numerical error made by each algorithm, in the presentation of the numerical methods.

Objectives

- Define 1D and 2D model systems for atoms and molecules.

- Compute energies and stationary states of these systems numerically (TISE).
- Compute the time-dependent wave function in presence of an EM field (TDSE).
- Analyze the time-dependent wave function to extract physical insight, and measurable quantities relevant for experiments.
- In each case, find the best compromise between numerical cost and numerical error.

II.1 One dimensional systems

One dimensional systems are perfect toy models for which we can make extensive numerical simulations, and thus get physical insight into intricate physical phenomena. They are particularly adapted to the case of tunnel ionization since the introdution of parabolic coordinates reduces the problem of the hydrogen atom in a static electric field to a one dimensional problem [132]. They are also suited to study HHG in atoms and molecules aligned along the electric field. This can be seen from the solution of the SFA equations developed in the previous chapter. We can show that the momentum $\mathbf{p}$ of the electron, which is solution of (I.104a) for atoms and of (I.120a) for aligned molecules, will actually always be parallel to the laser polarization direction.

II.1.1 Definition of the system

Our one dimensional model systems are composed of an electron initially trapped in a potential well V_0. For atoms, unless otherwise stated, it will always consist of a Soft-Coulomb potential [133]:

$$V_0(x) = -\frac{Z}{\sqrt{a^2 + x^2}}, \tag{II.1}$$

where Z is the electric charge of the nucleus, and a is the regularization parameter which is chosen to adjust the ionization potential I_p of the atom. Our diatomic molecules are modelled by the sum of two shifted wells:

$$V_0(x) = -\frac{Z/2}{\sqrt{a_1^2 + (x + R/2)^2}} - \frac{Z/2}{\sqrt{a_2^2 + (x - R/2)^2}}, \tag{II.2}$$

where R is the internuclear distance, and a_1, a_2 can be used to adjust the ionization potential I_p and the asymmetry - thus the permanent dipole moment - of the molecule.

The time-dependent wave function $\psi(x,t)$ is represented on a one-dimensional finite spatial grid defined by N_x points separated by a constant step Δx going from $-L$ to $+L$. It is stored as the vector $(\psi(x_i,t))_{i=1,N_x}$ whose components are the values ψ takes at each grid point. We choose the boundary conditions so that the wave function cancels at the border of the box $\psi(-L) = \psi(L) = 0$. The potential $V_0(x)$ is diagonal in this representation. The momentum and Laplace operators are calculated by the central difference formulas, involving errors proportional to Δx^2:

$$\frac{\mathrm{d}f}{\mathrm{d}x}(x) = \frac{f(x+\Delta x) - f(x-\Delta x)}{2\Delta x} + O\left(\Delta x^2\right) \tag{II.3a}$$

$$\frac{\mathrm{d}^2 f}{\mathrm{d}x^2}(x) = \frac{f(x+\Delta x) + f(x-\Delta x) - 2f(x)}{\Delta x^2} + O\left(\Delta x^2\right), \tag{II.3b}$$

and are tridiagonal in this representation. The total field-free Hamiltonian is thus tridiagonal:

$$\hat{H}_0 = -\frac{1}{2}\frac{\mathrm{d}^2}{\mathrm{d}x^2} + V_0(x) = \begin{pmatrix} \frac{1}{\Delta x^2} + V_0(x_1) & -\frac{1}{2\Delta x^2} & & (0) \\ -\frac{1}{2\Delta x^2} & \frac{1}{\Delta x^2} + V_0(x_2) & \ddots & \\ & \ddots & \ddots & -\frac{1}{2\Delta x^2} \\ (0) & & -\frac{1}{2\Delta x^2} & \frac{1}{\Delta x^2} + V_0(x_{N_x}) \end{pmatrix}. \tag{II.4}$$

In presence of the laser field, the interaction Hamiltonian is diagonal in length gauge:

$$\hat{x}F_{\mathrm{L}}(t) = \begin{pmatrix} x_1 F_{\mathrm{L}}(t) & & & (0) \\ & x_2 F_{\mathrm{L}}(t) & & \\ & & \ddots & \\ (0) & & & x_{N_x} F_{\mathrm{L}}(t) \end{pmatrix}, \tag{II.5}$$

and tridiagonal in velocity gauge:

$$\hat{p}A_{\mathrm{L}}(t) = \begin{pmatrix} 0 & -\mathrm{i}\frac{A_{\mathrm{L}}(t)}{2\Delta x} & & (0) \\ \mathrm{i}\frac{A_{\mathrm{L}}(t)}{2\Delta x} & 0 & \ddots & \\ & \ddots & \ddots & -\mathrm{i}\frac{A_{\mathrm{L}}(t)}{2\Delta x} \\ (0) & & \mathrm{i}\frac{A_{\mathrm{L}}(t)}{2\Delta x} & 0 \end{pmatrix}. \tag{II.6}$$

The time-dependent Hamiltonian is thus tridiagonal independently of the choice of gauge. We will see that this property is actually very important for numerical simulations since it drastically reduces the number of operations needed to perform algebraic operations on these matrices.

In theory, i.e. with an infinite box $N_x \to \infty$, and with an infinitely small step $\Delta x \to 0$, an electron trapped in the potential V_0 has an infinite number of states: an infinite number of discrete bound states, with negative energies E_i on the one hand, and a continuum of states of positive energies E ranging from 0 to $+\infty$ on the other hand. However, with the discretization of space that we just described, the Hamiltonian (II.4) is a finite size matrix, and has thus a finite number of eigenstates. With the parameters used in this thesis we typically find a few tens of bound states, and a few thousands of positive energy states. We will call *continuum* states these positive energy states, even if they are indeed discrete.

The first five bound states are represented in Figure II.1, for an atomic (II.1) and a homonuclear molecular (II.2) potentials. Since the potential is even, the ground state is even, and the excited states are alternatively odd or even[1]. As we can see, the energy gap between the states strongly depend on the internuclear distance R. In particular when R increases, the energy difference between the ground and the first excited states decreases.

[1] It is actually possible to show mathematically that, under certain conditions for the potential (which are fulfilled by both the Coulomb and Soft-Coulomb potentials), the ground state, if it exists, is positive and non degenerate (section XIII.12 of [134]). It will thus be symmetric under all the transformations that commute with the Hamiltonian, in this case the parity operator.

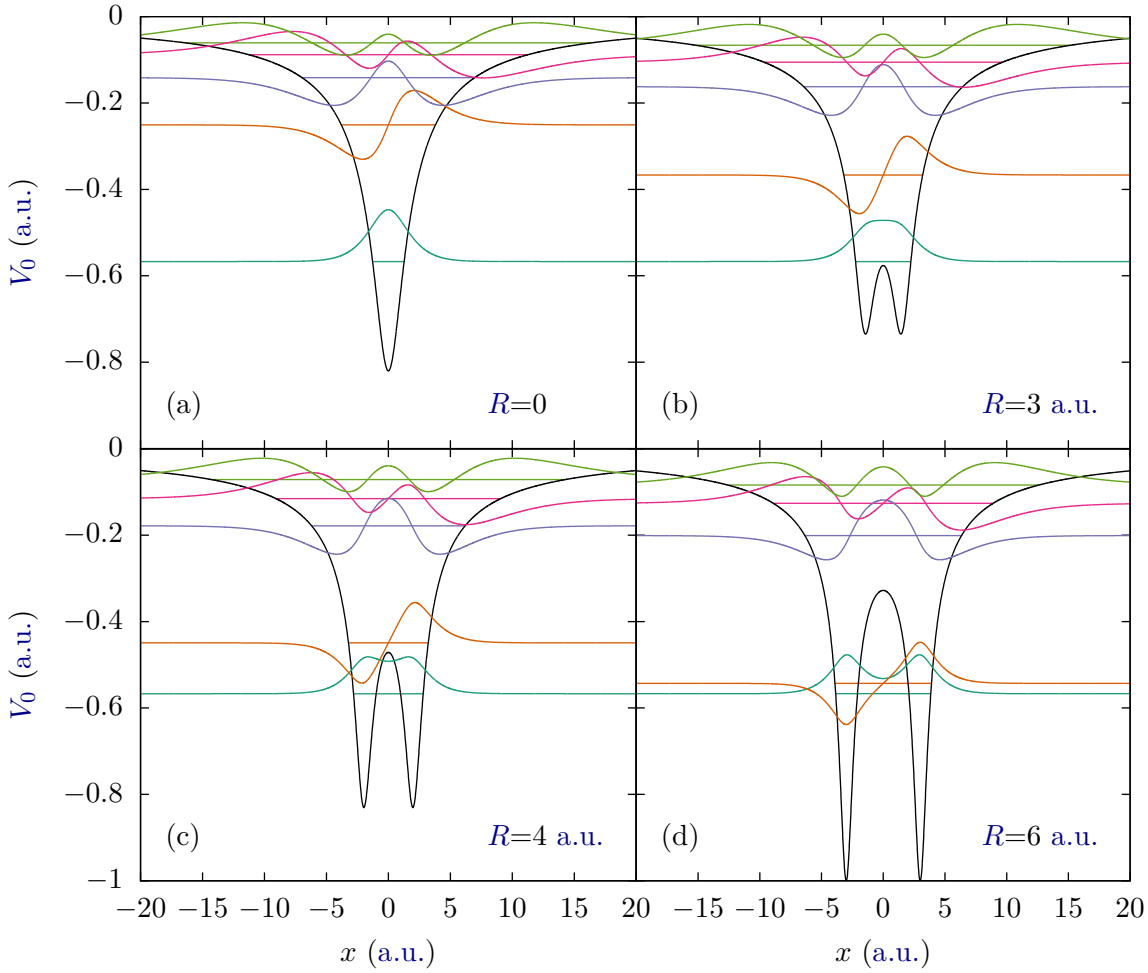

Figure II.1 *First bound states of the atom* (II.1) *and of the symmetric molecule* (II.2) *for different internuclear distances. The regularization parameter* a *is chosen to keep the ionization potential constant* ($I_\mathrm{p} = -E_0 = -0.567$ a.u.).

This is actually quite intuitive because when the two centers are completely apart, the electron is localized on either one of the two nuclei. Note that this is the basis of the famous LCAO approximation.

While the bound states, and their associated energies, are almost independent of the simulation box, on the contrary, the properties of the "continuum" energies are directly related to the grid parameters N_x and Δx. This is illustrated in the case of the free particle in Appendix B, where we derive the expression for the energies:

$$E_n = \frac{2}{\Delta x^2} \sin^2\left(\frac{n\pi}{2L}\Delta x\right). \tag{II.7}$$

We first remark that these energies never reach $+\infty$ but have a maximum at $E_\mathrm{max} = 2/\Delta x^2$ which is directly related to the discretization of space. This is related to Fourier transform limitations: basically we cannot describe a function that would have an oscillation period

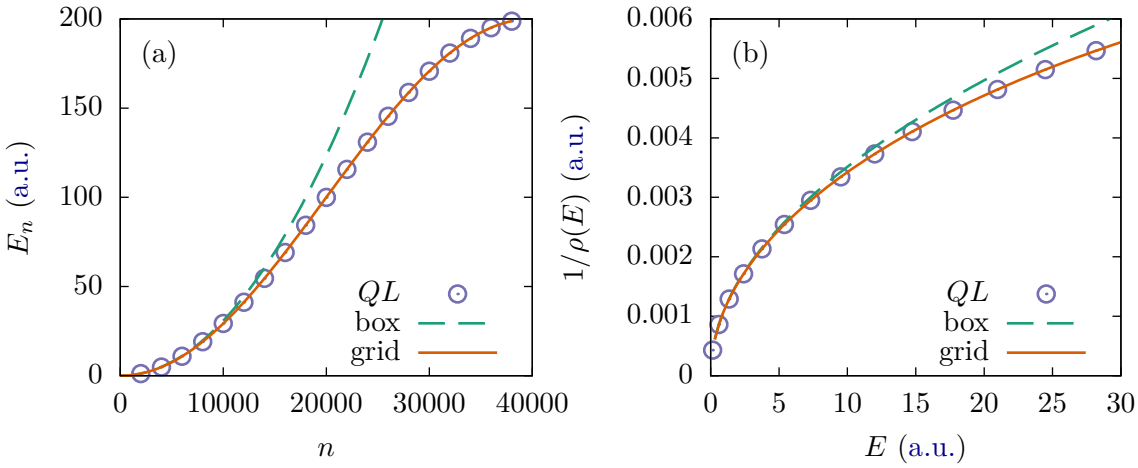

Figure II.2 *Continuum energies of the same atomic system as in panel (a) of Figure II.1 for a grid with parameters* $L = 2 \times 10^3$ a.u. *and* $\Delta x = 0.1$ a.u.. *Panel (a) : energy* E_n *as a function of* n. *Panel (b) : density of states* (II.9) *as a function of energy. The purple circles are numerical results obtained with the QL algorithm (see section II.1.3), the solid orange line is the free particle in a grid formula* (II.7), *and the dashed green line is the free particle in a box formula* (II.8).

smaller that Δx.

We also see that these energies are not continuous but discrete. This is a consequence of the finite size of the simulation box L, and is related to the well known particle in a box problem [135]. Indeed, our grid case converges to the particle in a box case when $\Delta x \to 0$:

$$E_n \underset{\Delta x \to 0}{\longrightarrow} \frac{n^2 \pi^2}{2(2L)^2}. \tag{II.8}$$

This "discreteness of the continuum" can be characterized through the density of states in the continuum which is defined as the number of states per unit of energy:

$$\rho(E) = \frac{\mathrm{d}n}{\mathrm{d}E}. \tag{II.9}$$

For a free particle in a box (II.8) gives

$$\rho(E) = \frac{2L}{\pi\sqrt{2E}}. \tag{II.10}$$

The "continuum" of our numerical atom in a grid (purple circles) is compared with the free particle in a grid (solid orange line) and the free particle in a box (dashed green line) in Figure II.2. We see that energies and density of state of our atom are identical, to the naked eye, to those of a free particle in a grid. However they differ from those of a free particle in a box as soon as the energy $E \gtrsim 10$ a.u.. This indicates that the continuum of our atom is very much alike the one of a free particle. Besides, the discrete nature of our grid does not seem to perturb strongly the continuum. Indeed significant differences only appear when the energy is no longer small compared to $E_{\max} = 2/\Delta x^2$, here when $E \gtrsim 10$ a.u., i.e. $E \gtrsim 270$ eV.

II.1.2 Solution of the time-dependent Schrödinger equation

a) Time discretization

The solution of the TDSE (I.3), starting from an initial state $|\psi(t_0)\rangle$ at time $t = t_0$, can be expressed as

$$|\psi(t)\rangle = \exp\left[-\mathrm{i}\int_{t_0}^{t} \hat{H}(\tau)\,\mathrm{d}\tau\right]|\psi(t_0)\rangle\,. \tag{II.11}$$

Therefore if one can compute the evolution operator $U(t, t+\Delta t)$:

$$U(t, t+\Delta t) = \exp\left[-\mathrm{i}\int_{t}^{t+\Delta t} \hat{H}(\tau)\,\mathrm{d}\tau\right], \tag{II.12}$$

then one can get the wave function at any time $t > t_0$. This turns out to be quite a task. Firstly because the integral of the Hamiltonian cannot, in general, be computed analytically. And second, because computing the exponential of a matrix is in general equivalent to diagonalize this matrix, which requires a large number of numerical operations. To circumvent the first problem, the most widespread technique relies on the discretization of time. If the two limits of the integral are close enough, i.e. if Δt is small enough, the evolution operator may be approximated as

$$U(t, t+\Delta t) = \exp\left[-\mathrm{i}\hat{H}\left(t + \frac{\Delta t}{2}\right)\Delta t + O\left(\Delta t^3\right)\right]. \tag{II.13}$$

Note that $\hat{H}$ is evaluated at the middle of the integration interval. This is crucial to get an error that is proportional to Δt^3 rather that Δt^2, and thus to get a faster convergence. This is a general feature of the approximation of integrals, and can easily be seen from the Taylor expansion of the integrand:

$$\int_a^{a+\epsilon} f(x)\,\mathrm{d}x = \int_a^{a+\epsilon} \mathrm{d}x\left[f(a) + (x-a)f'(a) + O\left((x-a)^2\right)\right] \tag{II.14}$$

$$= f(a)\epsilon + \frac{f'(a)}{2}\epsilon^2 + O\left(\epsilon^3\right) \tag{II.15}$$

$$= f(a)\epsilon + O\left(\epsilon^2\right). \tag{II.16}$$

In (II.14) we have expanded the integrand around one of the limits of the integral, and got an error proportional to the square of the integration interval width ϵ^2 (II.16). However, if we expand around the middle of the integration interval, the odd terms of the expansion

do not contribute to the integral:

$$\int_a^{a+\epsilon} f(x)\,\mathrm{d}x = \int_a^{a+\epsilon} \mathrm{d}x \left[f\left(a+\frac{\epsilon}{2}\right) + \cancel{\left(x-a-\frac{\epsilon}{2}\right) f'\left(a+\frac{\epsilon}{2}\right)} + \frac{1}{2}\left(x-a-\frac{\epsilon}{2}\right)^2 f''\left(a+\frac{\epsilon}{2}\right) + \cancel{\frac{1}{6}\left(x-a-\frac{\epsilon}{2}\right)^3 f^{(3)}\left(a+\frac{\epsilon}{2}\right)} + O\left(\left(x-a-\frac{\epsilon}{2}\right)^4\right)\right] \tag{II.17}$$

$$= f\left(a+\frac{\epsilon}{2}\right)\epsilon + \frac{1}{24} f''\left(a+\frac{\epsilon}{2}\right)\epsilon^3 + O\left(\epsilon^5\right) \tag{II.18}$$

$$= f\left(a+\frac{\epsilon}{2}\right)\epsilon + O\left(\epsilon^3\right), \tag{II.19}$$

and we get an error proportional to the third power of the integration interval width ϵ^3 (II.19).

b) Crank Nicolson algorithm

The naive way to compute the evolution operator (II.13) would be to make a Taylor expansion up to second order:

$$U(t,t+\Delta t) = \mathbb{1} - \mathrm{i}\hat{H}\left(t+\frac{\Delta t}{2}\right)\Delta t - \hat{H}^2\left(t+\frac{\Delta t}{2}\right)\frac{\Delta t^2}{2} + O\left(\Delta t^3\right). \tag{II.20}$$

The problem is that this is not a unitary operator anymore:

$$UU^\dagger = \left(\mathbb{1} - \mathrm{i}\hat{H}\Delta t - \hat{H}^2\frac{\Delta t^2}{2}\right)\left(\mathbb{1} + \mathrm{i}\hat{H}\Delta t - \hat{H}^2\frac{\Delta t^2}{2}\right) \tag{II.21}$$

$$= \mathbb{1} + \hat{H}^4\frac{\Delta t^4}{4}. \tag{II.22}$$

This has dramatic consequences: a propagation scheme that would use the expression (II.20) would not preserve the norm of the wave function. This would lead to unphysical results, but also to numerical instabilities. Thus we use instead the Crank Nicolson (CN) propagator [83]:

$$U_{\mathrm{CN}}(t,t+\Delta t) = \left[\mathbb{1} + \mathrm{i}\hat{H}\left(t+\frac{\Delta t}{2}\right)\frac{\Delta t}{2}\right]^{-1}\left[\mathbb{1} - \mathrm{i}\hat{H}\left(t+\frac{\Delta t}{2}\right)\frac{\Delta t}{2}\right]. \tag{II.23}$$

This expression also implies an error proportional to Δt^3, which can be seen by expanding the first factor:

$$U_{\mathrm{CN}} = \left[\mathbb{1} + \mathrm{i}\hat{H}\frac{\Delta t}{2}\right]^{-1}\left[\mathbb{1} - \mathrm{i}\hat{H}\frac{\Delta t}{2}\right] \tag{II.24}$$

$$= \left[\mathbb{1} - \mathrm{i}\hat{H}\frac{\Delta t}{2} - \hat{H}^2\frac{\Delta t^2}{4} + O\left(\Delta t^3\right)\right]\left[\mathbb{1} - \mathrm{i}\hat{H}\frac{\Delta t}{2}\right] \tag{II.25}$$

$$= \mathbb{1} - \mathrm{i}\hat{H}\Delta t - \hat{H}^2\frac{\Delta t^2}{2} + O\left(\Delta t^3\right) \tag{II.26}$$

$$= \mathrm{e}^{-\mathrm{i}\hat{H}\Delta t} + O\left(\Delta t^3\right). \tag{II.27}$$

Step	Operation	Complexity tridiagonal	Complexity general
$t_i = i\Delta t$			
$\chi = \left[\mathbb{1} - \mathrm{i}\hat{H}\frac{\Delta t}{2}\right]\psi(x, t_i)$	Matrix×vector multiplication $Y = AX$	$O(N_x)$	$O(N_x^2)$
$\left[\mathbb{1} + \mathrm{i}\hat{H}\frac{\Delta t}{2}\right]\psi(x, t_i + \Delta t) = \chi$	Inversion of the linear system $AX = Y$	$O(N_x)$	$O(N_x^2)$
Repeat for $t_{i+1} = (i+1)\Delta t$			

Table II.1 – Summary of the Crank Nicolson algorithm. The complexity is taken from [136] and is given in the case of a tridiagonal Hamiltonian $\hat{H}$, and in the general case.

But with the advantage that, since $\hat{H}$ commutes with itself, it is unitary:

$$U_{\mathrm{CN}}U_{\mathrm{CN}}^{\dagger} = \left[\mathbb{1} + \mathrm{i}\hat{H}\frac{\Delta t}{2}\right]^{-1}\left[\mathbb{1} - \mathrm{i}\hat{H}\frac{\Delta t}{2}\right]\left[\mathbb{1} - \mathrm{i}\hat{H}\frac{\Delta t}{2}\right]^{\dagger}\left(\left[\mathbb{1} + \mathrm{i}\hat{H}\frac{\Delta t}{2}\right]^{-1}\right)^{\dagger} \tag{II.28}$$

$$= \left[\mathbb{1} + \mathrm{i}\hat{H}\frac{\Delta t}{2}\right]^{-1}\left[\mathbb{1} - \mathrm{i}\hat{H}\frac{\Delta t}{2}\right]\left[\mathbb{1} + \mathrm{i}\hat{H}\frac{\Delta t}{2}\right]\left[\mathbb{1} - \mathrm{i}\hat{H}\frac{\Delta t}{2}\right]^{-1} \tag{II.29}$$

$$= \mathbb{1}. \tag{II.30}$$

To sum up, if we know the wave function at time t, the CN propagator (II.23) allows to compute the wave function at a later time $t + \Delta t$ by:

$$\left[\mathbb{1} + \mathrm{i}\hat{H}\left(t + \frac{\Delta t}{2}\right)\frac{\Delta t}{2}\right]|\psi(t + \Delta t)\rangle = \left[\mathbb{1} - \mathrm{i}\hat{H}\left(t + \frac{\Delta t}{2}\right)\frac{\Delta t}{2}\right]|\psi(t)\rangle\,, \tag{II.31}$$

which is just a rewriting of (II.23). This kind of method is called a *propagation* method, because the wave function is computed, i.e. *propagated*, from one time step to the next. The CN propagation step (II.31) is done numerically by splitting it into two consecutive stages, listed in Table II.1. The complexity of each stage represents the maximal number of operations needed to perform this step with a given algorithm. It is given in Table II.1 for standard algorithms such as the ones implemented in [136, 137] in the case of a general and of a tridiagonal Hamiltonian. It is clear that we greatly benefit from this tridiagonal form in terms of computational cost, and that the CN algorithm is particularly suited to this kind of matrices.

As we saw, each algorithm time step introduces an error proportional to Δt^3, so that after a time $t = N\Delta t$, the error is actually proportional to Δt^2. But the proportionality factor, and thus the absolute value of the error, will actually depend on the specific Hamiltonian, i.e. on the system, and on the chosen gauge when modelling the interaction with the EM field. Therefore the parameters that we used to get accurate results are specific to each simulation. For example, as we have seen in Section I.1.4, in general the velocity gauge induces a smaller error than the length gauge, so that we can use a larger

value of Δt in the former than in the latter. Each calculation has thus to be meticulously and individually checked for convergence with respect to all simulation parameters.

In this thesis we always choose the initial state of the propagation to be the ground state of our system. As we said in Chapter I, we will concentrate on the gas phase. In most experiments, the emitting system consists of supersonic gas jets [138]. The atoms and molecules in those jets are actually very cold, and a large majority of them are in the electronic and vibrational ground state. Besides, the ground state and more generally all eigenstates, of the Hamiltonian are very useful for the subsequent analysis of the numerical results. We will see in the next section how to compute these eigenstates.

c) Absorbing boundary conditions

In some cases, e.g. for large values of the ponderomotive potential U_p, the laser electric field may ionize the system, and create some highly energetic free electrons. Depending on the time duration of the laser pulse, those electrons may actually travel very far from the nuclei during the propagation. In those cases, a very large simulation box is a priori needed, otherwise those electrons would hit the boundaries of the box, artificially reflect on these boundaries and pollute the propagation. However, it may happen that we do not really need those electrons to describe the physical process of interest. For example if we are only interested in the time-dependent populations in the bound states of the system, then the part of the wave function that leaves the nuclei, and never return, is not particularly relevant. Indeed we saw in Figure II.1 that the bound states of the system are localized close to the nuclei. So all the information that is required to compute these populations is contained in a very small part of the wave function. Alternatively if we are interested in HHG, then we saw in section I.3.2 that some of the ionized electron trajectories leave the nuclei and never return, hence never participate in HHG. We also saw that the trajectories that return to the nuclei never go beyond the limit $2x_\alpha$, so that the part of the wave function that lies after this limit is unnecessary for the simulation of HHG.

We would like to reduce the size of the simulation box to the bare minimum, and thus decrease our computational cost, without inducing spurious unphysical reflexions at the boundaries of the box. To do this we use absorbing boundary conditions. There are several ways to implement such an absorber [139–142]. Among them we choose an absorbing mask [143], which consists in multiplying the wave function at each time step by the mask function:

$$f_\mathrm{abs} = \begin{cases} = 1 & \text{if} \quad |x| \leq L - h_\mathrm{abs} \\ = \cos^\zeta\left(\dfrac{|x| - L + h_\mathrm{abs}}{2h_\mathrm{abs}}\pi\right) & \text{if} \quad L - h_\mathrm{abs} \leq |x| \leq L \end{cases}, \tag{II.32}$$

where the width h_abs and the exponent ζ of the absorber are optimized for each propagation. Note that the optimization of the exponent ζ is strongly related to the value of the time step Δt. Indeed a simulation with a Δt twice smaller requires a ζ twice smaller to reach the same absorbing conditions.

II.1.3 Computations of eigenstates

a) Energies

The energies and eigenstates of our field-free Hamiltonian $\hat{H}_0$ are important quantities. We use them for example to determine the initial state of our propagation, to analyze our wave function by computing the population in the bound states, to understand qualitatively our results, or to make analytical derivations.

Since the Hamiltonian of our system cannot be diagonalized analytically, we have to do it numerically. Our field-free Hamiltonian is real, so we compute its eigenvalues with the QL algorithm implemented by [137] (see [144] for the mathematical description of the algorithm, and proof of its convergence). It relies on the QL decomposition that can be done for any real matrix A:

$$A = QL, \tag{II.33}$$

where Q is an orthogonal matrix, and L is a lower triangular matrix. For our $N_x \times N_x$ symmetric tridiagonal Hamiltonian, this decomposition has a complexity of $O(N_x)$, and needs to be done typically a few times for each of its N_x eigenvalues, resulting in a global complexity of $O(N_x^2)$. This is reasonable, as long as $N_x \lesssim 10^4$, since it only has to be done once before the propagation itself.

b) Bound eigenstates

The QL algorithm can also be used to compute the eigenvectors of a matrix, but with a complexity of $O(N_x^3)$, which is in general prohibitive. Besides we do not necessarily need all the eigenvectors, the ground and a few excited states are sufficent for most of the cases treated in this thesis. We thus use a much more efficient algorithm called inverse iteration [144, 137]. We make an initial guess for an eigenvalue ε_0, for example using the result of the above mentioned QL algorithm, and for the associated eigenvector $\mathbf{y}_0$, then we inverse the system (II.34a) to get $\mathbf{w}_0$. The vector $\mathbf{w}_0$ is normalized (II.34b) to get $\mathbf{y}_1$, and we iterate these two steps (II.34):

$$(A - \varepsilon_0)\mathbf{w}_k = \mathbf{y}_k \tag{II.34a}$$

$$\mathbf{y}_{k+1} = \frac{\mathbf{w}_k}{\sqrt{\mathbf{w}_k \cdot \mathbf{w}_k}} \tag{II.34b}$$

If the initial guess ε_0 is sufficiently close to an eigenvalue λ of A, then $\mathbf{y}_k$ will converge to the corresponding eigenvector in a few steps. As ε_0 differed from the exact eigenvalue λ, we can use $\mathbf{y}_k$, which is an improved approximation of the exact eigenvector, to compute a new and better guess for the eigenvalue:

$$\varepsilon_{i+1} = \varepsilon_i + \frac{1}{\mathbf{w}_{k_i} \cdot \mathbf{y}_{k_i}}. \tag{II.35}$$

Once the vector $\mathbf{y}_k$ has converged to an eigenvector $\mathbf{y}$ of the Hamiltonian, it is then renormalized with the L^2 norm to get the eigenstates $|\varphi\rangle$:

$$|\varphi\rangle = \frac{\mathbf{y}}{\sqrt{\sum_j |y^{(j)}|^2 \Delta x}}, \tag{II.36}$$

where the $y^{(j)}$ are the components of the vector $\mathbf{y}$. We thus get a normalized eigenstate $\langle\varphi|\varphi\rangle = 1$.

As we saw in Table II.1, the inversion of a linear system such as (II.34) has a complexity of $O(N_x)$. Since it only needs to be executed a few times, the global complexity involved in computing an eigenstate, and possibly a better evaluation of its associated eigenvalue, is only of $O(N_x)$. In practice we will compute all the eigenvalues with the QL algorithm on a relatively small simulation box, with typically $N_x \sim 10^3$, and use inverse iteration on a larger box to compute the eigenstates, plus the eigenvalues that we need with a high precision.

c) Continuum eigenstates

As we said in section II.1.1 the "continuum" states energies strongly depend on the grid parameters L and Δx. Therefore we cannot compute first their energy in a small grid and then the state in a larger grid as explained for the bound eigenstates. We can only start inverse iteration with a random energy, close to the one we are looking for, and the algorithm will converge to the state that is the closest in energy.

However, if we want to compute the continuum state at a precise energy E, we use another method to solve the TISE: the shooting method. The principle is to see the TISE as a linear differential equation, that can be solved with e.g. the Fourth order Runge-Kutta (RK4) algorithm [145]. We start at $x = 0$ with arbitrary initial conditions that satisfy the desired symmetry properties:

even	odd
$\begin{cases}\varphi(0) = 1 \\ \varphi'(0) = 0\end{cases}$	$\begin{cases}\varphi(0) = 0 \\ \varphi'(0) = 1\end{cases}$

(II.37)

Then we propagate the TISE with the RK4 method until the required size is reached. This results in an unnormalized eigenstate of energy E. Note that in this case we do not impose boundary conditions on the wave function at the border of the box, so that the energy E can be any positive value (as long as it remains below the Fourier limit of $2/\Delta x^2$).

The state that we obtain cannot be normalized with the L^2 norm as we did with the bound states because the exact continuum states are not square integrable. Instead we normalize them in energy:

$$\langle\varphi_E|\varphi_{E'}\rangle = \delta(E - E') \tag{II.38}$$

with the Strömgren method detailed in appendix C. This method applies to radial functions in 3D, or to odd/even states in 1D. The principle is to fit the eigenstate with the general asymptotic form:

$$\varphi_E(x) \underset{x\to\pm\infty}{\longrightarrow} \frac{C}{\sqrt{\pi k(x)}} \sin\left[\theta(x)\right], \tag{II.39}$$

where

$$k(x) = \frac{\mathrm{d}\theta}{\mathrm{d}x}(x) \underset{x\to\pm\infty}{\longrightarrow} \sqrt{2E}, \tag{II.40}$$

and where the factor C is the normalization constant that we want to compute.

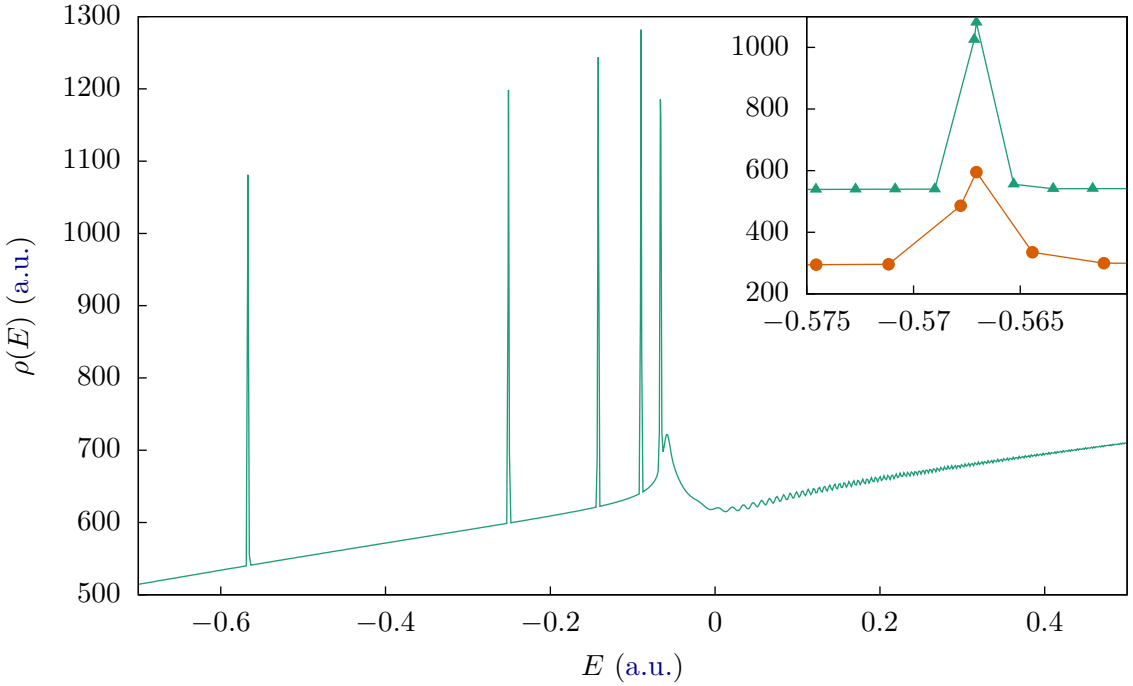

Figure II.3 *Continuum density of states of the same atomic system as in panel (a) of Figure II.1 in a static electric field* $F = 10^{-3}$ a.u., *computed with the QL algorithm with* $\Delta x = 0.1$ a.u.. *The inset is a zoom on the peak corresponding to the* pseudo *ground state. Solid green line and green triangles in the inset correspond to* $L = 2 \times 10^3$ a.u., *whereas orange dots and line to* $L = 10^3$ a.u..

II.1.4 Energies in a static electric field

When an atom or a molecule is placed in a static electric field, as small as this electric field may be, its bound states become coupled with the continuum of ionized states. This has several important consequences. Firstly, these states are embedded in the continuum, they are not isolated discrete eigenstates, but rather resonances in a continuous set of eigenstates. This can be seen from the density of states in presence of the field, as shown in Figure II.3. We observe peaks at energies corresponding to these resonances. Secondly, these bound states are not strictly bound anymore, but *pseudo-bound* states, i.e. they acquire a certain finite width related to their lifetime, or ionization rate. In the framework of non-Hermitian quantum mechanics (see e.g. [146]) this width is associated with the imaginary part of the energy, as will be explained in section II.3.1. Lastly, the value of the energy of these *pseudo-bound* states is shifted with respect to its field-free value:

$$\widetilde{E}_i(\mathbf{F}_\mathrm{L}) = E_i + E_\mathrm{S}(\mathbf{F}_\mathrm{L}), \tag{II.41}$$

where this energy shift E_S is known as the Stark shift.

The computation of the resonances energies is more delicate than in the field-free case. Indeed, if we look closer at one particular peak, as illustrated in the inset of Figure II.3 for the ground state, we see that the width of the peaks is actually limited by the energy separation between two consecutive states, i.e. by the number of states per unit energy.

And we saw in section II.1.1 that this density of states is actually related to the length L of the simulation box. To compute the energy of the resonance with a high precision, we need to have a small energy separation with respect to the resonance natural width. Depending on the value of the electric field, this may require a very large simulation box, and thus be prohibitive. For example, with a box of size $L = 2 \times 10^3$ a.u. (green triangles in the inset of Figure II.3), we see that we only get a precision of $\sim 1\%$ on the energy of the resonance.

To overcome this limitation we use the "*Rbox* method", developped in [147]. It relies on the fact that the energy of a particular "continuum" state depends on the size of the box, unless it is resonant with a pseudo bound state. To illustrate this, we diagonalize the Hamiltonian for various box sizes L, and then plot the energy of the "continuum" states as a function of L on Figure II.4 for different field values. We indeed remark that the energy of a particular state depends almost linearly on the box size L. However when it reaches the energy $\widetilde{E}_0$ of the resonance, the energy is then almost constant, until it *crosses* another "continuum" state. The two states do not actually cross, but have an avoided crossing, as becomes more visible for increasing values of the electric field. We deduce the energy of the resonance from the energy of the state at the inflexion point, i.e. where its second derivative changes sign.

We see on Figure II.5 that each "continuum" state has an avoided crossing with every pseudo bound state, so that we can deduce all resonance energies from one *Rbox* calculation. We mention that the width of the resonance can also be extracted from the *Rbox* method [148, 149], however we did not implement this feature, and prefered to rely on the numerical solution of the TDSE (see section II.3.1).

II.2 Two dimensional systems

II.2.1 Different kinds of 2D systems

Two dimensional systems are toy models in the same spirit as 1D systems, with relatively low computational cost, albeit much more flexible and potentially accounting for a wider variety of physical processes. They are thus highly valuable for the development of interpretative analytical models. We use two dimensional grids to describe such systems, where the two dimensions do not necessarily correspond to space coordinates of the electron, but may represent different variables. In this thesis we use three different kinds of 2D grids:

1 electron - 2 space dimensions :

In this case the two dimensions represent the position of the electron (x, y). The system is composed of one electron trapped in a two dimensional Soft-Coulomb potential well, which is a simple generalization of the 1D case. For atoms it reads

$$V_{2\mathrm{D}}(\mathbf{r}) = -\frac{Z}{\sqrt{a^2 + r^2}}, \tag{II.42}$$

and for diatomic molecules:

$$V_{2\mathrm{D}}(\mathbf{r}) = -\frac{Z/2}{\sqrt{a_1^2 + (\mathbf{r} + \mathbf{R}/2)^2}} - \frac{Z/2}{\sqrt{a_2^2 + (\mathbf{r} - \mathbf{R}/2)^2}}. \tag{II.43}$$

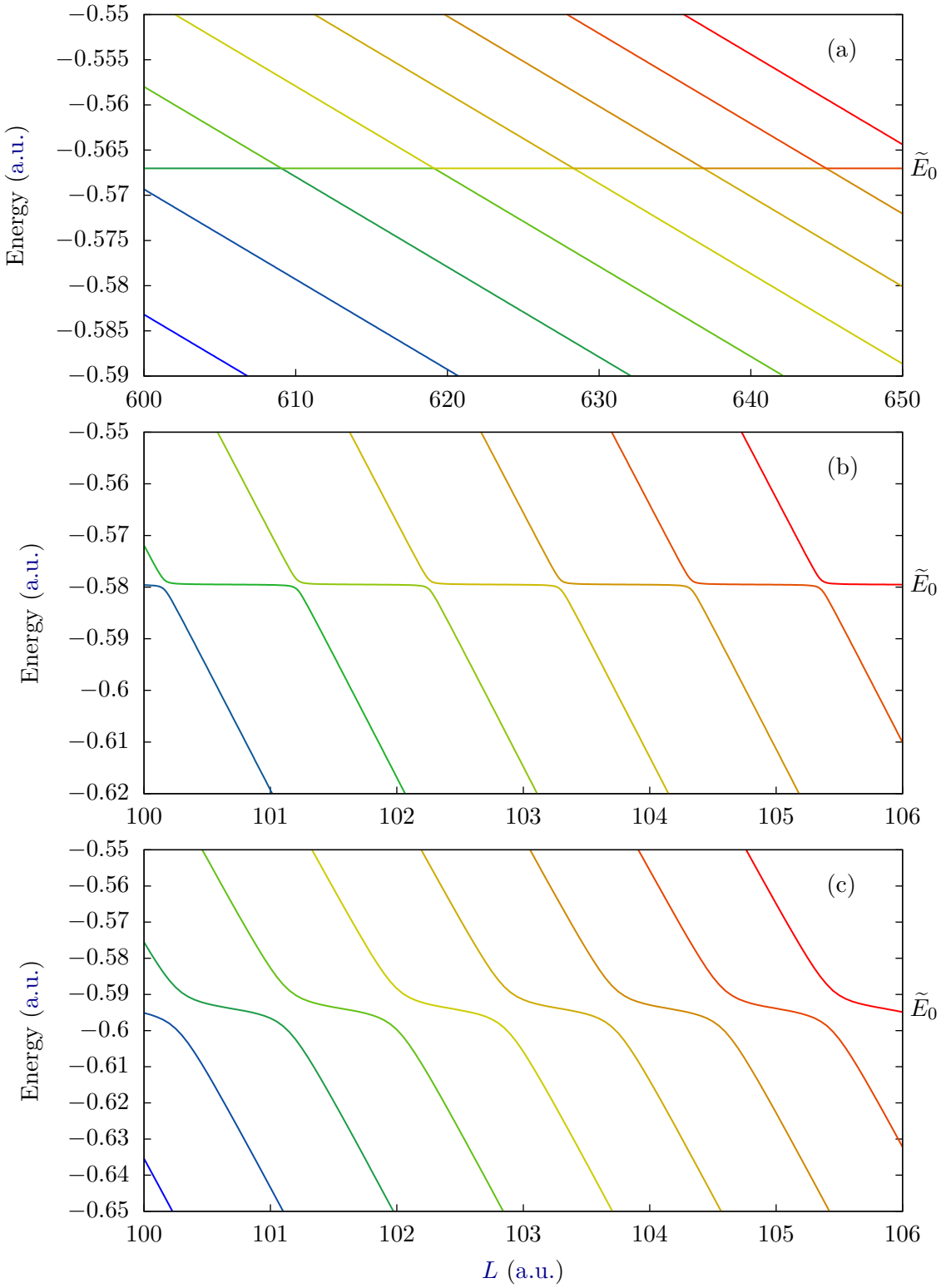

Figure II.4 *Continuum energies of the same atomic system as in panel (a) of Figure II.1 in a static electric field with (a)* $F_{\mathrm{L}} = 10^{-3}$ a.u., *(b)* $F_{\mathrm{L}} = 5 \times 10^{-2}$ a.u., *(c)* $F_{\mathrm{L}} = 7 \times 10^{-2}$ a.u.. *Energies computed by the QL algorithm with* $\Delta x = 0.1$ a.u., *and for several values of* L.

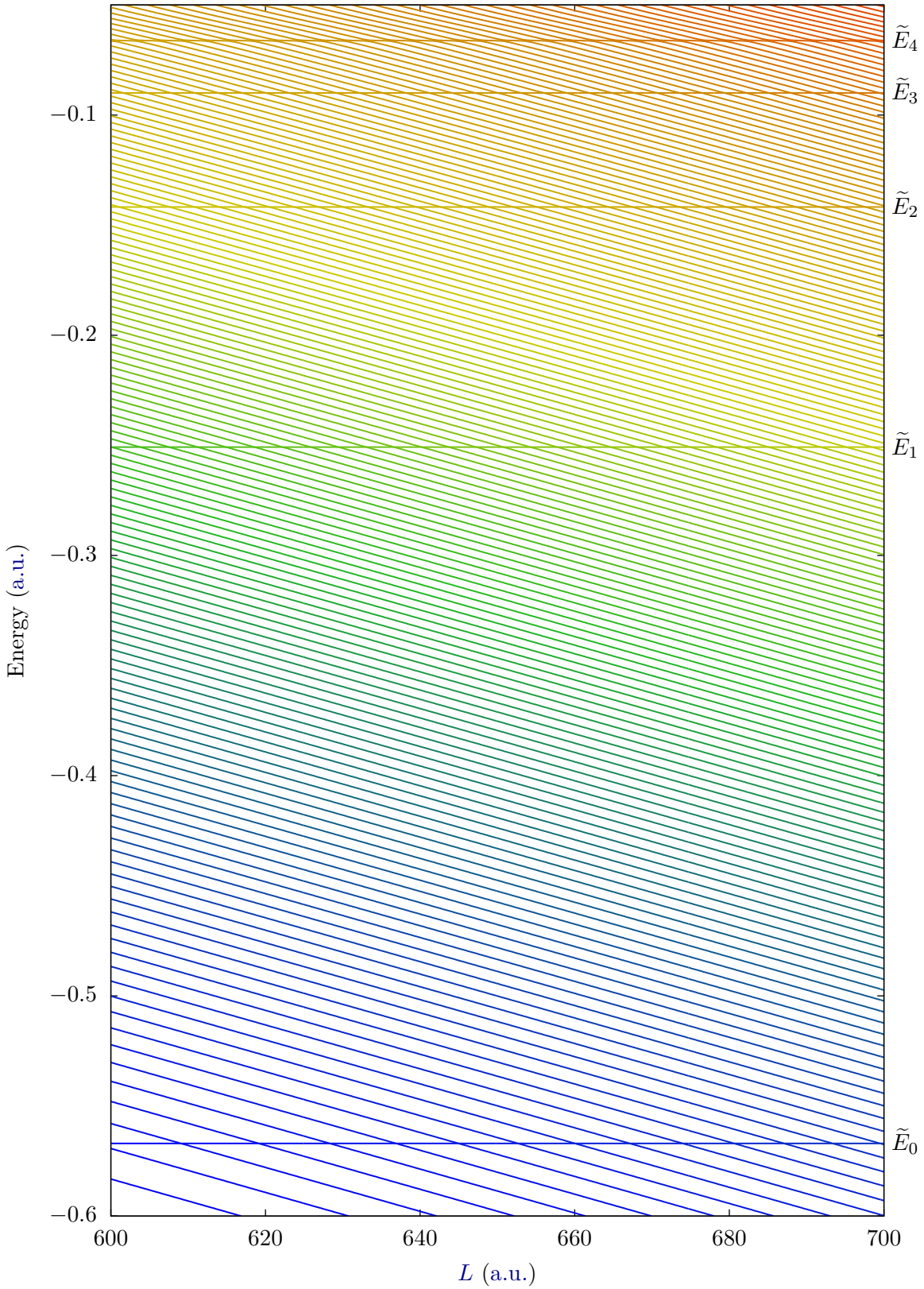

Figure II.5 *Same as in Figure II.4 (a) but on a larger range of energy.*

The field-free Hamiltonian is very similar to the 1D case:

$$\hat{H}_{\mathrm{2D}} = -\frac{1}{2}\frac{\partial^2}{\partial x^2} - \frac{1}{2}\frac{\partial^2}{\partial y^2} + V_{\mathrm{2D}}(\mathbf{r}). \tag{II.44}$$

This system allows e.g. to study diatomic molecules that can have different orientations with respect to the laser polarization.

2 electrons - 1 space dimension each :

In this case, the two dimensions are the positions of two electrons (x_1, x_2), that are trapped in a one dimensional Soft-Coulomb potential well, which is defined in (II.1) and (II.2). An additional term in the Hamiltonian accounts for the inter-electronic repulsion:

$$V_{\mathrm{ee}}(x_1, x_2) = \frac{1}{\sqrt{b^2 + (x_1 - x_2)^2}}. \tag{II.45}$$

The field-free Hamiltonian thus reads

$$\hat{H}_{\mathrm{2E}} = -\frac{1}{2}\frac{\partial^2}{\partial x_1^2} - \frac{1}{2}\frac{\partial^2}{\partial x_2^2} + V_0(x_1) + V_0(x_2) + V_{\mathrm{ee}}(x_1, x_2). \tag{II.46}$$

This systems is a very simple model to study electron correlations.

1 nucleus and 1 electron - 1 space dimension each :

This system is composed of two nuclei and a one dimensional electron. The two dimensions are the position of the electron and the internuclear distance (x, R). Compared to the 1D case, the Hamiltonian have two additional terms : one for the kinetic energy of the nuclei and another for the internuclear repulsion[2] V_{NN}. Note that the internuclear distance R that appeared in the electron-nucleus interaction potential is now a variable, instead of a parameter. The Hamiltonian thus reads

$$\hat{H}_{\mathrm{XR}} = -\frac{1}{2\mu}\frac{\partial^2}{\partial R^2} + V_{\mathrm{NN}}(R) - \frac{1}{2}\frac{\partial^2}{\partial x^2} + V_0(R, x), \tag{II.47}$$

where

$$V_0(R, x) = -\frac{Z}{\sqrt{a_1(R)^2 + (x + R/2)^2}} - \frac{Z}{\sqrt{a_2(R)^2 + (x - R/2)^2}}. \tag{II.48}$$

The parameters a_1 and a_2 are adjusted so that the electronic potential energy surface of the ground state reproduces the one of the system we want to model, e.g. the H_2 molecule.

This is a simple model that allows to go beyond the Born-Oppenheimer (BO) approximation, and investigate vibronic dynamics in molecules.

[2] In general, the latter is adjusted on the ionic potential energy surface of interest.

II.2.2 Split-operator method

For the three 2D systems just described the Hamiltonian is sparse, i.e. it has a large number of matrix elements that are zero, but is not tridiagonal. The CN algorithm for propagation that we described in section II.1.2 b) is not adapted to this case: it involves steps with a complexity of $O(N^2)$, while we had a complexity of $O(N)$ in the tridiagonal case. Note that N is here the total size of the 2D grid, and is in general much larger than the size N_x of the 1D grid. We can do better than this $O(N^2)$ complexity by using another propagation scheme: the split operator algorithm. This scheme relies on a decomposition of the Hamiltonian into two terms: a kinetic energy term $\hat{T}$ diagonal in the **p** representation, and a potential energy term $\hat{V}$ diagonal in the **r** representation. It is therefore tempting to apply each of these terms separately, interspersed with simple changes of representation. However $\hat{T}$ and $\hat{V}$ do not commute:

$$\left[\hat{V}, \hat{T}\right] \neq 0, \tag{II.49}$$

so, if we simply decompose the evolution operator:

$$\mathrm{e}^{-\mathrm{i}\hat{H}\Delta t} = \mathrm{e}^{-\mathrm{i}(\hat{T}+\hat{V})\Delta t} \simeq \mathrm{e}^{-\mathrm{i}\hat{T}\Delta t}\,\mathrm{e}^{-\mathrm{i}\hat{V}\Delta t}, \tag{II.50}$$

we get an error proportional to Δt^2 (see appendix D). Instead the split operator method uses the decomposition

$$\mathrm{e}^{-\mathrm{i}(\hat{T}+\hat{V})\Delta t} = \mathrm{e}^{-\mathrm{i}\hat{V}\Delta t/2}\,\mathrm{e}^{-\mathrm{i}\hat{T}\Delta t}\,\mathrm{e}^{-\mathrm{i}\hat{V}\Delta t/2} + O\left(\Delta t^3\right), \tag{II.51}$$

with an error proportional to Δt^3, as shown in appendix D.

To sum up, the split-operator propagation scheme can be written as

$$\boxed{|\psi(t+\Delta t)\rangle = \mathrm{e}^{-\mathrm{i}\hat{V}\Delta t/2}\,\mathrm{e}^{-\mathrm{i}\hat{T}\Delta t}\,\mathrm{e}^{-\mathrm{i}\hat{V}\Delta t/2}\,|\psi(t)\rangle\,,} \tag{II.52}$$

where the potential $\hat{V}$ is diagonal in the **r** representation:

$$\mathrm{e}^{-\mathrm{i}\hat{V}\Delta t/2}\,\psi(x_1,x_2,t) = \mathrm{e}^{-\mathrm{i}V(x_1,x_2)\Delta t/2}\,\psi(x_1,x_2,t), \tag{II.53}$$

and the kinetic energy $\hat{T}$ is diagonal in the **p** representation:

$$\mathrm{e}^{-\mathrm{i}\hat{T}\Delta t}\,\widetilde{\psi}(p_1,p_2,t) = \mathrm{e}^{-\mathrm{i}\frac{p_1^2}{2\mu_1}-\mathrm{i}\frac{p_2^2}{2\mu_2}}\,\widetilde{\psi}(p_1,p_2,t), \tag{II.54}$$

where x_1 and x_2 are generic names for the two dimensions of the grid, and p_1 and p_2 are the associated momenta. The **r** and **p** representations are related through a Fourier transform, which can be computed efficiently with the FFT algorithm, implemented in the Fastest Fourier Transform in the West (FFTW) library [150]. The complexity of the FFT depends on the size of the matrix, and more precisely on its prime decomposition. In general it is of the form $O(N \log N)$, which is much better that $O(N^2)$. One step of the split-operator algorithm is summarized in Table II.2. We see that its overall complexity is limited by the Fourier transform steps.

Step	Operation	Complexity
$t_i = i\Delta t$		
$\chi(\mathbf{x}, t_i) = \mathrm{e}^{-\mathrm{i}\hat{V}\Delta t/2}\psi(\mathbf{x}, t_i)$	Diagonal matrix × vector multiplication $Y = DX$	$O(N)$
$\widetilde{\chi}(\mathbf{p}, t_i) = \int \chi(x, t_i)\, \mathrm{e}^{-\mathrm{i}\mathbf{x}\cdot\mathbf{p}}$	Fourier transform	$O(N \log N)$
$\widetilde{\chi}(\mathbf{p}, t_i) = \mathrm{e}^{-\mathrm{i}\hat{T}\Delta t}\widetilde{\chi}(\mathbf{p}, t_i)$	Diagonal matrix × vector multiplication $Y = DX$	$O(N)$
$\chi(\mathbf{x}, t_i) = \frac{1}{2\pi}\int \widetilde{\chi}(\mathbf{p}, t_i)\, \mathrm{e}^{\mathrm{i}\mathbf{x}\cdot\mathbf{p}}$	Inverse Fourier transform	$O(N \log N)$
$\psi(\mathbf{x}, t_i + \Delta t) = \mathrm{e}^{-\mathrm{i}\hat{V}\Delta t/2}\chi(\mathbf{x}, t_i)$	Diagonal matrix × vector multiplication $Y = DX$	$O(N)$
Repeat for $t_{i+1} = (i+1)\Delta t$		

Table II.2 – Summary of the split-operator algorithm.

II.2.3 Imaginary time propagation

Since the field-free Hamiltonian is not tridiagonal in our 2D grid, the inverse iteration algorithm described in section II.1.3 to compute the eigenvectors and eigenvalues of $\hat{H}$ has a complexity of $O(N^2)$. This quickly becomes prohibitive when N increases. We thus choose another algorithm to compute the eigenstates of our system: imaginary time propagation. As its name suggests, it relies on the propagation of the TDSE albeit with a purely imaginary time $t \in \mathrm{i}\mathbb{R}$. In practice we will use the same propagation scheme as in the real time $t \in \mathbb{R}$ case: the split-operator algorithm that we described in the previous section.

To understand the advantages of imaginary time propagation, we assume that at time $t = 0$ the initial state $|\psi_0\rangle$ is chosen at random in the Hilbert space. The eigenvectors $|\varphi_i\rangle$ of the field-free Hamiltonian $\hat{H}_0$ form a basis of the Hilbert space, so that we can decompose $|\psi_0\rangle$ onto this basis:

$$|\psi_0\rangle = \sum_{j\geq 0} c_j\, |\varphi_j\rangle\,, \tag{II.55}$$

where we assume that the energies E_j are sorted in increasing order and non-degenerate $E_j < E_{j+1}$. After a time t, the solution of the TDSE is

$$|\psi(t)\rangle = \mathrm{e}^{-\mathrm{i}\hat{H}_0 t}\, |\psi_0\rangle \tag{II.56}$$

$$= \sum_{j\geq 0} c_j\, \mathrm{e}^{-\mathrm{i}\hat{H}_0 t}\, |\varphi_j\rangle \tag{II.57}$$

$$= \sum_{j\geq 0} c_j\, \mathrm{e}^{-\mathrm{i}E_j t}\, |\varphi_j\rangle\,. \tag{II.58}$$

If t is purely imaginary, i.e. $t = -i\tau$ with $\tau \in \mathbb{R}^+$, this gives

$$|\psi(t)\rangle = \sum_{j\geq 0} c_j\, \mathrm{e}^{-E_j \tau}\, |\varphi_j\rangle\,. \tag{II.59}$$

If $c_0 \neq 0$, we can factorize:

$$|\psi(t)\rangle = c_0 \, \mathrm{e}^{-E_0\tau} \left(|\varphi_0\rangle + \sum_{j\geq 1} \frac{c_j}{c_0} \, \mathrm{e}^{-(E_j - E_0)\tau} \, |\varphi_j\rangle \right). \tag{II.60}$$

Since E_0 is the minimum of all E_j, $E_j - E_0 > 0$ and all terms are exponentially dumped with respect to the first one. If we renormalize the wave function at each time step, or every few time steps, it converges exponentially to the ground state of the system. More generally, if all the i first coefficients are zero $c_0 = \ldots = c_{i-1} = 0$, and if we note c_i the first non vanishing coefficient, we get

$$|\psi(t)\rangle = c_i \, \mathrm{e}^{-E_i\tau} \left(|\varphi_i\rangle + \sum_{j\geq i+1} \frac{c_j}{c_i} \, \mathrm{e}^{-(E_j - E_i)\tau} \, |\varphi_j\rangle \right). \tag{II.61}$$

In this case, the renormalized wave function converges exponentially to state $|\varphi_i\rangle$.

In practice we start by a random state with the appropriate symmetry and propagate to get the ground state of the system. Once we have the ground state, we start again but we orthonormalize at each time step, or every few time steps, the wave function with respect to $|\varphi_0\rangle$. We thus get the first excited state of the system. We then repeat this process, by orthonormalizing each time with respect to all previously computed eigenstates, until we get as many states as desired.

II.3 Wave function analysis

Once we know the time-dependent wave function $|\psi(t)\rangle$, in principle we know everything about the system's dynamics. However the wave function in itself can be quite hard to interpret. If we take the example of HHG, the semi-classical model developed in section I.3.2 gave us more physical insight that the time-dependent wave function shown in Figure I.8. Moreover since the wave function is not directly measurable, we cannot use it as such to analyze the results of an experiment. We thus resort to various analysis tools to extract physical information from the wave function.

In general, these analysis tools rely on two basic quantities: the scalar product of two states, which, in our case, is computed by

$$\langle\varphi|\psi\rangle = \sum_{\mathbf{x}_i \in \text{grid}} \varphi(\mathbf{x}_i)^* \psi(\mathbf{x}_i) \prod_{j=1}^{d} \Delta x_j, \tag{II.62}$$

where d is the number of dimensions and Δx_j is the grid space step in dimension j. And the expectation value of an observable $\hat{A}$, which is actually a particular case of (II.62):

$$\langle A\rangle = \langle\psi|A|\psi\rangle = \sum_{\mathbf{x}_i \in \text{grid}} \psi(\mathbf{x}_i)^* \hat{A} \, \psi(\mathbf{x}_i) \prod_{j=1}^{d} \Delta x_j. \tag{II.63}$$

With these two basic operations we construct the tools we will use in this thesis.

II.3.1 Ionization rate

a) Ionization probability

As we saw in section I.2.2, when an atom or a molecule is submitted to an electric field, it may be ionized. Consequently, the wave function can be separated into two orthogonal parts, a bound part and an ionized part:

$$|\psi(t)\rangle = |\psi_{\text{bnd}}(t)\rangle + |\psi_{\text{ion}}(t)\rangle\,, \tag{II.64}$$

where the bound part can be decomposed onto the field-free bound states of the system:

$$|\psi_{\text{bnd}}(t)\rangle = \sum_{i\in\text{bound}} |\varphi_i\rangle\,\langle\varphi_i|\psi(t)\rangle\,, \tag{II.65}$$

and the ionized part can be similarly decomposed onto the field-free continuum states.

The ionization probability at time t can be deduced from the norm of the ionized part, which itself is deduced from the norm of the bound part:

$$\begin{aligned} P_{\text{ion}}(t) &= \langle\psi_{\text{ion}}(t)|\psi_{\text{ion}}(t)\rangle && \text{(II.66)}\\ &= 1 - \langle\psi_{\text{bnd}}(t)|\psi_{\text{bnd}}(t)\rangle && \text{(II.67)}\\ &= 1 - \sum_{i\in\text{bound}} |\langle\varphi_i|\psi(t)\rangle|^2. && \text{(II.68)} \end{aligned}$$

With equation (II.68) we can deduce the ionization probability from the populations in all bound states. These populations are computed on the grid with the general formula (II.62). In this thesis we are generally far from any resonance, so that the populations in the excited states $|\varphi_i\rangle$ quickly become negligible for growing values of i. We thus only need to compute the populations in the first few bound states to get an accurate evaluation of the ionization probability.

b) Ionization rate in a static electric field

In the particular case of a static electric field, the population in the bound states exponentially decreases with time:

$$P_{\text{bnd}}(t) = \sum_{i\in\text{bound}} |\langle\varphi_i|\psi(t)\rangle|^2 = \mathrm{e}^{-\Gamma t}\,. \tag{II.69}$$

The decay rate Γ is called the ionization rate. In the framework of non-Hermitian quantum mechanics (see e.g. [146]) where the energies can be complex, this rate is directly related to the imaginary part of the energy $\varepsilon_0(\mathbf{F}_{\text{L}})$ of the perturbed ground state:

$$\varepsilon_0(\mathbf{F}_{\text{L}}) = \widetilde{E}_0(\mathbf{F}_{\text{L}}) - \mathrm{i}\frac{\Gamma}{2}. \tag{II.70}$$

Indeed, the perturbed ground state $|\widetilde{\varphi}_0\rangle$ evolves under the TDSE as:

$$\begin{aligned} |\psi(t)\rangle &= \mathrm{e}^{-\mathrm{i}\hat{H}t}\,|\widetilde{\varphi}_0\rangle && \text{(II.71)}\\ &= \mathrm{e}^{-\mathrm{i}\widetilde{E}_0 t}\,\mathrm{e}^{-\Gamma t/2}\,|\widetilde{\varphi}_0\rangle\,. && \text{(II.72)} \end{aligned}$$

Since the Hamiltonian is not Hermitian, the norm of this wave function is not conserved. Because only $|\widetilde{\varphi}_0\rangle$ is populated, the norm is equal to the population in the perturbed ground state, and reads:

$$\langle\psi(t)|\psi(t)\rangle = |\langle\widetilde{\varphi}_0|\psi(t)\rangle|^2 = \mathrm{e}^{-\Gamma t}, \tag{II.73}$$

where we recognize the exponential decay of (II.69). Since $|\widetilde{\varphi}_0\rangle$ can be decomposed onto the basis of the field-free bound states of $\hat{H}_0$, the population in this state is equal to the population P_{bnd} in all bound states. Besides, using first order time-independent perturbation theory [135], we can show that the states that contribute most in this decomposition are those that are the closest to the ground state in energy. This justifies the restriction to the first few bound states in the computation of P_{bnd}.

In practice, to compute the ionization rate Γ in a constant field F_0, we start the propagation in the field-free ground state $|\varphi_0\rangle$. The electric field is initially zero, and is then smoothly brought to its constant value by a sine square ramp:

$$F_{\mathrm{L}}(t) = \begin{cases} F_0 \sin^2(\Omega t) & \text{if} \quad 0 \leq t \leq \dfrac{\pi}{2\Omega} \\ F_0 & \text{if} \quad \dfrac{\pi}{2\Omega} \leq t \end{cases}. \tag{II.74}$$

Once the field is constant, we compute the population P_{bnd} in the first few (typically five) bound states, and we deduce the ionization rate Γ by

$$\Gamma = -\frac{1}{P_{\mathrm{bnd}}}\frac{\mathrm{d}P_{\mathrm{bnd}}}{\mathrm{d}t}. \tag{II.75}$$

II.3.2 HHG spectrum

a) Dipole operators

The HHG spectrum consists of the power spectrum of the radiation emitted by the system. Three different forms of the dipole are commonly used to compute this power spectrum: the dipole (II.76a), velocity (II.76b) and acceleration forms (II.76c), which give the spectra

$$S_{\mathrm{d}}(\omega) = \left| \int \langle\psi(t)|\hat{\mathbf{D}}_{\mathrm{d}}|\psi(t)\rangle\, \mathrm{e}^{-\mathrm{i}\omega t} \right|^2 \tag{II.76a}$$

$$S_{\mathrm{v}}(\omega) = \left| \int \langle\psi(t)|\hat{\mathbf{D}}_{\mathrm{v}}|\psi(t)\rangle\, \mathrm{e}^{-\mathrm{i}\omega t} \right|^2 \tag{II.76b}$$

$$S_{\mathrm{a}}(\omega) = \left| \int \langle\psi(t)|\hat{\mathbf{D}}_{\mathrm{a}}|\psi(t)\rangle\, \mathrm{e}^{-\mathrm{i}\omega t} \right|^2, \tag{II.76c}$$

where $\hat{\mathbf{D}}_{\mathrm{d}}$ is the dipole operator, and where the velocity $\hat{\mathbf{D}}_{\mathrm{v}}$ and acceleration $\hat{\mathbf{D}}_{\mathrm{a}}$ dipole operators are defined with the Ehrenfest theorem [151]:

$$\hat{\mathbf{D}}_{\mathrm{d}} = \hat{\mathbf{r}} \tag{II.77a}$$

$$\hat{\mathbf{D}}_{\mathrm{v}}^{(l)} = \mathrm{i}\left[\hat{H}_{\mathrm{l}}, \hat{\mathbf{r}}\right] = \hat{\mathbf{p}} \tag{II.77b}$$

$$\hat{\mathbf{D}}_{\mathrm{v}}^{(v)} = \mathrm{i}\left[\hat{H}_{\mathrm{v}}, \hat{\mathbf{r}}\right] = \hat{\mathbf{p}} + \mathbf{A}_{\mathrm{L}}(t) \tag{II.77c}$$

$$\hat{\mathbf{D}}_{\mathrm{a}} = -\left[\hat{H}, \left[\hat{H}, \hat{\mathbf{r}}\right]\right] + \frac{\mathrm{d}\mathbf{D}_{\mathrm{v}}}{\mathrm{d}t} = -\boldsymbol{\nabla} V_0 - \mathbf{F}_{\mathrm{L}}(t). \tag{II.77d}$$

Note that the velocity dipole operator does not commute with $\hat{\mathbf{r}}$, and its definition is thus different if we are in length (II.77b) or velocity (II.77c) gauge for the interaction with the laser field (be careful not to be confused between the length and velocity *gauge* for the EM field, and the length, velocity and acceleration *form of the dipole*). We remind that, as discussed in section I.1.3, the operators may depend on the gauge but obviously their average value, when computed exactly, does not.

The average value of the three dipole forms are related by

$$\left\langle \hat{\mathbf{D}}_\mathrm{a} \right\rangle = \frac{\mathrm{d}\left\langle \hat{\mathbf{D}}_\mathrm{v} \right\rangle}{\mathrm{d}t} \tag{II.78}$$

$$\left\langle \hat{\mathbf{D}}_\mathrm{v} \right\rangle = \frac{\mathrm{d}\left\langle \hat{\mathbf{D}}_\mathrm{d} \right\rangle}{\mathrm{d}t}. \tag{II.79}$$

Therefore, if we integrate (II.76a) by part:

$$\int \langle\psi(t)|\hat{\mathbf{D}}_\mathrm{d}|\psi(t)\rangle\, \mathrm{e}^{-\mathrm{i}\omega t} = \frac{1}{\mathrm{i}\omega}\int \langle\psi(t)|\hat{\mathbf{D}}_\mathrm{v}|\psi(t)\rangle\, \mathrm{e}^{-\mathrm{i}\omega t} \tag{II.80}$$

$$= -\frac{1}{\omega^2}\int \langle\psi(t)|\hat{\mathbf{D}}_\mathrm{a}|\psi(t)\rangle\, \mathrm{e}^{-\mathrm{i}\omega t}, \tag{II.81}$$

we can relate the different power spectra:

$$\omega^2 S_\mathrm{d} = S_\mathrm{v} = \frac{1}{\omega^2} S_\mathrm{a}. \tag{II.82}$$

We can therefore choose any dipole operator (II.77) to compute the spectrum, and then multiply by the appropriate factor of ω to get the desired form S_d, S_v or S_a. In practice we will compute the average value of the acceleration dipole $\mathbf{D}_a$ because, for numerical reasons, it is generally less noisy at high frequencies [152].

There are no clear consensus on which form of S_d, S_v or S_a should be used to get the HHG spectrum. An accelerated classical dipole emits a radiation whose total power, given by the Larmor formula [78], is proportional to the square of the dipole acceleration. One could conclude that the acceleration form is more adapted. Nevertheless it was recently shown by Baggesen and Madsen [131] that the electric field of the emitted radiation along the laser propagation direction is proportional to the velocity dipole. We will thus use the velocity form S_v. In practice we will compute S_a by taking the square modulus of the Fourier transform of the average value of the acceleration dipole (II.76c) and we will then divide by ω^2 (II.82) to get the velocity form of the power spectrum S_v.

b) Time-Frequency analysis

As we saw in sections I.3.2 and I.3.3, according to the 3-step model, each harmonic frequency of the spectrum is actually emitted at a different time: the return time of the electron. The different harmonics thus have different phases and are not perfectly synchronized. This results in a chirp of the emitted radiation, called atto-chirp [153–156]. However, we cannot get any information on this time of emission from the HHG power spectrum. It is theoretically encoded in the phase of the Fourier transform of the dipole, but this is difficult to translate in emission times. To extract these harmonics

emission times from TDSE simulations more easily, we can perform a Short Time Fourier Transform (STFT) of the dipole, i.e. we multiply the dipole by a moving window function w and then take the Fourier transform of the product:

$$\mathrm{STFT}_w[\mathbf{D}](\omega, t) = \int \mathrm{d}\tau\, \mathbf{D}(\tau) w(\tau - t)\, \mathrm{e}^{-\mathrm{i}\omega\tau}\,. \tag{II.83}$$

In this thesis, we use a Gaussian window function. This particular case of STFT is called Gabor transform.

We get a function of two variables, time and frequency, that physically represents the spectrum of the dipole as a function of time. The accuracy of this STFT cannot be as high as we want in both time and frequency. To have a high precision on the time of emission of a harmonic we need a very thin window function, but in that case the frequency is computed with very poor accuracy. This is of course related to the Fourier transform uncertainty relations.

We computed the Gabor transform of the dipole for our 1D Helium atom after a sine square laser pulse of two optical cycles with central wavelength $\lambda_\mathrm{L} = 800$ nm. In such a short laser pulse, there is only one generating half cycle. The HHG process occurs once, so the emitted radiation takes the form of a single isolated attosecond pulse. The Gabor transform of the dipole is plotted on the central panel of Figure II.6. The acceleration dipole $\langle D_\mathrm{a} \rangle$ and the laser electric field are shown in the top panel and the HHG spectrum S_v in the left panel. The Gabor transform allows to retrieve more information on the dynamics that what we just read in the HHG spectrum and in the dipole. In the spectrum we see that the emitted radiation contains all frequencies from the laser frequency ω_L to the cutoff frequency ω_c. The spectrum is flat and quasi continuous as expected from an isolated attosecond pulse, and as was explained with the help of the three step model in section I.3.2. However we do not have any information on the emission time of the harmonics. Nevertheless we see that the acceleration dipole smoothly follows the laser electric field variations during the first optical cycle, and then faster oscillations are superimposed to this fundamental during the second optical cycle. This indicates that the fundamental frequency $\omega = \omega_\mathrm{L}$ is re-emitted during the whole generating laser pulse, while the harmonics are only emitted during the second cycle. This behavior is also expected and explained by the three step model. However it is very hard to read from the dipole only the emission time of each individual frequency.

If we turn to the Gabor signal, we see a clear time-frequency mapping showing up, consistently with the 3-step model predictions. The low frequencies are emitted during the whole generating pulse, more precisely at each maximum of the field amplitude. We also clearly distinguish a bell-shaped feature that very much resembles the shape of the k inetic energy of the electron at the return time that we depicted in green in Figure I.12. This is also expected since we can directly relate harmonic emission time and electron return time on the one hand, and harmonic frequency and electron kinetic energy on the other hand. We can easily read the emission time of the harmonics on this 2D spectrogram as illustrated on the figure. We find as expected that each harmonic has two different emission times $t^{(L)}$ and $t^{(S)}$, corresponding respectively to the long and short trajectories that we described in section I.3.2. Of course we still have a (small) indetermination on these emission times, which is a consequence of the intrinsic finite precision of the transform mentioned above.

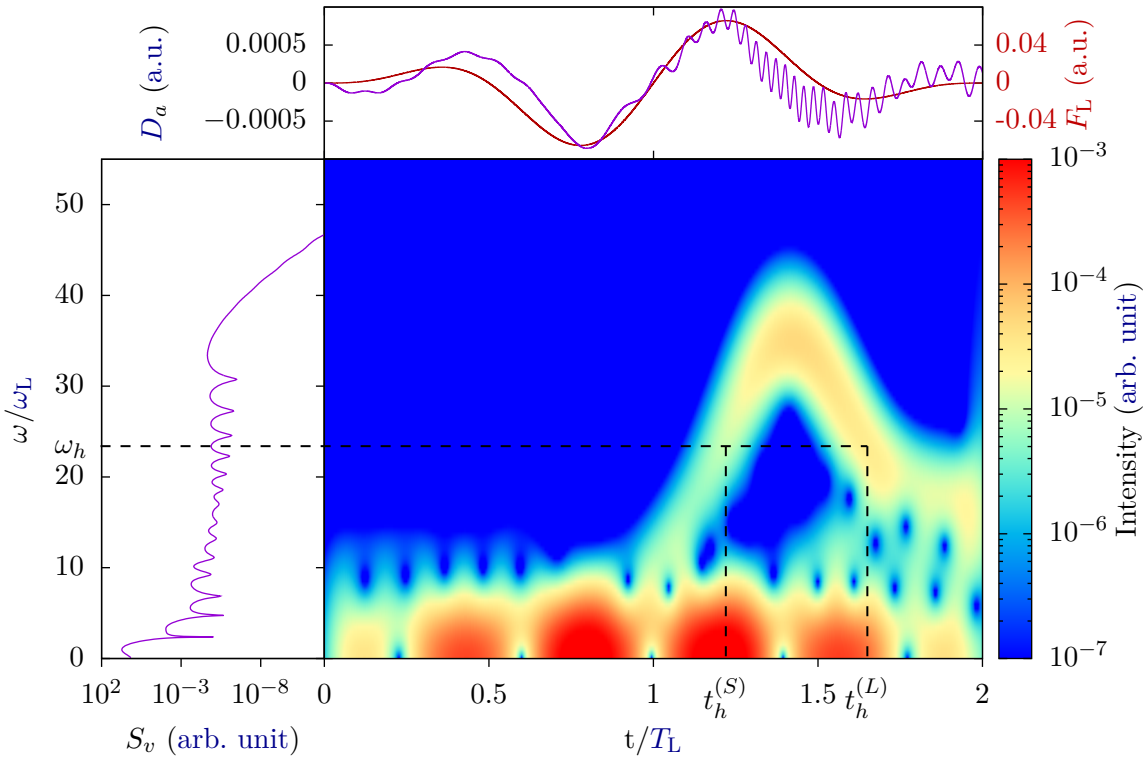

Figure II.6 *Gabor transform of the acceleration dipole D_a as a function of time and frequency respectively normalized by the laser period T_{L} and pulsation ω_{L}, for the 1D Helium atom after a sine square laser pulse of two optical cycles with central wavelength $\lambda_{\mathrm{L}} = 800$ nm and intensity $I = 2 \times 10^{14}$ W.cm^{-2}. In the top panel we plotted the acceleration dipole $\langle D_{\mathrm{a}} \rangle$ on the left axis and the laser electric field on the right axis. In the left panel we plotted the HHG spectrum S_v. An arbitrary energy of $\omega_H = 23\omega_{\mathrm{L}}$ is indicated, along with its corresponding emission times $t_h^{(S)}$ and $t_h^{(L)}$.*

We made the same analysis but with a longer laser pulse of 8 optical cycles. The results are shown on Figure II.7. In this case the time-dependent dipole resembles the schematic attosecond pulse train shown in Figure I.13. Since we have a pulse train, where each pulse alternatively changes sign, we only see odd multiples of ω_{L} in the spectrum. The Gabor spectrogram is very similar to the previous one, but the structure corresponding to the harmonic emission is repeated at each half cycle of the incident laser pulse. Note that we can easily distinguish the emission corresponding to each pulse of the train.

II.3.3 Trajectory separation

We saw in section I.3.2 that the HHG emission have two contributions, called the *long* and *short* trajectories. These two trajectory families have different behaviors and contain different informations on the system. We could learn a lot if we were able to disentangle these two contributions. This can be done experimentally since the propagation of the emitted radiation in the generating medium allows to spatially separate the emission of

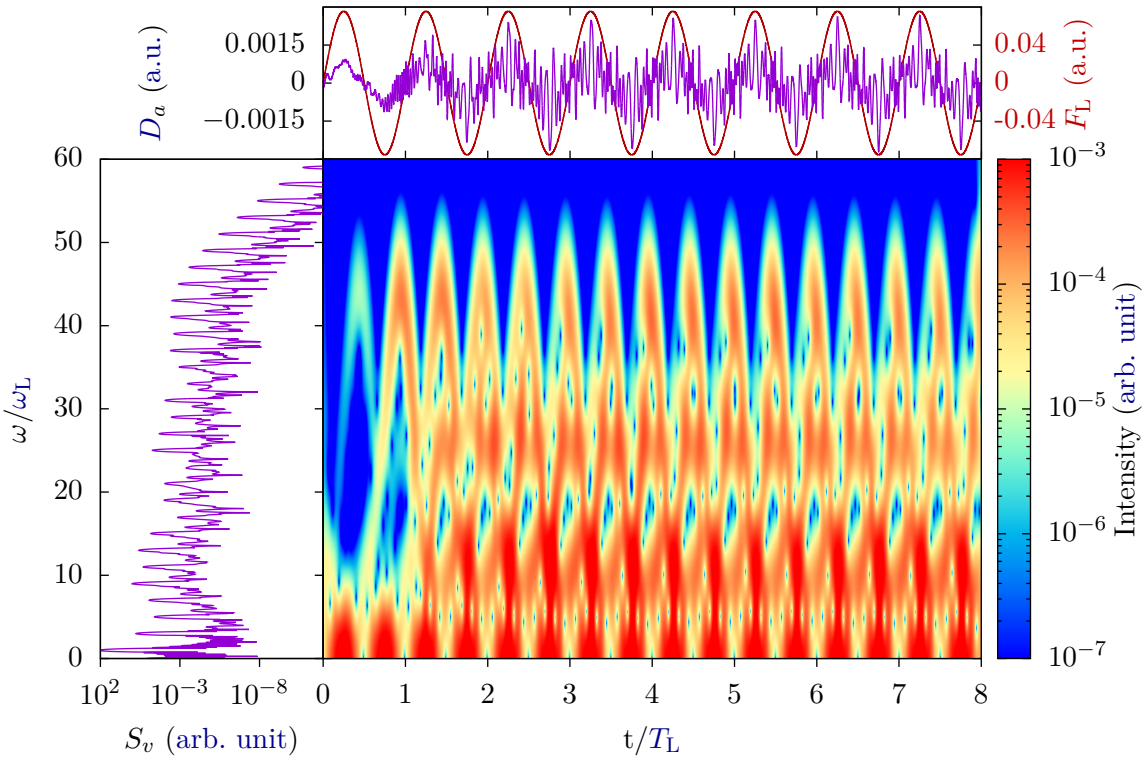

Figure II.7 *Same as Figure II.6 with a trapezoidal laser pulse of 8 optical cycles with linear ramps of 1 optical cycle.*

one family of trajectories from the other [95, 96]. Theoretically we do not need to consider these collective effects and can separate the trajectories at the single atom or molecule level. To this end we use the method that was developped by Risoud in his PhD [129, 157].

We benefit from the spatial separation of the electron wave packet in the long and in the short trajectories. Indeed we saw from our classical description of HHG in section I.3.2 that there exists a limit, located at $x_\alpha = F_0/{\omega_L}^2$, between long and short trajectories: none of the short trajectories go beyond this limit while each long trajectory crosses it. We can thus completely remove the contribution of the long trajectories by absorbing the part of the wave function that goes beyond x_α. This is achieved using absorbing boundary conditions as described in section II.1.1 c). As said in section I.3.3, the total dipole $\mathbf{D}_{\text{tot}}$ is the sum of the short trajectories $\mathbf{D}_S$ and long trajectories $\mathbf{D}_L$ dipoles. We can then deduce the contribution of the long trajectories from:

$$\mathbf{D}_L = \mathbf{D}_{\text{tot}} - \mathbf{D}_S. \tag{II.84}$$

In practice we need to perform two different propagations with two different box sizes. One simulation must have a sufficiently large box to entirely contain both the short and the long trajectories, i.e. the box size must satisfy at least $L \geq 2x_\alpha$. This gives the total wave function $|\psi_{\text{tot}}\rangle$, and the total dipole $\mathbf{D}_{\text{tot}} = \langle\psi_{\text{tot}}|\hat{\mathbf{D}}|\psi_{\text{tot}}\rangle$. The other simulation has a box size equal, or very close, to x_α. This results in a truncated wave function $|\psi_S\rangle$ from which we extract the dipole of the short trajectories $\mathbf{D}_S = \langle\psi_S|\hat{\mathbf{D}}|\psi_S\rangle$. We finally deduce the dipole of the long trajectories with (II.84).

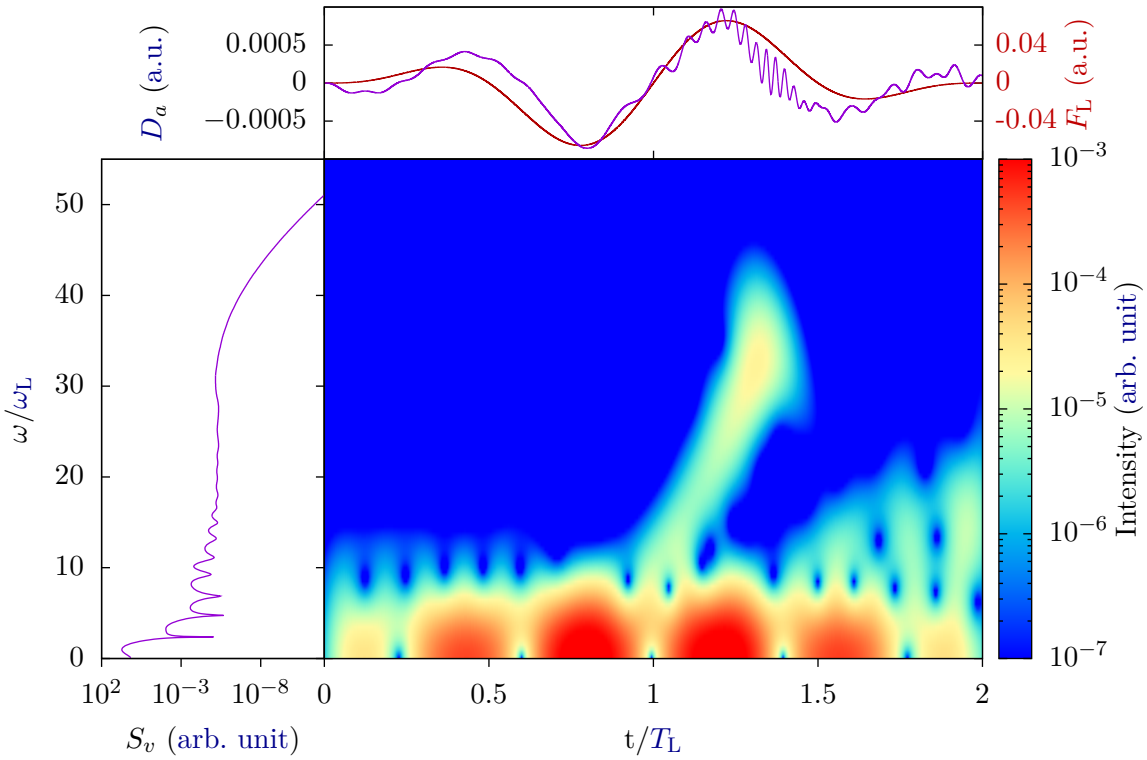

Figure II.8 *Gabor transform of the short trajectories acceleration dipole as a function of time and frequency respectively normalized by the laser period T_L and pulsation ω_L, for the 1D Helium atom after a sine square 2 optical cycle long laser pulse of central wavelength $\lambda_L = 800$ nm and intensity $I = 2 \times 10^{14}$ W.cm^{-2}. In the top panel is plotted the acceleration dipole on the left axis and the laser electric field on the right axis. In the left panel is plotted the HHG spectrum S_v.*

We can use the Gabor transform of the dipole to assess the efficiency of our trajectories separation method. Indeed, in section II.3.2 b), we have identified on this 2D spectrogram the contribution from each family of trajectories. We computed the Gabor spectrum of the short and of the long trajectories for the 1D Helium atom irradiated by a sine square laser pulse of 2 optical cycles with $\lambda_L = 800$ nm. The results are shown on Figures II.8 and II.9. The structure that was clearly visible on Figure II.6 was efficiently truncated in two. The first branch, corresponding to shorter emission times, is visible on the spectrogram of the short trajectories, and the second branch, corresponding to larger emission times, is visible on the spectrogram of the long trajectories.

Moreover, in the spectrum of the total dipole, shown on the left panel of Figure II.6, we see oscillations that clearly appear between $\omega = 18\omega_L$ and $\omega = 35\omega_L$. These oscillations have disappeared in the spectrum of the short and long trajectories. This indicates that these oscillations emerge from interferences between the emission of the two families of trajectories [11]. Since we genuinely managed to separate the two contributions, these interferences have vanished. This is another way to assess the success of our separation.

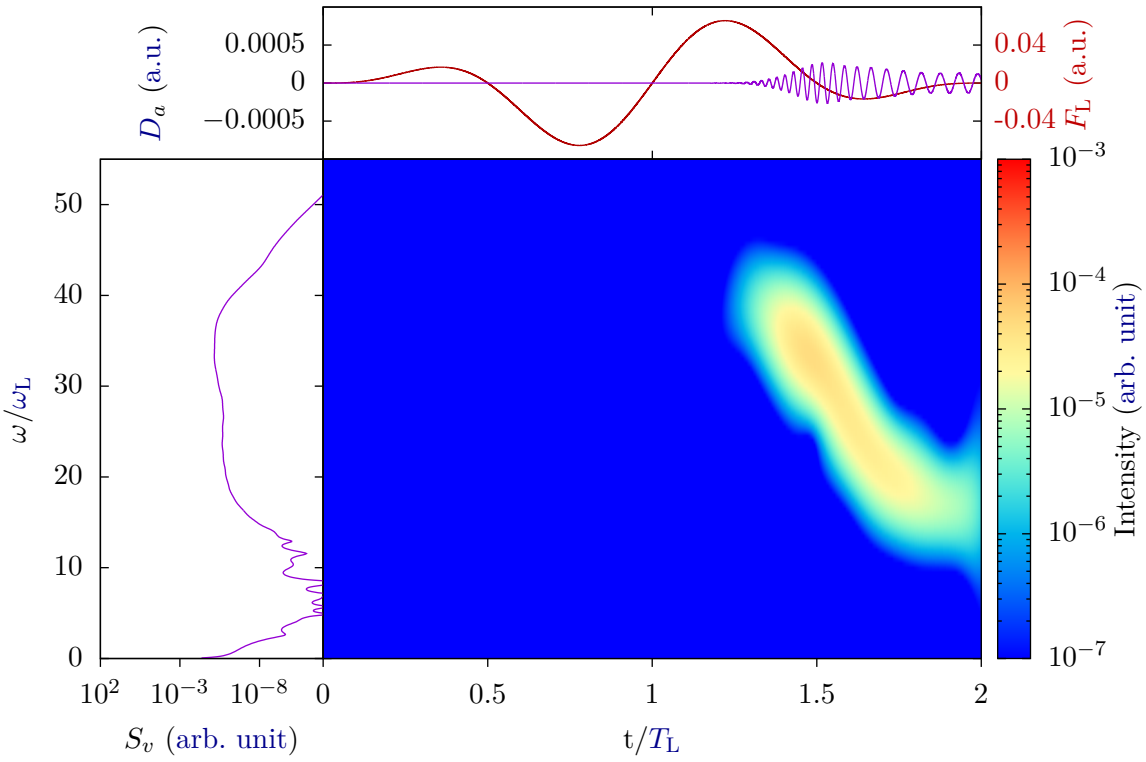

Figure II.9 *Same as Figure II.8 for the long trajectories dipole.*

II.3.4 Window method

a) Energy distribution

When electrons are ionized from an atomic or a molecular ensemble, it is possible experimentally to collect these electrons with guiding magnetic fields. Then we can measure the amount of time, called time of flight, that these electrons take to travel a known distance. This allows to retrieve their velocity and thus their kinetic energy [158–160]. From this kinetic energy, we can deduce a lot of information on the system, both for the stationary and the dynamical points of view [161, 162, 12, 112, 32, 163–165].

In quantum mechanics, of course, the electron does not have a definite kinetic energy, but an energy *distribution*, which is accessible experimentally by averaging over a large number of repeated experiments. Theoretically, there are several methods to compute this distribution. The most intuitive one relies on the use of an artificial detector: in analogy with the experimental measurement, the density flux $\mathbf{j}$ (II.85) is computed at a position $\mathbf{r}_\mathrm{d}$:

$$\mathbf{j}(\mathbf{r}_\mathrm{d},t) = \frac{1}{2\mathrm{i}}\left[\psi^*(\mathbf{r}_\mathrm{d},t)\boldsymbol{\nabla}\psi(\mathbf{r}_\mathrm{d},t) - \psi(\mathbf{r}_\mathrm{d},t)\boldsymbol{\nabla}\psi^*(\mathbf{r}_\mathrm{d},t)\right]. \tag{II.85}$$

This position has to be chosen far away from the nuclei so that its influence is negligible and the electron has reached its asymptotic kinetic energy at the detector. Moreover it must be placed such that, by the time the electron reaches the detector, the laser pulse is over, i.e. the electric field is zero and does not perturb the system anymore. In practice

this requires solving the TDSE in a large simulation box, and for a very long time. The numerical cost of such long propagations can become prohibitive in some cases.

Besides, there is no a priori need to continue the propagation after the end of the laser pulse. Indeed, remark that the energy distribution of the wave function, i.e. the probability density $\delta p(E)$ to find an energy E upon measurement, can be extracted from the populations in the eigenstates of the field-free Hamiltonian $\hat{H}_0$. These populations, and thus $\delta p(E)$, actually become time-independent as soon as the laser is switched off. We can therefore compute $\delta p(E)$ just after the end of the pulse, instead of computing the density flux, and hence reduce our numerical cost.

For a negative energy $E = E_i$ in the spectrum of the Hamiltonian $\hat{H}_0$, the probability density $\delta p(E)$ is equal to the population in the corresponding eigenstate, and for a negative energy E that is not in the spectrum of $\hat{H}_0$, this probability is equal to zero. On the contrary, for a positive energy E, there is always a continuum state corresponding to this energy, so that the probability density is equal to the population in the eigenspace of energy E. We can finally write $\delta p(E)$ as

$$\delta p(E) = \begin{cases} \displaystyle\sum_{i \in \text{bound}} |\langle \varphi_i | \psi(t_\text{f}) \rangle|^2 \delta(E - E_i) & \text{if} \quad E < 0 \\ \rho(E) \displaystyle\int \mathrm{d}\beta \, |\langle \varphi_{E,\beta} | \psi(t_\text{f}) \rangle|^2 & \text{if} \quad E \geq 0, \end{cases} \tag{II.86}$$

where the continuum states are labelled by their energy and all their other quantum numbers, represented by β, and where $\rho(E)$ is the density of states. The populations in the different eigenstates are computed at the time $t_\text{f} = \tau_\text{L}$ corresponding to the end of the laser pulse.

In practice this formula is not very useful, since it would require to compute all the eigenstates of the field-free Hamiltonian $\hat{H}_0$ and then to compute the projection of the wave function on each of these states. Since a numerical scalar product has a complexity of $O(N)$ the projection on all eigenvectors has a complexity of $O(N^2)$, where N is the total size of the numerical grid.

b) Window operator

Instead of projecting the wave function directly on the eigenstates of the $\hat{H}_0$, we use the window method [82] which is much more efficient. It relies on the computation of the expectation value of the window operator $\hat{W}$:

$$\hat{W}(E, n, \gamma) = \gamma^{2^n} \left[\left(\hat{H}_0 - E \right)^{2^n} + \gamma^{2^n} \right]^{-1}. \tag{II.87}$$

This operator acts as a projector over all eigenstates of energy in the range $[E - \gamma, E + \gamma]$. To see this, we decompose the wave function on the eigenstates of the Hamiltonian $\hat{H}_0$, emphasizing the difference between the bound and continuum states:

$$|\psi\rangle = \sum_{i \in \text{bound}} |\varphi_i\rangle \langle \varphi_i | \psi \rangle + \int_{E>0} \mathrm{d}E \, \mathrm{d}\beta \, \rho(E) \, |\varphi_{E,\beta}\rangle \langle \varphi_{E,\beta} | \psi \rangle \, . \tag{II.88}$$

The window spectrum $W(E,n,\gamma)$, defined as the average value of the window operator, thus reads:

$$\begin{aligned} W(E,n,\gamma) &= \langle\psi|\hat{W}(E,n,\gamma)|\psi\rangle && \text{(II.89)}\\ &= \sum_{i,j\in\text{bound}} \langle\psi|\varphi_i\rangle\,\langle\varphi_i|\,\hat{W}\,|\varphi_j\rangle\,\langle\varphi_j|\psi\rangle \\ &\quad + \int_{E',E''\geq 0} \mathrm{d}E'\,\mathrm{d}E''\,\mathrm{d}\beta'\,\mathrm{d}\beta''\,\rho(E')\rho(E'') \\ &\qquad\qquad \times \langle\psi|\varphi_{E',\beta'}\rangle\,\langle\varphi_{E',\beta'}|\,\hat{W}\,|\varphi_{E'',\beta''}\rangle\,\langle\varphi_{E'',\beta''}|\psi\rangle && \text{(II.90)}\\ &= \sum_{i\in\text{bound}} |\langle\varphi_i|\psi\rangle|^2 w(E-E_i,n,\gamma) \\ &\quad + \int_{E'\geq 0} \mathrm{d}E'\,\mathrm{d}\beta'\,\rho(E')\big|\langle\varphi_{E',\beta'}|\psi\rangle\big|^2 w(E-E',n,\gamma) && \text{(II.91)}\\ &= \int_{-\infty}^{+\infty} \mathrm{d}E'\,\delta p(E') w(E-E',n,\gamma), && \text{(II.92)} \end{aligned}$$

i.e. the window spectrum is equal to the integral of the probability density $\delta p(E)$ multiplied by the window function $w(x,n,\gamma)$:

$$w(x,n,\gamma) = \frac{\gamma^{2^n}}{x^{2^n}+\gamma^{2^n}}. \tag{II.93}$$

This window function w is plotted on Figure II.10 for different values of n. It is remarkable that for larger and larger values of n, it tends to a square window of width 2γ. The window spectrum $W(E,n,\gamma)$ indeed converges to the probability of measuring an energy in the range $[E-\gamma, E+\gamma]$:

$$W(E,n,\gamma) = \int_{-\infty}^{+\infty} \mathrm{d}E'\,\delta p(E') w(E-E',n,\gamma) \underset{n\to\infty}{\longrightarrow} \int_{E-\gamma}^{E+\gamma} \mathrm{d}E'\,\delta p(E'). \tag{II.94}$$

If γ is small enough compared to the typical variations of $\delta p(E)$, which can only be true for positive (continuum) energies, then we can compute the integral (II.94) approximately:

$$\begin{aligned} W(E,n,\gamma) &= \int_{-\infty}^{+\infty} \mathrm{d}E'\,\delta p(E') w(E-E',n,\gamma) && \text{(II.95)}\\ &\simeq \delta p(E) \int_{-\infty}^{+\infty} \mathrm{d}E'\,w(E-E',n,\gamma) && \text{(II.96)}\\ &\simeq \frac{\gamma\pi}{n\sin[\pi/(2n)]}\delta p(E) && \text{(II.97)}\\ &\underset{n\to\infty}{\longrightarrow} 2\gamma\,\delta p(E). && \text{(II.98)} \end{aligned}$$

We get a value that is proportional to the parameter γ. While in the negative energy region, if γ is small with respect to the energy gap between consecutive states, we get:

$$W(E,n,\gamma) = \begin{cases} |\langle\varphi_i|\psi\rangle|^2 & \text{if} \quad E=E_i, i\in\text{bound} \\ 0 & \text{otherwise} \end{cases}. \tag{II.99}$$

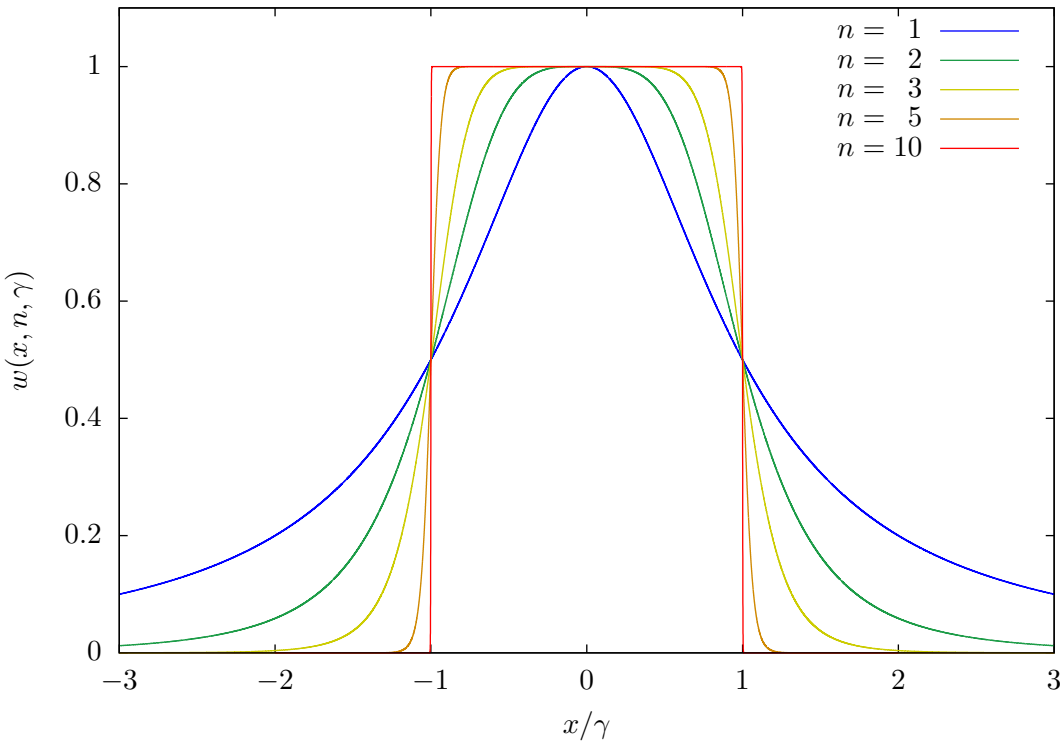

Figure II.10 *Window function* $w(x, n, \gamma)$ (II.93) *for different values of* n.

The parameter γ will in this case influence the *width* of the peak, but not the *value* of W at $E = E_i$.

The window spectrum thus behaves very differently in the positive and negative energy regions. We illustrate this on Figure II.11 with the window spectrum of a 1D Helium atom defined by a Soft-Coulomb potential (II.1) with regularization parameter $a = 0.707$ a.u. (see section II.1.1) after irradiation by a laser pulse with $\omega_L = 40$ eV. Since this photon energy is sufficient to ionize the Helium atom, we observe two peaks, whose positions are independent of the value of γ. The first peak is in the negative energy region, at the ground state energy $E = E_0$, and corresponds to the population that has not been ionized. The second peak is in the positive energy region at an energy $E = E_0 + \omega_L$, and corresponds to the ionized part of the wave function i.e. the *photoelectron*.

We observe that the two peaks behave very differently with respect to the parameter γ. For the peak that corresponds to the ground state, it appears clearly on the inset of Figure II.11 that its maximum value is independent of γ while its width is proportional to it. In this case γ mainly influences the background of the spectrum. Note that for sufficiently small values of γ, i.e. $\gamma \lesssim 0.5$ eV (green curve and curves below) we start to distinguish the populations in the excited states, 10 orders of magnitude below the ground state, from the background. On the contrary, for the peak of the photoelectron, its width and shape remain unchanged for all values of γ, but its maximum value grows linearly with γ. This is a direct consequence of (II.97) stating that the whole positive energy part of the spectrum is proportional to γ.

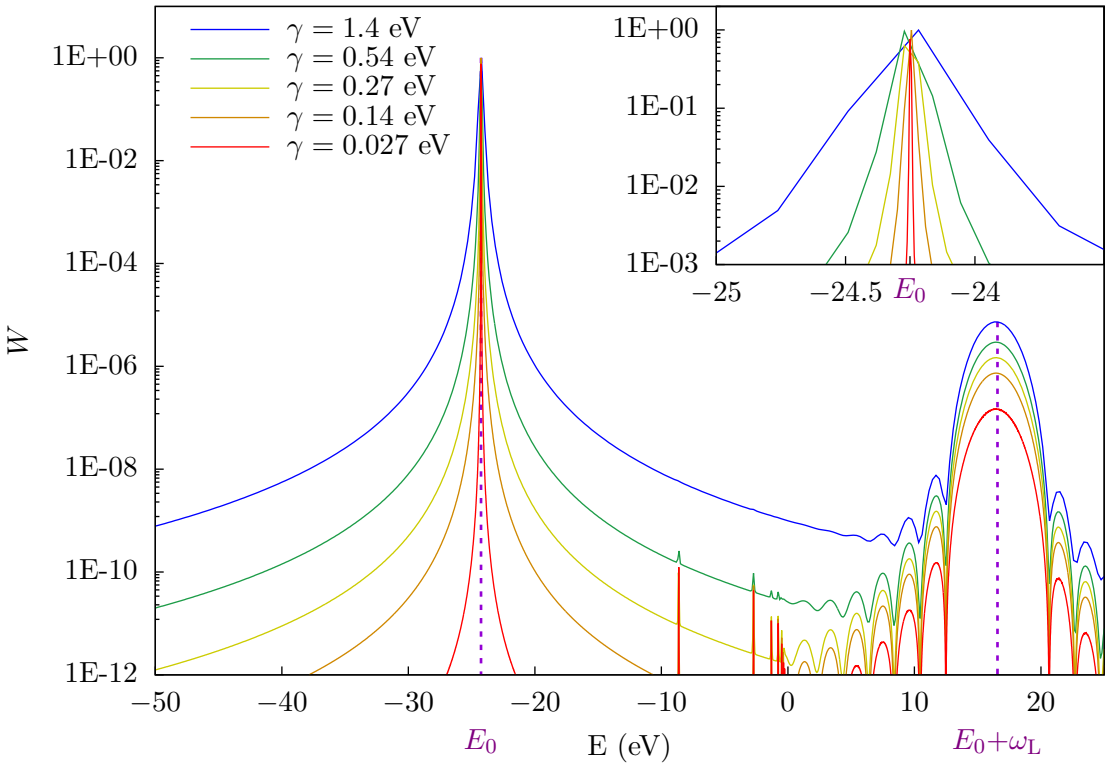

Figure II.11 *Window spectrum* $W(E, n = 2, \gamma)$ (II.100) *for different values of* γ *for a 1D Helium atom defined by a Soft-Coulomb potential* (II.1) *with regularization parameter* $a = 0.707$ a.u. *(see section II.1.1) after a sine square laser pulse of 20 optical cycles and* $\omega_{\mathrm{L}} = 40$ eV. *The upper right panel is a zoom on the top of the first peak.*

The important conclusion is that the relative height of positive and negative energy peaks has no physical meaning, and is simply related to the value of the arbitrary parameter γ. This artifact comes from the difference between a *probability* to be in a particular discrete state, and the probability *density* to be in a continuum state of energy E.

c) Computation of the window spectrum

In practice, we follow the recommendation of [82] and use $n = 2$, which gives a sufficient approximation of a square window. The window spectrum $W(E, \gamma)$ is computed using

$$W(E,\gamma) = \langle\psi(t_{\mathrm{f}})|\,\hat{W}(E, n=2, \gamma)\,|\psi(t_{\mathrm{f}})\rangle \tag{II.100}$$

$$= \gamma^4 \left\langle \psi(t_{\mathrm{f}}) \middle| \left[\left(\hat{H}_0 - E\right)^4 + \gamma^4\right]^{-1} \middle| \psi(t_{\mathrm{f}}) \right\rangle \tag{II.101}$$

$$= \gamma^4 \left\langle \psi(t_{\mathrm{f}}) \middle| \left[\left(\hat{H}_0 - E\right)^2 - \mathrm{i}\gamma^2\right]^{-1} \left[\left(\hat{H}_0 - E\right)^2 + \mathrm{i}\gamma^2\right]^{-1} \middle| \psi(t_{\mathrm{f}}) \right\rangle \tag{II.102}$$

$$= \gamma^4 \langle \chi_{E,\gamma} | \chi_{E,\gamma} \rangle\,, \tag{II.103}$$

Step	Operation	Complexity tridiagonal	Complexity general
$\left[\hat{H}_0 - E_k - \sqrt{\mathrm{i}}\gamma\right]\|\phi\rangle = \|\psi(t_\mathrm{f})\rangle$	Inversion of the linear system $AY = X$	$O(N)$	$O(N^2)$
$\left[\hat{H}_0 - E_k + \sqrt{\mathrm{i}}\gamma\right]\|\chi_{E_k,\gamma}\rangle = \|\phi\rangle$	Inversion of the linear system $AZ = Y$	$O(N)$	$O(N^2)$
$P(E_k,\gamma) = \gamma^4\langle\chi_{E_k,\gamma}\|\chi_{E_k,\gamma}\rangle$	Scalar product $\langle Z\|Z\rangle$	$O(N)$	$O(N)$
Repeat for $E_{k+1} = E_k + 2\gamma$			

Table II.3 – Summary of the window algorithm. The complexity is taken from [136] and is given in the case of a tridiagonal Hamiltonian $\hat{H}$, and in the general case.

where $|\chi_{E,\gamma}\rangle$ is computed by consecutively inverting two linear systems:

$$|\chi_{E,\gamma}\rangle = \left[\left(\hat{H}_0 - E\right)^2 + \mathrm{i}\gamma^2\right]|\psi(t_\mathrm{f})\rangle \tag{II.104}$$

$$= \left[\hat{H}_0 - E + \sqrt{\mathrm{i}}\gamma\right]\left[\hat{H}_0 - E - \sqrt{\mathrm{i}}\gamma\right]|\psi(t_\mathrm{f})\rangle\,. \tag{II.105}$$

The window algorithm is summarized in Table II.3. Remark that it is particularly adapted to the case of a tridiagonal Hamiltonian, i.e. to the one dimensional systems defined in section II.1.1.

d) Simulation box

To compute the energy distribution of the ionized electron, we need the simulation box to be sufficiently large to contain the whole wave function, including the ionized part. In general the box will have to be larger than needed to compute an HHG spectrum. Indeed, as discussed in section II.1.1 c), to compute an HHG spectrum we can safely and without losing any relevant information absorb the ionized part of the wave function that leaves the nuclei and never returns. This is obviously impossible when it is precisely the kinetic energy of this ionized part that we want to compute. In the case described above, we computed the spectrum up to energies of 25 eV and for an incident laser pulse of 2 fs, so that the simulation box size must be at least 60 Å.

However if we use such a minimal box size, then the density of state in the grid is too low to accurately describe the energy distribution in the continuum. On Figure II.12 we plot in gray the window spectrum computed after a propagation in a simulation box of size $L = 265$ Å. We see that we don't get the expected continuous curve. Instead, we see peaks at energies that correspond to the grid "continuum" states (see section II.1.1). To improve the window spectrum, we could perform the TDSE propagation on a larger grid. However, this would increase our numerical cost without any gain of information since the wave function is zero on this additional grid space. Indeed it is superfluous to propagate the wave function in a space that the photoelectron will never reach. The solution of this problem is to compute the window spectrum in a box of size L_W which is larger than

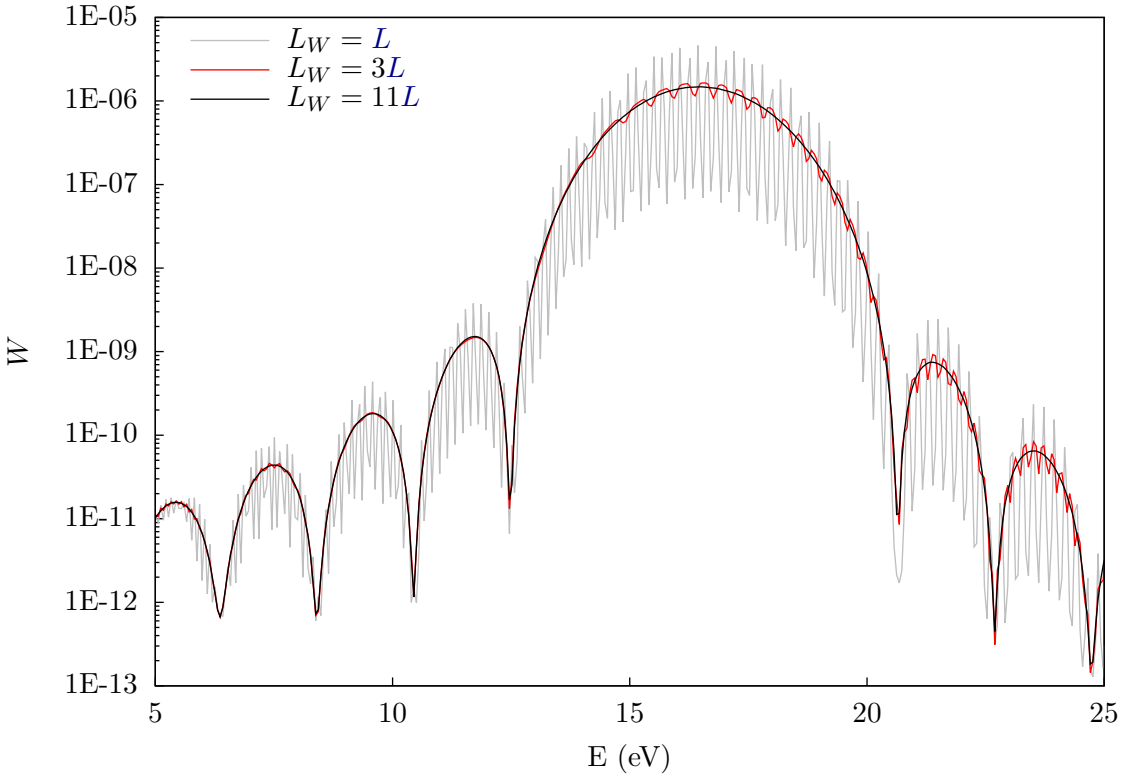

Figure II.12 *Window spectrum* $W(E, n = 2, \gamma = 0.27$ eV) (II.100) *for different values of* L_W *for a 1D Helium atom defined by a Soft-Coulomb potential* (II.1) *with regularization parameter* $a = 0.707$ a.u. *(see section II.1.1) after a sine square laser pulse of 20 optical cycles and* $\omega_L = 40$ eV *computed in a box of size* $L = 500$ a.u. $= 265$ Å.

the size L of the propagation box. The wave function ψ_W in the larger box is set to the propagated wave function where the two boxes coincide, and to zero elsewhere:

$$\psi_W(x) = \begin{cases} \psi(x, t_f) & \text{if} \quad |x| \leq L \\ 0 & \text{otherwise} \end{cases} . \tag{II.106}$$

We plot on Figure II.12 the window spectrum after propagation in the same box $L = 265$ Å but with different values of L_W. We observe a smoothing of the spectrum with increasing value of L_W. With $L_W = 3L$ (in red) we do not see a peak at each continuum state energy but we still observe some small spurious oscillations, while at $L_W = 11L$ (in black), the spectrum is completely smoothed and converged. This method is quite advantageous since the actual TDSE propagation with such a large box would be much too expensive numerically.

Chapter III

Tunnel ionization

As reviewed in Chapter I, the interaction between an atom or a molecule and an electric field can give rise to various phenomena depending on the considered time and energy scales. At low frequencies (typically infrared radiation) and high intensities (10^{13} W.cm^{-2} and beyond), we saw that the ionization of the system by a laser can no longer be described by the absorption of one or several photons depicted by perturbation theory. In such conditions, the laser field strongly distorts the atomic potential so that electrons can escape through tunnel effect. This phenomenon was first modeled by Keldysh [113] in the 60's and was then intensively investigated, since it represents the first step of the highly non-linear processes that we described in section I.3, such as HHG [91, 96], or non-sequential multiple ionization [94].

As for many non-linear processes, the only way to accurately describe tunnel ionization is to numerically solve the TDSE. However, because of its high numerical cost, this method can only be used for small systems, i.e. an atom with one or two electrons. The description of larger and more complex systems such as molecules is very delicate and requires some approximations: Single Active Electron approximation and frozen nuclei [166–168], Strong Field Approximation [169, 170] or low dimensionality [171]. On the other hand, one may rely on approximate models such as the Lewenstein model [11] that we reviewed in section I.3.3, or the Quantitative ReScattering theory [59]. The advantage of these models is to yield analytical formulas and derivations that are easier to handle than numerical simulations. Moreover, they allow to decompose each strong field process into different steps, e.g. the celebrated three-step model for HHG [9, 91], which provides valuable physical pictures and insights. As we have seen, tunnel ionization is the universal first step of all recollision processes, and is also the main source of their non-linearity, hence its central importance in strong field physics.

For all the reasons we just cited, approximate analytical formulas, see [172, 173] for more complete reviews, are often prefered to numerical simulations for the analysis and interpretation of experimental results. The most frequently used formulas rely on the adiabatic approximation, which holds when the Keldysh parameter, defined in (I.69), is very small $\gamma \ll 1$. Among them are the ones derived by Perelomov, Popov and Terent'ev (PPT) [174–176] or Ammosov, Delone and Krainov (ADK) [177] for atoms, and extended to molecules (Mo-ADK) by Tong et al. [178, 179] and Kjeldsen and Madsen [180], but also more advanced analytical works like the ones performed by Tolstikhin et al. [181, 182]. However, these analytical formulas have a limited accuracy as was extensively shown

recently by Lai et al. [183] and we investigated the causes of this discrepancies during my PhD. In fact, the adiabatic approximation allows to deduce the time-dependent rate *directly* from the static one. Consequently, the accuracy (or inaccuracy) of these *time-dependent* rates (PPT, ADK, Mo-ADK) strongly depends on the ionization rate in a *static* electric field.

This static rate is itself asymptotically exact when the electric field F goes to zero, i.e. $F \to 0$, and is thus called *asymptotic*. It was obtained at first order for the Hydrogen atom by Landau and Lifshitz (LL) [132] and extended to any atom by Smirnov and Chibisov (SC) [184]. Using advanced analytical derivation based on Siegert states, Tolstikhin et al. have recently achieved an asymptotic derivation of the ionization rate at higher orders for atoms [185–187], and molecules [188–190] including nuclear motion in the Born Oppenheimer approximation [171, 191]. At the same time, Manakov et al. performed a derivation for negative atomic [192] and molecular ions [193]. A correction for multielectron effects has been proposed in [194] that was shown to be particularly important for polar species [195, 196].

A more empirical, much more direct, and hence more widely used, approach has been developed for molecules [197, 167, 99]. It consists in a correction of the asymptotic SC (or ADK, which is equivalent) rate by adding an effect that was completely neglected in the original derivation: the perturbation of the energy levels by the static electric field, namely the Stark shift that we have presented in section II.1.4. The effect of the Stark shift correction has been shown to have a determinant contribution in tunnel ionization, especially for polar species [197, 198, 196]. However, this correction has been used in a rather inconsistent way considering the derivation made by LL [132] and SC [184].

In this chapter we consistently derive the corrected ionization rate formula taking into account the Stark shift. We then quantify the actual effectiveness of this correction for different 1D model systems. To do this, we confront the prediction of the analytical formula to *exact* results obtained with the numerical solution of the TDSE (see section II.1.2 b)). In particular we investigate the role of the polarizability and possible permanent dipole moment of the ionized species. We also discuss the different approximations that are commonly used to compute the Stark shift, and how they affect the predictions of the formula. Finally, we study in more details all the sources of inaccuracy at each step of the derivation to find the origin of the discrepancies between analytical and numerical predictions.

We mention here that the low dimensionality of the model systems that are studied here does not reduce the generality of the conclusions. Indeed the ionization of the hydrogen atom in a static field actually reduces to a one-dimensional problem through a change to parabolic coordinates (see e.g. [132]). The results presented here are hence most general and give physical insights that can easily be extended to the three-dimensional case. Most of the work presented in this chapter has been published in [199].

Objectives

- Derive a formula for the ionization rate that consistently includes the Stark shift.
- Assess qualitatively and quantitatively the impact of this Stark shift correction.
- Investigate the model inaccuracy by testing the validity of the approximations.

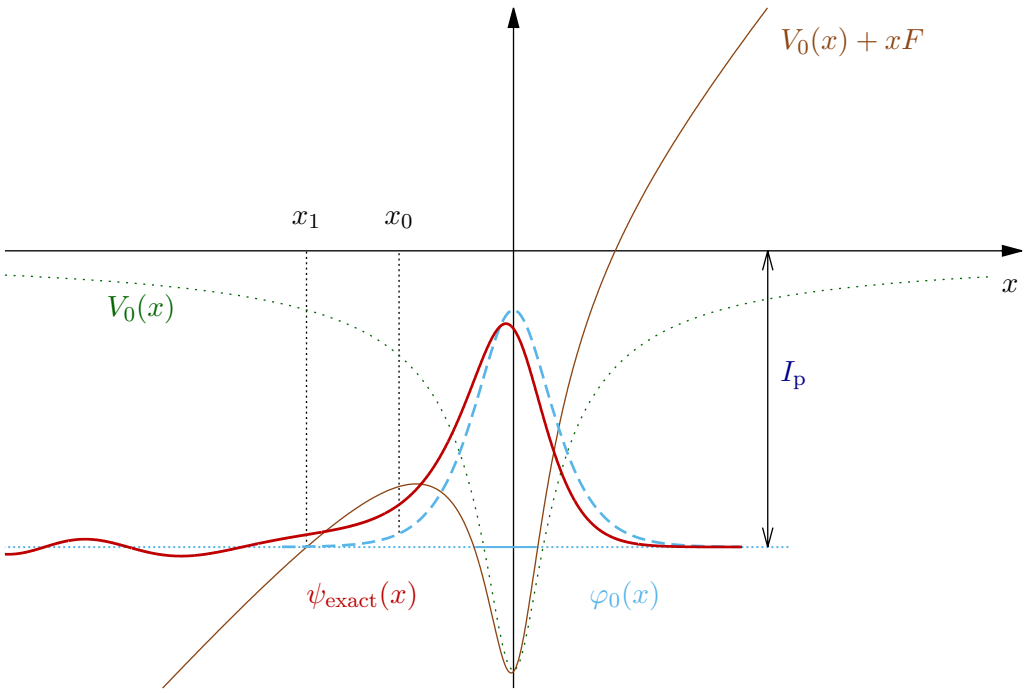

Figure III.1 *Schematic view of tunnel ionization of the atomic system described in section III.2.1 in a field $F = 6 \times 10^{-2}$ a.u.. Solid red line: exact wave function $\psi_\mathrm{exact}(x)$ dressed by the electric field and dashed blue line: exact ground state $\varphi_0(x)$ of the unperturbed system (both computed by inverse iteration [137]).*

III.1 Analytical rate

The tunnel ionization rate of an atom in a static field F has been derived by Smirnov and Chibisov in [184]. We adapted this rate to our 1D case to get

$$\Gamma_\mathrm{SC} = |B_\pm|^2 \sqrt{2I_\mathrm{p}} \left(\frac{4I_\mathrm{p}}{|F|}\right)^{\frac{2Z}{\sqrt{2I_\mathrm{p}}}} \exp\left(-\frac{2(2I_\mathrm{p})^{3/2}}{3|F|}\right), \tag{III.1}$$

where $B_\pm$ is the asymptotic coefficient of the atomic ground state φ_0, i.e. following [184],

$$\varphi_0(x) \underset{\pm\infty}{\sim} B_\pm \, |x|^{\frac{Z}{\sqrt{2I_\mathrm{p}}}} \, \mathrm{e}^{-\sqrt{2I_\mathrm{p}}|x|}, \tag{III.2}$$

and where of course, for a symmetric system $B_+ = B_- = B$. However, this derivation completely neglects the Stark shift, i.e. the influence of the electric field on the energy levels of the systems, and in particular on I_p.

This effect was included in subsequent works e.g. in [197, 167, 99] where it was empirically added to the ionization potential in the final formula (III.1). Here we propose a more consistent approach where we include the Stark shift from the beginning of the derivation. We follow the procedure initially performed by [132, 184], but adapted to

our one dimensional case. To recover the three dimensional rate, one should integrate the formula over the two remaining variables, as it is done in [132, 184]. Note that all the approximations that are made in this section will be extensively discussed later, in section III.3.

We consider the system depicted in Figure III.1 composed of an electron trapped in a potential well V_0 like e.g. the Soft Coulomb potential described in section II.1.1. We do not need to actually specify the shape of V_0 near the nuclei. We only suppose that it behaves asymptotically like a Coulomb potential. We place this bound electron in a very weak static electric field $F \ll (2I_\mathrm{p})^{3/2}$. We denote by $\widetilde{I_\mathrm{p}} = I_\mathrm{p} + \Delta I_\mathrm{p}$ the *corrected* ionization potential that include the Stark shift ΔI_p. For a weak electric field, the Stark shift can be treated through perturbation theory, and $\Delta I_\mathrm{p} \ll I_\mathrm{p}$. For a symmetric potential, the choice of sign of the electric field is irrelevant and we choose F positive, therefore ionization occurs in the region of space where x is negative. Note that the electric field induces a strong asymmetry, and that the ionization occurs only in the x negative region of space.

The ionization rate Γ can be computed as the electronic density flux far from the atomic potential, i.e. at a point $x \to -\infty$, out of the wave function $\psi(x)$ corresponding to the ground state dressed by the electric field:

$$\Gamma = -\operatorname{Im}(\psi^* \frac{\mathrm{d}\psi}{\mathrm{d}x}). \tag{III.3}$$

However, the wave function is not available in most practical cases, we thus use the semi-classical approximate expression:

$$\psi(x) = \begin{cases} \dfrac{C}{\sqrt{p}} \exp\left(\mathrm{i}\displaystyle\int_x^{x_1} p(x')\,\mathrm{d}x' - \frac{\mathrm{i}\pi}{4}\right), & x < x_1 \\ \dfrac{C'}{\sqrt{|p|}} \exp\left(\displaystyle\int_{x_1}^{x} |p(x')|\,\mathrm{d}x'\right), & x_1 < x \leq x_0\ , \end{cases} \tag{III.4}$$

where $p(x) = \sqrt{2(-\widetilde{I_\mathrm{p}} - V_0(x) - xF)}$ is the classical action, x_1 is the external turning point i.e. $p(x_1) = 0$, and where x_0 is a point *inside* the potential energy barrier, as depicted on Figure III.1. This point x_0 is chosen sufficiently close to zero so that the influence of the field is negligible $|x_0 F| \ll I_\mathrm{p}$, and also sufficiently far so that the influence of the potential is also negligible $|V_0(x_0)| \ll I_\mathrm{p}$. Note that the electric field needs to be very small for these two assumptions not to be contradictory. We will come back to this later. Using the connecting formulas in [132], we find the relations between C and C', and we can express the wave function as

$$\psi(x) = \begin{cases} \dfrac{C}{\sqrt{p}} \exp\left(\mathrm{i}\displaystyle\int_x^{x_1} p(x')\,\mathrm{d}x' - \frac{\mathrm{i}\pi}{4}\right), & x < x_1 \\ \dfrac{C}{\sqrt{|p|}} \exp\left(\displaystyle\int_{x_1}^{x} |p(x')|\,\mathrm{d}x' + \frac{\mathrm{i}\pi}{2}\right), & x_1 < x \leq x_0\ . \end{cases} \tag{III.5}$$

We got the wave function up to a constant factor C. The computation of this factor relies on a choice of normalization, of which the absolute value of the rate will depend, since if we insert (III.5) in (III.3) the rate becomes:

$$\Gamma = |C|^2. \tag{III.6}$$

The choice of Landau and Lifshitz in [132] and Smirnov and Chibisov in [184] is to connect the semi-classical wave function with the ground state φ_0 of the unperturbed system. To this end, in the same way as LL, we use $|x_0 F| \ll I_\mathrm{p}$, to neglect the influence of the electric field on the wave function close to zero:

$$\psi(x) = \varphi_0(x), \quad x_0 \leq x \leq 0. \tag{III.7}$$

Using the continuity of the wave function at x_0, this allows to determines the constant C and the final expression for $\psi(x)$ *outside* the barrier:

$$\psi(x) = \varphi_0(x_0) \frac{\sqrt{|p(x_0)|}}{\sqrt{p(x)}} \exp\left(-\int_{x_1}^{x_0} |p(x')|\,\mathrm{d}x'\right) \exp\left(\mathrm{i}\int_{x}^{x_1} p(x')\,\mathrm{d}x' - \frac{3\mathrm{i}\pi}{4}\right), \quad x < x_1, \tag{III.8}$$

and thus the ionization rate:

$$\Gamma = |\varphi_0(x_0)|^2\, |p(x_0)| \exp\left(-2\int_{x_1}^{x_0} |p(x')|\,\mathrm{d}x'\right). \tag{III.9}$$

Remark that this expression does not depend on the point x at which the electronic density flux is evaluated, which is satisfactory.

We need to compute the three factors of this product. First, in the preexponential factor we use both $|x_0 F| \ll I_\mathrm{p}$ and $|V_0(x_0)| \ll I_\mathrm{p}$ to approximate $|p(x_0)| \simeq \sqrt{2I_\mathrm{p}}$. Second, in the exponential we keep the first two terms of the expansion of $|p(x)|$ in powers of $V_0(x)/(xF + \widetilde{I_\mathrm{p}})$:

$$|p(x)| = \sqrt{2(xF + \widetilde{I_\mathrm{p}})} + \frac{V_0(x)}{\sqrt{2(xF + \widetilde{I_\mathrm{p}})}} + O\left(\frac{V_0(x)^2}{(xF + \widetilde{I_\mathrm{p}})^{\frac{3}{2}}}\right) \tag{III.10}$$

which, after integration gives

$$\int_{x_1}^{x_0} |p(x)|\,\mathrm{d}x = \frac{(2\widetilde{I_\mathrm{p}})^{\frac{3}{2}}}{3F}(1+\eta)^{\frac{3}{2}} - \frac{Z}{\sqrt{2\widetilde{I_\mathrm{p}}}} \ln\left(\frac{1+\sqrt{1+\eta}}{1-\sqrt{1+\eta}}\right) + O\left(\frac{Z^{\frac{3}{2}}F^{\frac{1}{2}}}{I_\mathrm{p}^{\frac{3}{2}}}\right), \tag{III.11}$$

where

$$\eta = |x_0 F|/\widetilde{I_\mathrm{p}}. \tag{III.12}$$

To be exhaustive, we have kept the factors in front of the powers of F in the $O(F^\alpha)$. We use $\eta \ll 1$ to make the expansion

$$\int_{x_1}^{x_0} |p(x)|\,\mathrm{d}x = \frac{(2\widetilde{I_\mathrm{p}})^{\frac{3}{2}}}{3F} + \underbrace{x_0\sqrt{2\widetilde{I_\mathrm{p}}}}_{\mathcal{A}} \underbrace{- \frac{Z}{\sqrt{2\widetilde{I_\mathrm{p}}}} \ln\left(\frac{4}{\eta} + O(1)\right)}_{\mathcal{B}} + O\left(\frac{x_0^2 F}{\sqrt{I_\mathrm{p}}}\right) + O\left(\frac{Z^{\frac{3}{2}}F^{\frac{1}{2}}}{I_\mathrm{p}^{\frac{3}{2}}}\right). \tag{III.13}$$

We will begin by explaining why we *can* neglect ΔI_p in terms $\mathcal{A}$ and $\mathcal{B}$, then point out why we *must* do it. As ΔI_p can be treated by perturbation theory we have $\Delta I_\mathrm{p} = O(x_0 F)$ when $F \to 0$. We use $\Delta I_\mathrm{p} \ll I_\mathrm{p}$ to make the expansion

$$\mathcal{A} = x_0\sqrt{2I_\mathrm{p}} + \frac{2x_0\Delta I_\mathrm{p}}{\sqrt{2I_\mathrm{p}}} \tag{III.14}$$

$$= x_0\sqrt{2I_\mathrm{p}} + O\left(\frac{x_0^2 F}{\sqrt{I_\mathrm{p}}}\right) \tag{III.15}$$

and remark that the second term can be inserted in the $O(x_0^2 F/\sqrt{I_\mathrm{p}})$ term in (III.13). We also expand $\mathcal{B}$ as

$$\mathcal{B} = \frac{Z}{\sqrt{2I_\mathrm{p}}}\ln\left(\frac{4I_\mathrm{p}}{|x_0|F} + \frac{4\Delta I_\mathrm{p}}{|x_0|F} + O(1)\right) + \left[\frac{Z\Delta I_\mathrm{p}}{(2I_\mathrm{p})^{\frac{3}{2}}} + O\left(\frac{Z{\Delta I_\mathrm{p}}^2}{{I_\mathrm{p}}^{\frac{5}{2}}}\right)\right]\ln\left(\frac{4I_\mathrm{p}}{|x_0|F} + O(1)\right). \tag{III.16}$$

Note that $4\Delta I_\mathrm{p}/(|x_0|F) = O(1)$, and that for $X \gg 1$ $\ln(X)$ is a $o(X^\epsilon)$ for any $\epsilon > 0$. So the last expression can be simplified:

$$\mathcal{B} = \frac{Z}{\sqrt{2I_\mathrm{p}}}\ln\left(\frac{4I_\mathrm{p}}{|x_0|F} + O(1)\right) + o\left(\frac{Z(x_0F)^{1-\epsilon}}{{I_\mathrm{p}}^{\frac{3}{2}-\epsilon}}\right). \tag{III.17}$$

If we choose $\epsilon < \frac{1}{2}$, we can insert this $o\Big(Z(x_0F)^{1-\epsilon}/{I_\mathrm{p}}^{\frac{3}{2}-\epsilon}\Big)$ in the $O\Big(Z^{\frac{3}{2}}F^{\frac{1}{2}}/{I_\mathrm{p}}^{\frac{3}{2}}\Big)$ term in (III.13). In the end we have consistently neglected all terms that contain ΔI_p in (III.13) except the first term $(2\widetilde{I_\mathrm{p}})^{\frac{3}{2}}/3F$. We can now plug (III.13) in (III.9):

$$\Gamma = |\varphi_0(x_0)|^2|x_0|^{-\frac{2Z}{\sqrt{2I_\mathrm{p}}}}\,\mathrm{e}^{2|x_0|\sqrt{2I_\mathrm{p}}}\sqrt{2I_\mathrm{p}}\left(\frac{4I_\mathrm{p}}{F}\right)^{\frac{2Z}{\sqrt{2I_\mathrm{p}}}}\exp\left(-\frac{2(2\widetilde{I_\mathrm{p}})^{\frac{3}{2}}}{3F}\right). \tag{III.18}$$

Finally we use $|V_0(x_0)| \ll I_\mathrm{p}$ to replace $\varphi_0(x_0)$ by its asymptotic form, i.e. (III.2), and notice that

$$|\varphi_0(x_0)|^2|x_0|^{-\frac{2Z}{\sqrt{2I_\mathrm{p}}}}\,\mathrm{e}^{2|x_0|\sqrt{2I_\mathrm{p}}} \xrightarrow[x_0\to\infty]{} |B|^2, \tag{III.19}$$

to get the final expression

$$\widetilde{\Gamma}_\mathrm{SC} = |B|^2\sqrt{2I_\mathrm{p}}\left(\frac{4I_\mathrm{p}}{|F|}\right)^{\frac{2Z}{\sqrt{2I_\mathrm{p}}}}\exp\left(-\frac{2(2\widetilde{I_\mathrm{p}})^{3/2}}{3|F|}\right). \tag{III.20}$$

This expression is very similar to the uncorrected one (III.1), but with $\widetilde{I_\mathrm{p}}$ instead of I_p in the exponential, thus including the Stark shift. In earlier attempts to improve this formula [197, 198, 196], the Stark shift correction was empirically included everywhere in the formula. We see from the complete derivation that it is actually inconsistent.

We now come back to the reason why we *must* neglect ΔI_p in terms $\mathcal{A}$ and $\mathcal{B}$. Indeed, if one kept $\widetilde{I_\mathrm{p}}$ instead of I_p then the simplification (III.19) would not work anymore, and the final formula for the ionization rate would unphysically depend on the arbitrary

quantity x_0. To avoid such an inconsistency, it is thus necessary to neglect the Stark shift as we have done. For the term in the dominant exponential, there is no such requirement, and one may keep the corrected ionization potential $\widetilde{I_\mathrm{p}}$.

Note that if we express the Stark shift using time-independent perturbation theory $\Delta I_\mathrm{p} = \mu F + \alpha F^2$, and following the same considerations, we find that we *can* consistently neglect the second term. Indeed, we can expand $\widetilde{I_\mathrm{p}}^{3/2}$ in (III.13) and insert the second order term in the $O(x_0^2 F/\sqrt{I_\mathrm{p}})$. However, and contrarily to the previous case, this is not *mandatory* in the sense that it does not induce any particular unphysical effects. Since we have no physical reasons to neglect it, we will determine numerically if the second order should or should not be included. To do this we directly compare the accuracy with and without the correction for different model systems.

III.2 Accuracy of the corrected formula for various illustrative systems

We now test the accuracy and identify the range of applicability of the corrected rate $\widetilde{\Gamma}_\mathrm{SC}$ (III.20) obtained in the previous section. We confront it to the *exact* numerical results obtained with the numerical solution of the TDSE computed as described in section II.1.2 b). We consider different model systems with different characteristics. First we examine an atomic system for which the Stark shift is very small, and hence often neglected in the description of tunnel ionization. We then treat symmetric molecular systems of different sizes, and thus different polarizabilities. Finally we describe asymmetric systems for which tunnel ionization becomes anisotropic.

III.2.1 Atoms

In the case of atoms, the polarizability is in general quite small due to the high degree of confinement of the electron. Consequently the Stark shift is often neglected to describe the tunnel ionization of these systems (see e.g. [183]). We want to determine if this omission is justified. We consider a model atom, defined by a Soft-Coulomb potential (II.1) with the parameters set to $Z = 1$ and $a = 1.1545$ a.u., with an ionization potential $I_\mathrm{p} = 0.594$ a.u.. We first confront the analytical uncorrected SC rate Γ_SC (III.1) to our exact TDSE results, then we will test the corrected rate $\widetilde{\Gamma}_\mathrm{SC}$ (III.20).

From Figure III.2 (a), we see that although it is derived for an asymptotically weak field $|F| \to 0$ the uncorrected SC formula (dotted purple line) gives the correct behavior for the ionization rate compared to the TDSE results (black circles). This observation remains true on a broad range of field values corresponding to eight orders of magnitude of Γ values. It is however difficult to appreciate the accuracy of the formula because of the logarithmic scale. This is why we show the ratio of the exact numerical results Γ_TDSE to the analytical ones on Figure III.2 (b). It becomes clear on this figure that the analytical formula Γ_SC can only be trusted up to $\simeq$ 10% in the best case. As expected from an asymptotic rate, the accuracy decreases with increasing fields, and the difference with the TDSE result exceeds 100% for fields larger than 6.5×10^{-2} a.u., which corresponds to intensities larger than 1.5×10^{14} W.cm^{-2}. It is therefore very delicate to use this formula for quantitative predictions of ionization rates at finite (nonzero) fields.

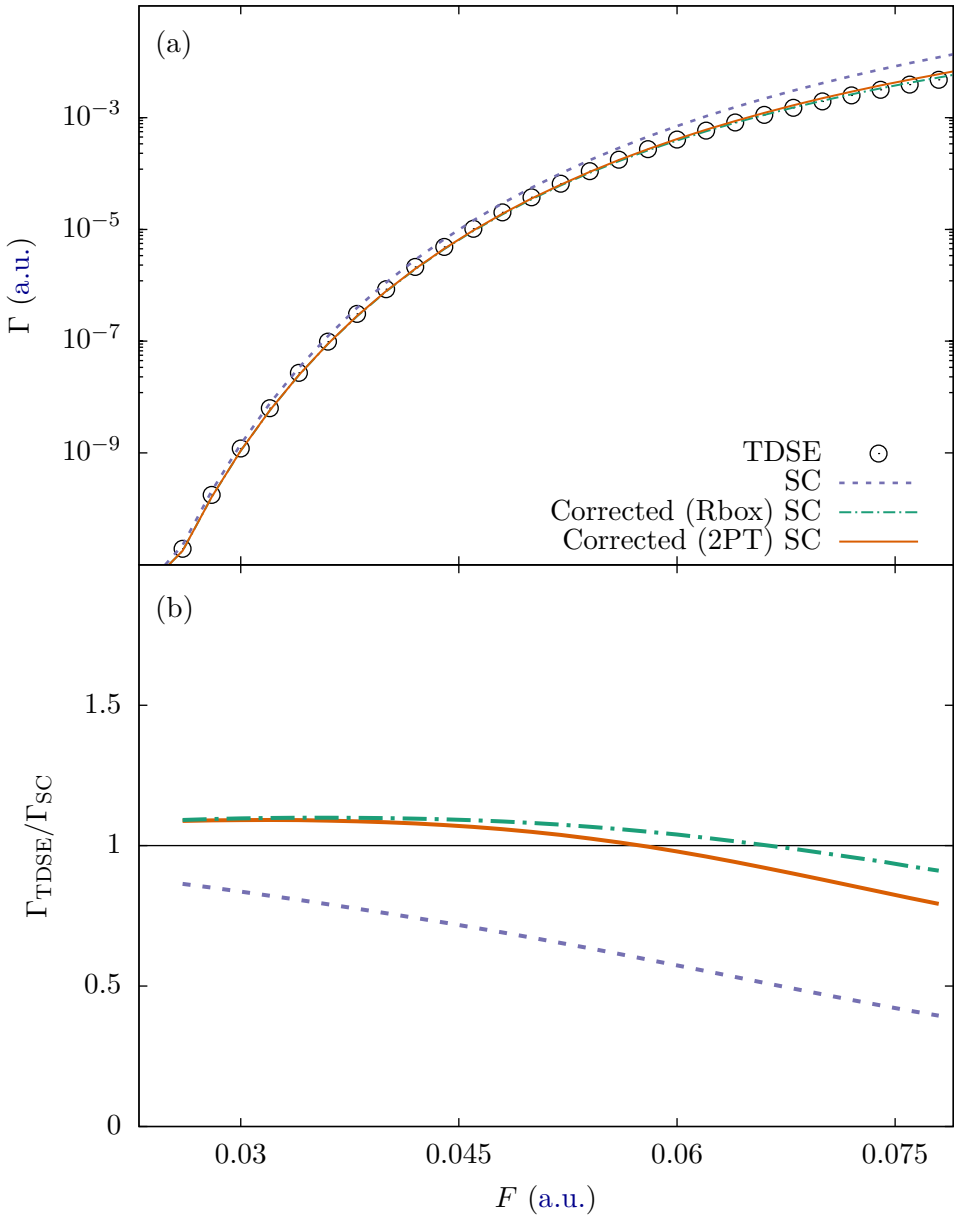

Figure III.2 *Tunnel ionization of the atomic system defined in section III.2.1. (a) Ionization rate as a function of the electric field: black circles for the reference value* Γ_{TDSE}*, dotted purple line for the SC analytical formula* Γ_{SC} (III.1)*, dash-dotted green line for the modified SC formula* $\widetilde{\Gamma}_{\mathrm{SC}}$ (III.20) *corrected with the exact* $\widetilde{I}_{\mathrm{p}}$ *and solid orange line for the same modified SC formula but with the 2PT approximation* $\widetilde{I}_{\mathrm{p}}^{\mathrm{2PT}}$ (III.21)*. (b) Ratio of the numerical to analytical ionization rates: dotted purple line for* $\Gamma_{\mathrm{TDSE}}/\Gamma_{\mathrm{SC}}$*, dash-dotted green line for* $\Gamma_{\mathrm{TDSE}}/\widetilde{\Gamma}_{\mathrm{SC}}$ *computed with the exact* $\widetilde{I}_{\mathrm{p}}$*, and solid orange line for* $\Gamma_{\mathrm{TDSE}}/\widetilde{\Gamma}_{\mathrm{SC}}$ *computed with the 2PT approximation* $\widetilde{I}_{\mathrm{p}}^{\mathrm{2PT}}$*.*

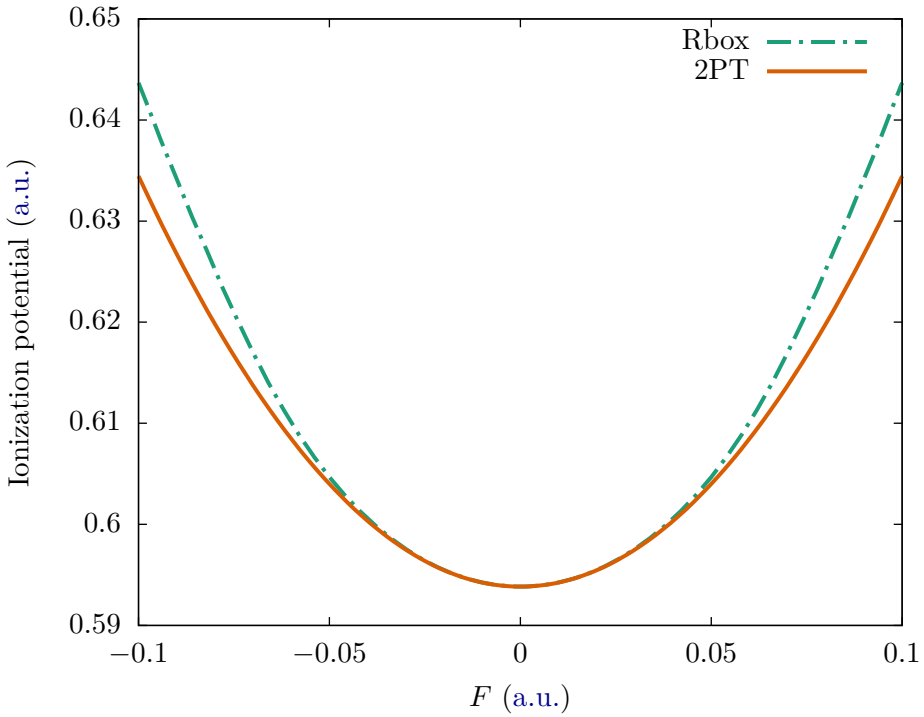

Figure III.3 *Stark shift of the atomic system defined in section III.2.1. Corrected ionization potential as a function of the electric field: dash-dotted green line for the numerical results and solid orange line for second order perturbation theory* $\widetilde{I_\mathrm{p}}^{(2\mathrm{PT})}$ (III.21).

To check the validity of the corrected formula $\widetilde{\Gamma}_{\mathrm{SC}}$ (III.20), we computed the Stark shift of this atomic system with the Rbox method explained in section II.1.4. As can be seen on Figure III.3, it is very well approximated by Second order Perturbation Theory (2PT):

$$\widetilde{I_\mathrm{p}}^{(2\mathrm{PT})} = I_\mathrm{p} + \alpha F^2, \tag{III.21}$$

where $\alpha = 4.06$ a.u. for this system. Then we compare the modified SC rate $\widetilde{\Gamma}_{\mathrm{SC}}$ (III.20) computed either with the *exact* $\widetilde{I_\mathrm{p}}$ (dash-dotted green line) or with the 2PT correction $\widetilde{I_\mathrm{p}}^{(2\mathrm{PT})}$ (solid orange line) to the TDSE results (black crosses) on Figure III.2 (a) and (b). We see that both versions of $\widetilde{\Gamma}_{\mathrm{SC}}$ are closer to the TDSE results than the uncorrected Γ_{SC}, indicating that the Stark shift correction systematically reduce the error made by the SC formula. Moreover we see in the lower panel that in both cases (*exact* and 2PT corrections) the exact to analytical ratio is flat, which indicates that the behavior predicted by this corrected formula is very close to the exact one.

To conclude, even for relatively low polarizability, the Stark shift strongly affects the tunnel ionization of atoms. Indeed, it appears in the dominant exponential term and *cannot* be neglected there. Besides, we see that the rate corrected with the 2PT approximation $\widetilde{I_\mathrm{p}}^{(2\mathrm{PT})}$ is in very good agreement with the one corrected with the *exact* $\widetilde{I_\mathrm{p}}$. This justifies the use of the 2PT approximation to compute the ionization rate, i.e. we only need to know the polarizability of the atom to accurately compute its ionization rate.

We have checked that the general behavior described here is insensitive to the values of the atomic parameters Z and a within ranges of physical relevance.

III.2.2 Homonuclear diatomic molecules

In the case of homonuclear diatomic molecules, the Stark shift is very sensitive to the interatomic bond length. This is because the energy gap between the ground and first excited state $\Delta E = E_1 - E_0$ decreases when the bond length increases. If this gap gets small, such that $\Delta E \lesssim \Delta I_\mathrm{p}$, then the Stark shift becomes linear and one has to use Degenerate Perturbation Theory (DPT) to compute the corrected ionization potential. This reads, at first order

$$\widetilde{I_\mathrm{p}}^{(\mathrm{DPT})} = -\frac{E_0 + E_1}{2} + \frac{1}{2}\sqrt{(E_1 - E_0)^2 + 4|\langle\varphi_0|x|\varphi_1\rangle|^2 F^2}. \tag{III.22}$$

To compare numerically the two different versions of perturbation theory, we consider two molecular systems S_1 and S_2 with the same asymptotic behavior ($Z = 1$) and the same ionization potential $I_\mathrm{p} = 0.573$ a.u. but different bond lengths. For the first system S_1 we take $a = 1$ a.u., $R = 2.2$ a.u. and obtain a field-free energy gap of $\Delta E = 0.260$ a.u., whereas for the second one S_2 we take $a = 0.6925$ a.u., $R = 4.0$ a.u. and get $\Delta E = 0.117$ a.u. We show their dressed *exact* ionization potential $\widetilde{I_\mathrm{p}}$ computed with the *Rbox* method applied to the two perturbation theories $\widetilde{I_\mathrm{p}}^{\mathrm{2PT}}$ and $\widetilde{I_\mathrm{p}}^{\mathrm{DPT}}$ on Figure III.4. We notice quantitative differences: in the first case (Figure III.4 (a)) 2PT (solid orange line) gives the best agreement with numerical results (dash-dotted green line), while in the second case (Figure III.4 (b)), DPT (dashed pink line) seems more adequate. This clearly illustrates that second order approximation of the Stark shift can be ill-fitting and has to be considered with care, especially for molecules.

We now use the two Stark shift perturbation expansions (2PT and DPT) to obtain two different corrected ionization rate formulas $\widetilde{\Gamma}_\mathrm{SC}$ (III.20) and compare them to our exact numerical results Γ_TDSE on Figures III.5 and III.6. The results for the smaller molecule (Figure III.5) are quite similar to the ones obtained for the atom. The error made by the uncorrected rate (dotted purple line) increases with the field and becomes rapidly too large for quantitative applications. The corrected rate $\widetilde{\Gamma}_\mathrm{SC}$ is closer to the exact one, especially for high fields. In this case, the 2PT (solid orange line) and DPT (dashed pink line) corrections give similar results, which is consistent with the results of Figure III.4 (a).

However, in the case of the larger molecule shown on Figure III.6, the uncorrected formula (dotted purple line) fails to predict the right value of the rate. It is wrong by a factor of two for a field value corresponding to an intensity of $\simeq 5 \times 10^{13}$ W.cm^{-2} and the error is even larger at higher intensities. Besides, the corrected formula using 2PT (solid orange line) does not reduce the error at all. The only formula that predicts the right order of magnitude over a broad range of field values is the formula that uses the DPT correction (dashed pink line).

III.2.3 Heteronuclear diatomic molecules

We now turn to asymmetric molecules: we consider two different systems A_1 and A_2 with the same asymptotic behavior ($Z = 1$), internuclear length ($R = 2.2$ a.u.), ionization po-

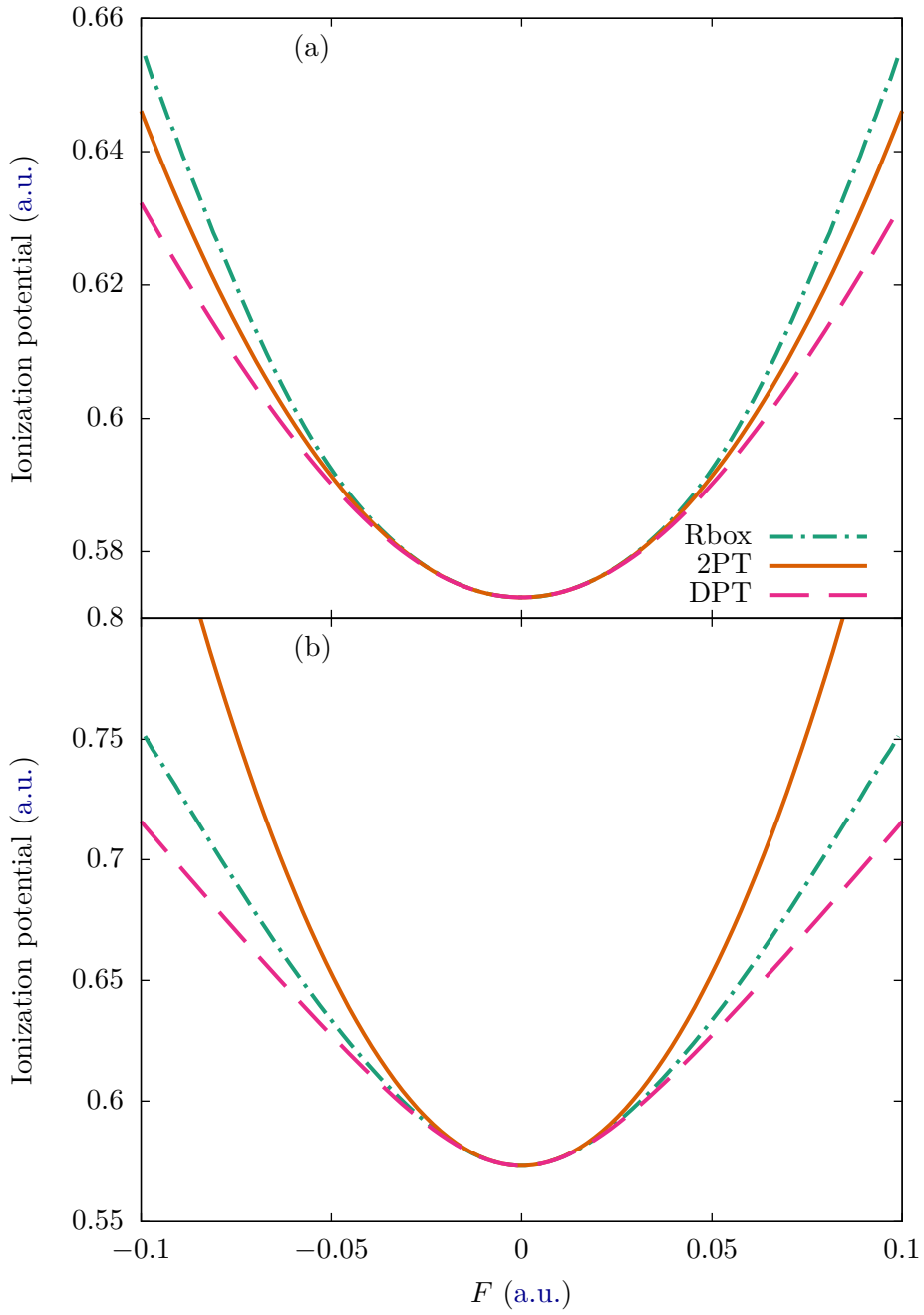

Figure III.4 *Stark shift of molecules S_1 on panel (a) and S_2 on panel (b) (section III.2.2). Corrected ionization potential as a function of the electric field: dash-dotted green line for numerical results, solid orange line for second order perturbation theory $\widetilde{I_p}^{2PT}$ (III.21) and dashed pink line for degenerate perturbation theory $\widetilde{I_p}^{DPT}$ (III.22).*

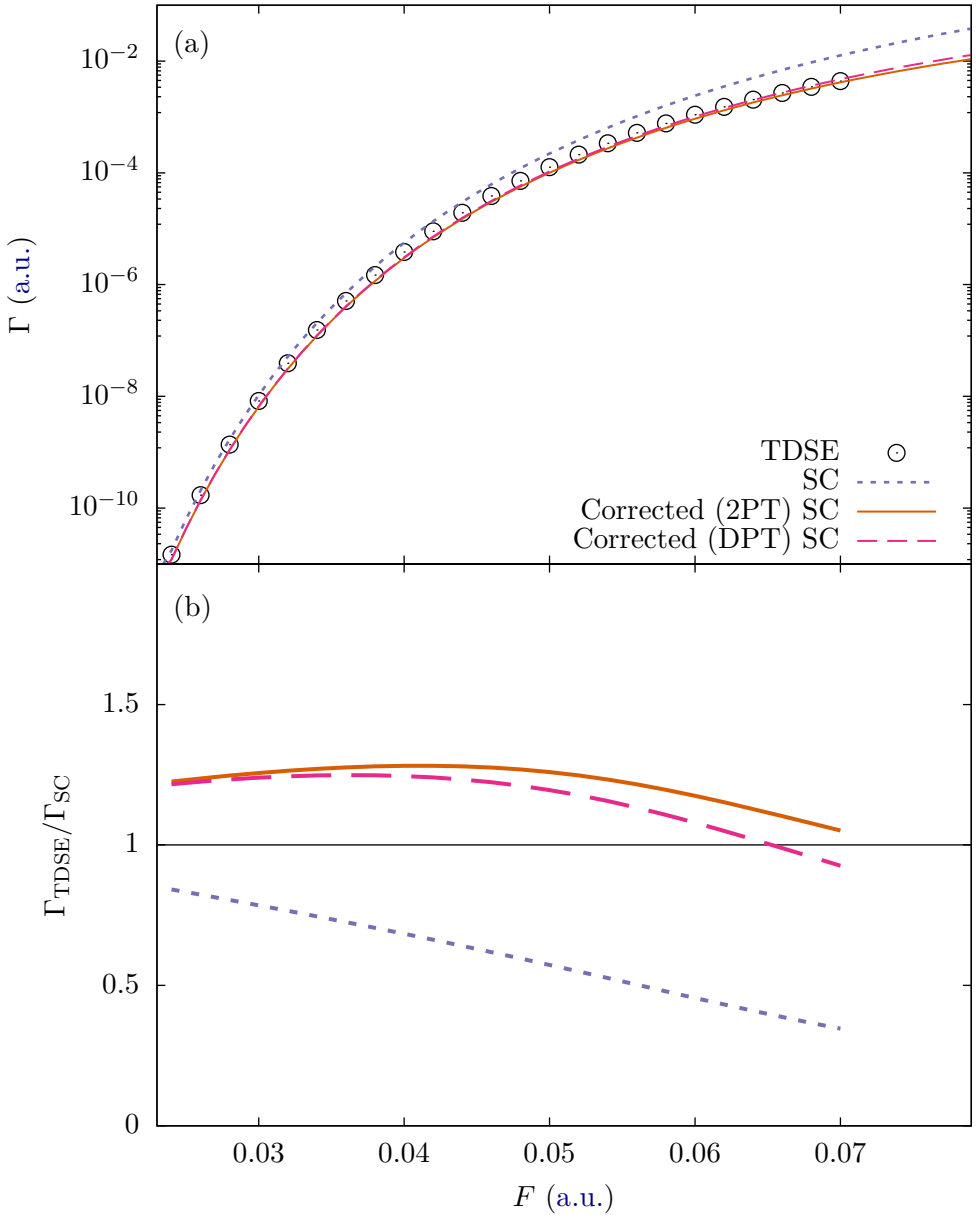

Figure III.5 *Tunnel ionization of molecules S_1 (section III.2.2). (a) Ionization rate as a function of the electric field : black circles for the reference value Γ_{TDSE}, dotted purple line for the SC analytical formula Γ_{SC} (III.1), dashed pink line for the modified SC formula $\widetilde{\Gamma}_{\mathrm{SC}}$ (III.20) corrected with the DPT approximation of $\widetilde{I_{\mathrm{p}}}$ and solid orange line for the same modified SC formula but with the 2PT approximation of $\widetilde{I_{\mathrm{p}}}$. (b) Ratio of the numerical to analytical ionization rates.*

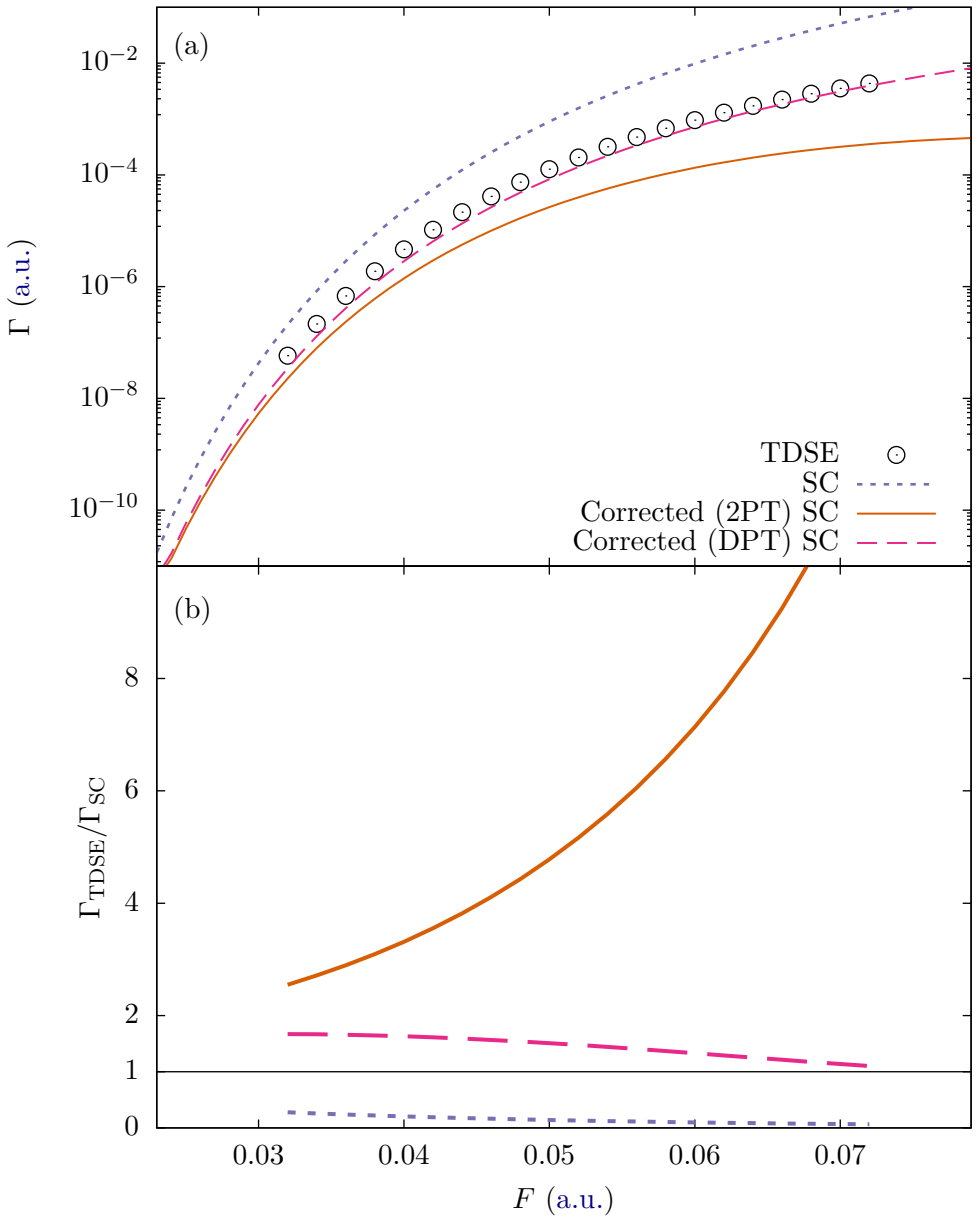

Figure III.6 *Same as in Figure III.5 for the molecule S_2.*

tential ($I_\mathrm{p} = 0.573$ a.u.) defined by two sets of parameters: $a_1 = 1.1$ a.u., $a_2 = 0.919$ a.u. for A_1, and $a_1 = 1.2$ a.u., $a_2 = 0.863$ a.u. for A_2. Those systems display an anisotropic electronic density in the ground state and mimic molecules with non-zero dipole moments μ. Thus, both the ionization rate and the Stark shift of these systems are anisotropic, and the 2PT expression of $\widetilde{I_\mathrm{p}}$ reads

$$\widetilde{I_\mathrm{p}} = I_\mathrm{p} + \underbrace{\mu F + \alpha F^2}_{\Delta I_\mathrm{p}}. \tag{III.23}$$

It was argued in [188] that when $|F| \to 0$ the asymptotic ionization rate includes only the first order in F, and that the second order should be neglected for consistency considerations. We thus want to quantify the accuracy improvement or depletion of the corrected rate by this second order. To this end, on Figure III.7, we compare the exact TDSE results to the three analytical rates, i.e. the uncorrected SC, the first order and the second order corrected rates. We see that for a negative field (lower panel) the first order correction does not significantly improve the accuracy of the SC rate. For a positive field (upper panel), the first order correction even tends to increase the error, whereas the second order correction systematically improves agreement with the numerical simulations. We checked that similar results hold for the A_2 system.

This shows that, even though including the second order Stark shift correction can be considered inconsistent in the $|F| \to 0$ limit [188], it is perfectly justified and even imperative in the case of a finite field $|F| > 0$.

To further investigate the anisotropy of the ionization and since the ionization direction is completely determined by the sign of the electric field, we compute, at different levels of approximation, the ratio Γ_-/Γ_+ where Γ_+ (Γ_-) is the rate in a positive (negative) field. From the uncorrected SC rate given in (III.1), we get

$$\frac{\Gamma_-}{\Gamma_+} = \frac{B_+}{B_-}. \tag{III.24}$$

and from the corrected rate $\widetilde{\Gamma}_\mathrm{SC}$, if we expand $(\widetilde{I_\mathrm{p}})^{3/2} = (I_\mathrm{p} + \mu F + \alpha F^2)^{3/2}$ in the exponential, we get

$$\frac{\widetilde{\Gamma}_-}{\widetilde{\Gamma}_+} = \frac{B_+}{B_-}\, \mathrm{e}^{4\mu\sqrt{2I_\mathrm{p}}}. \tag{III.25}$$

We see that we only need the first order Stark shift to compute the latter quantity. Indeed, the second order does not depend on the sign of F and gives the same contribution to the ionization rate whether the field is positive of negative. We also notice that there is only one contribution to the uncorrected ratio of (III.24): the electronic density favors the ionization in the direction of its maximum. This is rather intuitive since we expect a higher probability for the electron to leave the core in the direction where there is an excess of electronic density. However, in the corrected ratio of (III.25), there is an opposite contribution: the permanent dipole moment enhances in general the ionization in the direction of the electronic density's minimum. This is illustrated on Figure III.8 for molecules with a negative dipole moment (i.e. $\mathrm{e}^{4\mu\sqrt{2I_\mathrm{p}}} < 1$) and an excess of density in the $x > 0$ region of space (i.e. $B_+/B_- > 1$) as is the case for A_1 and A_2.

To determine which one is the prevailing contribution, we plot the exact and analytical Γ_-/Γ_+ ratios on Figure III.9. For both systems the ratio is below 1, which

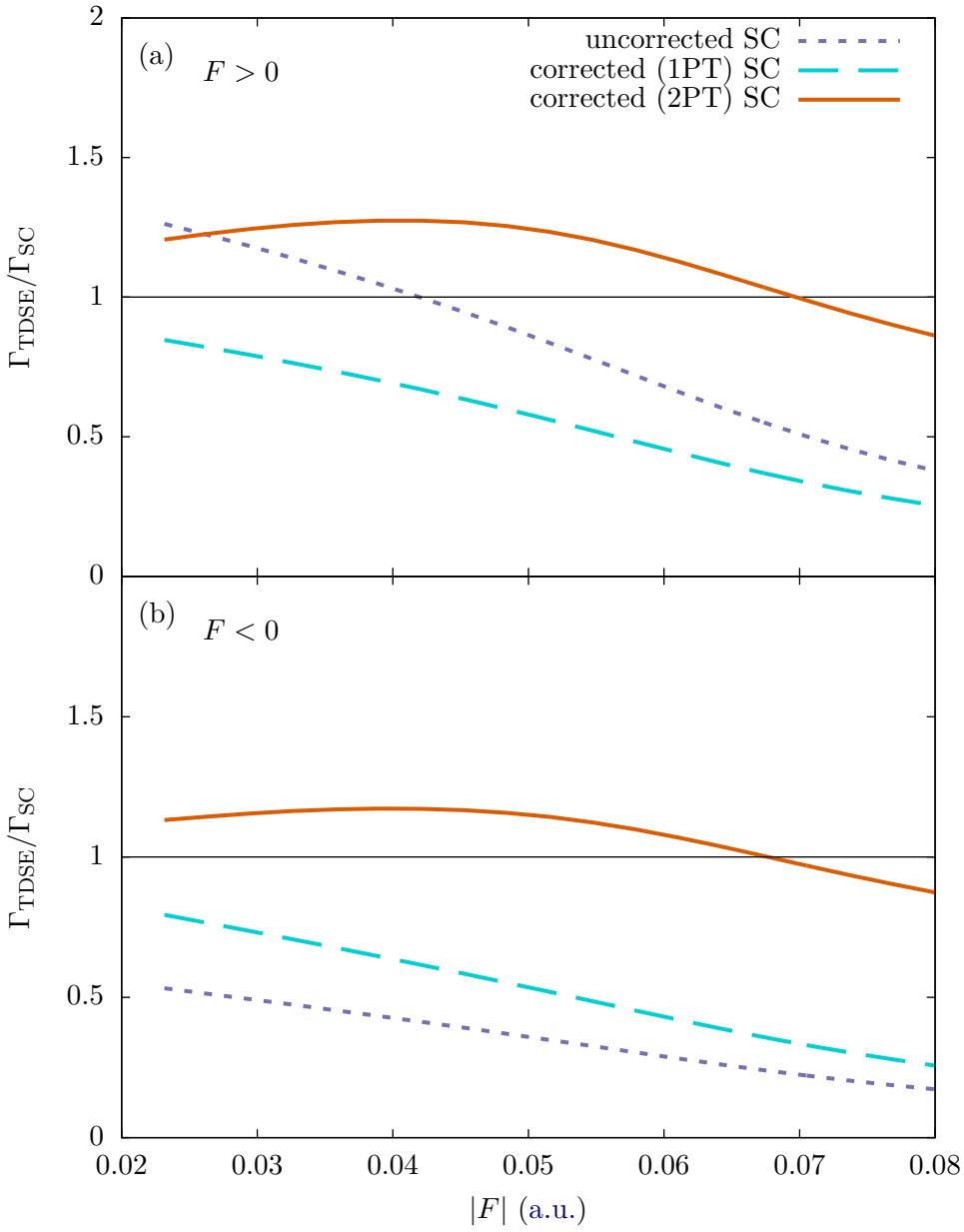

Figure III.7 *Ionization rate of the polar molecule A_1 (section III.2.3): dotted purple line for the ratio of the TDSE to the uncorrected SC rate, dashed turquoise line for the ratio of the TDSE to the first order corrected rate and solid orange line for the ratio of the TDSE to the second order corrected rate. (a) positive electric field, (b) negative electric field.*

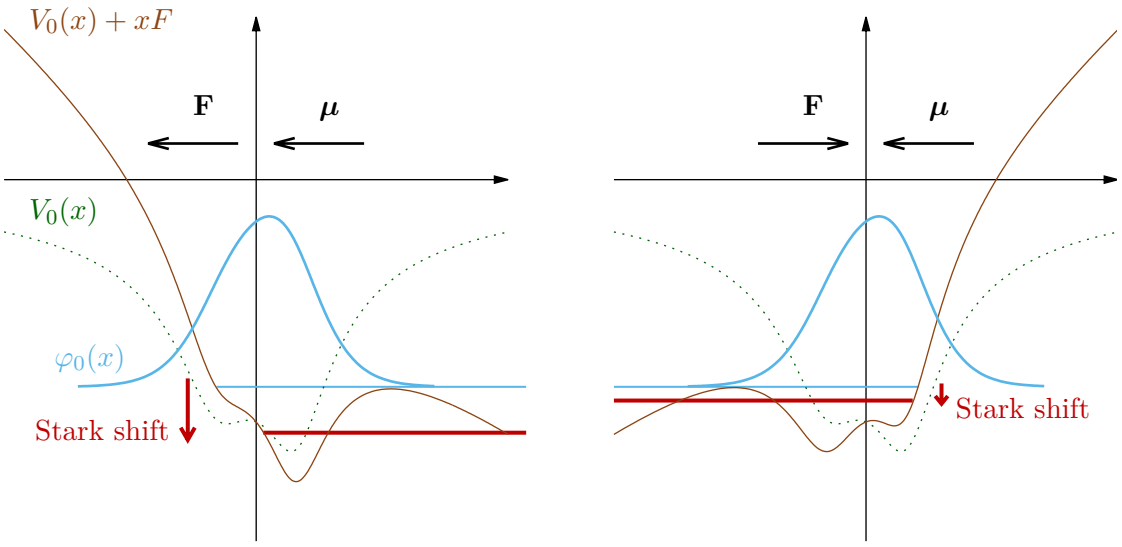

Figure III.8 *Schematic view of the tunnel ionization of asymmetric molecules: dotted black line for the atomic potential, solid black line for the perturbed potential in the presence of an electric field F, and dashed blue line for the electronic density of the atomic ground state. The horizontal thin black line denotes the ground state energy, and the horizontal thick red line the shifted energy in the presence of the field. The electron sees a thinner and lower potential barrier when the field is antiparallel to the dipole moment (right hand side), it will therefore escape more easily into the continuum.*

indicates that tunnel ionization is enhanced in the direction of the electronic density's *minimum*. This rather counter-intuitive result shows that the Stark shift anisotropy ultimately controls the anisotropy of the ionization. This also reveals that the uncorrected ratio predicts a completely unphysical behavior, and that the Stark shift correction is mandatory in this case even to get *qualitative* results. These results are consistent with the works of [197, 167, 198, 196].

III.3 Error analysis

In the previous section we have seen that while the Stark shift correction can improve the accuracy of the analytical rate, discrepancies with *exact* TDSE results remain. In order to identify the origin of the error, we analyze all the approximations that are made to establish the ionization rate by gradually introducing them in approximate evaluations of the ionization rate. Then we analyze the error resulting from each of these approximations to determine which one of our hypothesis is not fulfilled.

The first approximation we use is the semi-classical approximation (III.5) in the regions of space *inside* the potential barrier and "far" from the atomic core. It is justified as long as the spatial variations of the De Broglie wavelength of the electron are small [132],

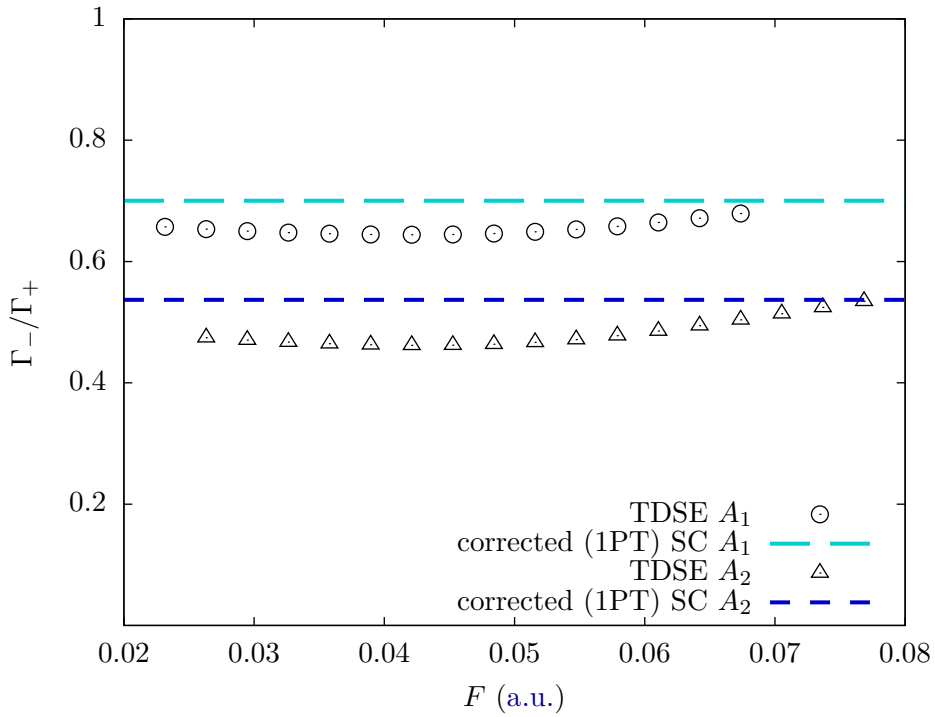

Figure III.9 *Ionization rate of polar molecular systems. The exact TDSE ratio Γ_-/Γ_+ is denoted by empty black circles for A_1 and by empty black triangles for A_2; the corrected analytical ratio given in (III.25) is denoted by a long-dashed turquoise line for A_1 and by a short-dashed dark-blue line for A_2, the uncorrected ratio given in (III.24) is larger than 1.*

which can be written as

$$\frac{1}{|p|^2}\left|\frac{\mathrm{d}p}{\mathrm{d}x}\right| \ll 1. \tag{III.26}$$

If we use only this approximation, we find the following expression for the ionization rate:

$$\Gamma_1 = |\psi(x_0)|^2 |p(x_0)| \exp\left(-2\int_{x_1}^{x_0} |p(x)|\mathrm{d}x\right), \tag{III.27}$$

To evaluate the validity of the hypothesis (III.26), the quantity Γ_1 is computed numerically in the case of the atomic system of section III.2.1. For this, the exact wave function $\psi(x_0)$ dressed by the field is computed numerically (e.g. by inverse iteration [137] or Runge-Kutta propagation), and then normalized by

$$\int_{x_1}^{+\infty} |\psi(x)|^2 \mathrm{d}x = 1. \tag{III.28}$$

This choice of normalization is consistent with the way LL and SC build their approximate wave function [132, 184]. Note that it is also consistent with the approximation in equation (36) of [185]. The numerical Γ_1 is shown as red connected triangles on Figure III.10 for a field $F = 2.5 \times 10^{-2}$ a.u., which corresponds to an intensity of 2.2×10^{13} W.cm^{-2}. In

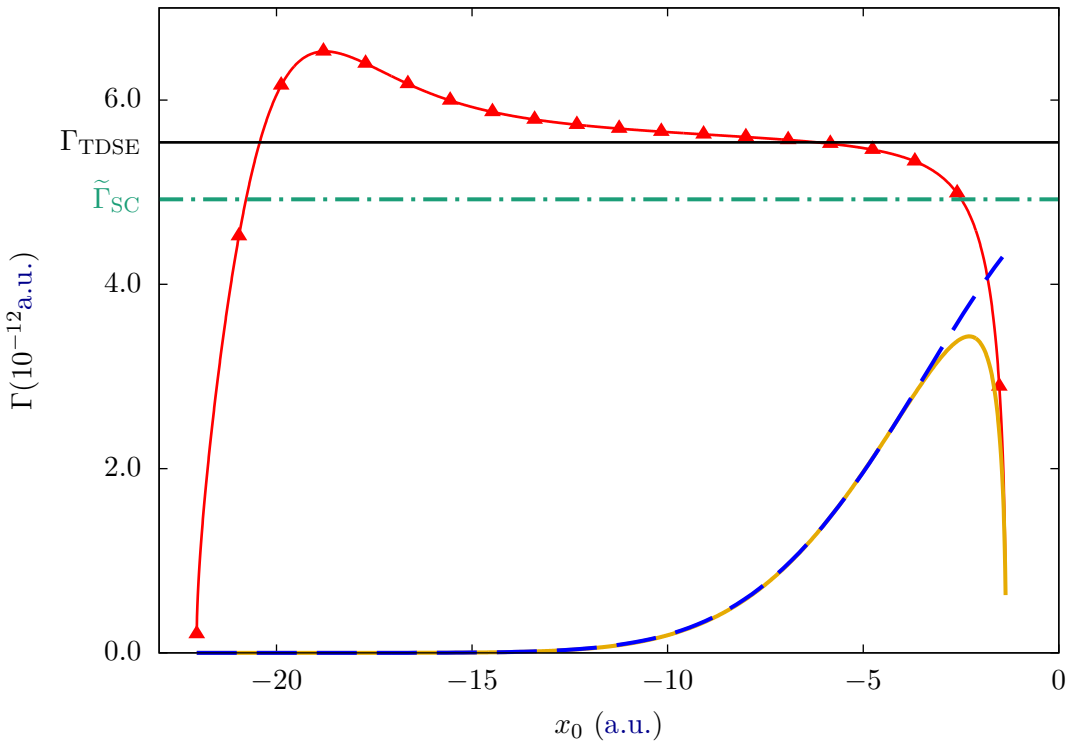

Figure III.10 *Ionization rate as a function of x_0 (see text) for an electric field $F = 2.5 \times 10^{-2}$ a.u.. Red connected triangles : Γ_1 given in (III.27). Solid yellow line : Γ_2 given in (III.29). Dashed blue line : Γ_3 (III.30). Dash-dotted green line : $\widetilde{\Gamma}_{\mathrm{SC}}$ given in (III.1). Horizontal black line: exact value obtained in TDSE simulations.*

these conditions $x_1 = -22.05$ a.u.. We see that if we choose x_0 in the range between 5 and 15 a.u., then the semi-classical approximation gives results close to the TDSE rate. Also, the rate Γ_1 is almost independent of the choice of the arbitrary parameter x_0, which is consistent with the fact that the ionization rate should not depend on x_0 at all. Remark that a different choice of normalization for ψ would only scale Γ_1 by a constant factor which would still be independent of the arbitrary parameter x_0.

The second hypothesis is that there exists an interval $\mathcal{I}$ *inside* the barrier where the wave function ψ can be approximated by the ground state φ_0 of the *unperturbed* atomic potential. According to [132, 184], this is justified if the interaction with the electric field is very small i.e. $|x_0 F| \ll I_{\mathrm{p}}$ for $x_0 \in \mathcal{I}$. By replacing the exact wave function $\psi(x_0)$ by $\varphi_0(x_0)$ in the expression of Γ_1 (III.27), we obtain the rate Γ_2:

$$\Gamma_2 = |\varphi_0(x_0)|^2 \, |p(x_0)| \exp\left(-2\int_{x_1}^{x_0} |p(x')| \, \mathrm{d}x'\right), \tag{III.29}$$

which corresponds to the expression (III.9) given in section III.1. We plotted Γ_2 as a solid yellow line in Figure III.10. We immediately see the huge difference between Γ_1 and Γ_2. First Γ_2 departs from Γ_1 and from the TDSE results, which indicates that the

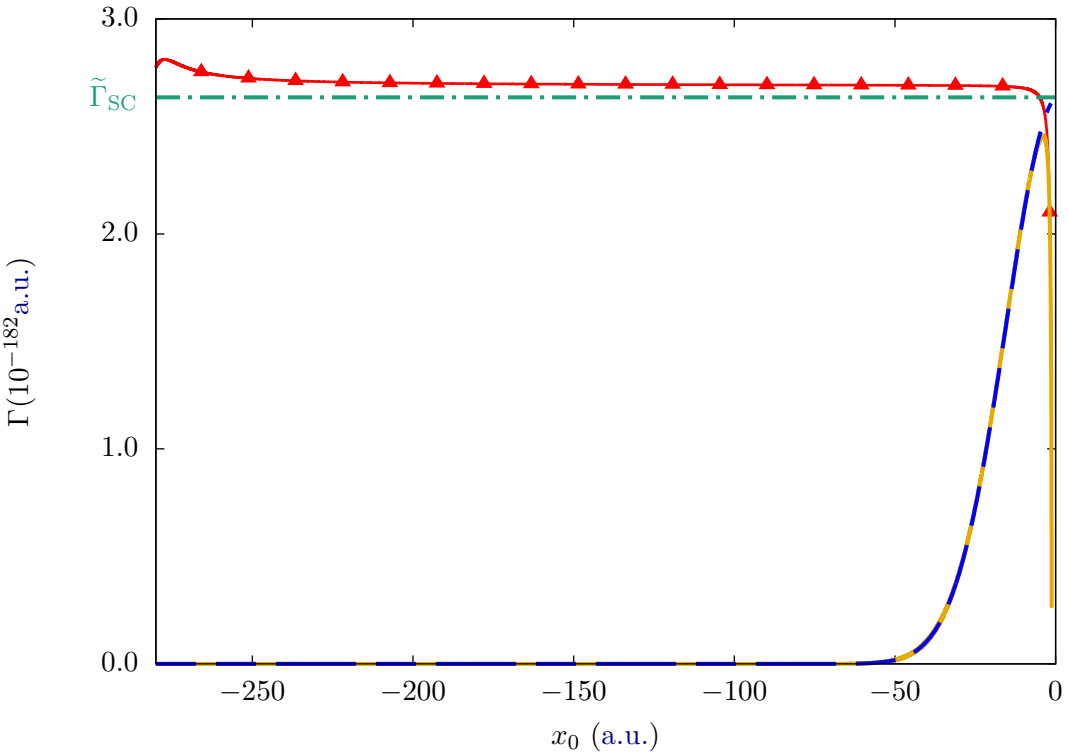

Figure III.11 *Same as in Figure III.10 for an electric field of* $F = 2 \times 10^{-3}$ a.u.. *The TDSE value is not displayed because it lies below the numerical accuracy of the simulation.*

approximation $\psi(x_0) \simeq \varphi(x_0)$ is not justified, whichever value of x_0 we choose. Moreover Γ_2 strongly depends on the unphysical parameter x_0, which is not satisfactory.

The third hypothesis is that $|x_0|$ is very large, such that $|V_0(x_0)| \ll I_\mathrm{p}$. This allows to use the asymptotic form of the atomic ground state (III.2). It also allows to neglect $V_0(x_0)$ in the expression of $|p(x_0)|$, and to expand $p(x)$ in powers of $V_0(x)/(xF + \widetilde{I_\mathrm{p}})$ as we did in (III.11). We insert all this in (III.9) to get

$$\Gamma_3 = |\psi(x_0)|^2 \sqrt{2\widetilde{I_\mathrm{p}}(1+\eta)}\, \mathrm{e}^{-2\mathcal{K}}, \tag{III.30}$$

where

$$\mathcal{K} = \frac{(2\widetilde{I_\mathrm{p}})^{\frac{3}{2}}}{3F}(1+\eta)^{\frac{3}{2}} - \frac{Z}{\sqrt{2\widetilde{I_\mathrm{p}}}} \ln\left(\frac{1+\sqrt{1+\eta}}{1-\sqrt{1+\eta}}\right), \tag{III.31}$$

and where η is defined in (III.12). This is shown as a dashed blue line in Figure III.10. We see that, as long as $x_0 > 4$ a.u., there is almost no difference between Γ_3 and Γ_2, which indicates that the hypothesis $|V_0(x_0)| \ll I_\mathrm{p}$ is justified.

Finally, the last approximation uses again $|x_0 F| \ll I_\mathrm{p}$ i.e. $\eta \ll 1$ to make the expansion (III.13) and to neglect $x_0 F$ in $|p(x_0)|$. This last step gives the $\widetilde{\Gamma}_{\mathrm{SC}}$ formula of (III.20), which is plotted with a dash-dotted green line in Figure III.10. We observe a dramatic difference between $\widetilde{\Gamma}_{\mathrm{SC}}$ and Γ_3, which indicates that, again, the condition $|x_0 F| \ll I_\mathrm{p}$ is

not fulfilled, whichever value of x_0 we consider, for a field of 2.5×10^{-2} a.u.. However it is remarkable that the error made by this last approximation almost perfectly compensates the error made by the approximation $\psi(x_0) \simeq \varphi(x_0)$ so that the SC formula eventually gives results relatively close to the *exact* TDSE computations.

We did the same analysis for a much weaker field value $F = 2 \times 10^{-3}$ a.u., which corresponds to an intensity of 1.4×10^{11} W.cm^{-2}. In these conditions $x_1 = -295.23$ a.u.. As can be seen in Figure III.11, at this field value the ionization rate is of the order of magnitude 10^{-182} a.u. which drastically highlights the extreme non-linearity of the process. It is well below any practical application, and obviously below the numerical accuracy of TDSE simulations, which is why we have no reference TDSE value for this value of F. Nevertheless, this academic case constitutes a severe test of the approximations relying on the weak influence of the external field on the electron at the position x_0. We find that the conclusions concerning the relative roles of the approximations are exactly the same as the ones obtained with $F = 2.5 \times 10^{-2}$ a.u.. Indeed, we see in Figure III.11 that the two rates Γ_1 and Γ_2 are very different from one another, and that Γ_2 still exhibits a strong x_0 dependency. Therefore the approximation that there exists a point x_0 that is at the same time very large, i.e. $|V_0(x_0)| \ll I_\mathrm{p}$, and very small, i.e. $|x_0 F| \ll I_\mathrm{p}$, is never justified, even for a field value as small as $F = 2 \times 10^{-3}$ a.u..

Indeed, for these two condition to be fulfilled at the same time, the electric field has to be much smaller than the condition one often finds in the literature [184, 174]:

$$F \ll (2I_\mathrm{p})^{3/2}. \tag{III.32}$$

For example in the case of hydrogen ($I_\mathrm{p} = 0.5$ a.u.), $(2I_\mathrm{p})^{3/2} = 1$ a.u. and the inequality (III.32) is fulfilled for the two field values used in Figure III.10 and Figure III.11. However, the expansion in (III.13) is, in this case, justified if

$$\mathrm{e}^{-\frac{2}{3F}(1-2|x_0|F)^{3/2}} \simeq \mathrm{e}^{-\frac{2}{3F}}\,\mathrm{e}^{2|x_0|}, \tag{III.33}$$

which will hold if the third term of the expansion is negligible, i.e.

$$\mathrm{e}^{-2|x_0|^2 F} \simeq 1. \tag{III.34}$$

As we have $|x_0| \gg 1$, we actually need $F \leq 10^{-4}$ a.u. for (III.34) to be true. This means that the hypotheses of the Landau and SC derivation are verified if the intensity is below 10^8 W.cm^{-2}, which corresponds to a meaningless tunnel ionization rate of about $\Gamma \lesssim 10^{-2891}$! However, once again, thanks to the error compensation evidenced with the stronger field as well as with the weaker one (see Figure III.10 and III.11), the Landau rate gives semi-quantitative results for intensities up to $10^{12} - 10^{13}$ W.cm^{-2}. The use of this formula for finite values of the electric field has therefore more empirical than theoretical foundations.

III.4 Conclusion

We computed the tunnel ionization rate in a static electric field for different symmetric systems using both the standard analytical formulas and *exact* numerical solution of the TDSE. By comparing the two approaches we found that the standard rate derived by

Smirnov and Chibisov [184] only yields qualitative trends in the best cases. We demonstrated that we can correct this formula by taking into account the Stark shift, and derived a consistent formula where the Stark shift correction only appears in the argument of the dominant exponential term. We tested this formula for model systems with different physical properties and showed that the correction systematically improves the accuracy of the ionization rate. We proved that if the energy gap between the two first bound states remains big enough compared to the Stark shift, then second order perturbation theory is sufficient to compute the Stark shift, implying that one only needs to know the permanent dipole moment and polarizability of the system under study. However, we showed that for highly polarizable systems, second order perturbation theory is a very poor approximation of the Stark shift and therefore a very bad correction of the ionization rate. In these cases, one has to consider degenerate perturbation theory. Furthermore we showed that for polar systems the Stark shift is the dominant contribution to the anisotropy of the ionization. It is therefore a central effect to take into account even for a qualitative description of tunnel ionization in molecules.

Finally, the main conclusion of this work is that the hypotheses used for the Landau derivation of the tunnel ionization rate are unjustified at working intensities to model quantitatively atoms and molecules interacting with strong laser fields. We showed that the accuracy of the Landau formula is difficult to predict since it originates from the compensation of different approximations. Consequently, all the dynamical formulas that are based on this static rate (ADK), or asymptotically equal to it in the limit of a zero frequency electric field (e.g. the rate derived by PPT [174]), should be handled with care when used for quantitative applications, even though they are very practical.

Chapter IV

Two-center interferences in high order harmonic generation

We saw that HHG has two aspects that give rise to very different types of experiments: it can be used either as a light source, or as a self-probe spectroscopic tool. In this chapter we concentrate on the latter, i.e. how we can extract information about the emitting system from the HHG spectrum. In particular, we consider homonuclear diatomic molecules. For such systems, we have seen in Chapter I.3 that the third and last step of the HHG process, namely the recombination step, may occur at any one of the two nuclei. The two centers of the molecule can therefore be seen as two coherent point sources. Exactly like Young's two slits, they can interfere constructively or destructively depending on the frequency of the emitted harmonic, and on the distance between the two centers. These interferences encode the structure of the molecule, and more precisely the structure of the orbitals that participate to the HHG process [200, 128, 201, 202].

Obviously, to efficiently retrieve this structural information from the HHG spectrum, we need accurate theoretical models. This remains a challenge since the direct solution of the TDSE is numerically too costly for such systems, so that SFA models are in general used to explain and interpret interference features in molecules. We have seen in Chapter I.3 that in the SFA framework the HHG spectrum is directly proportional to the recombination dipole. This quantity contains a lot of information on the emitting system. In particular for diatomic molecules it exhibits a zero at a particular energy which depends on the internuclear distance. This zero is a manifestation of the destructive two-center interference, and directly appears as a minimum in the HHG spectrum together with a jump of $\pm\pi$ of the harmonics phase. With the recent advances that allow to *align* an ensemble of molecules, this minimum has been experimentally observed in several systems such as CO_2 [203–208], N_2O [99, 209] and N_2 [210].

Although the standard version of the SFA that we have derived in section I.3.3 is able to predict such a minimum and phase jump, it has several drawbacks. As we will see in the following, because of the plane wave approximation, the position of this minimum is in agreement neither with experiments nor with direct solutions of the TDSE. More importantly the standard SFA predicts a peaked minimum along with a very sharp phase jump, whereas in experiments [204, 205, 99, 209] and in TDSE simulations [211, 200, 212], the minimum and the phase jump are smoothed over several harmonics. This smoothing

was attributed to a dressing of the ionized orbital by the instantaneous electric field [213–215].

To overcome the limitations of the atomic model, Chirilă and Lein [84] developed a new approach, called molecular SFA which incorporate the molecular structure, within the LCAO approximation, into the search of saddle points (as we have seen in section I.3.3 d)). This model was then intensively investigated by Figueira de Morisson Faria [128] who focused on the position and shape of the minimum, and by François Risoud during his PhD in our group (2013-2016) [129, 157] who also considered the position and shape of the phase jump for 1D systems considered as aligned molecules. We also derived a comprehensive analytical model by expanding the molecular SFA close to the *atomic* solution. This expansion allowed to give a direct interpretation of the smoothing of the phase jump, and to give precise conditions to observe a sharp jump: when the recombination time of the harmonic corresponding to the jump coincides with a zero of the laser electric field. However, this derivation was incomplete since the saddle point prefactor expression (see (I.109)) was not obtained, so that discrepancies between the expansion and the total molecular SFA remained. The sharp jump was actually observed for a recombination corresponding to a small but non zero value of the field. Besides, the derivation was only performed for molecules aligned in the direction of the field polarization.

In this work we complete the analytical work performed by François Risoud [129], and find the expression of the "ζ constant" which was mentioned in [157]. We also extend the study to two dimensional systems. In particular we investigate the influence of the orientation of the molecule with respect to the field, and we question the commonly accepted idea that the 2-center interference only depends on the orientation through a $\cos\theta$ factor. Finally we search for the origin of the observed discrepancies in the prediction of the minimum position. To this end, we compare the accuracy of the PWA and of the LCAO approximation, and we test the accuracy of the I_p correction that was proposed to improve the PWA.

Objectives

- Complete the analytical work of François Risoud: define without ambiguity the parameter of the expansion and find the expression of the prefactor.
- Investigate the effect of the orientation of the molecule with respect to the field.
- Find the limiting approximations at the origin of the discrepancies.

IV.1 Analytic expansion of the molecular SFA

We first derive the important expressions in sections IV.1.1 and IV.1.2 and then discuss these results in section IV.1.3.

IV.1.1 Molecular saddle point equations

We recall here the molecular saddle point equations as obtained in section I.3.3 d):

$$\int_{t'}^{t} [\mathbf{p} + \mathbf{A}_\mathrm{L}(\tau)]\,\mathrm{d}\tau + \left[(-1)^\alpha - (-1)^\beta\right] \frac{\mathbf{R}}{2} = 0 \tag{IV.1a}$$

$$\frac{[\mathbf{p} + \mathbf{A}_\mathrm{L}(t)]^2}{2} + I_\mathrm{p} - \omega + (-1)^\beta \mathbf{F}_\mathrm{L}(t) \cdot \frac{\mathbf{R}}{2} = 0 \tag{IV.1b}$$

$$\frac{[\mathbf{p} + \mathbf{A}_\mathrm{L}(t')]^2}{2} + I_\mathrm{p} + (-1)^\alpha \mathbf{F}_\mathrm{L}(t') \cdot \frac{\mathbf{R}}{2} = 0 \tag{IV.1c}$$

where $\mathbf{p}$ is the electron momentum, t the recombination time, t' the ionization time, $\mathbf{A}_\mathrm{L}$ the vector potential of the laser, and α, β label the nuclei of the molecule at which the electron is ionized and recombines, respectively.

We note that these equations are actually very similar to the *atomic* saddle point equations (I.104), but with additional terms that are proportional to $\mathbf{R}$. If we consider that these terms only induce a small perturbation to the original saddle point equations, we may actually expand the *solutions* of these equations in powers of $\mathbf{R}$. We assume that the field is polarized along the x axis, and that $\mathbf{R}$ belongs to the xy plane, with components R_x and R_y. We can thus rewrite the system of equations as

$$\int_{t'}^{t} [p_x + A_\mathrm{L}(\tau)]\,\mathrm{d}\tau + \left[(-1)^\alpha - (-1)^\beta\right] \frac{R_x}{2} = 0 \tag{IV.2a}$$

$$p_y(t - t') + \left[(-1)^\alpha - (-1)^\beta\right] \frac{R_y}{2} = 0 \tag{IV.2b}$$

$$p_z(t - t') = 0 \tag{IV.2c}$$

$$\frac{[\mathbf{p} + \mathbf{A}_\mathrm{L}(t)]^2}{2} + I_\mathrm{p} - \omega + (-1)^\beta F_\mathrm{L}(t) \frac{R_x}{2} = 0 \tag{IV.2d}$$

$$\frac{[\mathbf{p} + \mathbf{A}_\mathrm{L}(t')]^2}{2} + I_\mathrm{p} + (-1)^\alpha F_\mathrm{L}(t') \frac{R_x}{2} = 0 \tag{IV.2e}$$

and expand its solutions in powers of $\mathbf{R}$:

$$p^x_{\alpha\beta} = p_\mathrm{at} + R_x \partial_x p^x_{\alpha\beta} + R_y \partial_y p^x_{\alpha\beta} + O(R^2) \tag{IV.3a}$$

$$p^y_{\alpha\beta} = R_x \partial_x p^y_{\alpha\beta} + R_y \partial_y p^y_{\alpha\beta} + O(R^2) \tag{IV.3b}$$

$$t_{\alpha\beta} = t_\mathrm{at} + R_x \partial_x t_{\alpha\beta} + R_y \partial_y t_{\alpha\beta} + O(R^2) \tag{IV.3c}$$

$$t'_{\alpha\beta} = t'_\mathrm{at} + R_x \partial_x t'_{\alpha\beta} + R_y \partial_y t'_{\alpha\beta} + O(R^2) \tag{IV.3d}$$

where we noted ∂_i the partial derivatives with respect to R_i *taken at* $\mathbf{R} = 0$, and where we used the subscript "at" to denote the solutions of the *atomic* saddle point equations, i.e. where $\mathbf{R} = 0$. Note that these equations have no solution verifying $t = t'$, so that we always have $p^z_{\alpha\beta} = 0$. In the atomic case, we also have $p^y_{at} = 0$, i.e. the stationary momentum $\mathbf{p}_\mathrm{at}$ is parallel to the field polarization direction x. When we put this first order expansion in the saddle point equations (IV.3), we obtain a linear set of equations

for the first order derivatives :

$$0 = [p_{\rm at} + A_{\rm L}(t_{\rm at})]\,\partial_x t_{\alpha\beta} - [p_{\rm at} + A_{\rm L}(t'_{\rm at})]\,\partial_x t'_{\alpha\beta} + (t_{\rm at} - t'_{\rm at})\partial_x p^x_{\alpha\beta} + \frac{(-1)^\alpha - (-1)^\beta}{2} \tag{IV.4a}$$

$$0 = -[p_{\rm at} + A_{\rm L}(t_{\rm at})]\,F_{\rm L}(t_{\rm at})\partial_x t_{\alpha\beta} + [p_{\rm at} + A_{\rm L}(t_{\rm at})]\,\partial_x p^x_{\alpha\beta} + \frac{(-1)^\beta}{2}F_{\rm L}(t_{\rm at}) \tag{IV.4b}$$

$$0 = -[p_{\rm at} + A_{\rm L}(t'_{\rm at})]\,F_{\rm L}(t'_{\rm at})\partial_x t'_{\alpha\beta} + [p_{\rm at} + A_{\rm L}(t'_{\rm at})]\,\partial_x p^x_{\alpha\beta} + \frac{(-1)^\alpha}{2}F_{\rm L}(t'_{\rm at}) \tag{IV.4c}$$

$$0 = [p_{\rm at} + A_{\rm L}(t_{\rm at})]\,\partial_y t_{\alpha\beta} - [p_{\rm at} + A_{\rm L}(t'_{\rm at})]\,\partial_y t'_{\alpha\beta} + (t_{\rm at} - t'_{\rm at})\partial_y p^x_{\alpha\beta} \tag{IV.4d}$$

$$0 = -[p_{\rm at} + A_{\rm L}(t_{\rm at})]\,F_{\rm L}(t_{\rm at})\partial_y t_{\alpha\beta} + [p_{\rm at} + A_{\rm L}(t_{\rm at})]\,\partial_y p^x_{\alpha\beta} \tag{IV.4e}$$

$$0 = -[p_{\rm at} + A_{\rm L}(t'_{\rm at})]\,F_{\rm L}(t'_{\rm at})\partial_y t'_{\alpha\beta} + [p_{\rm at} + A_{\rm L}(t'_{\rm at})]\,\partial_y p^x_{\alpha\beta} \tag{IV.4f}$$

$$0 = (t_{\rm at} - t'_{\rm at})\partial_x p^y_{\alpha\beta} \tag{IV.4g}$$

$$0 = (t_{\rm at} - t'_{\rm at})\partial_y p^y_{\alpha\beta} + \frac{(-1)^\alpha - (-1)^\beta}{2} \tag{IV.4h}$$

From (IV.4g) we directly find that $\partial_x p^y_{\alpha\beta} = 0$, and from (IV.4h) we have:

$$\partial_y p^y_{\alpha\beta} = \frac{(-1)^\beta - (-1)^\alpha}{2(t_{\rm at} - t'_{\rm at})}, \tag{IV.5}$$

which leads to the final first order expression of the y component of the stationary momentum:

$$\boxed{p^y_{\alpha\beta} = \frac{(-1)^\beta - (-1)^\alpha}{2(t_{\rm at} - t'_{\rm at})} R_y} \tag{IV.6}$$

We conclude that, at first order, the trajectories where the electron is ionized at one center and recombines with the *same* center have a stationary momentum with a zero y component. This is actually quite intuitive since such trajectories behave similarly to the *atomic* ones. On the contrary, for the trajectories where the electron is ionized at one center and recombines with the *other* center, which are specific of the molecular case, the stationary momentum has a non zero y component.

From (IV.4a), (IV.4b), and (IV.4c), we get

$$\Big[F_{\rm L}(t'_{\rm at})\,[p_{\rm at} + A_{\rm L}(t_{\rm at})] - F_{\rm L}(t_{\rm at})\,[p_{\rm at} + A_{\rm L}(t'_{\rm at})] + F_{\rm L}(t_{\rm at})F_{\rm L}(t'_{\rm at})(t_{\rm at} - t'_{\rm at})\Big]\partial_x p^x_{\alpha\beta} = 0. \tag{IV.7}$$

We thus find that $\partial_x p^x_{\alpha\beta} = 0$ is *one* solution of the system of equations. It will be the *only* solution if

$$\Delta = F_{\rm L}(t'_{\rm at})\,[p_{\rm at} + A_{\rm L}(t_{\rm at})] - F_{\rm L}(t_{\rm at})\,[p_{\rm at} + A_{\rm L}(t'_{\rm at})] + F_{\rm L}(t_{\rm at})F_{\rm L}(t'_{\rm at})(t_{\rm at} - t'_{\rm at}) \neq 0. \tag{IV.8}$$

This term Δ is simply the determinant of the subsystem of equations (IV.4a,IV.4b,IV.4c). We checked numerically that it indeed does not vanish. From (IV.4d), (IV.4e), and (IV.4f), we obtain exactly the same equation for $\partial_y p^x_{\alpha\beta}$. We thus find that the x component of

the stationary moment is equal to the *atomic* one at first order:

$$p^x_{\alpha\beta} = p_{\rm at} \tag{IV.9}$$

By inserting this in (IV.4b), (IV.4c), (IV.4e) and (IV.4f) we easily find the first order expression of $t_{\alpha\beta}$ and $t'_{\alpha\beta}$:

$$t_{\alpha\beta} = t_{\rm at} + \frac{(-1)^\beta R_x}{2\left[p_{\rm at} + A_{\rm L}(t_{\rm at})\right]} \tag{IV.10}$$

$$t'_{\alpha\beta} = t'_{\rm at} + \frac{(-1)^\alpha R_x}{2\left[p_{\rm at} + A_{\rm L}(t'_{\rm at})\right]} \tag{IV.11}$$

These two expressions have a clear physical interpretation, as was pointed out in [129]. They indicate that the molecular ionization and recombination times comprise an additional *delay* compared to their atomic equivalent. This delay is equal to the time it takes for the electron to travel half the molecule size, which corresponds to the distance between the center of mass of the molecule and the nucleus at which the electron is ionized or at which it recombines. Note that since $\left[p_{\rm at} + A_{\rm L}(t_{\rm at})\right]^2 > 0$, this molecular recombination time delay is real, while since $\left[p_{\rm at} + A_{\rm L}(t'_{\rm at})\right]^2 < 0$, the molecular ionization time delay is purely imaginary. This is related to the fact that tunnel ionization has no classical equivalent.

We want to insist here on an issue that was not mentioned in [129]: these molecular time delays should only appear for trajectories where the electron is ionized at one center and recombines with the *other* center. For the *atomic*-like trajectories, that start at one center and end at the same center, we should not see any difference with the atomic case. Indeed, the effect of the molecular potential is neglected as soon as the electron is ionized, so that these trajectories should behave exactly like the atomic ones. This inconsistency is a direct consequence of the fact that the SFA framework is not *translationally invariant*. As was pointed out in [128], this can be tackled in the atomic case by choosing the origin at the position of the nucleus. However this cannot be done for both nuclei at the same time in the molecular case, hence this incoherence.

IV.1.2 HHG spectrum

In the molecular SFA model (see section I.3.3 d)) the HHG spectrum is proportional to the average value of the dipole which is given by

$$\widetilde{\mathbf{D}}_{\alpha,\beta}(\omega) = \sum_{\alpha,\beta=1}^{2} C_{\alpha,\beta}(t_{\alpha\beta}, t'_{\alpha\beta})\mathbf{L}\Big(\mathbf{p}_{\alpha\beta} + \mathbf{A}_{\rm L}(t_{\alpha\beta})\Big) M_\alpha\Big(\mathbf{p}_{\alpha\beta} + \mathbf{A}_{\rm L}(t'_{\alpha\beta}), t'_{\alpha\beta}\Big)\, \mathrm{e}^{-\mathrm{i}S_{\alpha,\beta}}, \tag{IV.12}$$

where $S_{\alpha,\beta}$ is the modified action defined in (I.119), M_α is the molecular ionization dipole defined in (I.113), $\mathbf{L}$ is the molecular recombination dipole (I.115) and $C_{\alpha,\beta}$ is the molecular prefactor defined in (I.109). To get the first order expansion of the dipole expression, we first expand separately $S_{\alpha,\beta}$, M_α, $\mathbf{L}$ and $C_{\alpha,\beta}$.

a) Semi-classical action

The modified semi classical action reads

$$\begin{aligned} S_{\alpha,\beta}(\mathbf{p}_{\alpha\beta}, t_{\alpha\beta}, t'_{\alpha\beta}) = &\int_{t'_{\alpha\beta}}^{t_{\alpha\beta}} \mathrm{d}\tau \left(\frac{[\mathbf{p}_{\alpha\beta} + \mathbf{A}_\mathrm{L}(\tau)]^2}{2} + I_\mathrm{p} \right) - \omega t_{\alpha\beta} \\ &+ (-1)^\alpha \left[\mathbf{p}_{\alpha\beta} + \mathbf{A}_\mathrm{L}(t'_{\alpha\beta}) \right] \cdot \frac{\mathbf{R}}{2} \\ &- (-1)^\beta \left[\mathbf{p}_{\alpha\beta} + \mathbf{A}_\mathrm{L}(t_{\alpha\beta}) \right] \cdot \frac{\mathbf{R}}{2} \end{aligned} \tag{IV.13}$$

which can be expanded as

$$\begin{aligned} S_{\alpha,\beta}(\mathbf{p}_{\alpha\beta}, t_{\alpha\beta}, t'_{\alpha\beta}) = &\int_{t'_\mathrm{at}}^{t_\mathrm{at}} \mathrm{d}\tau \left(\frac{[\mathbf{p}_\mathrm{at} + \mathbf{A}_\mathrm{L}(\tau)]^2}{2} + I_\mathrm{p} \right) - \omega t_\mathrm{at} \\ &+ \left[\frac{[\mathbf{p}_\mathrm{at} + \mathbf{A}_\mathrm{L}(t_\mathrm{at})]^2}{2} + I_\mathrm{p} - \omega \right] R_x \partial_x t_{\alpha\beta} \\ &- \left[\frac{[\mathbf{p}_\mathrm{at} + \mathbf{A}_\mathrm{L}(t'_\mathrm{at})]^2}{2} + I_\mathrm{p} \right] R_x \partial_x t'_{\alpha\beta} \\ &+ (-1)^\alpha \left[\mathbf{p}_\mathrm{at} + \mathbf{A}_\mathrm{L}(t'_\mathrm{at}) \right] \cdot \frac{\mathbf{R}}{2} \\ &- (-1)^\beta \left[\mathbf{p}_\mathrm{at} + \mathbf{A}_\mathrm{L}(t_\mathrm{at}) \right] \cdot \frac{\mathbf{R}}{2} + O(R^2), \end{aligned} \tag{IV.14}$$

where we recognized the *atomic* saddle point equations (I.104b) and (I.104c), and used them to simplify the expression of the action. We finally get

$$\boxed{S_{\alpha,\beta}(\mathbf{p}_{\alpha\beta}, t_{\alpha\beta}, t'_{\alpha\beta}) = S_\mathrm{at} + (-1)^\alpha \left[p_\mathrm{at} + A_\mathrm{L}(t'_\mathrm{at}) \right] \frac{R_x}{2} - (-1)^\beta \left[p_\mathrm{at} + A_\mathrm{L}(t_\mathrm{at}) \right] \frac{R_x}{2} + O(R^2)}, \tag{IV.15}$$

where S_at is the *atomic* action (I.108).

b) Ionization dipole

The molecular ionization dipole reads

$$\begin{aligned} M_\alpha\Big(\mathbf{p}_{\alpha\beta} + \mathbf{A}_\mathrm{L}(t'_{\alpha\beta}), t'_{\alpha\beta}\Big) = -\frac{F_\mathrm{L}(t'_{\alpha\beta})}{\sqrt{2(1+w(\mathbf{R}))}} \Bigg[&\mathrm{i} \frac{\partial \widetilde{\phi}_\mathrm{a}}{\partial p_x} (\mathbf{p}_{\alpha\beta} + \mathbf{A}_\mathrm{L}(t'_{\alpha\beta})) \\ &+ (-1)^\alpha \frac{R_x}{2} \widetilde{\phi}_\mathrm{a}\Big(\mathbf{p}_{\alpha\beta} + \mathbf{A}_\mathrm{L}(t'_{\alpha\beta})\Big) \Bigg]. \end{aligned} \tag{IV.16}$$

The overlap $w(\mathbf{R})$ is obviously an even function of $\mathbf{R}$, so that the first order term vanishes and we simply get

$$\boxed{w(\mathbf{R}) = 1 + O(R^2).} \tag{IV.17}$$

The ionization dipole thus expands as

$$\begin{aligned} M_\alpha\Big(\mathbf{p}_{\alpha\beta} + \mathbf{A}_\mathrm{L}(t'_{\alpha\beta}), t'_{\alpha\beta}\Big) =& M_\mathrm{at}\Big(\mathbf{p}_\mathrm{at} + \mathbf{A}_\mathrm{L}(t'_\mathrm{at}), t'_\mathrm{at}\Big) \\ &+ \frac{(-1)^\alpha R_x}{2} \mathcal{M}_X\Big(\mathbf{p}_\mathrm{at} + \mathbf{A}_\mathrm{L}(t'_\mathrm{at}), t'_\mathrm{at}\Big) \\ &+ \frac{[(-1)^\beta - (-1)^\alpha] R_y}{2} \mathcal{M}_Y\Big(\mathbf{p}_\mathrm{at} + \mathbf{A}_\mathrm{L}(t'_\mathrm{at}), t'_\mathrm{at}\Big) + O(R^2), \end{aligned} \tag{IV.18}$$

where

$$M_\mathrm{at}(\mathbf{p}, t') = -\mathrm{i}\frac{F_\mathrm{L}(t')}{2} \frac{\partial \widetilde{\phi}_\mathrm{a}}{\partial p_x}(\mathbf{p}), \tag{IV.19}$$

and where we defined

$$\mathcal{M}_X(\mathbf{p}, t') = -\frac{F_\mathrm{L}(t')}{2} \widetilde{\phi}_\mathrm{a}(\mathbf{p}) - \mathrm{i}\frac{{\omega_\mathrm{L}}^2 A_\mathrm{L}(t')}{2p_x} \frac{\partial \widetilde{\phi}_\mathrm{a}}{\partial p_x}(\mathbf{p}) + \mathrm{i}\frac{F_\mathrm{L}(t')^2}{2p_x} \frac{\partial^2 \widetilde{\phi}_\mathrm{a}}{\partial p_x^2}(\mathbf{p}) \tag{IV.20}$$

$$\mathcal{M}_Y(\mathbf{p}, t') = -\mathrm{i}\frac{F_\mathrm{L}(t'_\mathrm{at})}{2(t_\mathrm{at} - t'_\mathrm{at})} \frac{\partial^2 \widetilde{\phi}_\mathrm{a}}{\partial p_x \partial p_y}\Big(\mathbf{p}_\mathrm{at} + \mathbf{A}_\mathrm{L}(t'_\mathrm{at})\Big) \tag{IV.21}$$

c) Recombination dipole

The molecular recombination dipole writes

$$\mathbf{L}\Big(\mathbf{p}_{\alpha\beta} + \mathbf{A}_\mathrm{L}(t_{\alpha\beta})\Big) = \frac{\mathbf{p}_{\alpha\beta} + \mathbf{A}_\mathrm{L}(t_{\alpha\beta})}{\sqrt{2(1 + w(\mathbf{R}))}} \widetilde{\phi}_\mathrm{a}\Big(\mathbf{p}_{\alpha\beta} + \mathbf{A}_\mathrm{L}(t_{\alpha\beta})\Big). \tag{IV.22}$$

We mainly concentrate on its component along the direction of the laser field polarization, i.e. the x direction, which expands as

$$\begin{aligned} L_x\Big(\mathbf{p}_{\alpha\beta} + \mathbf{A}_\mathrm{L}(t_{\alpha\beta})\Big) =& L_\mathrm{at}\Big(\mathbf{p}_\mathrm{at} + \mathbf{A}_\mathrm{L}(t_\mathrm{at})\Big) \\ &+ \frac{(-1^\beta) R_x}{2} \mathcal{L}_X\Big(\mathbf{p}_\mathrm{at} + \mathbf{A}_\mathrm{L}(t_\mathrm{at}), t_\mathrm{at}\Big) \\ &+ \frac{[(-1)^\beta - (-1)^\alpha] R_y}{2} \mathcal{L}_Y\Big(\mathbf{p}_\mathrm{at} + \mathbf{A}_\mathrm{L}(t_\mathrm{at}), t_\mathrm{at}\Big) + O(R^2), \end{aligned} \tag{IV.23}$$

where

$$L_{\mathrm{at}}(\mathbf{p}) = \frac{p_x}{2}\widetilde{\phi}_{\mathrm{a}}(\mathbf{p}), \tag{IV.24}$$

and where

$$\mathcal{L}_X(\mathbf{p},t) = -\frac{F_{\mathrm{L}}(t_{\mathrm{at}})}{2p_x}\widetilde{\phi}_{\mathrm{a}}(\mathbf{p}) - \frac{F_{\mathrm{L}}(t_{\mathrm{at}})}{2}\frac{\partial\widetilde{\phi}_{\mathrm{a}}}{\partial p_x}(\mathbf{p}) \tag{IV.25}$$

$$\mathcal{L}_Y(\mathbf{p},t) = -\frac{p_x}{2(t_{\mathrm{at}}-t'_{\mathrm{at}})}\frac{\partial\widetilde{\phi}_{\mathrm{a}}}{\partial p_y}(\mathbf{p}). \tag{IV.26}$$

For the sake of exhaustivity, we also give here the expansion of the y component of the molecular recombination dipole:

$$\boxed{L_y\Big(\mathbf{p}_{\alpha\beta}+\mathbf{A}_{\mathrm{L}}(t_{\alpha\beta})\Big) = \frac{[(-1)^\beta-(-1)^\alpha]R_y}{4(t_{\mathrm{at}}-t'_{\mathrm{at}})}\widetilde{\phi}_{\mathrm{a}}\Big(\mathbf{p}_{\mathrm{at}}+\mathbf{A}_{\mathrm{L}}(t_{\mathrm{at}})\Big)+O(R^2).} \tag{IV.27}$$

d) Saddle point prefactor

The first order expansion of the saddle point prefactor was not obtained in [129], where its influence was only assessed numerically. I present here its derivation.

The saddle point prefactor expression reads

$$C_{\alpha\beta}(t_{\alpha\beta},t'_{\alpha\beta}) = \left(\frac{2\pi}{\mathrm{i}(t_{\alpha\beta}-t'_{\alpha\beta})}\right)^{\frac{3}{2}}\frac{\pi}{\sqrt{\det\mathcal{H}_{S^{(p)}_{\alpha\beta}}(t_{\alpha\beta},t'_{\alpha\beta})}}, \tag{IV.28}$$

where $\mathcal{H}_{S^{(p)}_{\alpha\beta}}$ is the Hessian matrix of $S^{(p)}_{\alpha\beta}(t,t') = S_{\alpha\beta}(\mathbf{p}_{\alpha\beta}(t,t'),t,t')$, with $\mathbf{p}_{\alpha\beta}(t,t')$ the solution of (IV.1a):

$$\det\mathcal{H}_{S^{(p)}_{\alpha\beta}}(t_{\alpha\beta},t'_{\alpha\beta}) = \frac{\partial^2 S^{(p)}_{\alpha\beta}}{\partial t^2}\frac{\partial^2 S^{(p)}_{\alpha\beta}}{\partial t'^2} - \frac{\partial^2 S^{(p)}_{\alpha\beta}}{\partial t\partial t'}^2. \tag{IV.29}$$

Using the chain rule for computing the derivative of this composition of functions, we find

$$\frac{\partial^2 S^{(p)}_{\alpha\beta}}{\partial t^2}(t,t') = -\mathbf{F}_{\mathrm{L}}(t)\cdot[\mathbf{p}_{\alpha\beta}+\mathbf{A}_{\mathrm{L}}(t)] - \frac{[\mathbf{p}_{\alpha\beta}+\mathbf{A}_{\mathrm{L}}(t)]^2}{t-t'} + \frac{(-1)^\beta R_x}{2}\omega_{\mathrm{L}}^2 A_{\mathrm{L}}(t) \tag{IV.30}$$

$$\frac{\partial^2 S^{(p)}_{\alpha\beta}}{\partial t'^2}(t,t') = \mathbf{F}_{\mathrm{L}}(t')\cdot[\mathbf{p}_{\alpha\beta}+\mathbf{A}_{\mathrm{L}}(t')] - \frac{[\mathbf{p}_{\alpha\beta}+\mathbf{A}_{\mathrm{L}}(t')]^2}{t-t'} - \frac{(-1)^\alpha R_x}{2}\omega_{\mathrm{L}}^2 A_{\mathrm{L}}(t') \tag{IV.31}$$

$$\frac{\partial^2 S^{(p)}_{\alpha\beta}}{\partial t\partial t'}(t,t') = \frac{[\mathbf{p}_{\alpha\beta}+\mathbf{A}_{\mathrm{L}}(t)]\cdot[\mathbf{p}_{\alpha\beta}+\mathbf{A}_{\mathrm{L}}(t')]}{t-t'}. \tag{IV.32}$$

We can thus expand the Hessian determinant as:

$$\det \mathcal{H}_{S^{(p)}_{\alpha\beta}}(t_{\alpha\beta}, t'_{\alpha\beta}) = \det \mathcal{H}_{S^{(p)}_{\mathrm{at}}}(t_{\mathrm{at}}, t'_{\mathrm{at}}) \Bigg\{ 1 - \frac{R_x}{2} \Bigg[\frac{(-1)^\alpha F_{\mathrm{L}}(t'_{\mathrm{at}})}{[p_{\mathrm{at}} + A_{\mathrm{L}}(t'_{\mathrm{at}})]^2} + \frac{(-1)^\beta F_{\mathrm{L}}(t_{\mathrm{at}})}{[p_{\mathrm{at}} + A_{\mathrm{L}}(t_{\mathrm{at}})]^2} - \frac{(-1)^\alpha}{(t_{\mathrm{at}} - t'_{\mathrm{at}})\,[p_{\mathrm{at}} + A_{\mathrm{L}}(t'_{\mathrm{at}})]} + \frac{(-1)^\beta}{(t_{\mathrm{at}} - t'_{\mathrm{at}})\,[p_{\mathrm{at}} + A_{\mathrm{L}}(t_{\mathrm{at}})]} \Bigg] \Bigg\} + O(R^2). \tag{IV.33}$$

We finally get

$$C_{\alpha\beta}(t_{\alpha\beta}, t'_{\alpha\beta}) = C_{\mathrm{at}}(t_{\mathrm{at}}, t'_{\mathrm{at}}) \Bigg\{ 1 + \frac{R_x}{2} \Bigg[\frac{(-1)^\alpha F_{\mathrm{L}}(t'_{\mathrm{at}})}{2\,[p_{\mathrm{at}} + A_{\mathrm{L}}(t'_{\mathrm{at}})]^2} + \frac{(-1)^\beta F_{\mathrm{L}}(t_{\mathrm{at}})}{2\,[p_{\mathrm{at}} + A_{\mathrm{L}}(t_{\mathrm{at}})]^2} + \frac{(-1)^\alpha}{(t_{\mathrm{at}} - t'_{\mathrm{at}})\,[p_{\mathrm{at}} + A_{\mathrm{L}}(t'_{\mathrm{at}})]} - \frac{(-1)^\beta}{(t_{\mathrm{at}} - t'_{\mathrm{at}})\,[p_{\mathrm{at}} + A_{\mathrm{L}}(t_{\mathrm{at}})]} \Bigg] \Bigg\} + O(R^2). \tag{IV.34}$$

e) Sum over electronic trajectories

Since the HHG emitted light is dominantly polarized along the field polarization direction, we will concentrate on the x component of the dipole $\widetilde{\mathbf{D}}_{\alpha,\beta}$. To compute its expression, we put back together the four expressions in (IV.15), (IV.18), (IV.23) and (IV.34) and sum over α and β, i.e. over the four electronic trajectories. We get an expression that can organized as:

$$\widetilde{D}^{(x)}(\omega) = -\omega C_{\mathrm{at}} \left[\mathcal{D}(p_{\mathrm{at}}, t_{\mathrm{at}}, t'_{\mathrm{at}}) + R_y d_{\mathrm{mix}}(p_{\mathrm{at}}, t_{\mathrm{at}}, t'_{\mathrm{at}}) \right] \mathrm{e}^{-\mathrm{i}S_{\mathrm{at}}}, \tag{IV.35}$$

where the term $\mathcal{D}$ is equal *at first order* to the factored expression:

$$\mathcal{D}(p_{\mathrm{at}}, t_{\mathrm{at}}, t'_{\mathrm{at}}) \overset{1^{\mathrm{st}}\,\mathrm{order}}{=} \tilde{d}_{\mathrm{rec}}\Big(p_{\mathrm{at}} + A_{\mathrm{L}}(t_{\mathrm{at}}), t_{\mathrm{at}}, t'_{\mathrm{at}}\Big)\, \tilde{d}_{\mathrm{ion}}\Big(p_{\mathrm{at}} + A_{\mathrm{L}}(t'_{\mathrm{at}}), t_{\mathrm{at}}, t'_{\mathrm{at}}\Big), \tag{IV.36}$$

where

$$\tilde{d}_{\mathrm{rec}}(\mathbf{p},t,t') = p_x\widetilde{\phi}_{\mathrm{a}}(\mathbf{p})\cos\left(\frac{\mathbf{p}\cdot\mathbf{R}}{2}\right) - \frac{\mathrm{i}R_x}{2}\left[F_{\mathrm{L}}(t)\frac{\partial\widetilde{\phi}_{\mathrm{a}}}{\partial p_x}(\mathbf{p}) + \frac{F_{\mathrm{L}}(t)}{2p_x}\widetilde{\phi}_{\mathrm{a}}(\mathbf{p}) + \frac{1}{t-t'}\widetilde{\phi}_{\mathrm{a}}(\mathbf{p})\right]\sin\left(\frac{\mathbf{p}\cdot\mathbf{R}}{2}\right) \tag{IV.37}$$

$$\begin{aligned}\tilde{d}_{\mathrm{ion}}(\mathbf{p},t,t') = &-\mathrm{i}F_{\mathrm{L}}(t')\frac{\partial\widetilde{\phi}_{\mathrm{a}}}{\partial p_x}(\mathbf{p})\cos\left(\frac{\mathbf{p}\cdot\mathbf{R}}{2}\right)\\ &-\frac{\mathrm{i}R_x}{2}\left\{-F_{\mathrm{L}}(t')\widetilde{\phi}_{\mathrm{a}}(\mathbf{p}) + \mathrm{i}\frac{F_{\mathrm{L}}(t')^2}{p_x}\frac{\partial^2\widetilde{\phi}_{\mathrm{a}}}{\partial p_x^2}(\mathbf{p})\right.\\ &\left.+\mathrm{i}\frac{\partial\widetilde{\phi}_{\mathrm{a}}}{\partial p_x}(\mathbf{p})\left[-\frac{3}{2(t-t')p_x} + \frac{F_{\mathrm{L}}(t')}{4I_p} - \frac{{\omega_{\mathrm{L}}}^2 A_{\mathrm{L}}(t')}{p_x}\right]\right\}\sin\left(\frac{\mathbf{p}\cdot\mathbf{R}}{2}\right)\end{aligned} \tag{IV.38}$$

$$\begin{aligned}d_{\mathrm{mix}}(\mathbf{p},t,t') = &\frac{[\mathbf{p}+\mathbf{A}_{\mathrm{L}}(t)]\cdot\mathbf{F}_{\mathrm{L}}(t')}{2(t-t')}\sin\left[\left(2\mathbf{p}+\mathbf{A}_{\mathrm{L}}(t)+\mathbf{A}_{\mathrm{L}}(t')\right)\cdot\frac{\mathbf{R}}{2}\right]\\ &\times\left[\frac{\partial\widetilde{\phi}_{\mathrm{a}}}{\partial p_x}\left(\mathbf{p}+\mathbf{A}_{\mathrm{L}}(t')\right)\frac{\partial\widetilde{\phi}_{\mathrm{a}}}{\partial p_y}\left(\mathbf{p}+\mathbf{A}_{\mathrm{L}}(t)\right) + \widetilde{\phi}_{\mathrm{a}}\left(\mathbf{p}+\mathbf{A}_{\mathrm{L}}(t)\right)\frac{\partial^2\widetilde{\phi}_{\mathrm{a}}}{\partial p_x\partial p_y}\left(\mathbf{p}+\mathbf{A}_{\mathrm{L}}(t')\right)\right].\end{aligned} \tag{IV.39}$$

IV.1.3 Discussion

We will first comment the case of a molecule that is *aligned* with the laser polarization direction, here x. In this case $R_y = 0$, and the above expression (IV.35) is *at first order* very similar to the one obtained in [129]:

$$\widetilde{D}^{(x)}(\omega) = -\omega C_{\mathrm{at}}\tilde{d}_{\mathrm{rec}}\left(p_{\mathrm{at}} + A_{\mathrm{L}}(t_{\mathrm{at}}), t_{\mathrm{at}}, t'_{\mathrm{at}}\right)\tilde{d}_{\mathrm{ion}}\left(p_{\mathrm{at}} + A_{\mathrm{L}}(t'_{\mathrm{at}}), t_{\mathrm{at}}, t'_{\mathrm{at}}\right)\mathrm{e}^{-\mathrm{i}S_{\mathrm{at}}}, \tag{IV.40}$$

but where the formulas for the modified ionization $\tilde{d}_{\mathrm{ion}}$ and recombination $\tilde{d}_{\mathrm{rec}}$ dipoles are slightly different because of the saddle point prefactor contribution that was neglected in [129]. Remind that the HHG spectrum is *proportional* to the dipole $\widetilde{D}^{(x)}$, so we will discuss this quantity $\widetilde{D}^{(x)}$ as if it were *directly* the HHG spectrum. It is obviously a misuse of language, but I think it simplifies the discussion.

From this factored form (IV.40) it is straightforward to see that a zero of $\tilde{d}_{\mathrm{rec}}$ or $\tilde{d}_{\mathrm{ion}}$ will result in a sharp minimum in the HHG power spectrum. As already predicted in [200] and detailed in [129], the ionization dipole has little influence, and the minimum in the spectrum is actually caused by a zero of the *recombination* dipole. This can be understood by looking at the argument in $\tilde{d}_{\mathrm{ion}}$, i.e. $p_{\mathrm{at}} + A_{\mathrm{L}}(t'_{\mathrm{at}})$, which, as can be deduced from (I.104c), is simply equal to $\pm\mathrm{i}\sqrt{2I_{\mathrm{p}}}$ and thus does not depend on the frequency of the emitted harmonic. The ionization dipole depends on the harmonic frequency, and thus influences the HHG spectrum, only through terms that do not contain any structural information on the molecule, i.e. $F_{\mathrm{L}}(t'_{\mathrm{at}})$, $A_{\mathrm{L}}(t'_{\mathrm{at}})$, and $(t_{\mathrm{at}} - (t'_{\mathrm{at}}))$.

On the contrary, the argument in $\tilde{d}_{\mathrm{rec}}$ is $p_{\mathrm{at}} + A_{\mathrm{L}}(t_{\mathrm{at}}) = \pm\sqrt{2(\omega - I_{\mathrm{p}})}$ (using (I.104b)) where ω is the frequency of the emitted harmonic. If the modified recombination dipole

$\tilde{d}_{\text{rec}}$ displays a zero at $\mathbf{p}_{\text{min}}$, the HHG spectrum will thus exhibit a sharp minimum at the harmonic frequency $\omega_{\text{min}} = I_{\text{p}} + [\mathbf{p}_{\text{min}} + \mathbf{A}_{\text{L}}(t_{\text{at}})]^2/2$. In the model developped by Lein [200], this zero coincides with the zero of the *unmodified* recombination dipole d_{rec} (I.114), and thus occurs at $[\mathbf{p}_{\text{min}} + \mathbf{A}_{\text{L}}(t_{\text{at}})] \cdot \mathbf{R}/2 = (2q+1)\pi/2$, where q is an integer. This creates a minimum in the spectrum at

$$\omega_{\text{min}} = I_{\text{p}} + \frac{(\pi + 2q\pi)^2}{2R^2}, \quad q \in \mathbb{Z}. \tag{IV.41}$$

This is the formula that is generally used to predict the position of the minimum in the HHG spectrum [216–219][1].

This value of $\mathbf{p}_{\text{min}}$ predicted by Lein actually corresponds to a zero of the cosine term in the expression of $\tilde{d}_{\text{rec}}$ (IV.37). However the second term of the expression, proportional to the sine function, does not vanish at $\mathbf{p} = \mathbf{p}_{\text{min}}$. As was thoroughly investigated by François Risoud [129, 157], this $\mathbf{p}_{\text{min}}$ thus does not correspond to a *zero* of the modified recombination dipole $\tilde{d}_{\text{rec}}$, but to a smoothed *minimum*. Nevertheless, there are some circumstances where both terms may cancel *simultaneously*, leading to a zero of the total modified recombination dipole, hence to a sharp minimum in the HHG spectrum. From the expression of $\tilde{d}_{\text{rec}}$ (IV.37), we see that this will occur when both the cosine function (IV.42), and the term in factor of the sine function (IV.43) vanishes:

$$[p_{\text{at}} + A_{\text{L}}(t_{\text{at}})]\frac{R}{2} = \frac{\pi}{2} + q\pi, \quad q \in \mathbb{Z} \tag{IV.42}$$

$$F_{\text{L}}(t_{\text{at}})\frac{\partial\widetilde{\phi}_{\text{a}}}{\partial p_x}\Big(\mathbf{p}_{\text{at}} + \mathbf{A}_{\text{L}}(t_{\text{at}})\Big) + \frac{F_{\text{L}}(t_{\text{at}})}{2\,[p_{\text{at}} + A_{\text{L}}(t_{\text{at}})]}\widetilde{\phi}_{\text{a}}\Big(\mathbf{p}_{\text{at}} + \mathbf{A}_{\text{L}}(t_{\text{at}})\Big)$$
$$+ \frac{1}{t_{\text{at}} - t'_{\text{at}}}\widetilde{\phi}_{\text{a}}\Big(\mathbf{p}_{\text{at}} + \mathbf{A}_{\text{L}}(t_{\text{at}})\Big) = 0. \tag{IV.43}$$

As explained in [129, 157] the *position* of the minimum is defined by the zero of the cosine function, i.e. by equation (IV.42), and thus only depends on R. The *shape* of the minimum is determined by the left hand side of (IV.43): if this term cancels then the minimum is sharp, otherwise it is smoothed. Note that this second condition depends on the laser intensity and frequency, but also on the considered electronic trajectory: indeed, both the short and long trajectories display a minimum at the same harmonic frequency - however this minimum may be smoothed for one type of trajectories, and sharp for the other. To observe the minimum in the spectrum, it is thus advantageous to separate the contributions of the two types of trajectories, as was done in [129, 157].

We draw the attention of the reader to the fact that we obtained a condition (IV.43) for the sharpness of the minimum which is in disagreement with the one given by François Risoud. In [129], because the saddle point prefactor contribution was neglected, the condition that was obtained was similar to (IV.43) but without the third term. The equation thus reduced to $F_{\text{L}}(t_{\text{at}}) = 0$ which was not in agreement with numerical simulations. To tackle the problem a constant ζ was empirically added to the expression. We find this is actually not a constant but depends on the saddle point solution, and thus on the

[1] Actually, in the formula used by [216, 217] the continuum energies are shifted by an amount of I_{p}. This is supposed to compensate for the PWA by taking into account the effect of the potential on the continuum states. We will come back on this correction in section IV.2.3.

intensity and wavelength of the laser. Our findings explain why the minimum was found to be sharp in conditions where $F_{\mathrm{L}}(t_{\mathrm{at}}) \neq 0$ [129], and settle the disparity between the numerical and analytical predictions.

In the case where the molecule is not aligned with the laser polarization direction, we have an additional term, proportional to $R_y = R\sin\theta$, in the expression of the dipole $\widetilde{D}^{(x)}$ (IV.35). Because of this term, the expression can no longer be factored out as we did in the aligned case (IV.40). Consequently the zeros of $\tilde{d}_{\mathrm{rec}}$ may not necessarily correspond to minima of the HHG spectrum. This is actually in contradiction with the commonly accepted idea that the aligned and the non-aligned case would be equivalent problems, and that to go from the former to the latter, one would only have to replace R by $R_x = R\cos\theta$, θ being the angle between the molecule and the electric field [200, 129]. Unfortunately we did not have time to assess analytically the influence of this d_{mix} term. We will thus try to understand the influence of the molecular orientation through numerical simulations in the next section.

IV.2 Numerical simulations

In this section we investigate the accuracy of the molecular SFA model by confronting its predictions to 1D and 2D numerical simulations.

IV.2.1 Methods

We consider a 2D system analogous to the 1D system used in [129, 157] where the electron is trapped in a two center Soft-Coulomb potential:

$$V(\mathbf{r}) = -\frac{1/2}{\sqrt{a^2 + (\mathbf{r}+\mathbf{R}/2)^2}} - \frac{1/2}{\sqrt{a^2 + (\mathbf{r}-\mathbf{R}/2)^2}}. \tag{IV.44}$$

This is a simple benchmark model for diatomic molecules. As in [129, 157], the parameter a is optimized at each value of R to keep the ionization potential of the system constant and equal to the ionization potential of the H_2 molecule $I_{\mathrm{p}}(R) = 0.567$ a.u. $= 15.43$ eV. This allows to forget the I_{p} dependency of the position and shape of the interference, and thus to concentrate on the contribution of the internuclear distance R, molecular orientation θ and laser intensity I_{L}.

We also consider a system that is designed to be "intermediary" between the 1D and the 2D case. In this case the electron is trapped in an asymmetric potential, which writes, in a frame where the molecule is aligned along the x axis:

$$V_\kappa(\mathbf{r}) = -\frac{1/2}{\sqrt{a^2 + (x+R/2)^2 + \kappa y^2}} - \frac{1/2}{\sqrt{a^2 + (x-R/2)^2 + \kappa y^2}}, \tag{IV.45}$$

where the parameter κ is smaller than 1 a.u., so that the potential wells are wider in the direction perpendicular to the molecular axis, i.e. the y direction. As a result the momentum of the electron is more confined in the y direction, and the electron behaves similarly to a 1D system.

Finally, to compare with the results of François Risoud, we also performed simulations on the 1D model system that was used in [129], and which is the one dimensional equivalent of our 2D H_2 system.

These systems are submitted to linearly polarized laser pulses of central wavelength $\lambda_L = 800$ nm, 2 optical cycle long, with a sine square envelope:

$$F_L(t) = F_L \sin(\omega_L t) \sin^2\left(\frac{\omega_L t}{4}\right). \tag{IV.46}$$

Such pulses have only one generating cycle, so that the system emits a single attosecond pulse with a continuous spectrum. We separate the contributions of the short and long trajectories with an adapted absorber, as explained in section II.3.3.

As discussed in [129], the phase of the harmonics evolves quite rapidly accross the HHG spectrum. This phase variation, known as the attochirp of the harmonic emission [153–155], prevents us to directly observe the phase jump of the 2-center interference. We thus need to remove this attochirp by substracting a reference phase. As in [129, 157] we take as a reference an atomic analog of our model molecule, i.e. a system with the same potential and the same ionization potential I_p, but with a zero internuclear distance $R = 0$. Note that, to observe more easily the minimum in the spectrum, the harmonic *intensity* is also normalized with respect to the intensity of the atomic reference.

IV.2.2 Results

In this section, we present the HHG spectrum intensity and phase of the short and long trajectories for the different 2D and 1D systems described in the previous section. We confront them to the 1D results previously obtained by François Risoud [129, 157], and to the predictions of the molecular SFA.

We first consider the case where the "molecules" are aligned with the field polarization direction and we investigate the effect of the internuclear distance on the position and shape of the minimum and of the phase jump. The results are presented on Figure IV.1 for the 1D H_2, and on Figure IV.2 for the 2D H_2.

In both cases, we observe the same qualitative features: the HHG spectrum intensity displays a minimum whose position and shape depend on the value of the internuclear distance R. The position of the minimum coincides with a jump of the harmonic phase from zero to $\simeq \pm\pi$. We remark that, for each value of R, the minimum occurs almost at the same harmonic frequency for the 1D and 2D systems considered here, which is consistent with results previously obtained by Lein [200]. As discussed in section IV.1.3, this is in agreement with the molecular SFA predictions that state that the minimum position is not strongly affected by the dimension, and only depends on the ionization potential I_p and internuclear distance R.

On the contrary, the *shape* of the minimum and phase jump can be very different for the 1D and 2D systems. In most of the cases the minimum and the phase jump are smoothed and cover several harmonics. If we look at the short trajectories (left panels on figures IV.1 and IV.2), we remark that the *shape* of the minimum and phase jump is similar for the two systems: it is always smoothed and covers several harmonics. However if we look at the long trajectories (right panels on figures IV.1 and IV.2), we notice particular *critical* values R_c of the internuclear distance for which the minimum in the

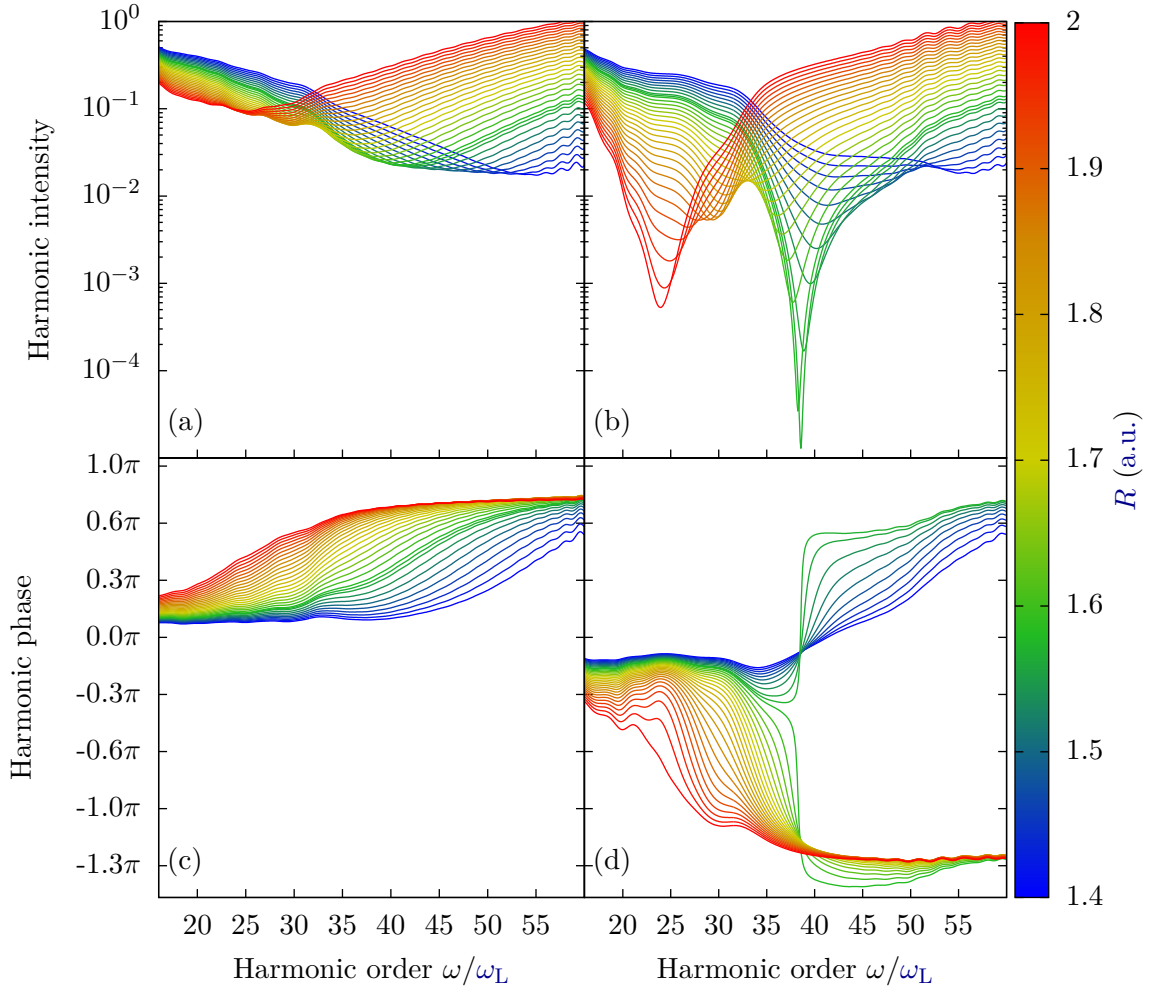

Figure IV.1 *HHG spectrum of the short (panels a and c) and long (panels b and d) trajectories for the 1D H_2 model system for different values of R between* 1.4 a.u. *and* 2 a.u. *Upper panels: intensity of the harmonics normalized by the equivalent atom, lower panels: phase of the harmonics, taking the equivalent atom as a reference.*

spectrum intensity is very deep and coincides with a sharp phase jump of the harmonic phase. It also corresponds to a *change of sign* of the phase jump. In the 1D case, we find a critical value of $R_c = 1.57$ a.u., while in the 2D case, we find $R_c = 1.8$ a.u.. We notice that in the 2D case, we also observe a sharpening of the phase jump for $R = 1.57$ a.u., *however* this value does not corresponds to a *change of sign* of this phase jump.

In the work of Śpiewanowski et al. [214, 215], the smoothing of the phase jump was attributed to a dressing of the ground state by the laser electric field. According to this model, the condition for the phase jump to be sharp coincides with a zero electric field at the recombination time of the corresponding harmonic. In his thesis [129] François Risoud came to the same conclusion through his expansion of the molecular SFA. The value of the harmonic frequency for which the electric field cancels at the recombination time (i.e.

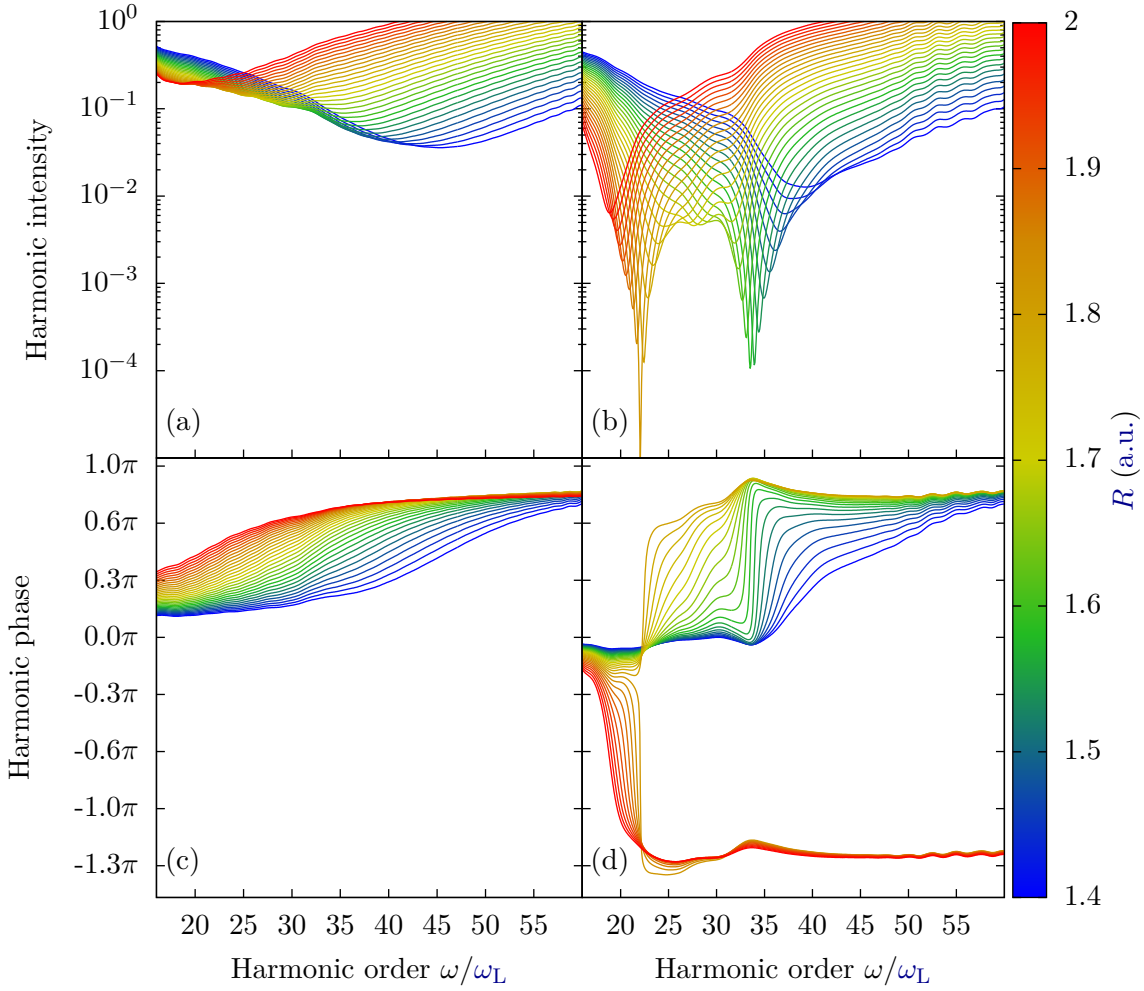

Figure IV.2 *HHG spectrum of the short (panels a and c) and long (panels b and d) trajectories for the 2D H_2 model system aligned with the laser polarization direction for different values of R between* 1.4 a.u. *and* 2 a.u.*. Upper panels: intensity of the harmonics normalized by the equivalent atom, lower panels: phase of the harmonics, taking the equivalent atom as a reference.*

at the time of emission of the harmonic) only depends on the ionization potential I_p and on the intensity and frequency of the incident laser field. According to this model, we should thus observe a sharp phase jump for the *same* critical harmonic ω_c for both the 1D and the 2D H_2 model systems. However we find $\omega_c = 38.5\omega_L$ in 1D and $\omega_c = 22.5\omega_L$ in 2D. Moreover, this model does not explain at all why, in the 2D case we witness a *second* particular harmonic value, at $\omega = 33\omega_L$ for which the phase jump is sharp, but does not change sign.

The emission time of the critical harmonic is not directly observed on the HHG spectrum. To access it, we performed a STFT of the dipole (see section II.3.3 for more details) for the critical internuclear distances, i.e. $R_c = 1.8$ a.u. for the 2D system and $R_c = 1.57$ a.u. for the 1D system. The results are presented on Figure IV.3. The STFT

has the expected bell shape, which allows a direct mapping of two different emission times for each harmonic, corresponding to the emission times of the short and of the long trajectories. In both cases we observe a dip in the spectrum, corresponding to the 2-center interference minimum. In agreement with our previous observations, we find that this dip is located on the part that corresponds to the long trajectories, and that it appears at a harmonic of $\omega_c = 22.5\omega_L$ for the 2D system (panel (a)) and $\omega_c = 38.5\omega_L$ for the 1D system (panel (b)). It becomes clear on this figure that the emission time of this critical harmonic are very different in the 2D and in the 1D case: we find $t_c = 1.63\ T_L$ in 2D and $t_c = 1.47\ T_L$ in 1D. Moreover, in both cases, this coincides with a *non zero* electric field at the time of emission of the harmonic.

These findings are thus in disagreement with the interpretation that the smoothing of the phase jump would simply be a consequence of the dressing of the ground state by the electric field. It is also in disagreement with the conclusion of François Risoud in [129]. However we saw in section IV.1.3 that in the calculation performed by François Risoud, the influence of the saddle point prefactor was neglected. We shown in section IV.1 that, by adding this contribution, the phase jump was not necessarily sharp for a zero electric field at the recombination time. Instead we found a different condition, given in (IV.43), which, in the LCAO approximation, explicitly depends on the orbital Fourrier transform and on its derivative. Our calculation thus allows to understand why the shape of the minimum and phase jump may actually depend on the system geometry, and not only on its ionization potential as was suggested in [129]. These disparities between the 1D and the 2D simulations may also be caused by the difference of spreading of the wave packet during the propagation step. Indeed, in 2D the ionized wave packet has the possibility to spread in the direction transverse to the propagation, which is forbidden in 1D.

To better understand the differences between the 1D and the 2D case, we performed the same analysis on the intermediate system presented in the previous section. For these systems, the electron is trapped in a *stretched* two dimensional potential. The ground state is thus closer to the 1D case, but the electron wave packet still has the possibility to spread in two dimensions, which is impossible in 1D. This is why we call them "intermediate" between 1D and 2D.

The results are presented on Figure IV.4 for a system with $\kappa = 0.1$ a.u. and on Figure IV.5 for a system with $\kappa = 0.5$ a.u.. The spectrum intensity and phase are comparable to the previous results. For a given value of R, the harmonic where the minimum appears (and the phase jump) is always the same, with only small differences, for all the systems that we considered in this section. Here again the shape of the minimum and of the phase jump that we observe in the *short* trajectories is very similar to the previous observations: it is always smoothed and cover several harmonics. The spectrum of the *long* trajectories behaves differently. Interestingly we find that, for the system that is the most stretched i.e. with $\kappa = 0.1$, the minimum and the phase jump appear very sharp *for the same* critical harmonic $\omega_c = 38.5\omega_L$ as in the 1D case. By performing the STFT of the dipole we also find that it corresponds to the same emission time of $t_c = 1.47\ T_L$. As we said, an electron trapped in this 2D stretched potential behaves similarly to a 1D electron, *except* that the ionized wave packet has the possibility to spread in the transverse direction during the propagation in the continuum. Therefore, the fact that the 1D and the stretched 2D potentials have the same critical harmonic seems to indicate that this spreading of the wave packet does play a role in the 2-center

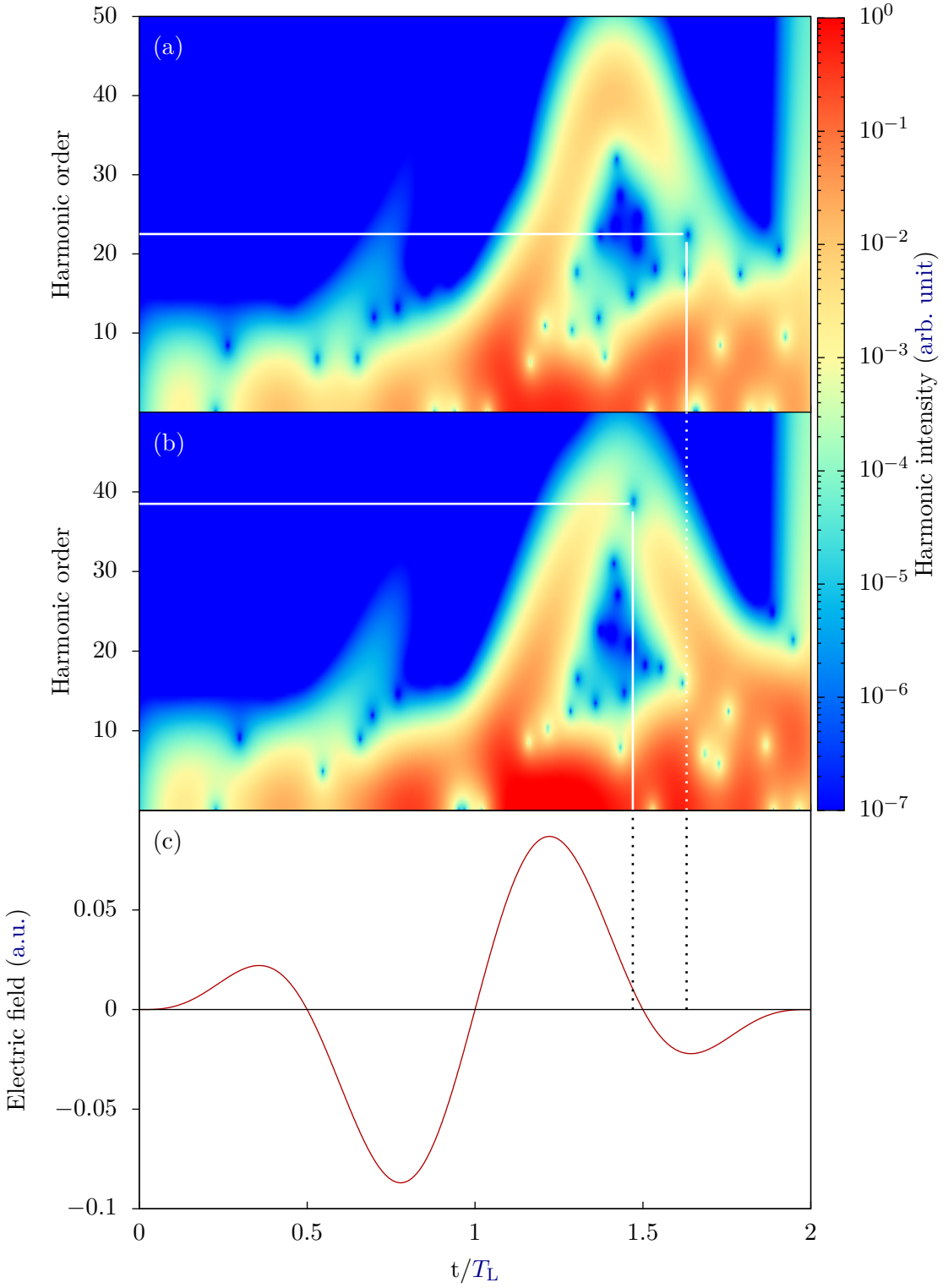

Figure IV.3 *STFT of the dipole at the critical internuclear distance R_c. (a) 2D H_2 model system R_c = 1.8 a.u., (b) 1D H_2 model system R_c = 1.57 a.u.. The laser electric field is shown on panel (c).*

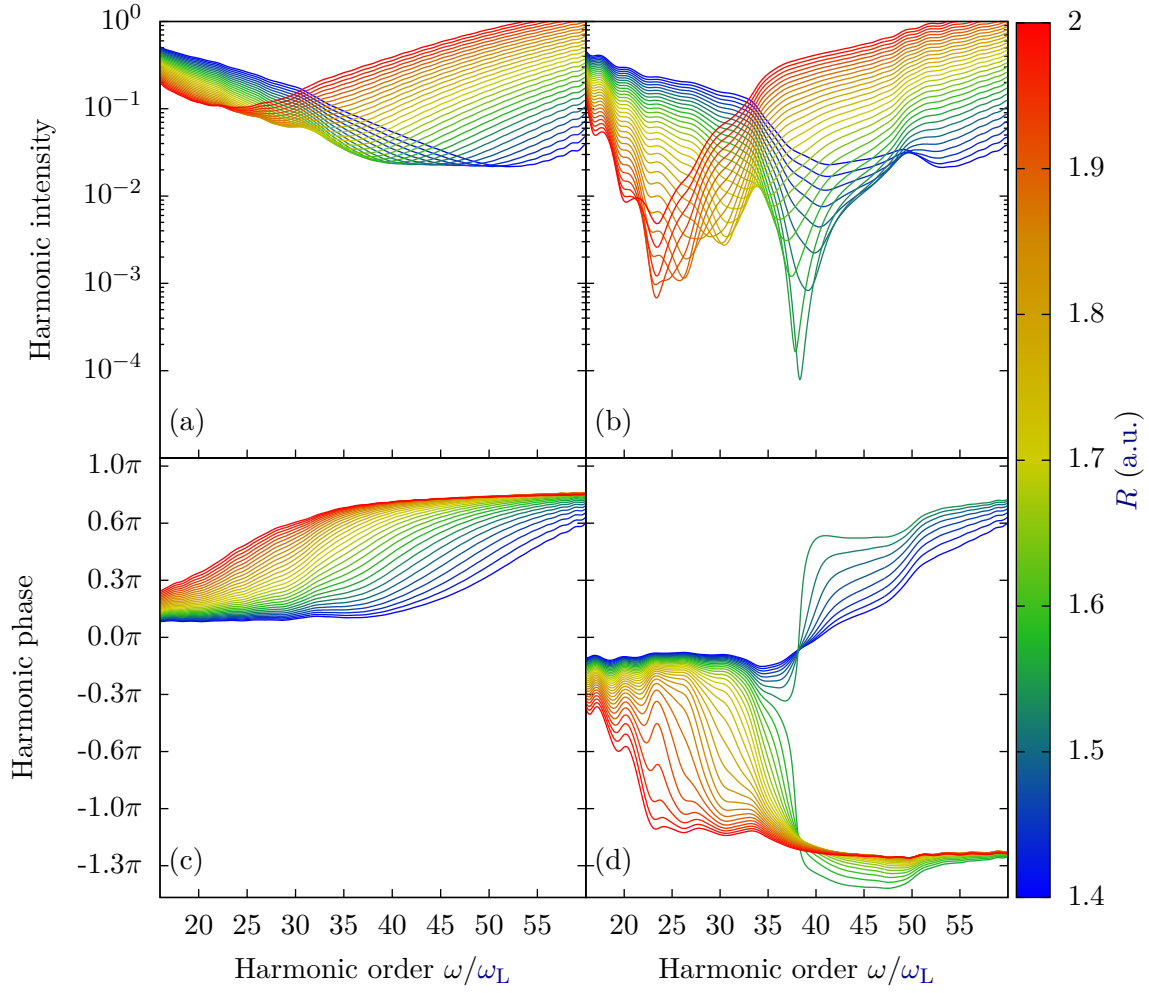

Figure IV.4 *HHG spectrum of the short (panels a and c) and long (panels b and d) trajectories for the 2D asymmetric H_2 system with $\kappa = 0.1$ aligned with the laser polarization direction for different values of R between* 1.4 a.u. *and* 2 a.u.*. Upper panels: intensity of the harmonics normalized by the equivalent atom, lower panels: phase of the harmonics, taking the equivalent atom as a reference.*

interference. This effect is however difficult to disentangle from the influence of the ground state geometry.

We just saw that if we completely stretch our two dimensional potential, we recover almost the same behavior as in the 1D case. But what happens in between, i.e. if we stretch it only a little? Would we observe a sharp phase jump with sign inversion at a critical harmonic of $\omega_c = 38.5\omega_L$ as in the 1D case, or at $\omega_c = 22.5\omega_L$ as in the 2D case? If we look at the results for the system with $\kappa = 0.5$ a.u., presented on Figure IV.5, we remark that, surprisingly, *both* $\omega_c = 38.5\omega_L$ *and* $\omega_c = 22.5\omega_L$ correspond to a sharp phase jump with sign inversion. We even see a third sign inversion in between at $\omega_c = 28\omega_L$. This highlights once again the fact that this sign inversion of the phase jump cannot be simply attributed to a value of the electric field at the recombination time. Nevertheless,

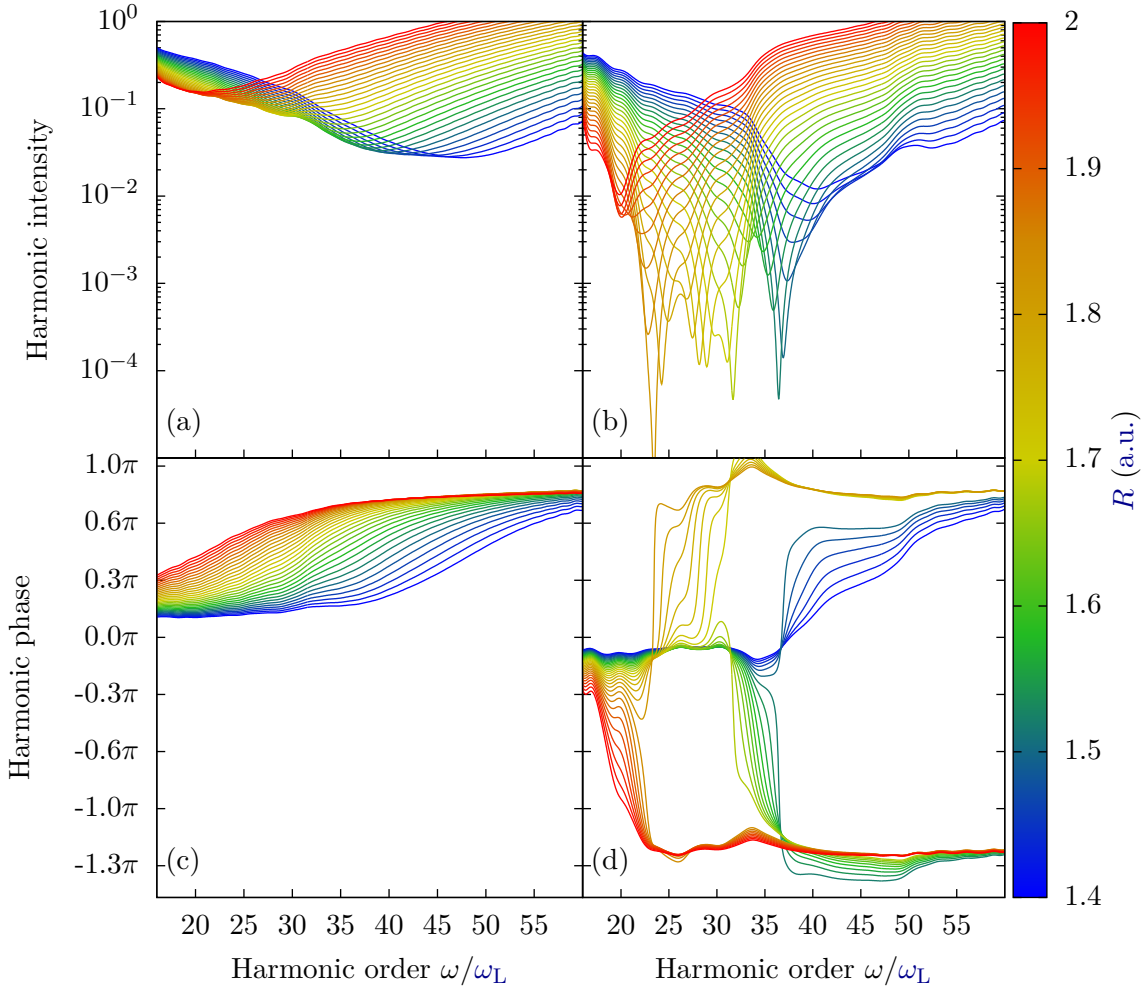

Figure IV.5 *HHG spectrum of the short (panels a and c) and long (panels b and d) trajectories for the 2D asymmetric H_2 system with $\kappa = 0.5$ aligned with the laser polarization direction for different values of R between* 1.4 a.u. *and* 2 a.u.. *Upper panels: intensity of the harmonics normalized by the equivalent atom, lower panels: phase of the harmonics, taking the equivalent atom as a reference.*

more simulations are required to investigate the physical reasons why we may observe, in some cases, several sign inversions of the phase jump. We just remind that the sign of an abrupt phase jump is actually not really defined, so that it may be difficult to predict and to interpret.

We now turn to the case where the "molecule" is not necessarily aligned along the laser polarization direction. In this case, as was investigated by Lein [200], the position of the minimum is now a function of $R\cos\theta$ where θ is the angle between the molecular axis and the laser polarization. It was argued in [129] that the aligned and non-aligned configurations were completely equivalent, and one would only needs to replace R by $R\cos\theta$ to recover the same physics. To investigate this assumption we performed simulations of our 2D model system for H_2 with a fixed internuclear distance $R_0 = 2$ a.u. and for different

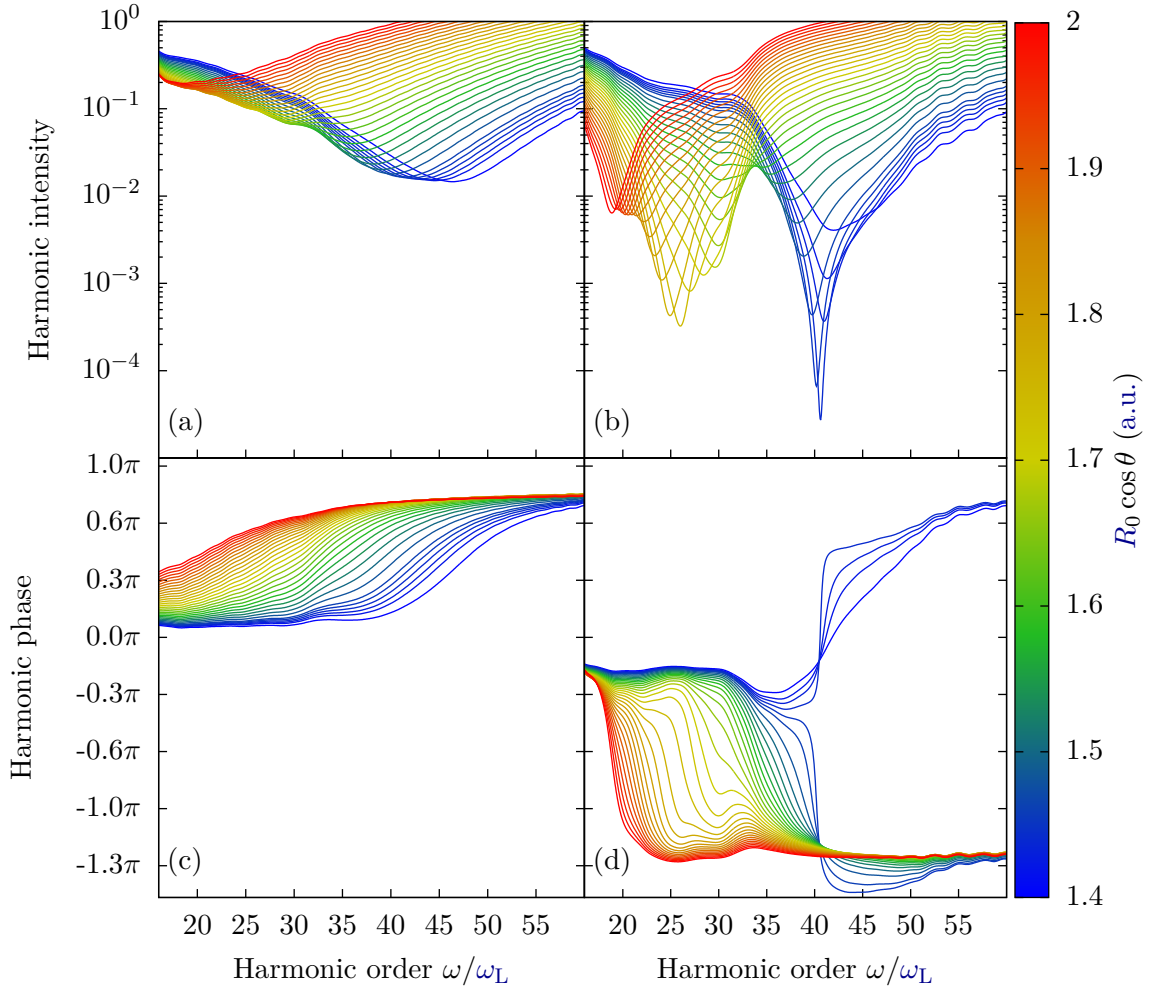

Figure IV.6 *HHG spectrum of component parallel to the incident field polarization of the short (panels a and c) and long (panels b and d) trajectories for the 2D H_2 model system with $R_0 = 2$ a.u. for different orientations with the laser polarization direction between 0 and $\theta = 0.253\pi$ corresponding to $R_0 \cos\theta = 1.4$ a.u.. Upper panels: intensity of the harmonics normalized by the equivalent atom, lower panels: phase of the harmonics, taking the equivalent atom as a reference.*

orientations with respect to the laser polarization and thus different values of $R_0 \cos\theta$.

The HHG spectrum intensity and phase for the short and long trajectories are shown on Figure IV.6. As in the aligned case, the HHG spectrum intensity presents a minimum which coincides with a jump of the harmonic phase. The position of this minimum for a given value of θ is very close to the position in the aligned case for the corresponding value of $R_\parallel = R_0 \cos\theta$. The short trajectories (left panels) present the same behavior as in the aligned case: the minimum and phase jump are smoothed for all the orientations presented here. As in the aligned case, the long trajectories show a critical angle $\theta_c = 0.24\pi$ for which the minimum is deeper and the phase jump is steeper. However this critical value

corresponds to $R_0 \cos\theta_c = 1.46$ a.u., which is different from the critical value $R_c^{\parallel} = 1.8$ a.u. that we obtained in the aligned case. Moreover this sharp phase jump appears at a critical harmonic $\omega_c = 40\omega_L$ which is also different from the critical harmonic $\omega_c^{\parallel} = 22.5\omega_L$ that we had in the aligned case. The two configurations are thus not equivalent at all, indicating that the orientation of the molecule with respect to the field does influence the 2-center interference beyond the celebrated $R\cos\theta$ dependency.

These results can once again be rationalized with the analytic expansion that we performed in IV.1. Indeed we saw that if the molecule is parallel to the laser polarization, then the final expression of the HHG spectrum (IV.35) cannot be factored as in the aligned case (IV.40). This is due to an additional term, d_{mix}, that arises when the molecule in not aligned with the field. This new term explains why a zero of the modified recombination dipole matrix element $\tilde{d}_{\text{rec}}$ will correspond to a zero (or deep minimum and sharp phase jump) of the HHG spectrum (IV.40) in the *aligned* case, but only to a smoothed minimum in the *non-aligned* case. Nevertheless, more simulations are needed to really understand the effect of the new term d_{mix} on the shape of the interference.

IV.2.3 Plane wave approximation, LCAO, and position of the minimum

In the previous section, we have studied the *shape* of the 2-center interference as it appears in the HHG spectrum intensity and phase. We have seen that the molecular SFA model allows to qualitatively understand the physical laws that govern the smoothing or sharpening of the phase jump. However, it was pointed out in [129, 157] that this model is not able to quantitatively predict the *position* of the interference minimum. As we have seen in sections I.3.3 d) and IV.1, the molecular SFA is based on two very strong approximations, that are used to compute the recombination and ionization dipole: the Linear Combination of Atomic Orbitals (LCAO) and the Plane Wave Approximation (PWA). The latter is often corrected through a shift in energy [200, 84, 216, 217] by considering that a plane wave with wavevector $\mathbf{k}$ corresponds to a continuum state of energy $k^2/2 - I_p$ instead of $k^2/2$. This empirical correction is supposed to compensate the effect of the potential on the continuum state close to the nucleus. However, it was shown in [129] that it does not substantially improves the prediction of the minimum position. To understand why the prediction of the molecular SFA is not in agreement with the "exact" TDSE results, we quantitatively assess the accuracy of the two approximations used in this model, i.e. LCAO and PWA. In particular we question the pertinence of the "I_p correction" that we just mentioned.

We start with the one dimensional model system for the H_2 molecule that we described in section IV.2.1. Two different wave functions are needed to compute the recombination dipole: the ground state, and the continuum state. In 1D, it is possible to compute both of them "exactly", i.e. up to numerical precision. The continuum states are calculated with the method explained in section II.1.3 c) and the ground state by inverse interation as detailed in section II.1.3 b). We could thus compute the "exact" recombination dipole. But we could also compute the same quantity using only the LCAO approximation for the ground state, or only the PWA for the continuum states, or both approximation at the same time. As explained in [129], to properly predict the position of the interference minimum in the HHG spectrum, we need to find the zeros of the recombination dipole. So we extracted, for each value of the internuclear distance R, the energy E_{min} corresponding

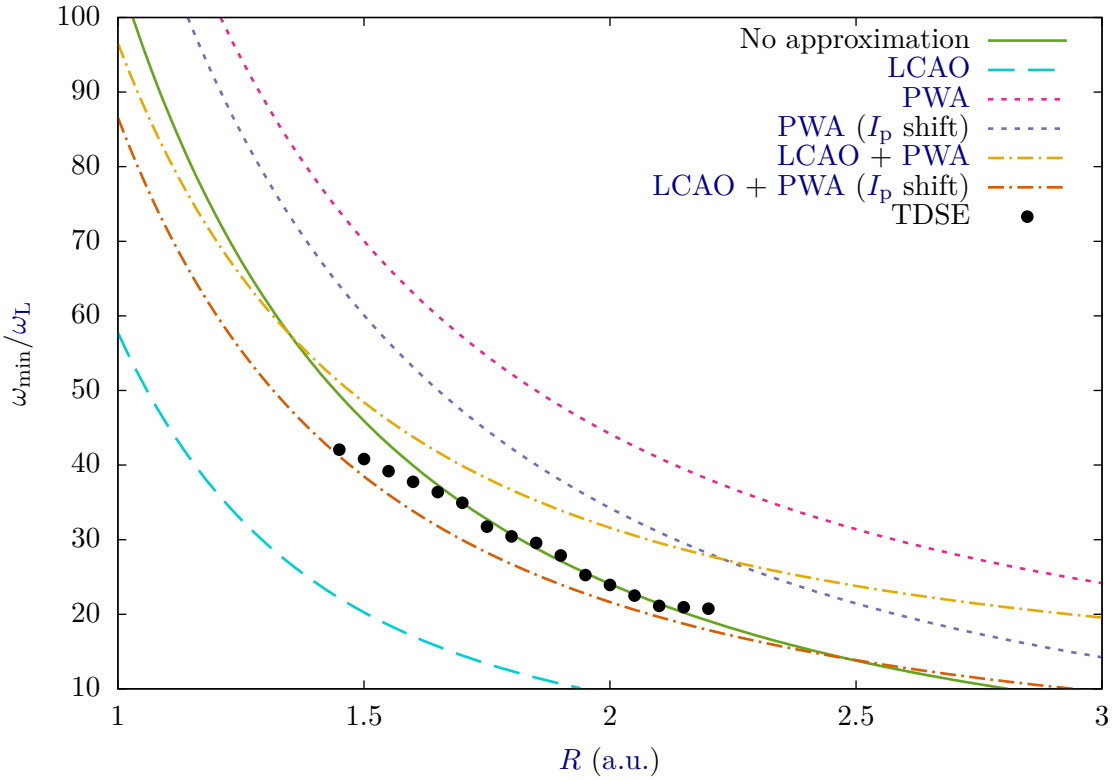

Figure IV.7 *Harmonic order of the minimum extracted from TDSE simulations and from the first zero of different approximation of the recombination dipole for the 1D H_2 model system.*

to the first zero of the recombination dipole. We deduced the harmonic frequency of the minimum $\omega_{min} = E_{min} + I_p$ from the energy conservation relation (I.104b). This is plotted as a function of R on Figure IV.7.

We observe, in agreement with our previous results, that the harmonic frequency of the minimum decreases with increasing R. We also confirm, in agreement with the findings of François Risoud [129], that the minimum in the HHG spectrum (black dots) is very close to the first zero of the *exact* recombination dipole (solid green line). However, if we make the LCAO approximation for the ground state, then the first zero of the recombination dipole (dashed blue line) strongly underestimates the minimum position, by approximately $30\omega_L \sim 45$ eV. This indicates that this approximation is not really justified to compute the recombination dipole. If we now make the PWA for the continuum states and keep the "exact" numerical ground state, then in this case the first zero of the recombination dipole (pink dotted line) strongly *overestimate* the minimum position. If we correct the plane wave energies with the "I_p shift" mentioned above, then indeed the disagreement decreases, but the minimum position is still overestimated by approximately $10\omega_L \sim 15$ eV. Therefore, with or without the "I_p correction", in both cases, the PWA is not justified to compute the recombination dipole. It is however striking that if we use *both* approximations (dash-dotted curves) *at the same time*, then the position of the first zero is much closer to the exact one. This is a clear manifestation of error compensation.

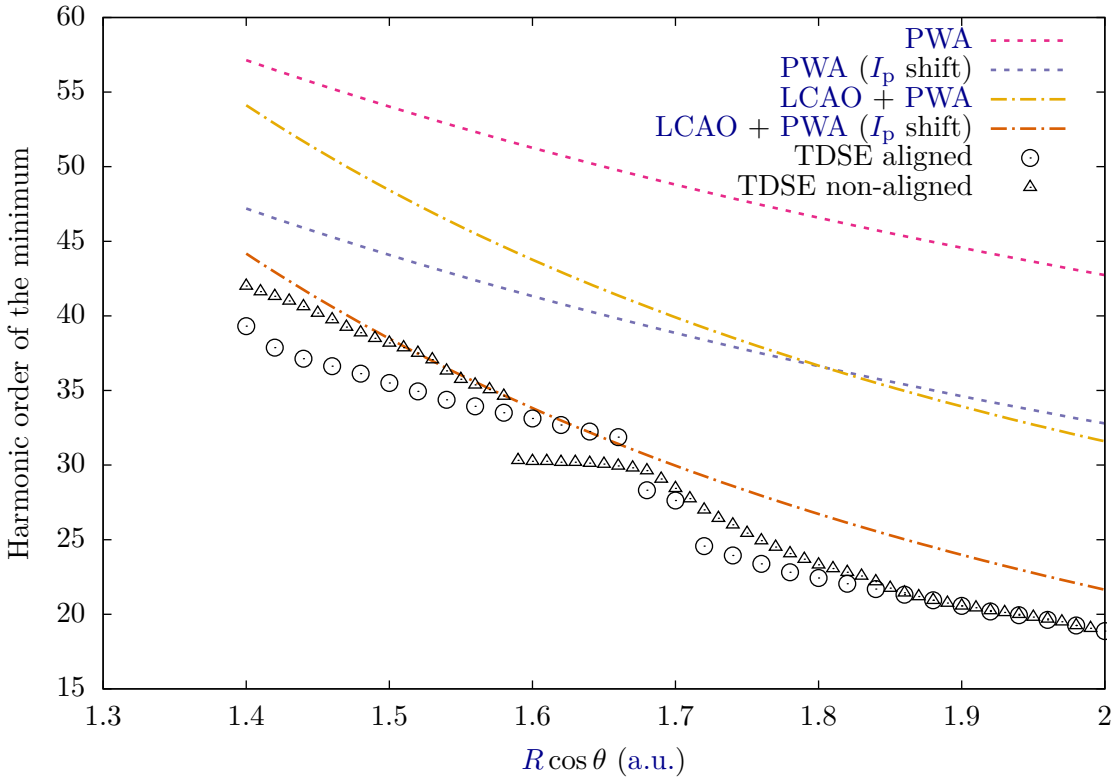

Figure IV.8 *Harmonic order of the minimum extracted from TDSE simulations and from the first zero of different approximation of the recombination dipole for the 2D H_2 model system.*

The predictions of the minimum with the "I_p correction" (dash-dotted orange line) seems a little bit closer to the TDSE results than the predictions without this correction (dash-dotted yellow line). Nevertheless, since this agreement is caused by error compensation, the fact that this "I_p correction" improves the accuracy of the result seems more related to chance than to a real physical effect.

In the 2D case, we did not compute numerically the continuum states because of the high numerical cost it would have implied. However we could get the "exact" groundstate with imaginary time propagation (see section II.2.3) so that we can still evaluate the accuracy of the LCAO approximation. And since we could extract the exact position of the minimum from the TDSE simulations, we can also estimate the accuracy of the PWA. The position of the minimum in the HHG spectrum extracted from the TDSE simulations, and the first zero of the recombination dipole are shown on Figure IV.8. We observe exactly the same trend as in the 1D case: the position of the minimum decreases with increasing R. As predicted by Lein [200], the position of the minimum only depends on the orientation through a $\cos\theta$ factor. As in the 1D case, we see that when the continuum states are computed with the PWA (dotted curves), then the first zero of the recombination dipole dramatically overestimates the position of the minimum. The "I_p correction" improves the agreement but is definitely not sufficient to compensate for this approximation. However, if we add the LCAO approximation of the ground state

(dashed-dotted curves), then once again we compensate almost all the error that was introduced by the PWA.

One has thus to be extremely careful when trying to use the molecular SFA model to make quantitative predictions. Indeed, the error compensation that we witness for the position of the minimum is not guaranteed to be as efficient for other observables. There may very well be some cases where the errors of the two approximation add up instead of compensating each other, with dramatic consequences.

IV.3 Conclusion

In this chapter we studied analytically and numerically the two center interference signature that is observed in the HHG spectrum of diatomic molecules. We have completed the analytical work of François Risoud in [129]. Our contribution allows to reach a better agreement between the qualitative predictions of both approaches. In particular we could explain why the sharp interference structures in the spectrum were not observed for a zero electric field at recombination time. We found another condition for this sharpening, and we saw that it strongly depends on the emitting system, and on the molecular orientation with respect to the laser polarization. Our preliminary results seems to indicate that it is affected by the spreading of the ionized wave packet during the propagation step as well as the ground state geometry.

Finally we investigated the question of the quantitative agreement between the TDSE results and the molecular SFA model developped by Chirilă and Lein [84]. We closely looked at the effect of the LCAO and PWA on the computation of the recombination dipole, and more precisely on the position of its first zero. We showed that each of these two approximations induces a relatively large error of a few tens of eV on the prediction of the minimum position. However these errors almost perfectly compensate when we use both approximations at the same time. This indicates that one must be very careful when using the molecular SFA for quantitative predictions. Moreover this reduces the perspective of improvement of the model. Indeed any correction of the error induced by one of its underlying approximation may actually spoil this error compensation and would thus only deteriorate the accuracy. We believe that the main strength of the molecular SFA lies in its qualitative predictions, and on the physical interpretations that they bring, rather than on its quantitative accuracy.

Chapter V

Diatomic molecules in strong fields: ultrafast vibronic dynamics

In the previous chapters we studied the *electronic* dynamics of molecules submitted to strong fields. We completely neglected the motion of the nuclei, and its influence on the electrons. This approximation is justified if the nuclei can be considered to be very slow at the time scale of the electron dynamics. For heavy molecules the vibrational period is typically of the order of 100 fs, and the Titane:Sapphire laser has a period of 2.7 fs, so that as long as the incident laser pulse is limited to a few optical cycles, we can consider that the nuclei did not have sufficient time to move during the pulse. On the contrary, in the case of H_2 the vibrational period in the ground state is 8 fs, we can thus start to observe vibrational dynamics even during very short pulses of a few femtoseconds, see [220, 221] and references therein.

Recently, these femtosecond nuclear dynamics have been experimentally measured in D_2 [222], where a fs infrared pulse induced a coherent transfer of population from the ground to the first vibrational excited state of the Electronic Ground State (EGS). However this population transfer raises the question of the vibrational excitation mechanism. Indeed for homonuclear diatomic molecules, the electric field does not couple the vibrational states within a given electronic state. The absorption of one or several photons is thus forbidden by symmetry. Two different mechanisms were proposed to explain this vibrational excitation in the EGS: Bond-Softening (BS) and Lochfraß (LF) [223]. Both are based on an adiabatic approach in a Born-Oppenheimer (BO) representation of the time-dependent wave function (V.10) where the electronic and nuclear dynamics are treated separately (see section V.1.2). The former, BS, is caused by the instantaneous Stark shift E_S while the latter, LF, is caused by the instantaneous tunnel ionization rate Γ (II.70). In the Born-Oppenheimer representation (V.15) they can be seen as potential terms that depend on the internuclear distance R, and that effectively distort the Potential Energy Surface (PES) of the electronic ground state. The Stark shift distorts the real part of the PES while the ionization rate distorts its imaginary part, i.e. the lifetime of the dressed state [224, 225]. Both effects thus occur simultaneously, and may even interfere with each other. Nevertheless they behave differently and were given different interpretations [223].

In the case of the BS, since the polarizability of the molecule increases with the internuclear distance, the Stark shift attracts the Nuclear Wave Packet (NWP) towards

larger values of R, and induces some nuclear dynamics. In this mechanism it is the coupling of the electronic ground state to the excited states, and especially to the first excited states, that causes the Stark shift, and hence the nuclear dynamics. It is generally accepted that another interpetation of the BS can be given in terms of Raman two-photon transitions [222], where both photon energies are found within the broad frequency width of the femtosecond pulse. The adiabatic interpretation relies on the states that are dressed by the instantaneous electric field, while the Raman interpretation relies on field-free states.

The other mechanism, LF (which can be translated from german as *whole eating*), is caused by the instantaneous tunnel ionization rate. In general the R-dependence of the ionization rate will be mostly inherited from the R-dependence of the vertical ionization potential defined within the BO framework as $I_p(R) = E_{H_2^+}(R) - E_{H_2}(R)$. Indeed, as we saw in Chapter III, the tunnel ionization rate depends exponentially on the ionization potential. For values of R that remain close to the equilibrium distance, the ionization potential decreases with R, and the ionization rate thus increases with R. The accepted interpretation, initially given in [223, 222], is that the electronic ground state is depopulated ("eaten") faster at large internuclear distances, inducing a nuclear dynamics. In this mechanism the nuclear dynamics is caused by the coupling of the electronic ground state to the continuum states.

Although the BS and LF mechanisms occur simultaneously and may in principle interfere, they are usually thought of as being independent from each other, and are thus treated separately [222, 223, 226]. For BS one needs to solve the BO nuclear TDSE (V.15) taking into account only the Stark shift E_S, while for LF one solves (V.15) with only the ionization rate Γ. In the two cases one finds that, at the end of the pulse, some population has been transfered from the ground to the first vibrational excited state, and that the population in the higher excited states remains negligible (see Figure V.3). The NWP thus starts to oscillate at a frequency ω_{vib} equal to the energy difference between these two vibrational states (see Figure V.4). In particular the average value of R can be written as $\langle R \rangle = \langle R_0 \rangle + \delta_R \cos(\omega_{vib} t - \Phi)$, where the phase Φ of this oscillation depends on the considered mechanism. If one takes only LF into account then $\Phi_{LF} = \pi$, while if only BS is considered then $\Phi_{BS} = \pi/2$ [222]. This phase was experimentally measured in [222] for D_2 where they obtained $\Phi_{exp} = 0.946\pi$, and in [227] for I_2 where $\Phi_{exp} = 0.81\pi$. In both cases they concluded that it was a direct experimental proof of the observation of Lochfraß.

However there is no established theoretical background relating the value of this phase Φ to the relative importance of LF and BS which would support such a conclusion. Besides, simulations that include only one or the other of the two mechanisms are somewhat artificial. To justify such a separation, one would have to consider that BS and LF are completely decoupled. This is far from being intuitive, since they can occur simultaneously, and both affect the NWP dynamics. For example we might see some enhancement effects since BS attracts the NWP towards larger values or R where LF is more efficient, or on the contrary some inhibition since LF localizes the NWP towards smaller values of R where BS is less efficient. Moreover, to the best of our knowledge, there have been no rigorous derivation of the modified nuclear TDSE (V.15) that would prove that the electronic degrees of freedom could be averaged in such a way. In particular, the effects of the nuclei-electron correlation which is completely neglected in this model has never

been investigated.

In this work we question the ability of the uncorrelated BO framework to describe the vibronic dynamics of diatomic molecules in strong laser fields. We study a simple 2D model system, with one dimension for the electron position x and one dimension for the internuclear distance R. We first assess the qualitative relevance of the previous approaches [222, 223, 226] where the LF and BS mechanisms were treated separately. We compare the predictions of the LF and BS to the full BO model where both mechanisms are included to question the limits of the interpretations based on the LF/BS dichotomie. Then we investigate the limits of the this BO model by comparing its results to fully correlated bidimensional simulations. Finally, we propose a consistent analytic derivation of the nuclear TDSE for the case of BS, and we give hints for the derivation of the total BO model that would also include LF.

Objectives

- Derive analytically the nuclear TDSE in the Born-Oppenheimer and adiabatic approximations.
- Find the limits of this approach to describe nuclear dynamics in strong fields.
- Investigate the effects of the correlation between the nuclei and the electrons.

V.1 Methods

We investigate the nuclear dynamics of a homonuclear diatomic model molecule submitted to a strong femtosecond infrared pulse. We use two different approaches: the Born-Oppenheimer adiabatic approach that was proposed in [223] taking into account *both* the BS and LF, and a correlated approach where both nuclear and electron are treated within the same level of theory. We use a 2D model system, where the electron is confined in the direction of the molecular axis, for which extensive simulations can easily be performed. It can be argued that the BS mechanism is predominant on the LF in this case. Indeed the Stark shift, which is responsible for BS but that inhibits tunnel ionization and thus LF, is maximal for a parallel alignment of the molecule with the field. To be able to compare BS and LF, we thus consider different model systems: (i) an analogue of H_2, (ii) a more artificial system (in the sense that it has no direct physical analogue), that we will call A_2 in the following, for which LF is enhanced, and (iii) to investigate the role of the electronic excited states, we also consider and a short range system that we call G_2 that has only two bound electronic states.

V.1.1 Two dimensional model systems

We consider 2D model systems like the one described in section II.2.1 where the first dimension corresponds to the electron position x, and the second dimension to the internuclear distance R. The total Hamiltonian reads:

$$H(x,R,t) = -\frac{1}{2\mu}\frac{\partial^2}{\partial R^2} - \frac{1}{2}\frac{\partial^2}{\partial x^2} + V_{\mathrm{NN}}(R) + V_{\mathrm{Ne}}(x,R) + H_{\mathrm{int}}(x,t) \tag{V.1}$$

where the first two terms are kinetic energy terms with μ the reduced mass of the nuclei, V_{NN} is the nucleus-nucleus interaction which will be taken to be equal to the PES of the ground state of H_2^+, V_{Ne} is the nuclei-electron interaction potential and H_{int} is the interaction with the field. To remain consistent with the adiabatic approximation which is formulated in length gauge, we will use the expression:

$$H_{\mathrm{int}} = xF_{\mathrm{L}}(t). \tag{V.2}$$

The nucleus-electron interaction depends on the system. For the H_2 analogue we use a molecular Soft-Coulomb potential:

$$V_{\mathrm{Ne}}^{H_2}(x,R) = -\frac{0.5}{\sqrt{a(R)^2+(x+R/2)^2}} - \frac{0.5}{\sqrt{a(R)^2+(x-R/2)^2}}, \tag{V.3}$$

where the regularization parameter $a(R)$ is adapted so that the electronic ground state at each value of R has the same energy as the one of the real H_2 molecule. Our system is to some extent comparable to a real H_2 molecule that would be aligned with the laser electric field. In particular the BO vibrational states and energies are identical.

We also define the system A_2 for which we use a simple Soft-Coulomb potential:

$$V_{\mathrm{Ne}}^{A_2}(x,R) = -\frac{1}{\sqrt{a(R)^2+(x+R/2)^2}}, \tag{V.4}$$

where again we fit the regularization parameter $a(R)$ so that the electronic ground state energy matches the one of the real H_2 molecule. This system has no physical counterpart, but it will have a nuclear dynamics quite close to the one of H_2 since it evolves on the same PES. In particular since it is a single-well potential, its polarizability is strongly reduced, so that LF is enhanced with respect to BS.

Finally, to study the influence of the electronic excited states, we also consider a system, that we call G_2. For this system we use a short range Gaussian potential:

$$V_{\mathrm{Ne}}^{G_2}(x,R) = -A(R)\,\mathrm{e}^{-(x+R/2)^2/2\sigma} - A(R)\,\mathrm{e}^{-(x-R/2)^2/2\sigma}, \tag{V.5}$$

where again the prefactor $A(R)$ is fitted so that the electronic ground state energy matches the one of the real H_2 molecule and where we chose $\sigma = 0.8$ a.u. so that the system has only one electronic excited state.

The TDSE is solved with the split-operator method described in section II.2.2. To avoid unphysical reflections at the borders of the simulation box, we use absorbing conditions (II.32) with a width of $h_{\mathrm{abs}} = 100$ a.u. in the x dimension of the grid (see section II.1.2 c)). The results obtained this way are *exact* up to numerical accuracy and will be considered as a reference in the following. We will denote them as the XR results. In this representation the wave function is computed on a bidimensional grid, so that we get all possible excited and ionized states. To compare with the experiments [222, 227] that measure the average value of R in the Electronic Ground State (EGS) $\langle R\rangle_{\mathrm{EGS}}$, we will *project* our 2D wave function on the EGS $\varphi_0^{(\mathrm{BO})}(x;R)$ computed with the BO approximation

$$\psi_{\mathrm{EGS}}(x,R,t) = \varphi_0^{(\mathrm{BO})}(x;R)\frac{\int \varphi_0^{(\mathrm{BO})}(x';R)\psi(x',R,t)\,\mathrm{d}x'}{\sqrt{\int\left|\int \varphi_0^{(\mathrm{BO})}(x';R)\psi(x',R,t)\,\mathrm{d}x'\right|^2\mathrm{d}R}}. \tag{V.6}$$

and compute the average value of R in this projected wave function $|\psi_{\mathrm{EGS}}(t)\rangle$:

$$\langle R\rangle_{\mathrm{EGS}}(t) = \langle\Psi_{\mathrm{EGS}}(t)|R|\Psi_{\mathrm{EGS}}(t)\rangle \tag{V.7}$$

$$= \frac{\int R\left|\int \varphi_0^{(\mathrm{BO})}(x;R)\psi(x,R,t)\,\mathrm{d}x\right|^2 \mathrm{d}R}{\int\left|\int \varphi_0^{(\mathrm{BO})}(x';R)\psi(x',R,t)\,\mathrm{d}x'\right|^2 \mathrm{d}R}. \tag{V.8}$$

From the wave function we also have a direct access to the population $P_i(t)$ in the exact vibronic states of the molecule $\varphi_i(x,R)$, by simple projection:

$$P_i(t) = \left|\int \varphi_i(x,R)\psi(x,R,t)\,\mathrm{d}x\,\mathrm{d}R\right|^2. \tag{V.9}$$

V.1.2 Born Oppenheimer and adiabatic approximations

In the same spirit as the usual time-independent BO formalism, the wave function is factored in an electronic and a nuclear contribution:

$$\psi(x,R,t) = \widetilde{\varphi}_0(x;R,t)\chi(R,t), \tag{V.10}$$

where $\widetilde{\varphi}_0(x;R,t)$ is the electronic ground state *dressed* by the instantaneous electric field $F_{\mathrm{L}}(t)$ for which R and t are just parameters, and $\chi(R,t)$ is the nuclear wave packet that propagates on this dressed electronic state. The adiabatic approximation supposes that this field-dressed state $\widetilde{\varphi}_0(x;R,t)$ instantaneously adapt to the value of the time-dependent electric field. It is thus solution, for each time t, of the field-dressed electronic time-"independent" (in the sense that the time is just a constant parameter) Schrödinger equation:

$$\left[-\frac{1}{2}\frac{\partial^2}{\partial x^2} + V_{\mathrm{Ne}}(x,R) + xF_{\mathrm{L}}(t)\right]\widetilde{\varphi}_0(x;R,t) = \varepsilon_0(R,F_{\mathrm{L}}(t))\widetilde{\varphi}_0(x;R,t), \tag{V.11}$$

where $\hat{H}_{\mathrm{el}}(x,R,t) = -\frac{1}{2}\frac{\partial^2}{\partial x^2} + V_{\mathrm{Ne}}(x,R) + xF_{\mathrm{L}}(t)$ is the electronic Hamiltonian comprising the kinetic energy of the electrons $-\frac{1}{2}\frac{\partial^2}{\partial x^2}$, the electron-nuclei interaction potential V_{Ne}, and the electron-field interaction in length gauge $xF_{\mathrm{L}}(t)$ (see section I.1.2), and where the field-dressed energy is given by

$$\varepsilon_0(R,F) = E_0(R) + E_{\mathrm{S}}(R,F) - \mathrm{i}\frac{\Gamma(R,F)}{2}, \tag{V.12}$$

where $E_0(R)$ is the field-free PES of the electronic ground state, E_{S} is the DC Stark shift (see section II.1.4) and Γ is the tunnel ionization rate (see section II.3.1). It is important to understand that in this representation, the internuclear distance R and the time t that appear in (V.11) and (V.12) are only fixed parameters, and not variables. The fact that R is a parameter is related to the BO approximation, while for t it is related to the adiabatic approximation. The total TDSE (V.13) can thus be reorganized as (V.14):

$$\mathrm{i}\frac{\partial\psi}{\partial t}(x,R,t) = \left[-\frac{1}{2\mu}\frac{\partial^2}{\partial R^2} + V_{\mathrm{NN}}(R) + H_{\mathrm{el}}\right]\psi(x,R,t) \tag{V.13}$$

$$\mathrm{i}\widetilde{\varphi}_0(x;R,t)\frac{\partial\chi}{\partial t}(R,t) = \widetilde{\varphi}_0(x;R,t)\left[-\frac{1}{2\mu}\frac{\partial^2}{\partial R^2} + V_{\mathrm{NN}}(R) + \varepsilon_0(R,F)\right]\chi(R,t). \tag{V.14}$$

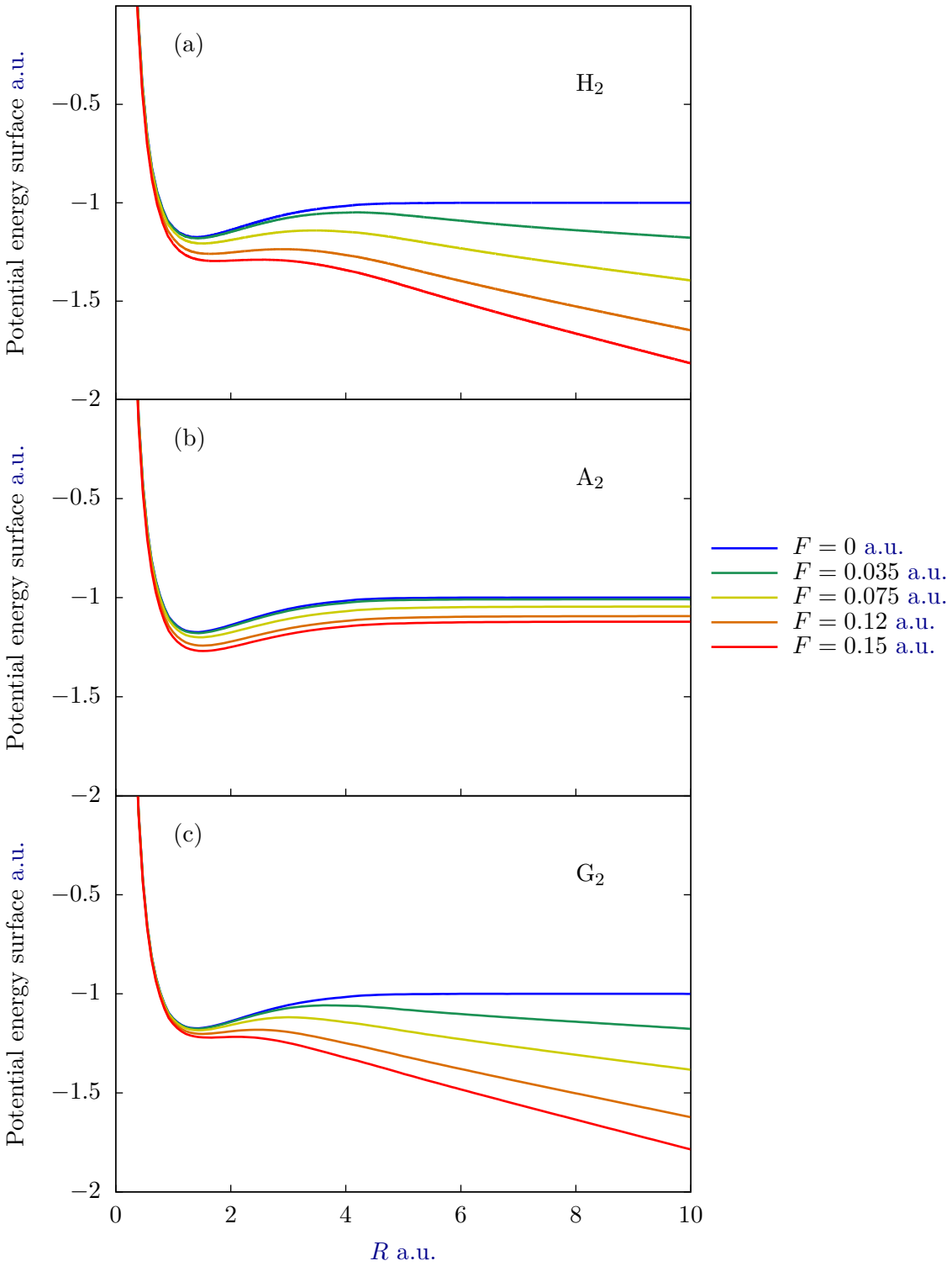

Figure V.1 *Potential energy surface of the electronic ground state, in presence of a static electric field, for (a) H_2, (b) A_2 and (c) G_2.*

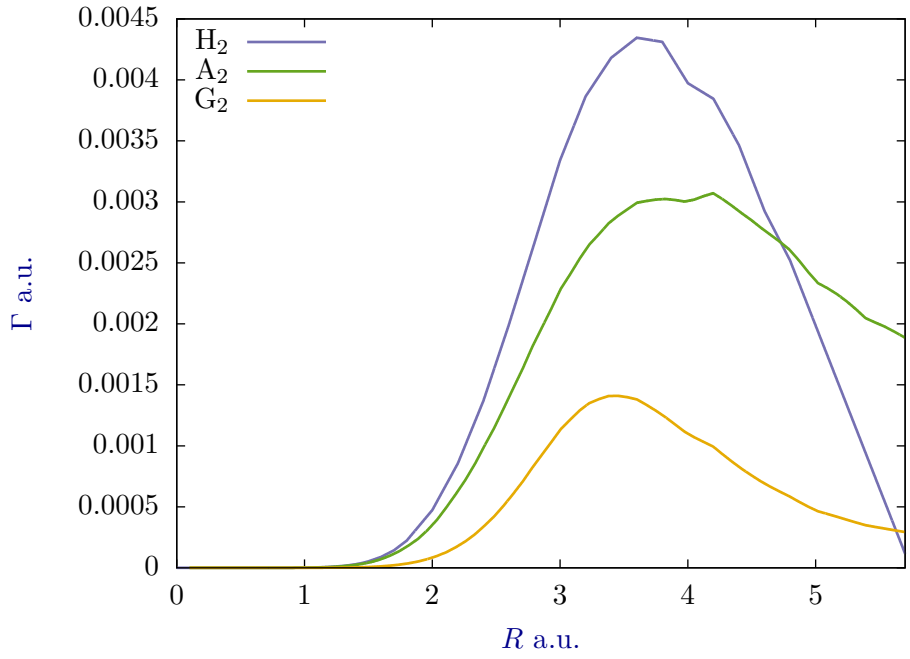

Figure V.2 *Ionization rate as a function of R for a field $F = 5 \times 10^{-2}$ a.u..*

Note that we neglected the $\partial\widetilde{\varphi_0}(x;R,t)/\partial t$ term using the adiabatic approximation, and the $\partial^2\widetilde{\varphi_0}(x;R,t)/\partial R^2$ term using the BO approximation. We can simplify (V.14) by $\widetilde{\varphi_0}(x;R,t)$ to get a purely nuclear TDSE:

$$\mathrm{i}\frac{\partial\chi}{\partial t}(R,t) = \left[-\frac{1}{2\mu}\frac{\partial^2}{\partial R^2} + V_{\mathrm{NN}}(R) + E_0(R) + E_{\mathrm{S}}(R,F_{\mathrm{L}}(t)) - \mathrm{i}\frac{\Gamma(R,F_{\mathrm{L}}(t))}{2}\right]\chi(R,t). \tag{V.15}$$

Therefore in this adiabatic BO formalism we completely separated the electronic and the nuclear dynamics. As mentioned in the introduction, we can thus concentrate on the nuclear dynamics by considering a nuclear wave packet that evolves on a field-dressed PES. The interaction with the electron and with the laser field is taken into account solely through the instantaneous Stark shift E_{S} and tunnel ionization rate Γ.

The nuclear equation (V.15) is solved with the Crank-Nicolson algorithm as described in section II.1.2 b). In the adiabatic approximation, the Stark shift E_{S} and the tunnel ionization rate Γ are computed for each value of R in a static electric field F. The Stark shift is computed with the *Rbox* method described in section II.1.4, and the tunnel ionization rate is computed by solving the electronic TDSE as described in section II.3.1. Both quantities are computed for a large number of R and F values, and then interpolated at each time step and on each grid point.

The field-dressed potential energy curves obtained for a few value of the electric field are shown on Figure V.1 for the three systems under study. For H_2 and G_2 the PES are quite similar: as mentioned in the introduction, as the polarization increases with R, the Stark shift is larger at higher values of R so that a potential energy barrier appears through which the NWP can tunnel out and dissociate. This behavior is in agreement

with the expected behavior in the real H_2 molecule [224, 221]. The behavior of the PES is very different in the case of A_2. Indeed, since there is only one potential well, the polarizability is almost independent of R, and the PES are almost parallel. Since the Stark shift does not strongly depend on R, it will almost not affect the nuclear dynamics, and the BS will be reduced and LF should dominate, which is exactly why we constructed this system.

The ionization rates, computed by solving the TDSE in a static field $F = 5\times10^{-2}$ a.u. for each model molecule, are shown in Figure V.2. We see that it behaves quite similarly for the three systems: it has a bell shape with a maximum located around 3.5 a.u., well beyond the equilibrium distance of $R = 1.45$ a.u.. This confirms that the ionization rate has a positive slope near the equilibrium distance. Since ionization in this model is accounted for by a R-dependent "absorption", LF should induce a motion of the NWP towards small values of R.

V.2 Results

The three systems described in the previous section are submitted to various laser pulses of central wavelength $\lambda_L = 800$ nm and of general shape:

$$F_L(t) = F_0 \sin(\omega_L t + \phi_{cep}) \sin^2\left(\frac{\omega_L}{2N_c}t\right), \tag{V.16}$$

where ω_L is the laser pulsation, N_c is the number of optical cycles in the pulse, and ϕ_{cep} is the Carrier Envelope Phase (CEP). We then follow the nuclear dynamics by computing the populations in the different vibrational states and the average value of the internuclear distance. Note that in the BO approach, the average value of R is computed on the *dressed* EGS $\widetilde{\varphi}_0(x;R)$ (V.11), while in correlated simulations we compute it on the *field-free* EGS $\varphi_0^{(BO)}(x;R)$. Nevertheless these two states become equivalent as soon as the laser pulse is switched off, so that we will concentrate on the oscillations of the NWP *after* the end of the pulse.

We will first come back on the difference between Lochfraß and Bond-Softening, then confront the BO results, taking into account both LF and BS, to the correlated results, to be able to investigate the limits of the BO approach. Note that, to be consistent with [222, 223, 227], throughout this section we define the origin of time at the maximum of the laser pulse rather than at the beginning of the simulation. This allows to compare more easily the results obtained with different pulse durations.

V.2.1 Lochfraß and Bond-Softening

We start by comparing the differences and similarities between LF and BS. For this we solve the nuclear TDSE (V.15) including *either* the Stark shift E_S or the ionization rate Γ (V.12) or both (see section V.1.2). The population in the three first vibrational excited states during the pulse are shown in Figure V.3 for the H_2 system submitted to an 8 optical cycle long pulse of intensity $I_L = 4\times10^{14}$ W.cm^{-2}. Note that in the LF simulation, the population in the EGS decreases during the propagation due to ionization. To compare with the BS case, we thus renormalize the population in the vibrational states to the total population in the EGS. We observe that, for both LF and

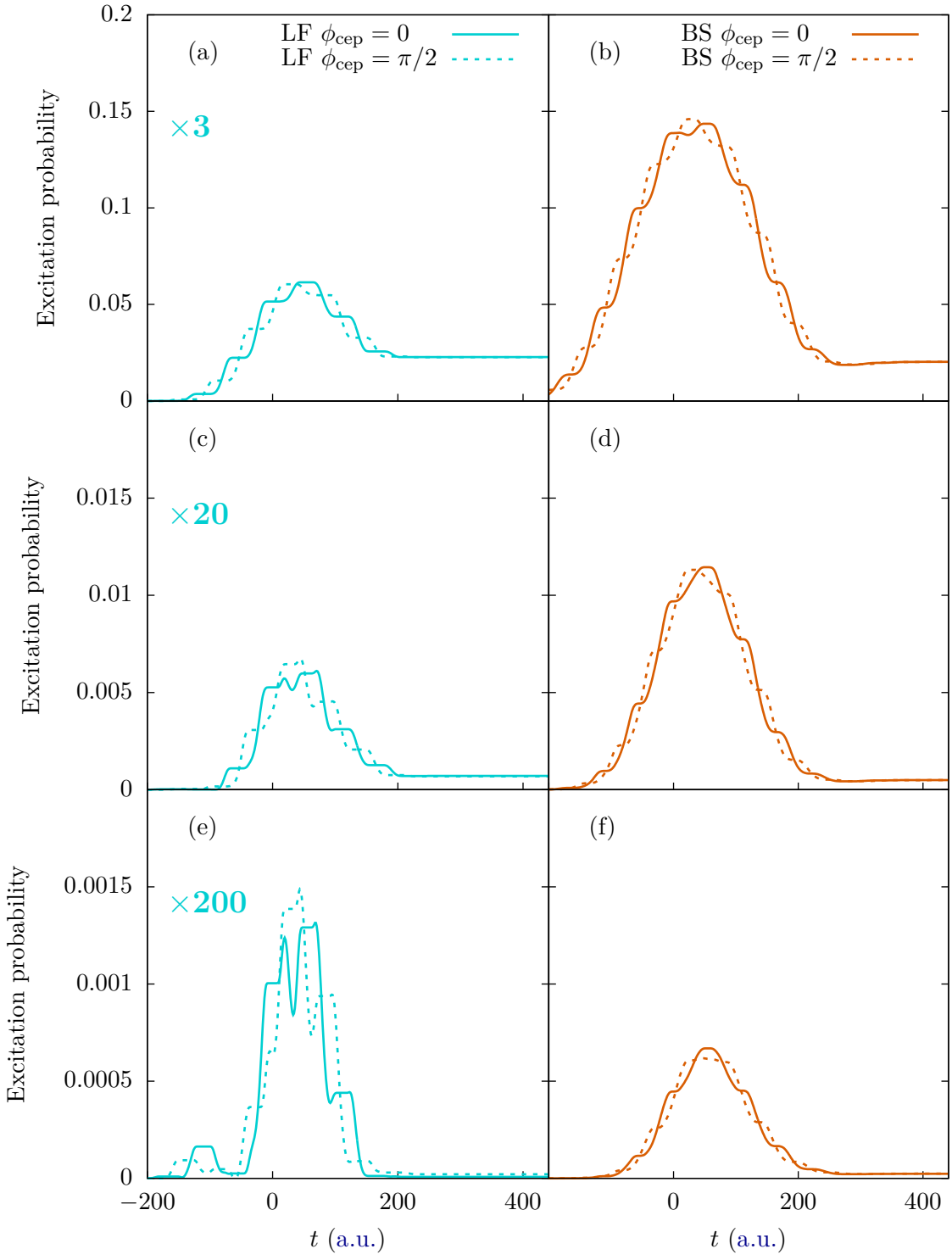

Figure V.3 *Population in the first three vibrational states, normalized by the total population in the electronic ground state, as a function of time for the H_2 model system submitted to an 8 optical cycle long laser pulse of $I_L = 4 \times 10^{14}$ W.cm^{-2}, and different CEP. (a) and (b) first vibrational excited state, (c) and (d) second vibrational excited state, (e) and (f) third vibrational excited state. (a) (c) (e) are computations taking only LF into account, while (b) (d) (f) only BS.*

BS, the different vibrational excited states get populated during the pulse, creating a vibrational wave packet in the EGS. In agreement with [222, 223], we find that almost only the first vibrational excited state (panel (a) and (b)) gets populated. The population in the higher excited states (panel (c), (d), (e) and (f)) remains negligible and will thus not affect the nuclear dynamics. Note that, as mentioned in [222], the CEP has very little effects on the dynamics. The differences between $\phi_{\text{cep}} = 0$ (solid lines) and $\phi_{\text{cep}} = \pi/2$ (dotted lines) that we observe during the pulse highlights the fact that BS and LF mainly occur at the maxima of the field, i.e. at each half cycle. As soon as the laser is switched off, these differences vanish and the two curves merge. We checked that these observations are generally insensitive to the pulse duration and intensity.

We find that both mechanisms actually predict a quite similar bell-shaped behavior for the populations in the different vibrational states as a function of time. In our case we find that the BS mechanism induces more excitation than the LF mechanism but as discussed in introduction this may be an effect of the reduced dimensionality. In any case, this difference in the absolute value of the population will only influence the *amplitude* δ_R of the oscillations of the wave packet, which is difficult to measure experimentally. To overcome this problem, in [222, 227], the *phase* Φ of these oscillations was used to distinguish between LF and BS.

To understand why, we plot the average value of R on Figure V.4 for our model systems H_2 (panel (a)) and A_2 (panel (b)). As expected we observe oscillations which, as soon as the laser is switched off, behave like

$$\langle R \rangle = R_0 + \delta_R \cos(\omega_{\text{vib}} t - \Phi). \tag{V.17}$$

Note that in the BO case, ω_{vib} has the same value for the two systems since they evolve on the same potential energy surface, and have thus exactly the same vibrational states.

We see on this figure that the distinction between LF and BS can be easily be accessed from the average value of R. Indeed each mechanism predicts a different phase Φ for the NWP oscillations. In agreement with [222, 223], we find that the phase predicted by the Lochfraß mechanism is close to π: for the conditions used in Figure V.4 we find $\Phi = 1.08\pi$ for H_2 and $\Phi = 1.05\pi$ for A_2. To see it more clearly we plot with a dashed green line on panel (c) a cosine with the same frequency ω_{vib} as H_2 and A_2 and with $\Phi = \pi$, that is visibly in phase with the LF predicted oscillations (dot-dashed blue line on panels (a) and (b)). More surprisingly, we find that the phase predicted by the BS mechanism is not exactly equal to $\pi/2$ as claimed in [222]: we find $\Phi = 0.69\pi$ for H_2 and $\Phi = 0.59\pi$ for A_2. We plotted a cosine with $\Phi = \pi/2$ on panel (c) (dotted yellow line), and we notice that it is slightly dephased with the BS predicted oscillations (dotted orange line on panels (a) and (b)).

An interpretation of the value of this oscillation phase Φ was given in [222, 223, 227]. This interpretation is based on the initial triggering of the nuclear motion. For LF it is related to the slope of the ionization rate: if the ionizate rate increases with increasing R, then the NWP is "eaten" faster at higher values of R and is thus initially "pushed" towards small values of R. The average value of R is thus *minimal* at $t = 0$ (i.e. at the maximum of the laser pulse) and the oscillation phase is $\Phi = \pi$. On the contrary for BS the NWP is first attracted towards large internuclear distances by the shape of the PES. The average value of R is thus *maximal* at $t = 0$, and the oscillation phase is $\Phi = \pi/2$. According to this interpretation, the oscillation phase Φ would be directly deduced from

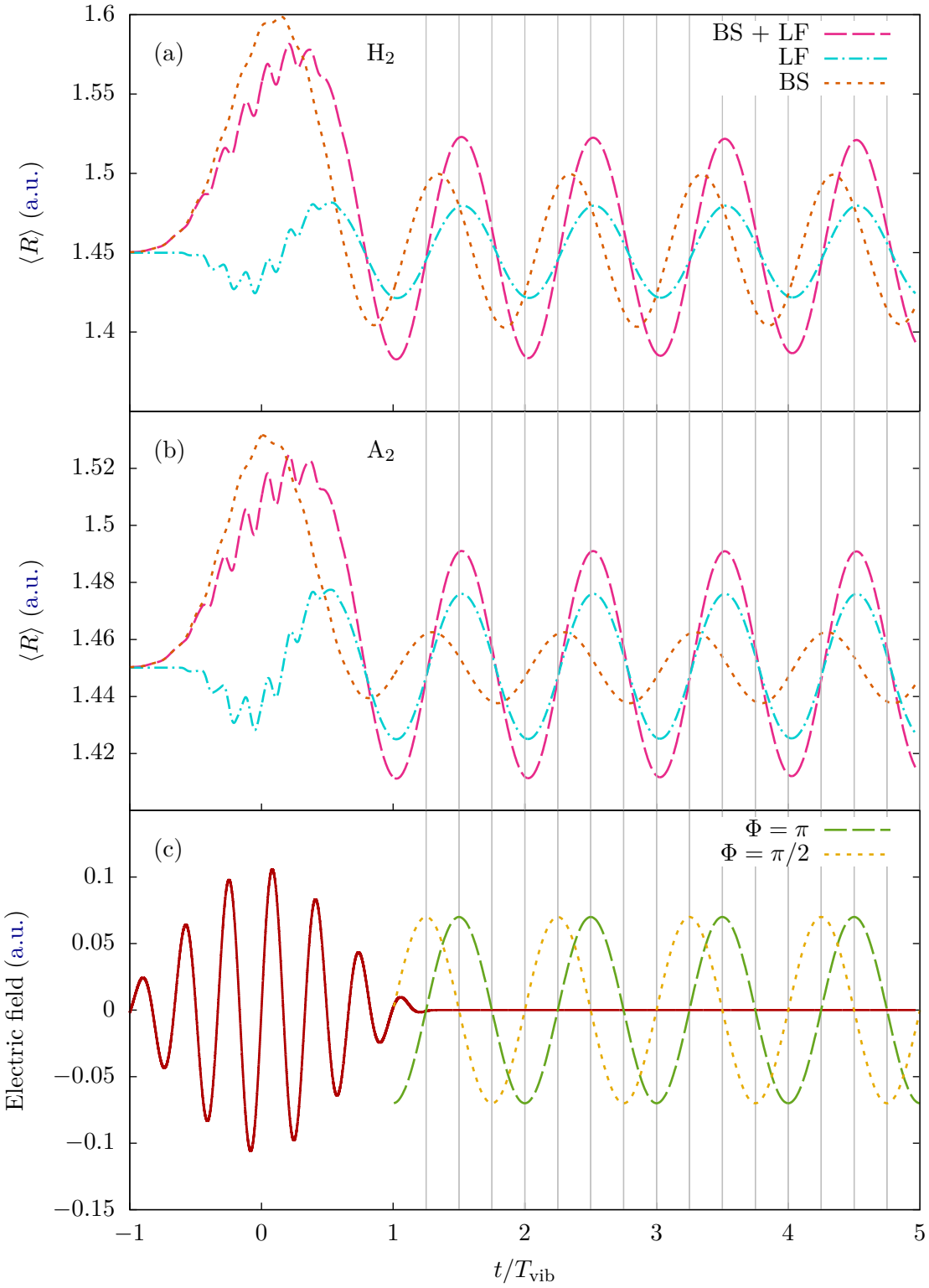

Figure V.4 *Average value of the internuclear distance in the electronic ground state for an 8 cycle long pulse of* $I_L = 4\times10^{14}$ W.cm^{-2}, *with a CEP of* $\phi_{cep} = 0$ *for (a)* H_2 *and (b)* A_2. *The laser field is drawn on panel (c), along with two cosine functions* $A\cos(\omega_{H_2}t - \Phi)$ *with arbitrary amplitude* A. *Gray lines are drawn at times* $t_n = n\frac{T_{vib}}{4}$.

the initial motion of the NWP: if it initially moves towards large R then $\Phi = \pi/2$, while if it initially moves towards small R then $\Phi = \pi$

Yet this interpretation only holds as long as one considers BS and LF *separately*. Since they actually occur simultaneously, we need to include them both at the same time to correctly describe the dynamics. When we do so (dashed pink line on panels (a) and (b)) we see that, for both systems, the average value of R is *maximal* at $t = 0$. The NWP thus starts to move towards large R, but the phase of the oscillation is close to $\Phi \simeq \pi$. This is the opposite of the predictions given by the interpretation of [222, 223, 227] ! This indicates that there is actually no direct relation between the phase of the oscillations and the displacement of the wave packet at $t = 0$. As a consequence, the slope of the ionization rate near the equilibrium distance cannot be deduced from this oscillation phase Φ, as was claimed in [227]. More importantly, it indicates that the interpretation of this oscillation phase is much more delicate than what was suggested in [222, 223, 227].

Since BS and LF predicts two very different values for the phase Φ of the NWP oscillations, it was claimed in [222, 223] that measuring the phase Φ could allow to distinguish between the two mechanisms. This assumption is based on the hypothesis that the prevailing mechanism imposes its phase on the global oscillations. For example, in the conditions used in Figure V.4, we see that, for the H_2 systems, the BS mechanism predicts a higher oscillation amplitude δ_R than LF and is thus the dominant mechanism. On the contrary, for A_2 the oscillation amplitude δ_R predicted by LF is the highest, indicating that LF is prevailing. However if we look at the results predicted by the complete model (dashed pink line), taking into account both LF and BS, we see that *both* H_2 and A_2, have the *same* phase for the wave packet oscillations. They both oscillate with a π phase, indicating that, in both cases, LF imposes its phase, even if it is not the dominant mechanism. This shows that the measure of Φ *cannot* allow to conclude on the prevailing mechanism, as was done in [222, 227].

To conclude, we find that the oscillation phase Φ is a consequence of the interplay between the two excitation mechanisms (LF and BS). It is thus very delicate to extract meaningful information from this quantity.

V.2.2 Influence of the vibronic correlation

In the previous section we have seen that, in the BO framework, it is mandatory to consider both LF and BS at the same time to get the proper behavior of the NWP. If one considers only one mechanism, this leads to unphysical results and interpretations. In this section, we investigate the limits of this BO model (with both LF and BS) by confronting its predictions to fully correlated simulations that treats the active electron and the nuclei at the same level of theory.

First, we will clarify what we mean by the term "correlation". In general, the correlations are defined by "all that is not included in the uncorrelated model". In our case, it will thus include all that is not described by the BO representation of the wave function. By looking at the two dimensional wave function, we see that the correlations may originate from different contributions. These contributions are schetched on Figure V.5 (a), where we draw them in the (x, R) plane. The contributions that are restricted to the R axis (i) or to the x axis (ii) are *uncorrelated*. They do not couple x and R, so that we expect them to be inlcuded in the BO model. On the other hand the diagonal

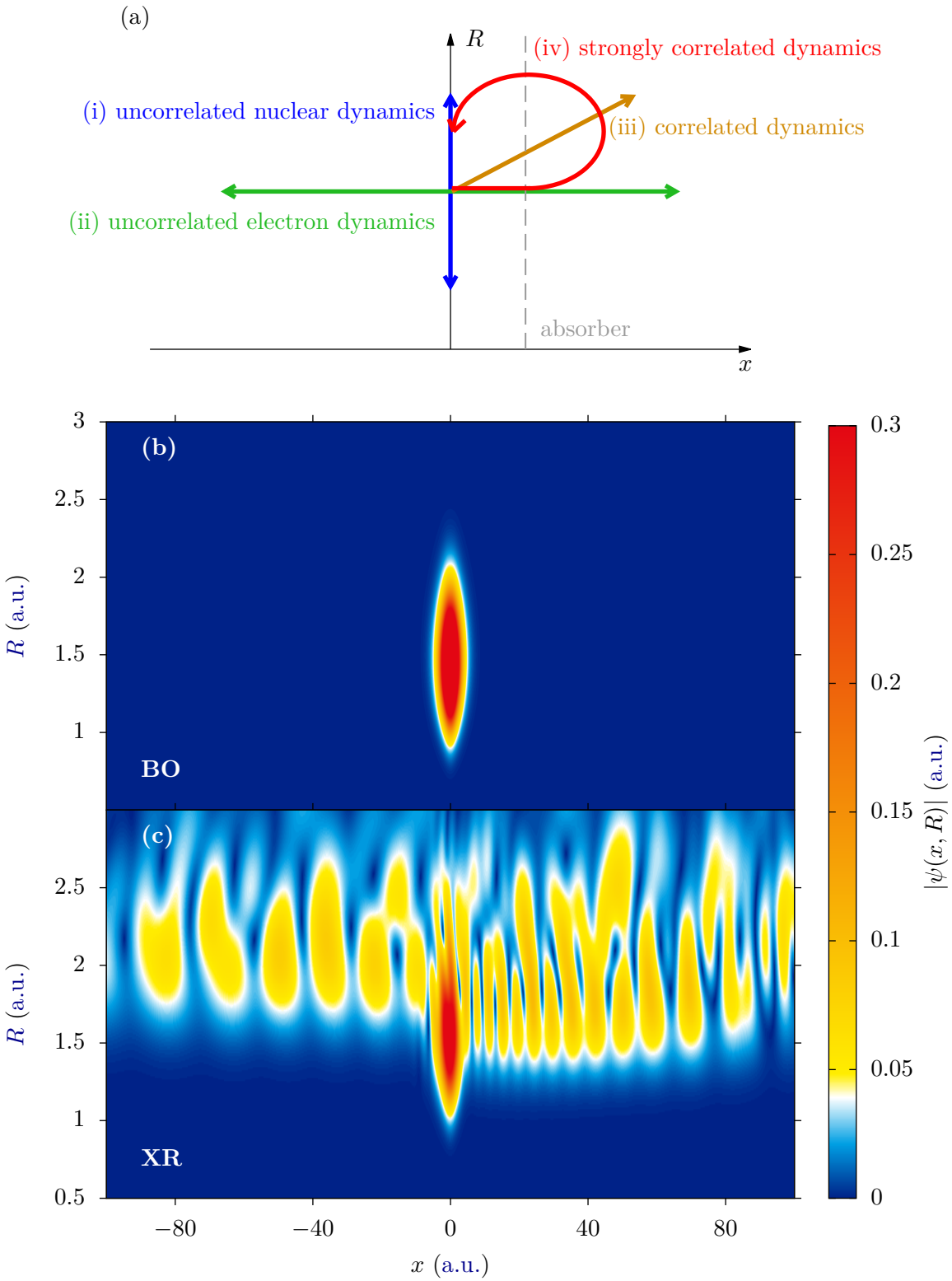

Figure V.5 *Illustration of the vibronic correlations. (a) Schematic representation of the different contributions to the vibronic correlations in the dynamics, and absolute value of the wave function at* $t = 0.27T_{\mathrm{vib}}$ *during an 8 optical cycle long laser pulse of* $I_{\mathrm{L}} = 3 \times 10^{14}$ W.cm^{-2} *and* $\phi_{\mathrm{cep}} = \pi/2$ *computed with (b) the BO model and (c) the XR correlated model.*

contributions (iii) will couple the electronic and nuclear degrees of freedom. We might intuitively think that they cannot be described in the BO formalism. This is actually true, these parts of the wave function will not be represented in the BO model. However, as long as these diagonal parts leave the EGS and never interfere with it afterwards, they will not affect the nuclear dynamics in this EGS. They will actually be handled by the R-dependent Stark shift E_S and tunnel ionization rate Γ in (V.15). Their influence on the nuclear dynamics will thus be included in the BO model, even if these parts of the wave function are not explicitely represented. On the contrary, the contributions that couple x and R and that subsequently return to the EGS (iv) will influence the nuclear dynamics. However in the BO formalism, we do not keep track of the parts of the wave function that leave the EGS. These contributions are therefore absent from this model, and will be refered to as "vibronic" correlations in the following. We assess their impact on the nuclear dynamics by confronting the BO results with the fully correlated simulations.

We mention that it is very difficult to disentangle the four contributions that we just mention directly from the time dependent wave function. This is illustrated on panel (b) and (c) of Figure V.5, where we show the wave function at an arbitrary time $t \simeq 0.27 T_{\text{vib}}$ during the laser pulse computed either in the BO formalism (b), or with the fully correlated XR model (c). As expected we see that the BO wave function can only represent the nuclear dynamics, close to the R axis, while the XR wave function contains all the different contributions. However it is very difficult to discriminate, from this wave function, between contributions (iv) that might come back to interfere with the EGS and contributions (iii) that leave and never return. We will thus rely on quantities that are related to physical obervables, like the populations in the vibrational states and the average value of the internuclear distance.

The populations in the first vibrational states of the H_2 model system are plotted on Figure V.6 for a laser pulse of $I_L = 10^{14}$ W.cm^{-2}, and on Figure V.7 for $I_L = 4 \times 10^{14}$ W.cm^{-2}. The BO model (right panels) predicts the similar bell-shaped behavior that we saw in Figure V.3 for the three first vibrational excited states. The correlated simulations are in very good agreement with the BO model for the first vibrational excited state (panels (a) and (b)). However, the agreement deteriorates when considering the 2$^{\text{nd}}$ (panels (c) and (d)) and 3$^{\text{rd}}$ (panels (e) and (f)) vibrational excited states. Not only are the shapes of the curves different during the pulse, but the populations at the end of the pulse are much higher in the correlated simulations. This indicates that there are some excitations in the higher vibrational levels of the neutral molecule that are not reproduced by the BO model. Moreover, in the correlated model, the populations in the vibrational excited levels now strongly depend on the CEP both during the pulse and after. This behavior is not predicted at all by the BO model, which suggests that it is caused by vibronic correlations. We remark that this effect increases strikingly with the laser intensity. At $I_L = 10^{14}$ W.cm^{-2}, the population in the first vibrational excited state is virtually insensitive to the CEP. The populations in the higher excited states are mostly affected by this parameter while the laser is on, but not so much after the pulse is finished. On the contrary at $I_L = 4 \times 10^{14}$ W.cm^{-2} all the populations substantially depend on the CEP.

To illustrate how this affects the dynamics of the NWP, we plot on Figure V.8 the average value of R for different intensities $I_L = 10^{14}$ W.cm^{-2}, $I_L = 3 \times 10^{14}$ W.cm^{-2} and $I_L = 4 \times 10^{14}$ W.cm^{-2}. As expected, we note a good agreement between the BO and the

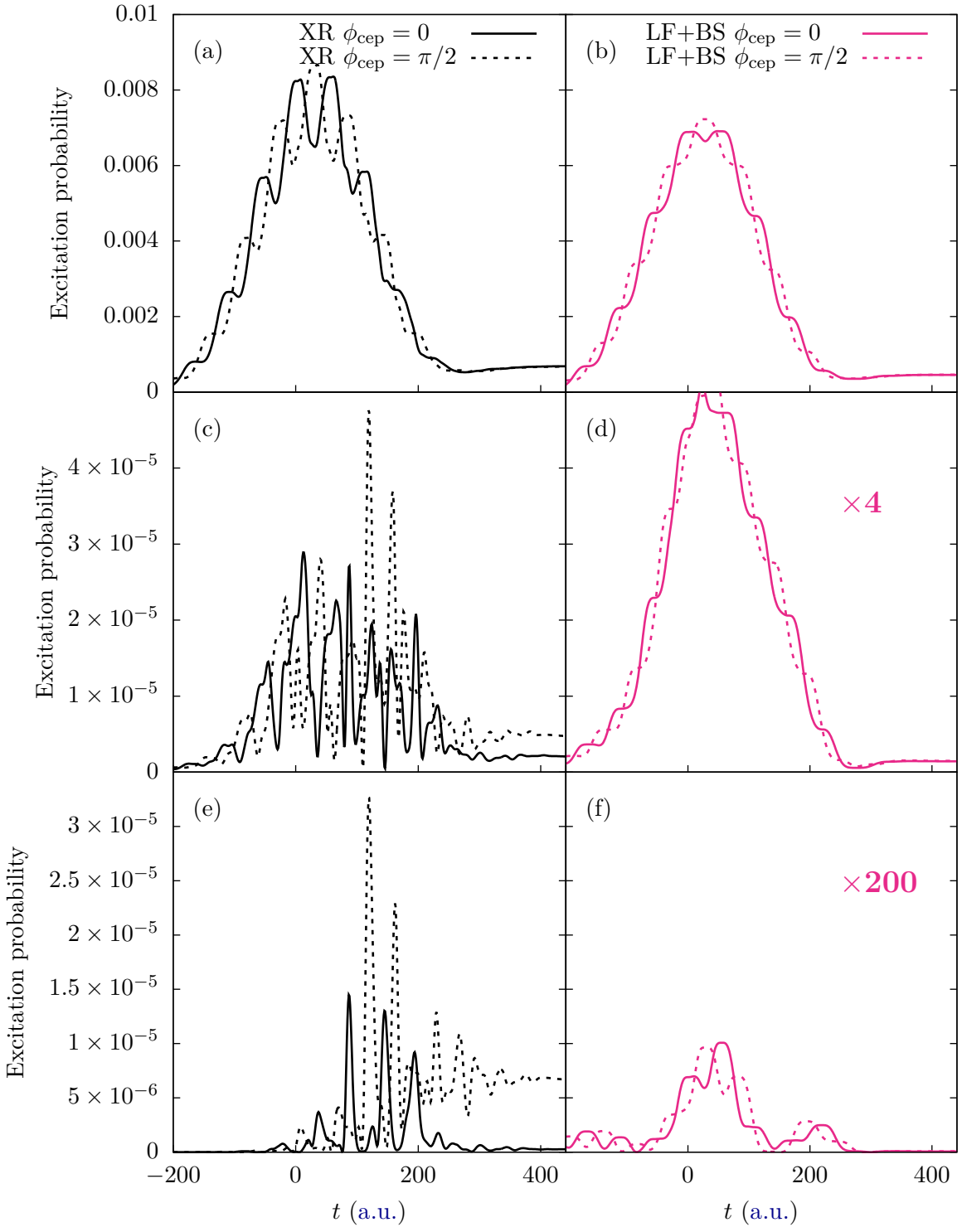

Figure V.6 *Population in the first vibrational states normalized to the total population in the electronic ground state as a function of time for the H_2 model system submitted to an 8 optical cycle long laser pulse of $I_L = 10^{14}$ W.cm^{-2}, and different CEP. (a) and (b) first vibrational excited state, (c) and (d) second vibrational excited state, (e) and (f) third vibrational excited state. (a) (c) (e) correlated simulations on a 2D grid, (b) (d) (f) BO computation taking BS and LF into account.*

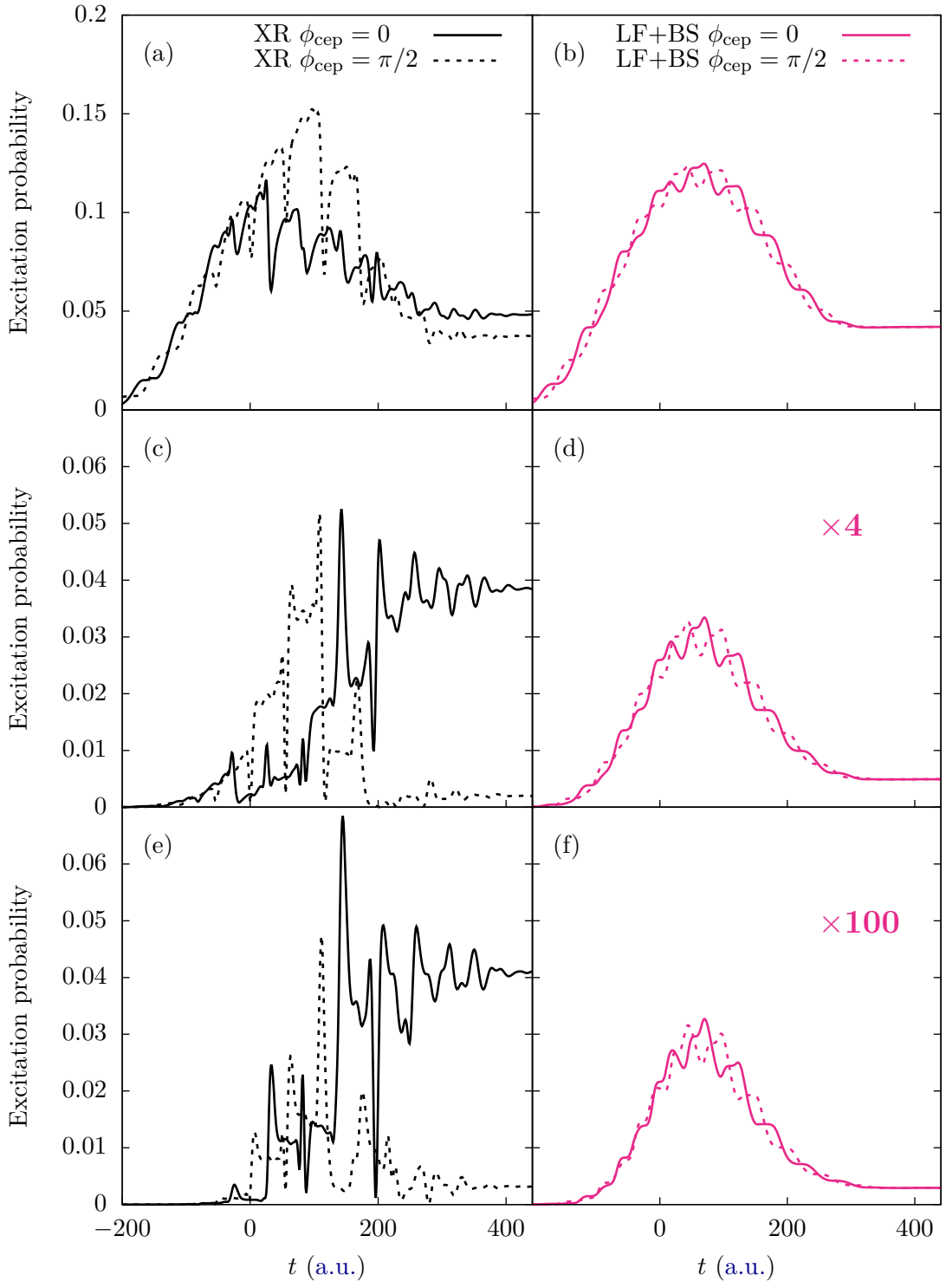

Figure V.7 *Population in the first vibrational states normalized to the total population in the electronic ground state as a function of time for the H_2 model system submitted to an 8 optical cycle long laser pulse of $I_L = 4 \times 10^{14}$ W.cm^{-2}, and different CEP. (a) and (b) first vibrational excited state, (c) and (d) second vibrational excited state, (e) and (f) third vibrational excited state. (a) (c) (e) correlated simulations on a 2D grid, (b) (d) (f) BO computation taking BS and LF into account.*

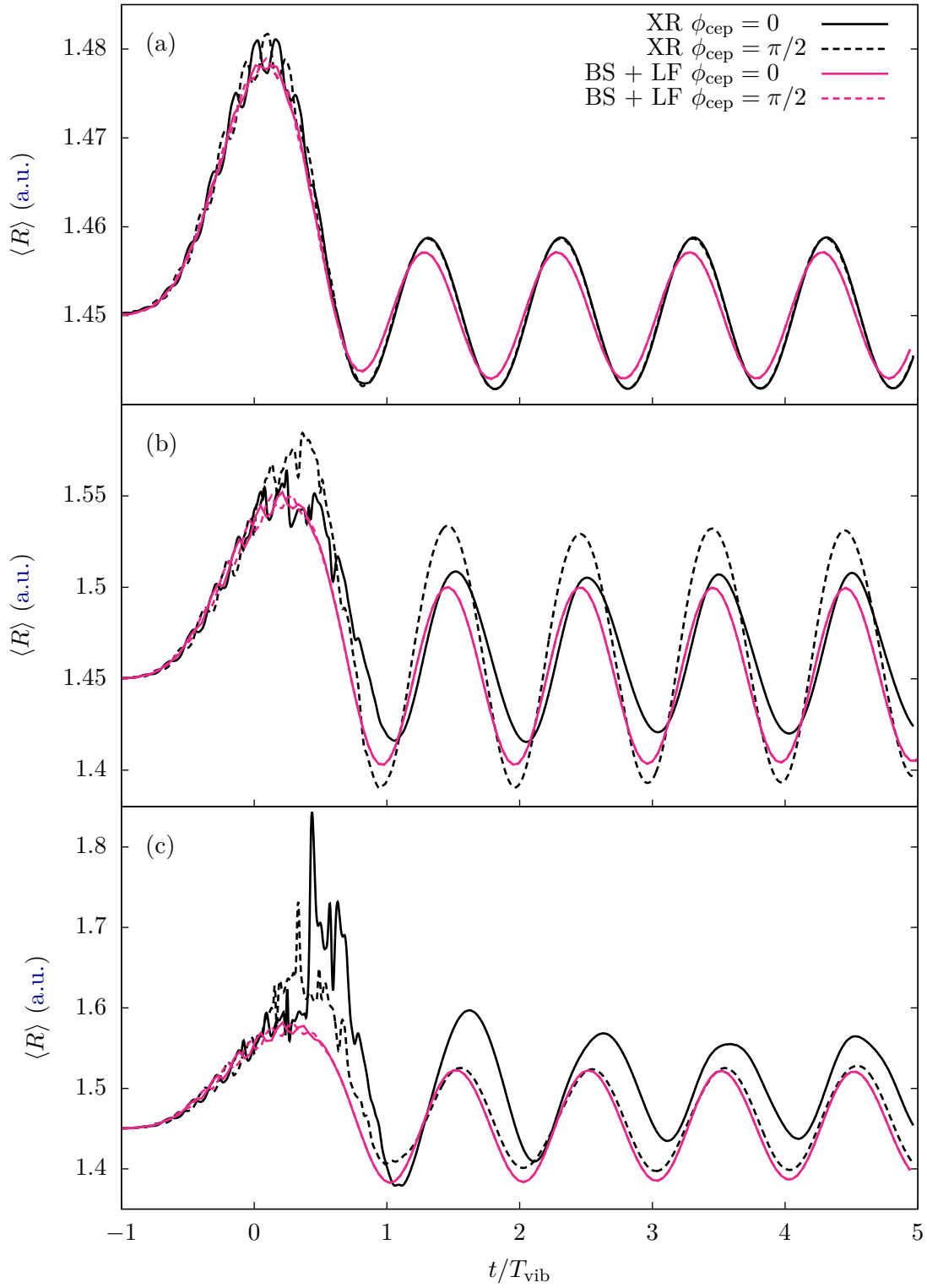

Figure V.8 *Average value of the internuclear distance of the H_2 system in the electronic ground state for an 8 cycle long pulse of (a) $I_L = 10^{14}$ W.cm^{-2}, (b) $I_L = 3 \times 10^{14}$ W.cm^{-2} and (c) $I_L = 4 \times 10^{14}$ W.cm^{-2}.*

correlated models at the lowest intensity (panel (a)). The correlated results are slightly dephased with respect to the BO ones: the XR model predicts a phase of $\simeq 0.63\pi$, while the BO model gives $\simeq 0.57\pi$. We also notice that, at this low intensity, the effect of the CEP is almost negligible during the laser pulse, and becomes invisible to the naked eye as soon as the pulse is over.

The results are quite different when we increase the laser intensity. At $I_{\mathrm{L}} = 3\times10^{14}$ W.cm^{-2} (panel (b)), we observe significant discrepancies between the two models. The correlated simulations predict that both the amplitude and phase of the oscillations remarkably depend on the CEP. However, this is completely neglected in the BO approximation, for which the curves at $\phi_{\mathrm{cep}} = 0$ or $\pi/2$ are indistinguishable to the naked eye. Even more striking are the results at $I_{\mathrm{L}} = 4 \times 10^{14}$ W.cm^{-2} (panel (c)). In this case, the NWP oscillations predicted by the correlated model cannot be fitted by a simple cosine, like (V.17). This is actually a consequence of the population in the higher vibrational excited states that we observed on Figure V.7 (panels (c) and (e)). It is thus very difficult to even define a global amplitude and phase for these oscillations. On the contrary the BO results still exhibit sinusoidal oscillations with only one frequency, which is a consequence of the fact that this model does not properly reproduce the population in the highly vibrational excited states, as observed on Figure V.7 (panels (d) and (f)).

Intuitively, one would think that this effect of the CEP is related to the laser pulse duration. Indeed, since the pulse envelop is not constant, for very short pulses the CEP affects the total energy that is carried by the pulse. However for longer pulses, this energy difference decreases with respect to the total energy. We would thus expect that this CEP effect vanishes for longer pulses. To check this, we plot on Figure V.9 the populations at the end of the pulse as a function of ϕ_{cep} for different pulse durations. We observe that the populations computed by the correlated model oscillates with ϕ_{cep}, while the BO model predicts a completely flat behavior. We can thus find fortuitus values of ϕ_{cep} where the agreement between the BO and XR models is perfect, and others where it is very bad. Surprisingly, we note that the ϕ_{cep} dependence gets even more pronounced when the pulse duration increases. This is actually the opposite of what we intuitively expected. To go deeper in the interpretation of this feature, we performed the same simulations, but with absorbing conditions very close to the nuclei. If the absorber is placed close enough, then it will remove all the ionized part of the wave function, but also a large part of the population in the electronic excited states. In these conditions, all the population that leaves the EGS is lost forever: the absorber prevents eventual recollisions, as illustrated on Figure V.5.

We plot the average value of R for different absorbing conditions on Figure V.10. In panel (a) we placed the absorber at $x_{\mathrm{abs}} = 54.8$ a.u. i.e. relatively far away from the nuclei, in panel (b) we placed it at $x_{\mathrm{abs}} = 34.8$ a.u. wich is approximately equal to x_α (I.79) (see section I.3.2) so that we only absorb the long trajectories and on panel (c) we placed it at $x_{\mathrm{abs}} = 14.8$ a.u. i.e. very close to the nuclei so that we also absorb the electronic excited states. We mention that the precise values of the position of the absorber are just related to simulation parameters and do not carry any physical meaning. We observe the same oscillations as before. When the absorber is placed at $x_{\mathrm{abs}} = 54.8$ a.u. (panel (a)), we do not observe much difference with the previous results. The dynamics strongly depends on the CEP, and the BO approximation fails to reproduce the proper oscillations of the NWP. This indicates that the absorber does not strongly perturb the dynamics, i.e.

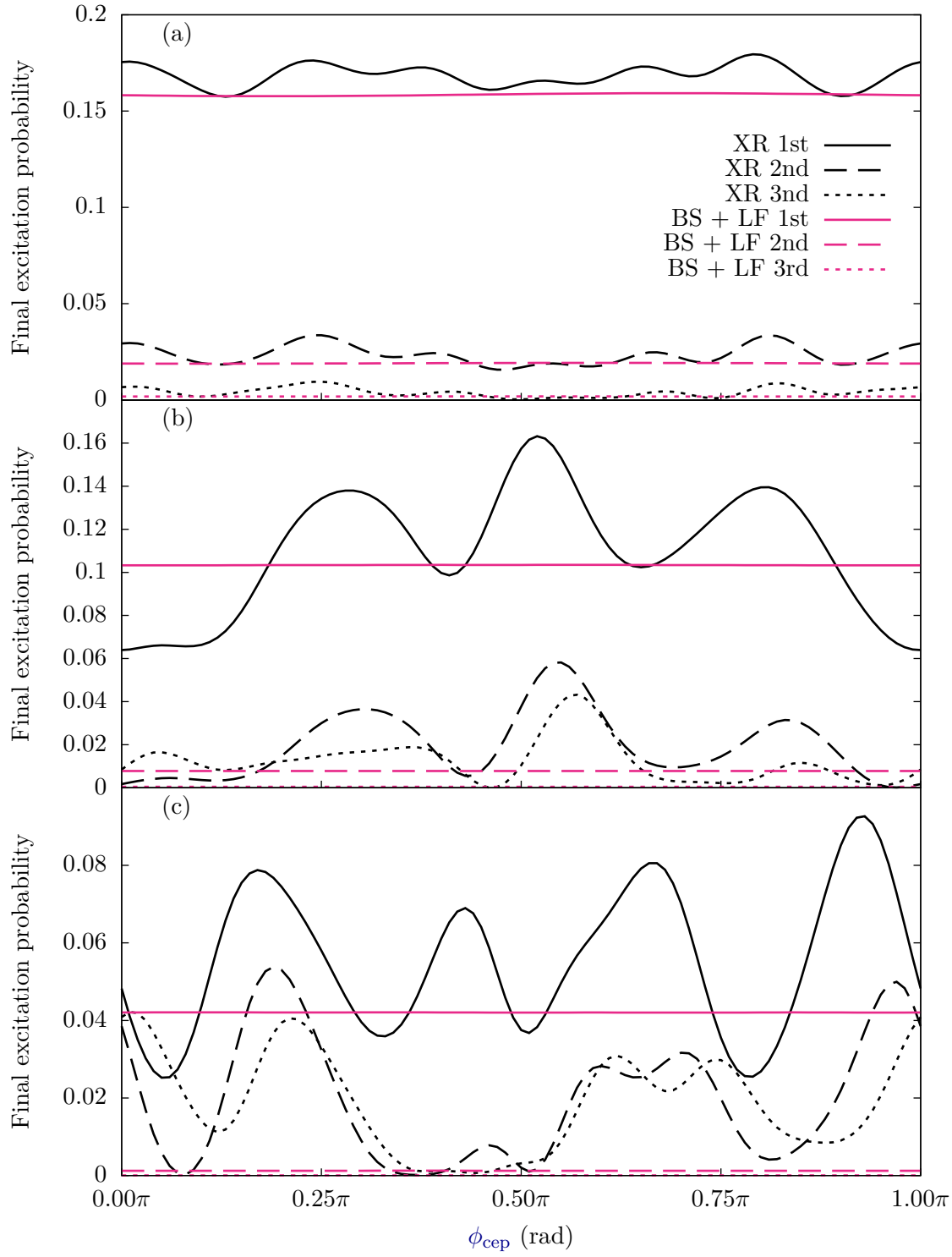

Figure V.9 *Effect of the CEP for the H_2 system submitted to a laser pulse of $I_L = 4 \times 10^{14}$ W.cm^{-2}, and of (a) 4 optical cycles, (b) 6 optical cycles and (c) 8 optical cycles. Population in the first (solid lines), second (dashed lines) and third (dotted lines) vibrational states at the end of the pulse computed by the 2D-XR correlated model (black lines), and the BO model with both BS and LF (pink lines).*

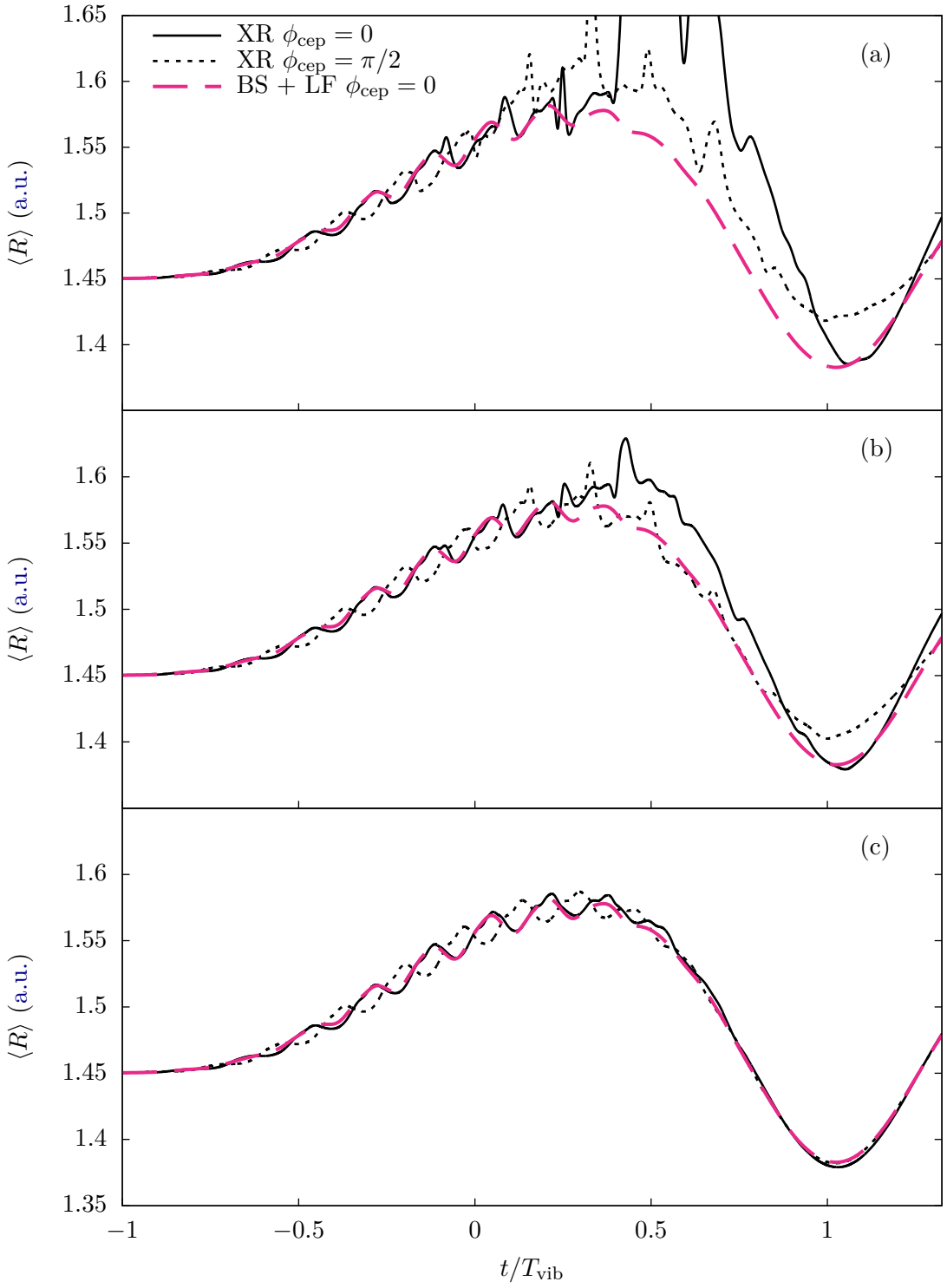

Figure V.10 *Average value of the internuclear distance of the H_2 system in the electronic ground state for an 8 cycle long pulse of $I_L = 4 \times 10^{14}$ W.cm^{-2}. The XR simulation is performed with a close absorber located at a distance of (a) 54.8 a.u., (b) 34.8 a.u., (c) 14.8 a.u. from the center of mass of the system.*

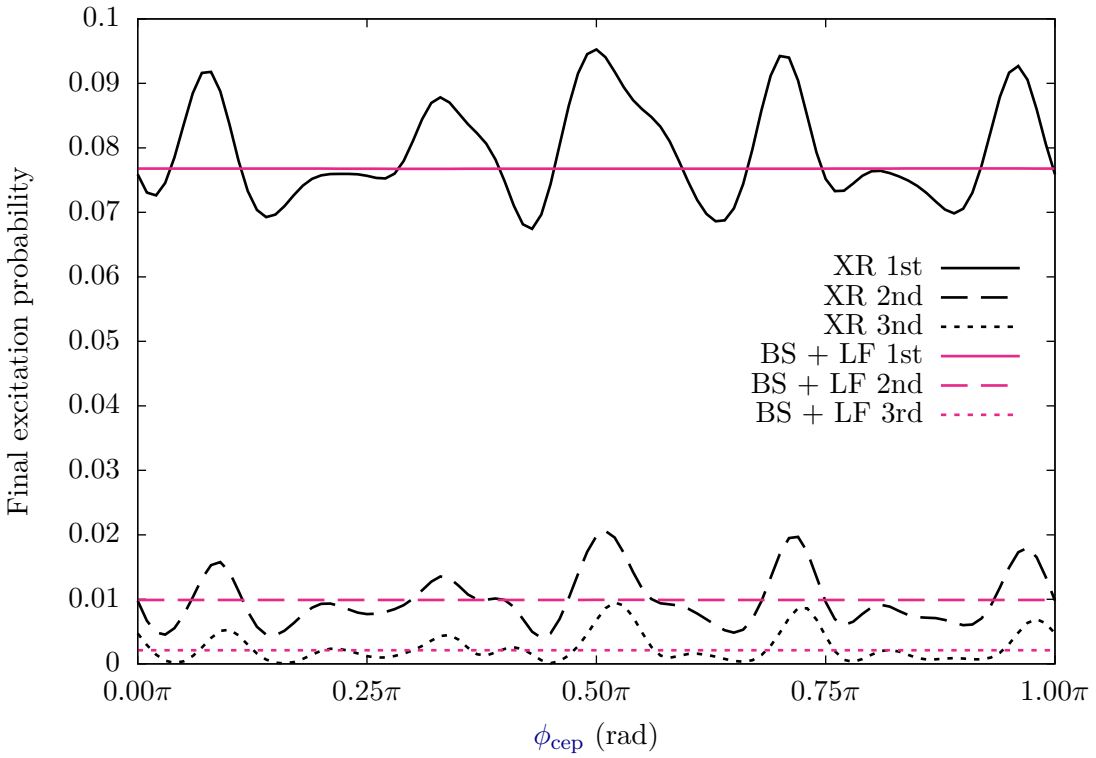

Figure V.11 *Effect of the CEP for the G_2 system submitted to a laser pulse of $I_L = 10^{15}$ W.cm^{-2}, and of 8 optical cycles. Population in the first (solid lines), second (dashed lines) and third (dotted lines) vibrational states at the end of the pulse computed by the 2D-XR correlated model (black lines), and the BO model with both BS and LF (pink lines).*

that the part of the wave function that goes beyond $x_{abs} = 54.8$ a.u. will actually never return to the core, and thus never recombines to the EGS. However, when we move the absorber closer to the center of mass of the system, it starts to affect the dynamics. At a distance $x_{abs} = 34.8$ a.u. (panel (b)) we already see that the correlated dynamics, for both $\phi_{cep} = 0$ and $\pi/2$, is much closer to the BO one. And at $x_{abs} = 14.8$ a.u. (panel (c)) we do not see any difference between the BO and correlated models. In particular the CEP-dependence completely disappears with such a close absorber. We thus concludes that the discrepancies between the two models are actually due to parts of the wave function that leave the EGS, goes into electronic excited or continuum states, and interfere with the ground state at a later time in the propagation. Of course, the BO is absolutely unable to describe such mechanism since it only treats the dynamics in the EGS, and discards the electronically excited part of the wave function.

At such a short distance of $x = 14.8$ a.u., we actually absorb both the electronically excited states and the continuum states. We cannot conclude from Figure V.10 if it is the excited or ionized part (or both) of the wave function that induces correlation and affects the dynamics. As we have seen in section I.3, recombination from continuum states would actually lead to HHG. Since the efficiency of this process is actually quite low, we expect

intuitively that it is mainly the recombination from electronic bound excited states that will induce the correlated effects that we have observed. To investigate this, we consider the G_2 model system, which has only two electronic bound states. We thus kill most of the excited states' influence and concentrate on the continuum states. As we did for H_2 in Figure V.9, we plot on Figure V.11 the population in the first vibrational states at the end of the laser pulse as a function of the CEP for the G_2 system. Since the G_2 system has a lower ionization rate than our H_2 system, we chose a higher intensity of $I_L = 10^{15}$ W.cm^{-2} to reach similar ionization probability at the end of the pulse. Similarly to the H_2 model, we observe that the final populations oscillate with ϕ_{cep}, indicating that we did not kill all the correlation by "removing" most of the electronic excited states. The amplitude of these oscillations is however much lower than in the case of H_2, indicating that the electronic excitation indeed does play a major role. Nevertheless, the fact that we sill observe discrepancies with the BO model suggests that the continuum states are not spectators, but also impact the nuclear dynamics.

To conclude, these results do not allow to fully understand the origin of the CEP-dependency in the nuclear dynamics. Since the continuum states seem to play a role in this respect, it may be related to interference between the wave packets that are emitted at each half cycle of the laser field as described in [114]. However more work is needed to discriminate between the effects of the electronic excited and continuum states.

V.3 Analytic derivation

To better understand the discrepancies between the BO and the fully correlated models, we propose an analytical derivation of the BO nuclear TDSE based on the Wigner-Weisskopf approach. This method is a very general way to model a quantum system in interaction with an environment. Since we are only interested in the system, we want to separate its dynamics from this environment. This separation relies on the hypothesis that the environment does not keep any memory of its interaction with the system, i.e. that any information is lost as soon as it reaches this environment. We follow the derivation as it is performed in [78] for a two-level system, and we adapt it to the case of a molecule in a classical EM field. In our case, the system is the electronic ground state of our neutral molecule, and the environment is composed of all the electronic excited and continuum states. In a first approach we concentrate on the BS mechanism, so that we only consider the electronic bound states of the molecule, and not the continuum states. The wave function is decomposed on the vibrational states $\left|v_j^{(i)}\right\rangle$ of all the electronic states $|\varphi_i\rangle$ of the neutral molecule:

$$|\psi(t)\rangle = \sum_{i,j} a_{i,j}(t) \left|\varphi_i, v_j^{(i)}\right\rangle ; \tag{V.18}$$

In the case of homonuclear diatomic molecules, the electric field does not couple the vibrational states within a given electronic state:

$$\left\langle \varphi_i, v_j^{(i)} \right| \boldsymbol{\mu} \cdot \mathbf{F_L} \left| \varphi_i, v_l^{(i)} \right\rangle = 0. \tag{V.19}$$

Since we want to focus on the dynamics in the ground state, we also assume that we can neglect the coupling between electronic excited states:

$$\left\langle \varphi_i, v_j^{(i)} \right| \boldsymbol{\mu} \cdot \mathbf{F_L} \left| \varphi_k, v_l^{(k)} \right\rangle = 0, \quad \text{if} \quad i, k \geq 1. \tag{V.20}$$

The Hamiltonian can be decomposed into blocks $H_{i,j}$ corresponding to each electronic state:

$$H = \begin{pmatrix} H_{1,1} & H_{1,2} & H_{1,3} & \dots & \\ H_{2,1} & H_{2,2} & 0 & \dots & 0 \\ H_{3,1} & 0 & H_{3,3} & 0 & \vdots \\ \vdots & \vdots & & \ddots & \end{pmatrix} \tag{V.21}$$

where the diagonal blocs are diagonal matrices of the vibrational energies:

$$H_{i,i} = \begin{pmatrix} \omega_{i,1} & 0 & \dots \\ 0 & \omega_{i,2} & \ddots \\ \vdots & & \ddots \end{pmatrix} \tag{V.22}$$

and where the non diagonal blocks contains the couplings between the vibrational states within the ground and electronic excited states:

$$H_{1,k} = \begin{pmatrix} V_{1,1,k} & V_{1,2,k} & \dots \\ V_{2,1,k} & V_{2,2,k} & \ddots \\ \vdots & & \ddots \end{pmatrix} \tag{V.23}$$

with

$$V_{j,k,l}(t) = -\left\langle \varphi_0, v_j^{(0)} \right| \boldsymbol{\mu} \cdot \mathbf{F_L}(t) \left| \varphi_k, v_l^{(k)} \right\rangle \tag{V.24}$$

$$= -\frac{F_L}{2} \left(\mathrm{e}^{\mathrm{i}\omega_L t} + \mathrm{e}^{-\mathrm{i}\omega_L t} \right) \left\langle \varphi_0, v_j^{(0)} \right| \mu_z \left| \varphi_k, v_l^{(k)} \right\rangle. \tag{V.25}$$

The coefficients $a_{i,j}(t)$ obey the following differential equations:

$$\frac{\mathrm{d}a_{0,j}}{\mathrm{d}t}(t) = -\mathrm{i}\omega_{0,j} a_{0,j}(t) - \mathrm{i} \sum_{k>0,l} V_{j,k,l}(t) a_{k,l}(t) \tag{V.26}$$

$$\frac{\mathrm{d}a_{k,l}}{\mathrm{d}t}(t) = -\mathrm{i}\omega_{k,l} a_{k,l}(t) - \mathrm{i} \sum_j V^*_{j,k,l}(t) a_{0,j}(t), \quad \text{if} \quad k > 0; \tag{V.27}$$

For $k \neq 0$, the coefficients $a_{k,l}$ can be formally computed as:

$$a_{k,l}(t) = -\mathrm{i} \sum_m \int_0^t \mathrm{d}t' V^*_{m,k,l}(t') \, \mathrm{e}^{\mathrm{i}\omega_{k,l}(t'-t)} \, a_{0,m}(t'). \tag{V.28}$$

Inserting this expression in (V.26), and defining $\tilde{a}_{0,j}(t) = a_{0,j}(t)\,\mathrm{e}^{\mathrm{i}\omega_{0,j}t}$, we get:

$$\frac{\mathrm{d}\tilde{a}_{0,j}}{\mathrm{d}t}(t) = -\sum_{k>0,l,m} \mathrm{e}^{\mathrm{i}(\omega_{0,j}-\omega_{0,m})t} \int_0^t \mathrm{d}t' V_{j,k,l}(t) V^*_{m,k,l}(t')\,\mathrm{e}^{\mathrm{i}(\omega_{k,l}-\omega_{0,m})(t'-t)}\,\tilde{a}_{0,m}(t') \quad \text{(V.29)}$$

$$= -\frac{F_L^2}{2}\cos\omega_L t \sum_{\alpha=\pm1}\sum_{k>0,l,m} \left\langle \varphi_0, v_j^{(0)} \right| \mu_z \left| \varphi_k, v_l^{(k)} \right\rangle \left\langle \varphi_k, v_l^{(k)} \right| \mu_z \left| \varphi_0, v_m^{(0)} \right\rangle$$

$$\times \int_0^t \mathrm{d}t'\,\mathrm{e}^{\mathrm{i}(\omega_{k,l}-\omega_{0,m}+\alpha\omega_L)(t'-t)}\,\tilde{a}_{0,m}(t') \quad \text{(V.30)}$$

$$= -\frac{F_L^2}{2}\cos\omega_L t \sum_{\alpha=\pm1} \mathrm{e}^{\mathrm{i}(\omega_{0,j}-\omega_{0,m}+\alpha\omega_L)t} \int_0^t \mathcal{N}_{l,m,\alpha}(\tau)\tilde{a}_{0,m}(t-\tau)\mathrm{d}\tau, \quad \text{(V.31)}$$

where we changed the integration variable from t' to $\tau = t - t'$, and where we defined

$$\mathcal{N}_{l,m,\alpha}(\tau) = \sum_{k>0,l,m} \left\langle \varphi_0, v_j^{(0)} \right| \mu_z \left| \varphi_k, v_l^{(k)} \right\rangle \left\langle \varphi_k, v_l^{(k)} \right| \mu_z \left| \varphi_0, v_m^{(0)} \right\rangle \mathrm{e}^{-\mathrm{i}(\omega_{k,l}-\omega_{0,m}+\alpha\omega_L)\tau}\,. \quad \text{(V.32)}$$

In the Wigner-Weisskopf approach, this $\mathcal{N}_{\updownarrow,\Updownarrow,\alpha}(\tau)$ term is considered to be very close to a Dirac delta function:

$$\int_0^t \mathcal{N}_{l,m,\alpha}(\tau)\tilde{a}_{0,m}(t-\tau)\mathrm{d}\tau \simeq \tilde{a}_{0,m}(t)\int_0^\infty \mathcal{N}_{l,m,\alpha}(\tau)\mathrm{d}\tau. \quad \text{(V.33)}$$

One can find different way to interpret this assumption. First we can consider the sum over k as a sum of terms of very different frequencies $\omega_{k,l}$ and similar amplitude. The different frequencies of this sum thus get very quickly out of phase as soon as $\tau \gtrsim 1/\omega_{0,m}$. This is referred to as the Markov approximation, and interpreted as a zero memory time of the "reservoir" made of the electronic excited states. Equivalently, it means that the electron is lost as soon as it is promoted to an excited state, i.e. to the reservoir, and the reservoir keeps no memory of having received this electron. The interpretation makes use of the Saddle Point Approximation on the integral over τ:

$$\int_0^t \mathrm{e}^{-\mathrm{i}(\omega_{k,l}-\omega_{0,m}+\alpha\omega_L)\tau}\,\tilde{a}_{0,m}(t-\tau)\mathrm{d}\tau \simeq \tilde{a}_{0,m}(t)\int_0^\infty \mathrm{e}^{-\mathrm{i}(\omega_{k,l}-\omega_{0,m}+\alpha\omega_L)\tau}\,\mathrm{d}\tau. \quad \text{(V.34)}$$

Since there is only one saddle point at $\tau = 0$, we get the following orders:

$$\int_0^t \mathrm{e}^{-\mathrm{i}(\omega_{k,l}-\omega_{0,m}+\alpha\omega_L)\tau}\,\tilde{a}_{0,m}(t-\tau)\mathrm{d}\tau \simeq \tilde{a}_{0,m}(t)\int_0^\infty \mathrm{d}\tau\,\mathrm{e}^{-\mathrm{i}(\omega_{k,l}-\omega_{0,m}+\alpha\omega_L)\tau}$$

$$- \frac{\mathrm{d}\tilde{a}_{0,m}}{\mathrm{d}t}(t)\int_0^\infty \tau\,\mathrm{e}^{-\mathrm{i}(\omega_{k,l}-\omega_{0,m}+\alpha\omega_L)\tau}\,\mathrm{d}\tau + \ldots \quad \text{(V.35)}$$

$$= \tilde{a}_{0,m}(t)\left(\pi\delta(\omega_{0,m}-\omega_{k,l}-\alpha\omega_L) + \mathrm{i}\mathcal{P}\mathcal{P}\frac{1}{\omega_{0,m}-\omega_{k,l}-\alpha\omega_L}\right)$$

$$+ \frac{\mathrm{d}\tilde{a}_{0,m}}{\mathrm{d}t}(t)\left(\mathrm{i}\pi\delta'(\omega_{0,m}-\omega_{k,l}-\alpha\omega_L) + \mathcal{P}\mathcal{P}\frac{1}{(\omega_{0,m}-\omega_{k,l}-\alpha\omega_L)^2}\right)$$

$$+ \ldots \quad \text{(V.36)}$$

where $\mathcal{PP}$ indicates that we consider the Cauchy principal value of the enclosed expression, and $\delta, \delta', ...$ are the Dirac delta function and its derivatives. We can now insert this in (V.31) to get:

$$\frac{\mathrm{d}\tilde{a}_{0,j}}{\mathrm{d}t}(t) = -\sum_m \mathrm{e}^{\mathrm{i}(\omega_{0,j}-\omega_{0,m})t}\left[\tilde{a}_{0,m}(t)\left(\frac{\Gamma_{j,m}(t)}{2}+\mathrm{i}\Delta_{j,m}(t)\right)+\frac{\mathrm{d}\tilde{a}_{0,m}}{\mathrm{d}t}(t)\Big(\Theta_{j,m}(t)+\mathrm{i}\,\Xi_{j,m}(t)\Big)\right] \tag{V.37}$$

where

$$\begin{aligned}\Gamma_{j,m}(t) =& \frac{\pi F_L^2}{2}\cos(\omega_L t)\sum_{\alpha=\pm1}\mathrm{e}^{\mathrm{i}\alpha\omega_L t}\\ &\times\sum_{k>0,l}\left\langle\varphi_0,v_j^{(0)}\right|\mu_z\left|\varphi_k,v_l^{(k)}\right\rangle\left\langle\varphi_k,v_l^{(k)}\right|\mu_z\left|\varphi_0,v_m^{(0)}\right\rangle\delta(\omega_{0,m}-\omega_{k,l}-\alpha\omega_L)\end{aligned} \tag{V.38}$$

$$\begin{aligned}\Delta_{j,m}(t) =& \frac{F_L^2}{2}\cos(\omega_L t)\sum_{\alpha=\pm1}\mathrm{e}^{\mathrm{i}\alpha\omega_L t}\\ &\times\sum_{k>0,l}\left\langle\varphi_0,v_j^{(0)}\right|\mu_z\left|\varphi_k,v_l^{(k)}\right\rangle\left\langle\varphi_k,v_l^{(k)}\right|\mu_z\left|\varphi_0,v_m^{(0)}\right\rangle\mathcal{PP}\frac{1}{\omega_{0,m}-\omega_{k,l}-\alpha\omega_L}\end{aligned} \tag{V.39}$$

$$\begin{aligned}\Theta_{j,m} =& \frac{F_L^2}{2}\cos(\omega_L t)\sum_{\alpha=\pm1}\mathrm{e}^{\mathrm{i}\alpha\omega_L t}\\ &\times\sum_{k>0,l}\left\langle\varphi_0,v_j^{(0)}\right|\mu_z\left|\varphi_k,v_l^{(k)}\right\rangle\left\langle\varphi_k,v_l^{(k)}\right|\mu_z\left|\varphi_0,v_m^{(0)}\right\rangle\mathcal{PP}\frac{1}{(\omega_{0,m}-\omega_{k,l}-\alpha\omega_L)^2}\end{aligned} \tag{V.40}$$

$$\begin{aligned}\Xi_{j,m} =& -\frac{\pi F_L^2}{2}\cos(\omega_L t)\sum_{\alpha=\pm1}\mathrm{e}^{\mathrm{i}\alpha\omega_L t}\\ &\times\sum_{k>0,l}\left\langle\varphi_0,v_j^{(0)}\right|\mu_z\left|\varphi_k,v_l^{(k)}\right\rangle\left\langle\varphi_k,v_l^{(k)}\right|\mu_z\left|\varphi_0,v_m^{(0)}\right\rangle\delta'(\omega_{0,m}-\omega_{k,l}-\alpha\omega_L).\end{aligned} \tag{V.41}$$

In the adiabatic approximation, the laser frequency can be considered very small with respect to all the energy gaps $\omega_{k,l}-\omega_{0,m}$. We can thus neglect the $\Gamma_{j,m}$ and the $\Xi_{j,m}$, and approximate the $\Delta_{j,m}$ (V.39) and $\Theta_{j,m}$ (V.40) by

$$\Delta_{j,m}(t) = F_L^2\cos^2(\omega_L t)\sum_{k>0,l}\frac{\left\langle\varphi_0,v_j^{(0)}\right|\mu_z\left|\varphi_k,v_l^{(k)}\right\rangle\left\langle\varphi_k,v_l^{(k)}\right|\mu_z\left|\varphi_0,v_m^{(0)}\right\rangle}{\omega_{0,m}-\omega_{k,l}} \tag{V.42}$$

$$\Theta_{j,m} = F_L^2\cos^2(\omega_L t)\sum_{k>0,l}\frac{\left\langle\varphi_0,v_j^{(0)}\right|\mu_z\left|\varphi_k,v_l^{(k)}\right\rangle\left\langle\varphi_k,v_l^{(k)}\right|\mu_z\left|\varphi_0,v_m^{(0)}\right\rangle}{(\omega_{0,m}-\omega_{k,l})^2} \tag{V.43}$$

If we only keep the first order of the SPA (i.e. the $\Delta_{j,m}$ terms) then we find the following differential equations for the $a_{0,j}$:

$$\mathrm{i}\frac{\mathrm{d}a_{0,j}}{\mathrm{d}t}(t) = \omega_{0,j}a_{0,j}(t)+\sum_m\Delta_{j,m}(t)a_{0,m}(t). \tag{V.44}$$

This is a new Schrödinger equation that describes the dynamics of the nuclear wave packet on the electronic ground state of the neutral molecule. The additional term Δ couples the different vibrational states of the electronic ground state through the interaction with the electronic excited states. This is the term responsible for the Bond-Softening mechanism. To recover the expression that we used in the previous section, we still need to neglect the differences between the *vibrational* energies with respect to the *electronic* energies E_k and get

$$\Delta_{j,m}(t) = F_L^2 \cos^2(\omega_L t) \sum_{k>0,l} \frac{\left\langle \varphi_0, v_j^{(0)} \right| \mu_z \left| \varphi_k, v_l^{(k)} \right\rangle \left\langle \varphi_k, v_l^{(k)} \right| \mu_z \left| \varphi_0, v_m^{(0)} \right\rangle}{E_0 - E_k}. \tag{V.45}$$

Lastly we suppose that we can write the vibronic states $|N_{k,l}, \varphi_k\rangle$ as BO products $\varphi_k(\mathbf{r};\mathbf{R})\chi_{k,l}(\mathbf{R})$, so that we can use the identity closure relation $\mathbb{1} = \sum_l |N_{k,l}\rangle \langle N_{k,l}|$ for each electronic state k:

$$\Delta_{j,m}(t) = F_L^2 \cos^2(\omega_L t) \left\langle v_j^{(0)} \right| \sum_{k>0} \frac{\left| \langle \varphi_0(\mathbf{r};\mathbf{R}) | \mu_z | \varphi_k(\mathbf{r};\mathbf{R}) \rangle_{\mathbf{r}} \right|^2}{E_0 - E_k} \left| v_m^{(0)} \right\rangle. \tag{V.46}$$

where $\langle | \rangle_{\mathbf{r}}$ indicates that we only integrate over $\mathbf{r}$. We recognize the expression of the second order Stark shift [135]. Using the expression of the polarizability:

$$\alpha(R) = \sum_{k>0} \frac{\left| \langle \varphi_0(\mathbf{r};\mathbf{R}) | \mu_z | \varphi_k(\mathbf{r};\mathbf{R}) \rangle_{\mathbf{r}} \right|^2}{E_k - E_0}, \tag{V.47}$$

the expression of the matrix Δ finally reduces to

$$\Delta = -\alpha(R) F_L^2 \cos^2(\omega_L t). \tag{V.48}$$

We thus find that the matrix Δ is equal to the statical R-dependent Stark shift, where we replaced the value of the static field by the time-dependent laser electric field. The fact that we only find the first non zero order of perturbation theory (i.e. the polarizability) for the Stark shift is a direct consequence of the approximation made in neglecting the coupling *between* electronic excited states. Indeed these couplings appear in the expression of the higher order terms [135].

If we include the following order of the SPA, i.e. the Θ matrix, we find additional terms. We apply the same approximations we just used for Δ to the Θ matrix to find:

$$\Theta = F_L^2 \cos^2(\omega_L t) \sum_{k>0,l} \frac{\left| \langle \varphi_0(\mathbf{r};\mathbf{R}) | \mu_z | \varphi_k(\mathbf{r};\mathbf{R}) \rangle_{\mathbf{r}} \right|^2}{(E_0 - E_k)^2}. \tag{V.49}$$

We denote by A_0 the vector of coefficients $a_{0,j}$ in order to write (V.31) under matrix form :

$$\mathrm{i}\frac{\mathrm{d}A_0}{\mathrm{d}t}(t) = [H + \Delta] A_0(t) - \mathrm{i}\Theta \frac{\mathrm{d}A_0}{\mathrm{d}t}(t) \tag{V.50}$$

$$= [\mathbb{1} + \Theta]^{-1} [H + \Delta] A_0(t). \tag{V.51}$$

We conclude that the nuclear wave packet in the electronic ground state evolves under the perturbed Hamiltonian $[\mathbb{1} + \Theta]^{-1} [H + \Delta]$. This Hamiltonian includes corrections that

describe the above mentioned *memory* of the "reservoir". It would thus be interesting to test if it can reproduce the recombinations, and the CEP-dependency, that we have observed in the previous section and that were not included in the first order equation (V.44). However we did not have time to perform the corresponding simulations, and leave this here as an open perspective.

We recovered the TDSE for the NWP in the electronic ground state for the BS mechanism. If we want to include the LF we need to add the electronic states of the ionized species to our initial description of the wave function (V.18):

$$|\psi(t)\rangle = \sum_{i,j} a_{\mathrm{i,j}}(t) \left|\varphi_i, v_j^{(i)}\right\rangle + \sum_l \int \mathrm{d}E\mathrm{d}\beta\, \rho(E) b_l(E,\beta,t) \left|E,\beta\right\rangle \left|v_l^+\right\rangle, \tag{V.52}$$

where the $\left|v_l^+\right\rangle$ refer to the vibrational states of the cationic molecule with energy $\omega_{+,l}$, and E is the energy of the ionized electron, and β a set of quantum numbers (see section I.1). We can perform the same Wigner-Weisskopf derivation with such an ansatz. We will find the same modified differential equations (V.31) for the coefficients $a_{0,j}$, but the expression of the Γ, Δ, Θ and Ξ matrices will be changed. We only give here the expression of the Γ terms:

$$\begin{aligned}\Gamma_{j,m}(t) =& \frac{\pi F_L^2}{2}\cos(\omega_L t) \sum_{\alpha=\pm 1} \mathrm{e}^{\mathrm{i}\alpha\omega_L t} \\ &\times \Bigg[\sum_{k>0,l} \left\langle \varphi_0, v_j^{(0)}\right| \mu_z \left|\varphi_k, v_l^{(k)}\right\rangle \left\langle \varphi_k, v_l^{(k)}\right| \mu_z \left|\varphi_0, v_m^{(0)}\right\rangle \delta(\omega_{0,m} - \omega_{k,l} - \alpha\omega_L) \\ &\quad + \sum_l \rho(E) \int \mathrm{d}\beta \left\langle \varphi_0, v_j^{(0)}\right| \mu_z \left|E,\beta, v_l^+\right\rangle \left\langle E,\beta, v_l^+\right| \mu_z \left|\varphi_0, v_m^{(0)}\right\rangle \Big|_{E=\omega_{0,m}-\omega_{+,l}-\alpha\omega_L} \Bigg].\end{aligned} \tag{V.53}$$

Compared to the previous expression (V.38), we get new terms (on the third line) that correspond to the interaction of the vibrational states mediated through the continuum states. Moreover, those terms form an (almost) anti-Hermitian matrix, exactly like the $-\mathrm{i}\Gamma(R, F_\mathrm{L}(t))$ matrix that we used for the BO model (see section V.1.2). It is thus highly tempting to conclude that it is the matrix that is responsible for the Lochfraß mechanism. Nevertheless, as before, we see from the energy conservation relation $E = \omega_{0,m} - \omega_{+,l} - \alpha\omega_L$, which can also be written $\omega_L = \pm(E + \omega_{+,l} - \omega_{0,m})$, that the photon energy has to match the energy difference between the vibrational state $\left|v_j^{(0)}\right\rangle$ and the mediating continuum state $|E,\beta\rangle$. Or, said otherwise, we only get the first non zero order of perturbation theory. This is somewhat expected from what we just said with the previous derivation: we cannot describe multiphoton transitions from the electronic ground state to the continuum if we do not couple the continuum states between themselves. In the case of BS this has minimal consequences because the first non zero order of perturbation theory is actually the dominant one. On the contrary, for the LF mechanism it is crucial to have all the higher orders to describe tunnel ionization. We thus need to include *couplings* between the continuum states. Unfortunately we also have to leave this part of the calculation as a perspective.

V.4 Conclusion

We have studied ultrafast correlated vibrational dynamics in small homonuclear diatomic molecules initiated by strong femtosecond IR laser pulses. We have tested the relevance of the commonly accepted Lochfraß/Bond-Softening interpretations of these dynamics. We showed that this dichotomy is actually highly limited since it erroneously supposes that the two mechanisms are decoupled. As a consequence, the previously used models where one consider only one of the two excitation mechanisms (BS or LF) leads to unphysical interpretations of the system dynamics. Since the two mechanisms are coupled, they actually have to be included simultaneously in the model to get correct results. In particular we showed that the information contained in the phase of the nuclear wave packet oscillations was more delicate to interpret than predicted in [222, 223, 227].

Moreover we investigated the influence of the vibronic correlation on the dynamics. We found that this correlation has minimal consequences for low intensity and very short laser pulses. On the contrary for high intensity and longer pulses, we found that we could not neglect the part of the wave function that left the electronic ground state and recombines with it later on. This recombination is a correlated process that is completely absent of the Born-Oppenheimer model. Our correlated numerical results indicate that it induces excitation in higher vibrational levels and is strongly dependent on the carrier envelop phase of the laser pulse. This CEP-dependency could be used as a signature of vibronic correlations in experimental measurements. We could not manage to identify the mechanism which explains this CEP-dependency. Our results with a short-range potential indicates that the recombination processes occurs mainly from the electronic excited states, but that the contribution of the continuum states, i.e. the ionized part of the wave function, cannot be neglected either. More work is required to further conclude on which electronic states are involved in the vibronic correlations.

Finally we derived the expression of the Bond-Softening term that appears in the nuclear TDSE using the Wigner-Weisskopf approach. We found a correction term that may allow to include some correlation while keeping a BO description of the wave function. More simulations are needed to determine to what extent it contributes. We could not directly apply the same approach for the Lochfraß term since the couplings between the continuum states have to be taken into account.

Chapter VI

Time-Dependent Configuration Interaction

In the previous chapters, we have studied the response of atomic and molecular systems to intense and ultrashort laser pulses. In many cases, reaching a clear understanding of the mechanisms that govern the electron dynamics is still a challenge that requires advanced theory [164]. It is therefore crucial to develop theoretical and computational methods capable of providing precise treatments of the fundamental electronic processes generated by a strong laser field [228–231]. To achieve this goal we can rely on two complementary approaches: accurate numerical calculations to get quantitative results, and approximate or simplified models to get more qualitative quantities but valuable physical insight. In the previous chapters we concentrated on the latter. Our strategy was either to develop approximate analytical models, or to consider simple systems with low dimensions, for which an intensive numerical treatment is possible. As we saw, this qualitative approach is very powerful because it allows to develop physical interpretations. In this chapter we follow the other approach: we investigate numerical methods that would be able to describe larger and more complex system.

In strong field physics, the most numerically accurate computational approaches usually rely on the Single Active Electron (SAE) approximation. This supposes that only one electron participates to the dynamics, and that all the other electrons remain "frozen". Indeed, we have seen in Chapter I that highly non-linear processes are initiated when tunnel ionization is induced by the laser electric field. This effect depends exponentially on the potential energy barrier, and thus on the energy of the orbital from which the electron is ionized: the deeper the orbital, the more difficult it is for the electron to tunnel out. For atomic systems the orbitals are in general sufficiently separated in energy so that only the highest one gets ionized, leaving the ion in its ground state. We can thus discard the electronic dynamics in the ion, and only describe the ionized electron. However, this approximation is not always justified. In Xenon it has been showed that the returning electron may interact with the electrons of the ion, leading to an extension of the HHG cutoff relative to the SAE predictions [232, 233] which has been experimentally measured [49]. In the case of molecules the energy differences between the Highest Occupied Molecular Orbital (HOMO) and the inner-valence orbitals (the so-called HOMO-1, HOMO-2...) is in general smaller than for atoms. In this case, several orbitals may be

ionized, leaving the ion in several excited states. The relative importance of these ionization *channels* will depend on the orbital geometry and on the orientation of the molecule with respect to the field. In the particular case of HHG, each ionization channel leads to a quantum path with the same initial and final states, so that they may interfere, and the interference signature could be seen in the emitted spectrum. Such interferences have been experimentally measured and used to retrieve the dynamics of the hole in the molecular ion [50, 234]. Obviously the computational methods based on the SAE approximation cannot account for such multi-electron effects.

Nowadays, the multi-electron dynamics problem in strong laser fields is tackled by two main families of theoretical methods: Time-Dependent Density Functional Theory (TDDFT) and time-dependent wave-function methods [164, 235–239]. Most developments in these approaches focus on the accurate description of electron correlation. However, because of the complexity of non-linear optical phenomena, such as HHG and ATI, another crucial aspect needs to be carefully addressed: the choice of the one-electron basis set for representing the time-dependent wave function involved in these models. In fact, a reliable description of the electron dynamics in strong laser fields depends on the accuracy in reproducing the bound states and, more importantly, the continuum states of the molecule. In addition, choosing a "good" basis set can improve the numerical convergence of the results and reduce the computational cost of simulations.

Most of the proposed numerical methods in the literature directly describe the system wave function on a real-space grid [10, 240–242] or through a numerically defined grid-based basis set of functions, as in the case of the discrete-variable representation method [141], the pseudospectral grid method, or the finite-element method [243]. Within these approaches, new schemes have been proposed to compute ATI spectra in molecules [244] and to study the different molecular orbital contributions to HHG spectra [245, 246]. Grid-based basis sets have demonstrated to be very efficient to describe non-linear optical phenomena. However, the computational cost can be very high and the development of strategies involving multi-level parallelization schemes for massively parallel simulations have been necessary [247].

Another recurrent basis set in the context of ultrafast electron dynamics is composed of B-splines, defined as piecewise polynomial functions with compact support [248]. They were first introduced in atomic calculations by B. Shore [249] and later extensively used to treat ionized and excited states [250, 251]. B-splines have proved to be a very powerful tool to describe multiphoton ionization processes in atoms and molecules in the frameworks of TDDFT and wave-function methods [252, 149, 253, 254]. The success of B-splines is due to a remarkable feature: B-splines can reproduce accurately and simultaneously both bound and continuum states. This numerical property is directly related to their effective completeness [255]. Today atomic packages based on B-splines are available [256–258] and recent studies show their ability to reproduce HHG and ATI spectra of molecules under the action of strong laser fields [259]. However, new algorithms have to be developed in order to increase the computational efficiency of calculations with B-splines for larger systems.

More recently, Gaussian-type orbital functions (abbreviated as Gaussian functions in the following), that extensively proved their efficiency for the computation of the bound state of many different chemical species, have been used to calculate HHG spectra in atoms and molecules in the framework of the Time-Dependent Configuration Interaction (TDCI)

method [260, 235, 261, 262]. The importance of diffuse basis functions and multi-centered basis functions to improve continuum states was pointed out [260, 235]. Alternatively, Gaussian functions with exponents optimized to improve the description of the continuum states have been used in the case of the H and He atoms [261, 263]. This latter strategy has lower computational cost, although it remains to be tested on molecular systems.

Finally, to overcome some of the limitations of the grid, B-splines, and Gaussian basis sets, hybrid basis sets have been proposed in recent years. Gaussian functions were used together with grid-based functions to reproduce electron dynamics in molecular systems [264], and Gaussian functions have also been combined with B-splines for studying ionization of H and He atoms [265, 266].

In this work, performed in collaboration with Felipe Zapata Abellán, Emanuele Coccia, Julien Toulouse, Valérie Véniard and Eleonora Luppi from the Laboratoire de Chimie Théorique at Sorbonne Université, we compare the performance of the three families of basis sets briefly reviewed above, i.e. Grid, B-splines, and Gaussians, for the calculation of HHG and ATI spectra of the molecular ion H_2^+. This benchmark system has been chosen because it has the advantage of having only one electron, which allows us not to bias our investigation with possible effects due to electron correlation. Indeed, with this simple case, we can focus on the effectiveness of the representation of the continuum states for the electron dynamics and the computational advantages of each basis set. Moreover, the presence of two nuclei in H_2^+ offers the opportunity to observe intricate physical features, such as quantum interferences in the HHG process [267, 268, 200] as we saw in Chapter IV. In this case we were able to perform calculations in 1D as well as in 3D. The 3D results, obtained by Emanuale Coccia and Eleonora Luppi will not be presented here.

We then investigate the perspective of generalization of the grid and Gaussian methods to bielectronic systems. In particular we study the ability of the TDCI method, developed in [235], to reproduce the HHG spectrum of the H_2 molecule and of the Helium atom, by comparing its predictions with converged results obtained on a bidimensional grid. In the present work we only did 1D simulations. Indeed, even the bidimensional grid calculations already needed to run for a few tens of hours to get converged results, so that 3D calculations were unreachable. In contrast, the Gaussian-based TDCI simulations only lasted a few minutes, which highlights why the latter method seems promising for the description of even larger systems.

Note that, as mentioned above, we will test that ability of the different method to reproduce the continuum states of the system. However, all these numerical models rely on a discretization of the Hilbert space, so that, as detailed for the real-space grid in section II.1.1, the spectrum of the discretized Hamiltonian do not present a real "continuum". Nevertheless, through misuse of language, we will call "continuum" the positive energy part of the spectrum.

Objectives

- Find a computational method able to accurately describe multi-electron systems in strong fields.
- Investigate the basis set on which to develop such a method.
- Test the ability of the TDCI method to reproduce the HHG spectrum of bielectronic

systems.

VI.1 One dimensional theoretical model of H_2^+

Our 1D model of H_2^+ is defined by a molecular Soft-Coulomb potential (II.2) (see section II.1.1). The regularization parameter a is chosen to reproduce the ionization potential $I_p = 30$ a.u. of the real H_2^+ molecule at a given value of the internuclear distance R ($a = 1.2$ a.u. at $R_{eq} = 2.0$ a.u.) [211]. HHG spectra were obtained from the solution of the discretized TDSE via the Fourier transform of the average value of the acceleration as depicted in section II.3.2, and ATI spectra were obtained with the Window method as detailed in section II.3.4.

VI.1.1 Real-space Grid

As in the previous chapters, and as described in section II.1.1, the 1D time-dependent wave function is discretized on a real-space grid of N_x points x_i separated by a constant step Δx. It is thus represented by the vector

$$|\psi(t)\rangle \equiv (\psi(x_1,t),\ldots,\psi(x_i,t),\ldots,\psi(x_N,t)). \tag{VI.1}$$

The TDSE is solved by means of the Crank-Nicolson propagation algorithm [83] (see section II.1.2 b)). The H_2^+ ground state computed by inverse iteration [137] (see section II.1.3) is taken as the initial state in the propagation. In addition, to avoid unphysical reflections at the boundaries of the simulation grid, a mask-type absorber function [143] was implemented with a spatial extension of $h_{abs} = 50$ a.u. (see section II.1.1 c)).

For ATI spectra, converged results were obtained with $N_x = 200001$ and $\Delta x = 0.02$ a.u., and with a time step $\Delta t = 8.41 \times 10^{-4}$ a.u.. For HHG spectra, we obtained converged results with $N_x = 160001$, $\Delta x = 0.01$ a.u., and $\Delta t = 1.35 \times 10^{-2}$ a.u..

VI.1.2 B-spline basis set

These calculations were performed by Felipe Zapata Abellán during his PhD at the Laboratoire de Chimie Théorique at Sorbonne Université, and we are grateful to be allowed to present his results here.

The time-dependent wave function with the B-spline basis set is represented as

$$\psi(x,t) = \sum_{i=1}^{M} c_i(t) B_i^k(x), \tag{VI.2}$$

where $c_i(t)$ are time-dependent coefficients and $B_i^k(x)$ are B-spline functions of order k and dimension M. The B-spline, $B_i^k(x)$, is a piecewise polynomial of degree $k-1$ defined inside an interval of the support grid $\mathbb{X}_i \leq x \leq \mathbb{X}_{i+k}$ and which vanishes outside this interval. The end-points of the support grid are chosen to be k-fold degenerate : $\mathbb{X}_1 = \mathbb{X}_2 = \ldots = \mathbb{X}_k = \mathbb{X}_{min}$ and $\mathbb{X}_{M+1} = \mathbb{X}_{M+2} = \ldots = \mathbb{X}_{M+k} = \mathbb{X}_{max}$ and for non-degenerate grid points the width of the interval is $\mathbb{X}_{i+1} - \mathbb{X}_i = \mathbb{X}_{max}/(M-k+1)$ [149].

In our calculations we used $k = 8$, $M = 15008$, $\mathbb{X}_{\min} = 0$ and $\mathbb{X}_{\max} = 8000$ a.u.. The system was placed at the center of the box at $x = 4000$ a.u..

ATI and HHG spectra were obtained by solving the TDSE with the Crank-Nicolson propagation algorithm [83, 137] using a time step of $\Delta t = 1.35\times10^{-2}$ a.u.. The H_2^+ ground state computed by inverse iteration [137] is taken as the initial state in the propagation. We did not use any absorber during the propagation.

VI.1.3 Gaussian basis set

For the Gaussian basis set we followed the TDCI procedure developed in our previous work [235], that we adapted to the present 1D H_2^+ model. The time-dependent wave function is represented here as

$$\psi(x,t) = \sum_{k\geq 0} c_k(t)\phi_k(x), \tag{VI.3}$$

where $\phi_k(x)$ are eigenstates of the field-free Hamiltonian $\hat{H}_0$, and $c_k(t)$ are time-dependent coefficients. The $\phi_k(x)$ are themselves expanded on a Gaussian basis set. In this work, we use uncontracted Gaussians localised on each nucleus and two "angular momenta" $\ell = 0, 1$, corresponding to odd and even functions. The basis functions are thus of the form $(x \pm R/2)^\ell \, \mathrm{e}^{-\alpha x^2}$. The Gaussian exponents α are of two different types. The first type of exponents are optimized to describe the bound part of the wave function. We used the uncontracted STO-3G basis set, i.e. three uncontracted Gaussians whose exponents are taken from the STO-3G basis set with $\zeta = 1$. We take the same exponents α for $\ell = 0$ and $\ell = 1$. The second type of exponents are optimized for the representation of the continuum.

In a previous collaboration with the Laboratoire de Chimie Théorique [235], we showed that to properly represent "continuum" states with gaussians, one needs to add large gaussians, with small exponants α, to the basis. However, if we simply add the commonly used *diffuse* gaussian basis functions then we only improve the representation of the Rydberg states [235]. However we demonstrated that we could selectively improve the "continuum" representation, by using specifically optimized uncontracted gaussian basis functions. They are computed with the procedure developed by Kaufmann [269] adapted to the 1D model, i.e. by optimizing the overlap between a 1D Slater type function $N_n^{(S)}(\zeta)x^n \, \mathrm{e}^{-\zeta|x|}$ and a Gaussian function $N_l^{(G)}(\alpha_{n,\ell})x^\ell \, \mathrm{e}^{-\alpha_{n,\ell}x^2}$, where $N_n^{(S)}$ and $N_l^{(G)}$ are normalization factors, and with $\zeta = 1$. Note that, in this case, the exponents used for the $\ell = 0$ shell and for the $\ell = 1$ shell are different. In the following, we will denote these Gaussians as "K functions". To sum up, we use 3 STO-3G exponents and 4 K functions for each angular momentum and localized on each nucleus, which makes a total of $(3+4)*4 = 28$ uncontracted Gaussian basis functions. However when we orthonormalize this basis set with the canonical orthonormalization procedure [270], we find linear dependencies that needs to be removed from the active space. For this we define a cutoff $\epsilon = 10^{-8}$ under which the eigenvalues of the overlap matrix are considered to be zero, and their corresponding eigenvectors are removed from the active space. We get an orthonormalized basis set of 24 basis functions.

To solve the TDSE we used the split-operator propagator (see section II.2.2), i.e. the time-dependent Hamiltonian is split into two terms, the field-free Hamiltonian $\hat{H}_0$ and

the interacting Hamiltonian (caused by the laser field) H_{int}:

$$|\psi(t+\Delta t)\rangle = \mathrm{e}^{-iH\left(t+\frac{\Delta t}{2}\right)\frac{\Delta t}{2}}\,|\psi(t)\rangle \simeq \mathrm{e}^{-i\hat{H}_0\frac{\Delta t}{4}}\,\mathrm{e}^{-iH_{\text{int}}\left(t+\frac{\Delta t}{2}\right)\frac{\Delta t}{2}}\,\mathrm{e}^{-i\hat{H}_0\frac{\Delta t}{4}}\,|\psi(t)\rangle\,. \tag{VI.4}$$

with a time step $\Delta t = 1.35\times10^{-2}$ a.u.. The field-free Hamiltonian is diagonal in the basis of its eigenvectors (ϕ_k), so that computing its exponential is straightforward. To compute the exponential of $H_{\text{int}}(t)$, we need to diagonalize it. Since it depends on time, we might have to do it at each time step but this matrix is of the form $x\mathbf{F}_{\text{L}}(t)$ in length gauge, and $p\mathbf{A}_{\text{L}}(t)$ in velocity gauge. We thus only need to diagonalize the x or p operator (depending on the chosen gauge) to know the eigenvectors of H_{int}, which can be done once and for all at the beginning of the propagation. We then go from the basis of the eigenvectors of $\hat{H}_0$ to the basis of the eigenvectors of H_{int} by a simple matrix vector multiplication. Note that this change of basis has a $O(N^2)$ complexity which is less efficient than the Fourier transform step described in section II.2.2. However, since the basis size is small, the computation cost remains very low.

In order to compensate for the unphysical absence of ionization, we use the double-d heuristic lifetime model proposed in [235]. This approach is the analogue of an absorber such as the one we described in section c) but in energy space. The continuum states are given an effective lifetime τ by adding an imaginary part to their energy:

$$\widetilde{E} = E - i\frac{1}{2\tau}. \tag{VI.5}$$

This lifetime is chosen as the time it would take for a free electron of kinetic energy E to travel a fixed distance d:

$$\tau = \frac{d}{\sqrt{2E}}. \tag{VI.6}$$

For the "double-d" model, we define two different values d_0 and d_1 for this escape length that we choose on the basis of the rescattering model [91, 11] (see section I.3.2). From this model, we know that only the continuum states whose energy is below the cutoff value $E_{\text{cutoff}} = I_{\text{p}} + 3.17U_{\text{p}}$ [91, 11] will effectively participate in the HHG process. For these continuum states we thus choose an escape length d_0 equal to the maximum electron excursion after ionization which is

$$x_{\max} = 2x_\alpha = \frac{2F_0}{{\omega_{\text{L}}}^2}. \tag{VI.7}$$

On the other hand, the continuum states whose energy lies above the cutoff will only pollute the simulation with spurious reflections and thus need to be absorbed faster. For these states, we choose an escape length $d_1 = 20$ a.u..

There is a fundamental difference between this approach and the previous approaches in Grid and B-splines. In fact, the TDSE with the Gaussian basis set is solved in the energy space. This permits to have a more direct and intuitive interpretation of the role of bound and continuum states in HHG and ATI spectroscopies. In addition, the use of Gaussians reduces considerably the computational time required in time propagation. This makes it a promising tool for the modelization of larger molecules.

VI.1.4 Laser field

The interaction with the laser field is computed in length gauge (see section I.1.2). The laser electric field is chosen as $F_{\mathrm{L}}(t) = F_0 f(t) \sin(\omega_{\mathrm{L}} t)$ where F_0 is the maximum amplitude of the pulse, ω_{L} is the carrier frequency, and $f(t)$ is a trapezoidal envelope:

$$f(t) = \begin{cases} t/T_{\mathrm{L}}, & 0 \leq t < T_{\mathrm{L}} \\ 1, & T_{\mathrm{L}} \leq t < 9T_{\mathrm{L}} \\ 10 - t/T_{\mathrm{L}}, & 9T_{\mathrm{L}} \leq t < 10T_{\mathrm{L}}, \end{cases} \tag{VI.8}$$

with $2\pi/T_{\mathrm{L}} = \omega_{\mathrm{L}}$. The duration of the pulse is thus $\tau_{\mathrm{L}} = 10\ T_{\mathrm{L}}$ (i.e. 10 optical cycles). The Fourier transform is performed on the 8 optical cycles corresponding to the plateau part of the laser pulse.

VI.2 Results and discussion for H_2^+

VI.2.1 Spectrum of the field-free Hamiltonian

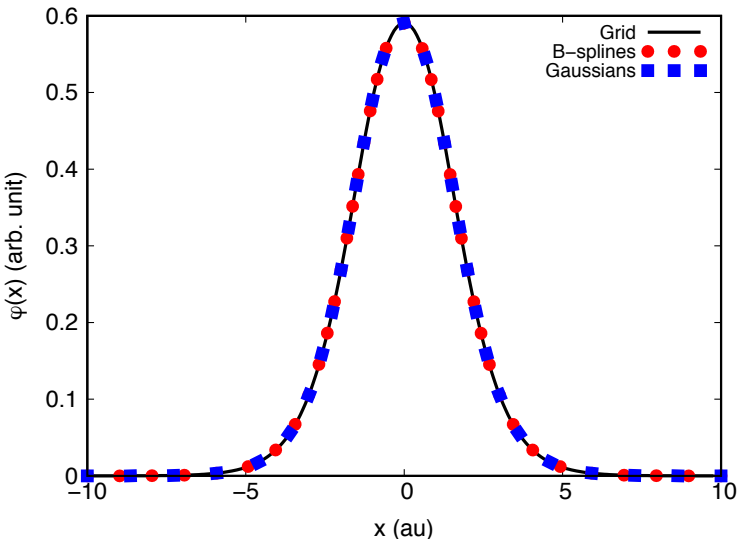

Figure VI.1 *Ground state of H_2^+ calculated using Grid, B-splines and Gaussian basis sets.*

The three implemented bases span different Hilbert spaces in which the system will evolve during the time propagation. To illustrate how these Hilbert spaces look like, we first decided to compute the spectrum and eigenstates of the field-free Hamiltonian $\hat{H}_0$, i.e. to solve the TISE. These *time-independent* results will give us some useful information to subsequently understand the differences between the *time-dependent* results obtained with the three bases.

In Figure VI.1 the ground state is shown. The three basis sets reproduce exactly the ground state of the 1D H_2^+ model. In panel (a) of Figure VI.2 we report the eigenvalues of the 30 first energy ordered states, and in panel (b) of Figure VI.2 we show the inverse

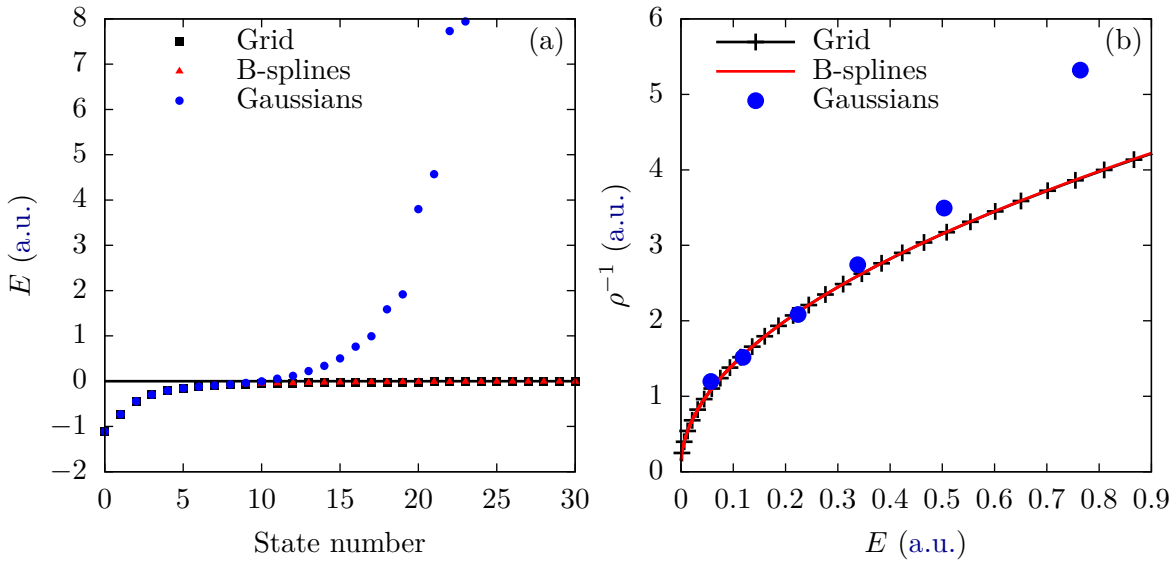

Figure VI.2 *(a) Eigenvalues up to the* 30^{th} *eigenstate. (b) Inverse of the normalized density of continuum states.*

of the density of the continuum states which is defined as

$$\rho(E_j) = \frac{1}{E_{j+1} - E_j}, \tag{VI.9}$$

where E_j is a positive eigenvalue. In order to compare the three basis sets, the density has been normalized to the length of the simulation box in the case of Grid and B-splines and to an arbitrary constant in the case of Gaussians. Since the three basis sets contain a finite number of elements, the "continuum" part of the spectrum obviously contains a finite number of eigenstates. As we have seen in section II.1.1, the "continuum" computed on a grid is actually very close to the exact "continuum" of a free particle in a box, if we remain at low energies. We observe that this is also the case for the B-splines, and that there are virtually no differences between the grid and the B-splines results. Surprisingly the density of states computed with the Gaussians is actually quite close to the one of the particle in a 25 a.u. box. However the number of "continuum" states is much lower that in the case of the Grid or the B-splines. This issue is a direct consequence of the relatively small size of the Gaussian basis set compared to the number of Grid or B-splines used. Indeed, the basis STO-3G+4K contains only 24 Gaussian basis functions whereas we used 40001 grid points and 15000 B-splines. In principle, we could increase the number of Gaussians but this quickly leads to numerical instabilities, as will be discussed in section VI.2.3. This problem prevents us to use more than a few tens of optimized Gaussian functions. This fact, as we will see in the following sections, can have important consequences on the calculation of HHG and, in particular, of ATI spectra.

To investigate the accuracy of Grid, B-splines and Gaussian in the description of the "continuum" wave functions, we have chosen two "continuum" energies representative of two different positive energy regions : low energy $E = 0.06$ a.u. and high energy $E = 1.97$ a.u.. For each of these energies, we reported in Figure VI.3 the correspond-

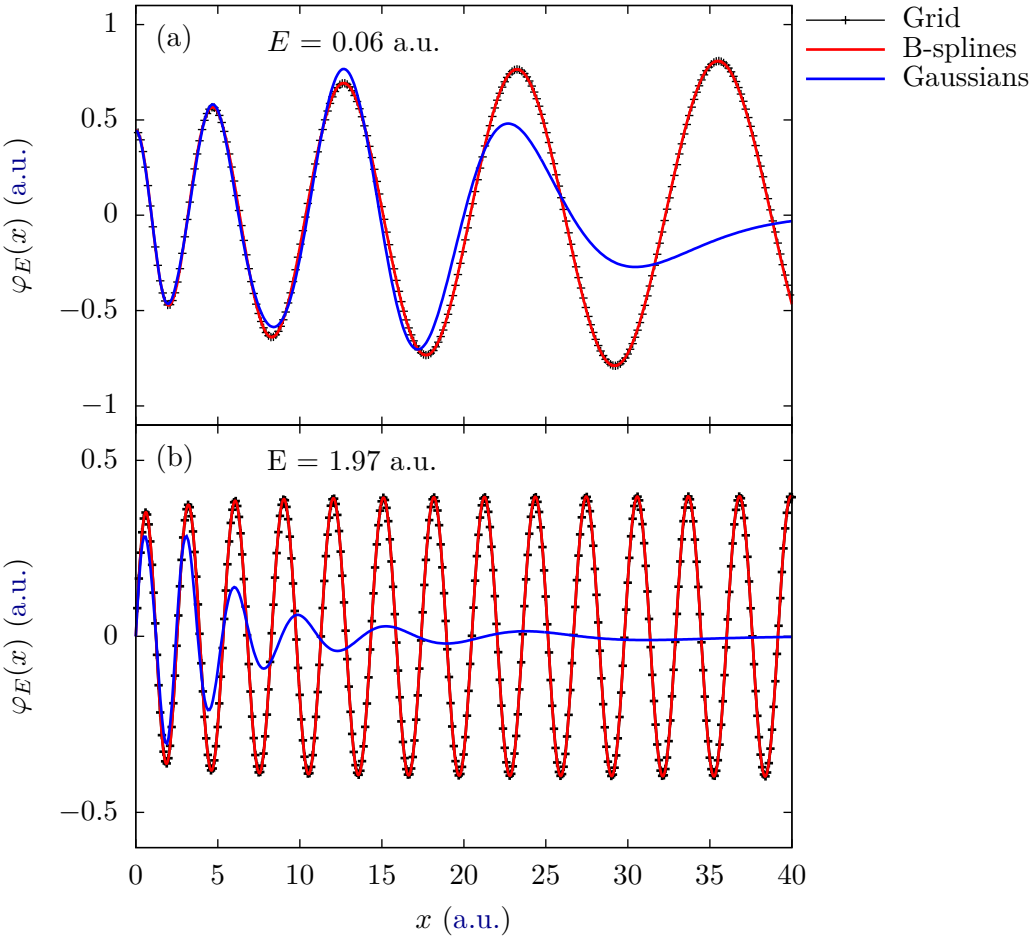

Figure VI.3 *(a) Spatial dependency of the even wave function φ_E(x) corresponding to E = 0.06 a.u.. (b) Spatial dependency of the odd wave function φ_E(x) corresponding to E = 1.97 a.u..*

ing wave functions. For the Grid basis set, the continuum wave functions were obtained by propagating the time-independent Schrödinger equation at the chosen positive energy E with a fourth order Runge-Kutta algorithm [137], and then normalizing with the Strömgren procedure [271] as described in section II.1.1 c). Instead, for B-splines and Gaussians, the wave functions were obtained from a direct diagonalization of $\hat{H}_0$. In this case, the resulting "continuum" states were renormalized using the procedure proposed by Macías et al. in [272]. We verified numerically that Strömgren and Macías procedures are equivalent. The "continuum" wave functions computed with both Grid and B-splines basis sets reproduce the same oscillations in the low and in the high energy regions of the "continuum".

On the other hand the inherent local nature of Gaussian functions strongly limits their ability to represent delocalized continuum states. On Figure VI.3, it is clear that the Gaussian basis set can reproduce only few of the oscillations. We already observed this behaviour in the case of the hydrogen atom in a 3D calculation [261] where the crucial

role of K functions was pointed out in order to obtain these oscillations. The continuum states represented by Gaussians will therefore be close to the exact one only within a limited space region, close to the nuclei, which size gets smaller as the continuum state energy gets higher.

This feature may not necessarily be prohibitive for subsequent time-dependent calculations. Indeed if one needs to describe an electron that remains in the vicinity of the nucleus, these *local* continuum states will still be a good approximation of the exact continuum states. In particular in the case of HHG, as we have seen in section I.3, the electron is ionized by the strong field, accelerated in the continuum, and then brought back close to its parent ion where it can recombine to emit a photon. The classical three-step model that describe HHG gives an estimate of the maximal excursion $x_{\max}$ (VI.7) the electron undergo during this process. As long as this quantity remains smaller than the effective size of the Gaussian continuum states, we expect the Gaussian basis to be well adapted for HHG computations. As is evident from the simple formula (VI.7), the main limitations will arise when the intensity of the incident laser is too high, or when its frequency is too small.

VI.2.2 HHG

We studied HHG in the dipole and acceleration form for H_2^+ at internuclear distance $R = 1.8$ a.u., 2.0 a.u. (equilibrium) and 2.2 a.u. for a Ti:Sapphire laser with a carrier frequency $\omega_L = 0.057$ a.u. (1.55 eV, 800 nm) and intensities $I_L = 5 \times 10^{13}$ W.cm^{-2}, 10^{14} W.cm^{-2}, 2×10^{14} W.cm^{-2}, 5×10^{14} W.cm^{-2} and 7×10^{14} W.cm^{-2}. The pulse has a trapezoidal form (VI.8) and a duration of 10 optical cycles.

In Figure VI.4 we show the dipole form of HHG at $R = 2.0$ a.u. in the case of laser intensities $I_L = 5 \times 10^{13}$ W.cm^{-2}, 10^{14} W.cm^{-2}, 2×10^{14} W.cm^{-2}, 5×10^{14} W.cm^{-2} and 7×10^{14} W.cm^{-2}. All the three basis sets reproduce well the expected features of an HHG spectrum, regardless of the applied field intensity: the intensity of the low-order harmonics decreases rapidly, then a plateau region follows where the intensity remains nearly constant, and at high frequencies the harmonic intensity decreases again. Because the system has inversion symmetry, only odd harmonics are emitted, which is a well known feature of HHG in isotropic media. We estimated the cutoff energy by calculating $E_{\text{cutoff}} = I_p + 3.17U_p$ as given in the rescattering model [91, 11]. This gives $E_{\text{cutoff}} = 25.6\omega_L$, $31.7\omega_L$, $43.9\omega_L$, $80.5\omega_L$ and $104.9\omega_L$ respectively for the laser intensities $I_L = 5 \times 10^{13}$ W.cm^{-2}, 10^{14} W.cm^{-2}, 2×10^{14} W.cm^{-2}, 5×10^{14} W.cm^{-2} and 7×10^{14} W.cm^{-2}. These values are indicated in Figure VI.4 by a dot-dashed line.

We observe that Grid and B-splines HHG spectra are indistinguishable for all the laser intensities. On the other hand, the agreement of Gaussian with STO-3G+4K with Grid and B-splines deteriorates when the laser intensity increases. This is clearly observed for the plateau region in the case of $I_L = 5 \times 10^{14}$ W.cm^{-2} and for both the plateau and the cutoff region for $I_L = 7 \times 10^{14}$ W.cm^{-2}. These findings are fully consistent with the analysis reported above on the spectrum of the field free Hamiltonian (see VI.2.1). Note that, in Figure VI.4 we indicated by an arrow the expected position of the two-center interference minimum extracted from the recombination dipole. This will be detailed in the next section VI.2.4).

To analyze in more details the fine structures of the peaks we show in Figure VI.5 the

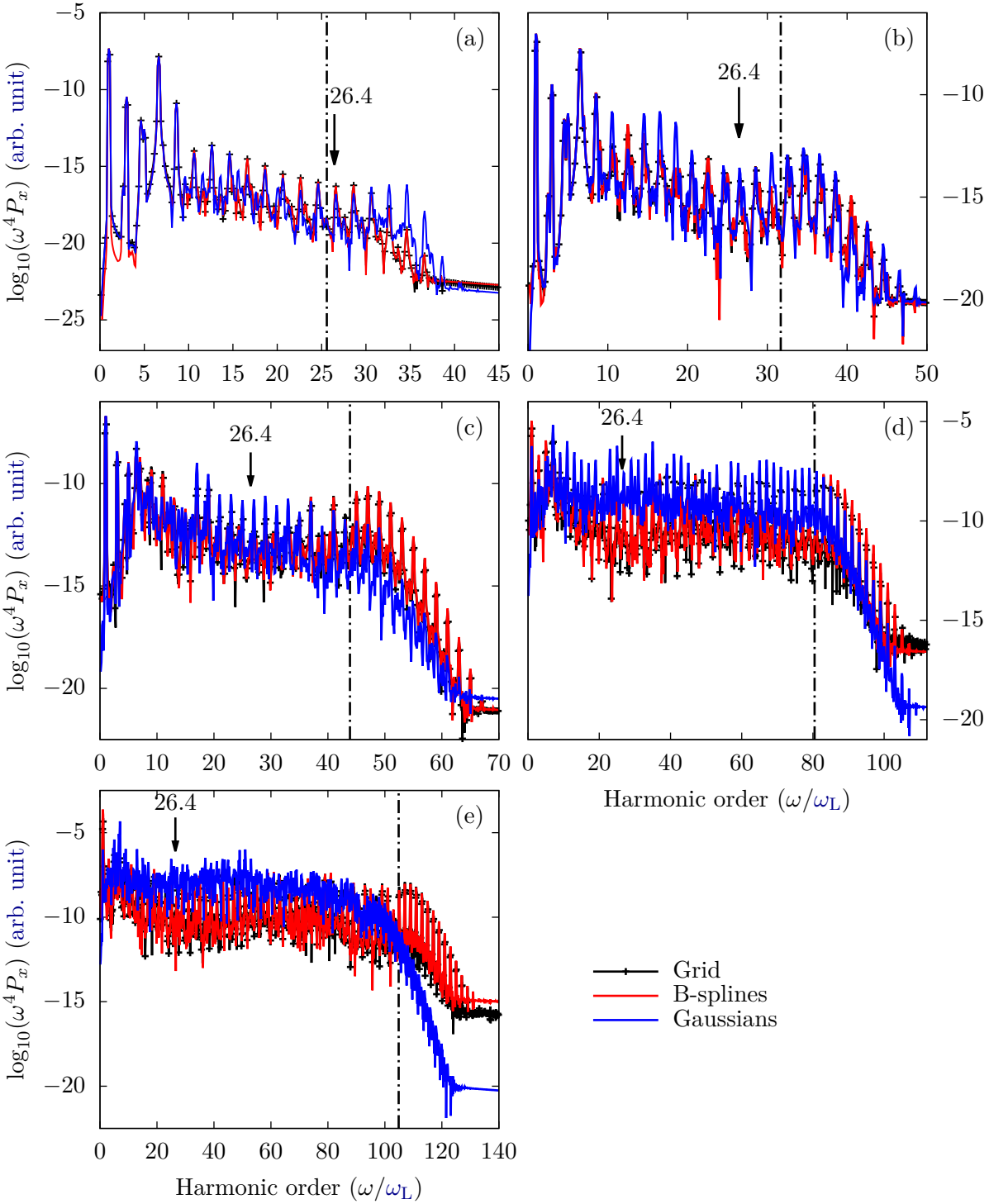

Figure VI.4 *HHG spectra from the dipole at the equilibrium internuclear distance* $R = 2.0$ *a.u. with laser intensities: (a)* $I_L = 5 \times 10^{13}$ W.cm^{-2}, *(b)* $I_L = 10^{14}$ W.cm^{-2}, *(c)* $I_L = 2 \times 10^{14}$ W.cm^{-2}, *(d)* $I_L = 5 \times 10^{14}$ W.cm^{-2} *and (e)* $I_L = 7 \times 10^{14}$ W.cm^{-2}. *For each HHG spectrum, the dot dashed line reproduce the cutoff energy* $E_{cutoff} = I_p + 3.17U_p$ *given by the rescattering model [91, 11] which is (a)* $E_{cutoff} = 25.6\omega_L$, *(b)* $E_{cutoff} = 31.7\omega_L$, *(c)* $E_{cutoff} = 43.9\omega_L$, *and (d)* $E_{cutoff} = 80.5\omega_L$, *and (e)* $E_{cutoff} = 104.9\omega_L$. *The arrow points to the expected position of the two center interference minimum extracted from the recombination dipole (see section VI.2.4).*

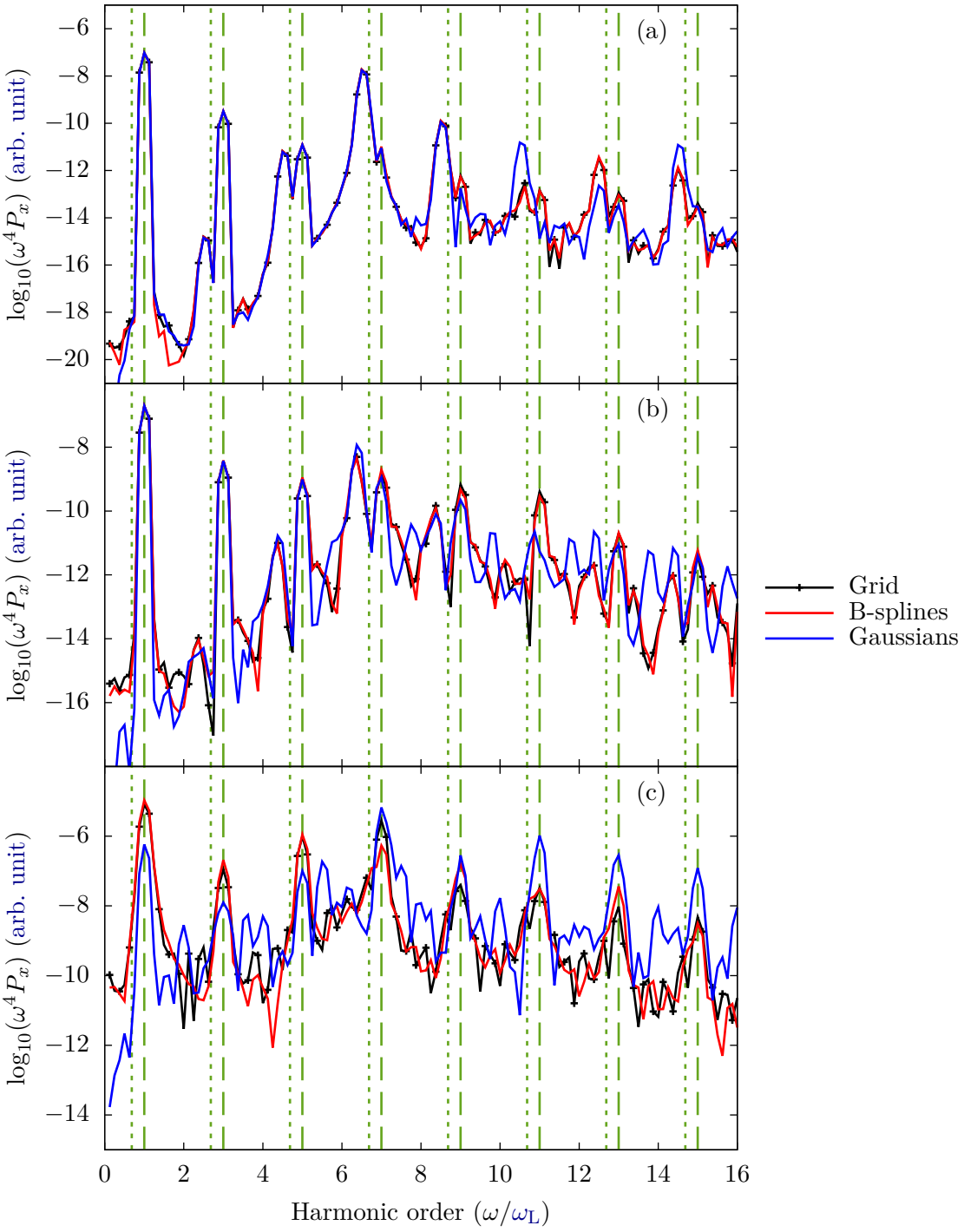

Figure VI.5 *HHG spectra from the dipole at the equilibrium internuclear distance* $R = 2.0$ a.u. *up to the 15th harmonic with laser intensities: (a)* $I_L = 10^{14}$ W.cm^{-2}, *(b)* $I_L = 2 \times 10^{14}$ W.cm^{-2}, *and (c)* $I_L = 5 \times 10^{14}$ W.cm^{-2}. *The dashed line indicates the position of the harmonics while the dotted line indicates the resonances due to the first excited state of* H_2^+.

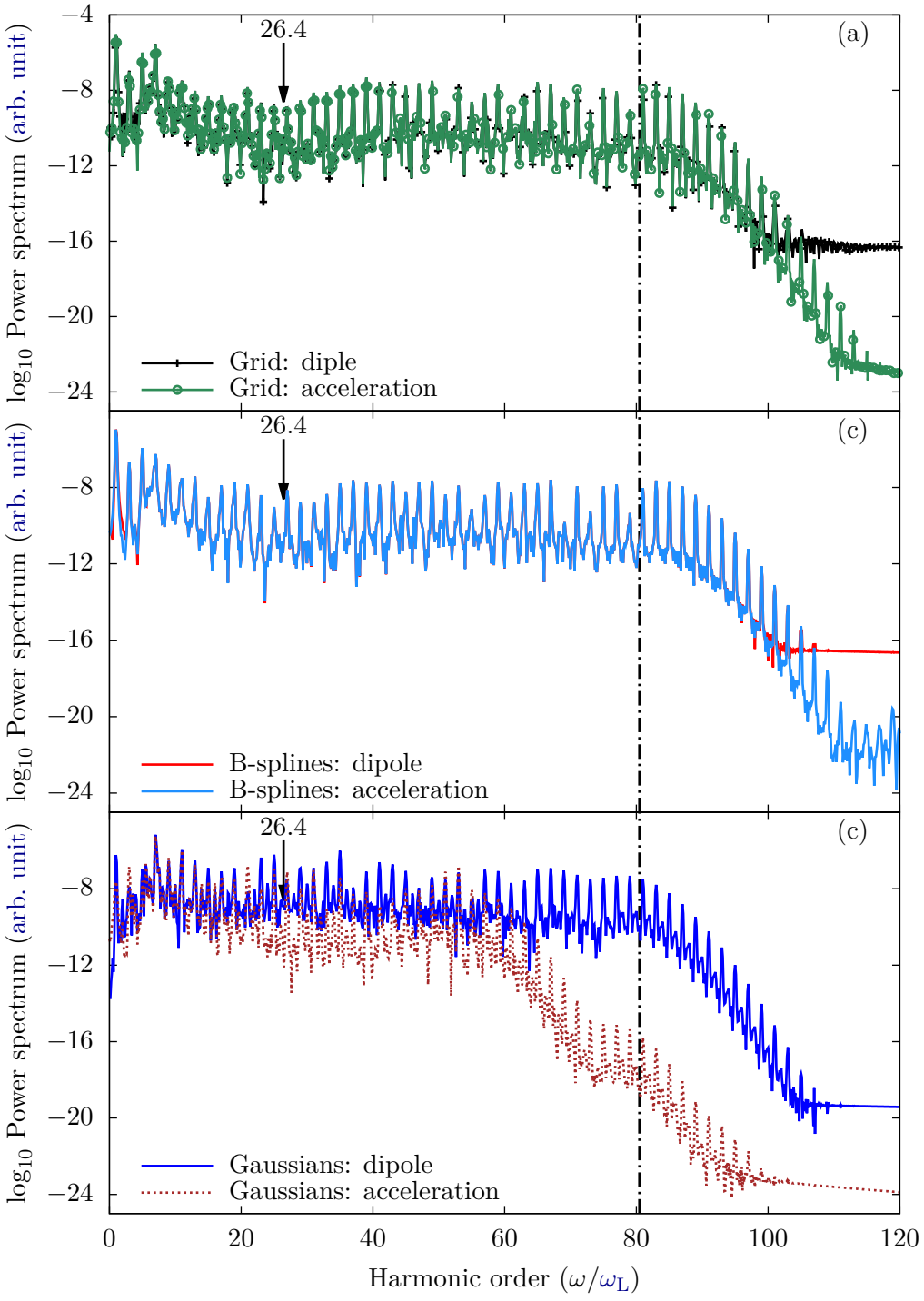

Figure VI.6 *HHG spectra in the dipole and acceleration form at the equilibrium internuclear distance $R = 2.0$ a.u. with laser intensity $I_L = 5 \times 10^{14}$ W.cm^{-2} calculated using (a) Grid, (b) B-splines and (c) Gaussians basis sets. The dash-dotted line is the cutoff energy $E_{cutoff} = 80.5\omega_L$. The arrow points to the expected position of the two center interference minimum extracted from the recombination dipole which is identical to the one extracted from the recombination acceleration (see section VI.2.4).*

same HHG spectra as in Figure VI.4 but up to the 15th harmonics. B-splines and Grid are almost identical except some very small differences which becomes more pronounced when the laser intensity increase. Gaussians reproduce the features of B-splines and Grid but increasing the laser intensity induces new structures, probably spurious, between the harmonic peaks.

In the spectra it is also possible to identify another series of peaks besides those corresponding to the odd order harmonics. Starting to considering the HHG spectrum for $I_{\mathrm{L}} = 10^{14}$ W.cm^{-2}, we observe a strong and large peak around $6.69\omega_{\mathrm{L}}$ which clearly dominates with respect to the 7th harmonic. The energy difference between these two peaks is $0.31\omega_{\mathrm{L}}$. Other strong peaks are found all shifted by $-0.31\omega_{\mathrm{L}}$ from odd harmonics. These peaks comes from a resonance with the first excited state which exactly corresponds to $6.69\omega_{\mathrm{L}}$ for H_2^+ and are related to so-called hyper-Raman transitions [273]. Observing the evolution of the harmonic and resonant peaks with laser intensity from $I_{\mathrm{L}} = 10^{14}$ W.cm^{-2} up to 5×10^{14} W.cm^{-2}, it is clear that the harmonic signal becomes stronger than the resonant peaks. This is in agreement with previous results on hyper-Raman transitions [273].

All these observations were confirmed by using the acceleration form to calculate the HHG spectra. The only exception we found was for Gaussians in the case of laser intensity $I_{\mathrm{L}} = 5 \times 10^{14}$ W.cm^{-2} (panel (c) Figure VI.6) and $I_{\mathrm{L}} = 7 \times 10^{14}$ W.cm^{-2}. In fact, the acceleration form seems to largely underestimate the position of the cutoff but to much better reproduce the harmonics of the plateau.

VI.2.3 Convergence and linear dependencies

The convergence properties are crucial features of any numerical method since it is the only way to systematically estimate the error introduced by the different approximations of the method. In the case of the Grid and B-spline representations, we had no problem reaching convergence with respect to the different simulation parameters (data not shown), and could therefore reach a precision comparable to the standard double precision numerical accuracy.

However, in the case of the Gaussian representation, convergence is a more delicate issue. We plot in Figure VI.7 (a) the same HHG spectrum shown in Figure VI.4 (b) but with three different Gaussian basis sets. The spectrum obtained with the Grid is also displayed as a reference, and the spectrum obtained with the B-splines is not displayed for clarity reasons.

We observe a good convergence of the low-energy part of the spectrum with respect to the number of Gaussians. However, the cutoff region does not really converge, and even deteriorates when the number of Gaussians is too large. This rather counter-intuitive feature is related to numerical instabilities caused by near linear dependencies in the Gaussian set.

These linear dependencies are observed as near zero eigenvalues of the overlap matrix of the primitive Gaussians. If these eigenvalues are too small compared to the numerical accuracy, then the set is, from a numerical point of view, linearly dependent and cannot be numerically orthonormalized. As explained in section VI.1.3, we circumvent this issue by introducing a cutoff ϵ under which the eigenvalues of the overlap matrix are considered to vanish. The corresponding eigenvectors are then removed from the active space to get

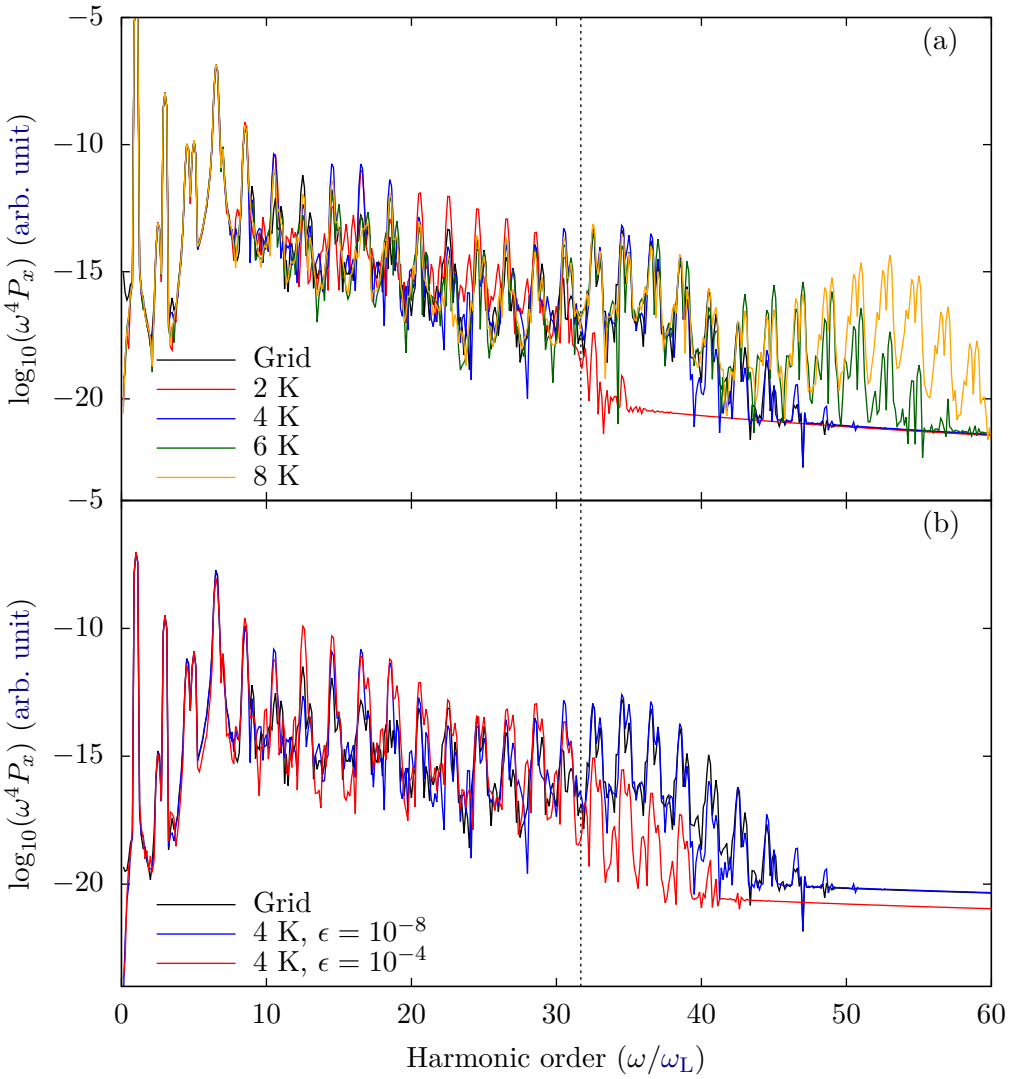

Figure VI.7 *HHG spectra at the equilibrium distance $R = 2.0$ a.u. with $I_0 = 1 \times 10^{14}$ W/cm^2 obtained with the Grid and with different Gaussian basis sets: STO-3G + 2, 4, 6 or 8 Kaufmann Basis functions on panel (a); and STO-3G + 4 Kaufmann Basis functions with $\epsilon = 10^{-8}$ or $\epsilon = 10^{-6}$ (see text) on panel (b).*

a smaller orthonormalized basis. However, when doing so, the quality of the basis is strongly affected, and the optimization procedures that were used to choose the primitive Gaussians cannot be fully efficient anymore. This is illustrated on Figure VI.7 (b) where we clearly see that when we use a larger value of ϵ, i.e. when we remove more vectors from the active space, the accuracy of the HHG spectrum decreases.

VI.2.4 Two-center interference

The accuracy of Grid, B-splines and Gaussian was also investigated through their ability to reproduce the signature of the two-center interference in the HHG spectrum [211]. As we have seen in Chapter IV, this phenomenon can be seen as a microscopic analog

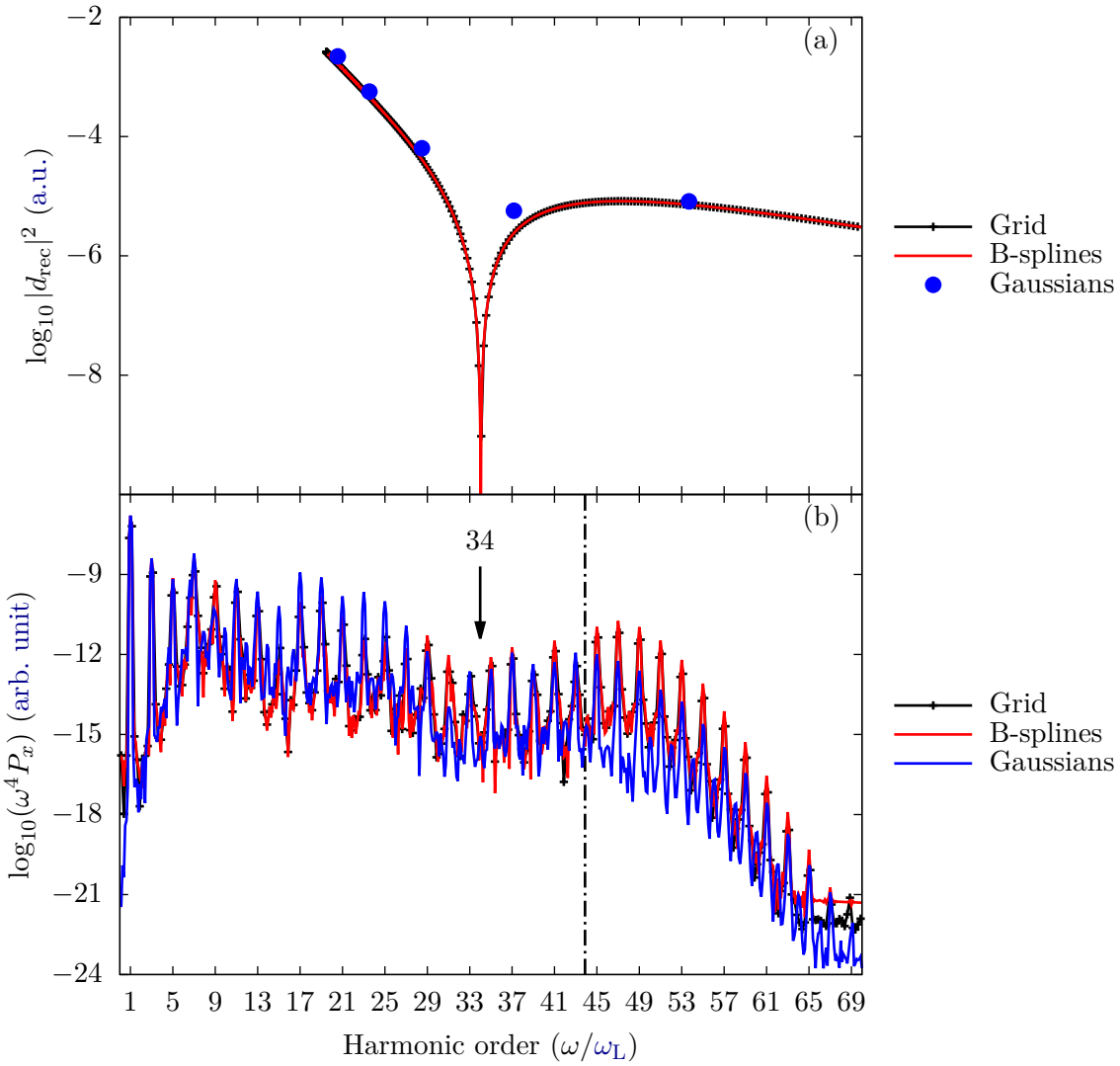

Figure VI.8 *Two center interferences at $R = 1.8$ a.u. : (a) recombination dipole and (b) HHG spectrum at $I_{\rm L} = 2 \times 10^{14}$ W.cm^{-2}. The arrow points to the expected position of the two center interference minimum extracted from the recombination dipole. The dot dashed line is the cutoff energy $E_{cutoff} = 43.9\omega_{\rm L}$.*

of Young's two slit experiment because the electron may recombine at either of the two nuclei to emit a photon in the third step of the HHG process. The light emitted by each nucleus will interfere either constructively or destructively depending on its frequency and the interference pattern will superimpose to the HHG spectrum. We have seen that this 2-center interference can be understood with the help of the molecular SFA model first developed by Lein [200]. Since this model has been proposed, a great number of numerical analyses came forth pointing out the role of internuclear distance, molecular orientation and vibration, recombination to excited states and laser intensity [267, 231, 217, 274, 84, 275, 46, 276, 216, 50].

We have seen in section IV.2.3 that the position of the minimum in the spectrum is

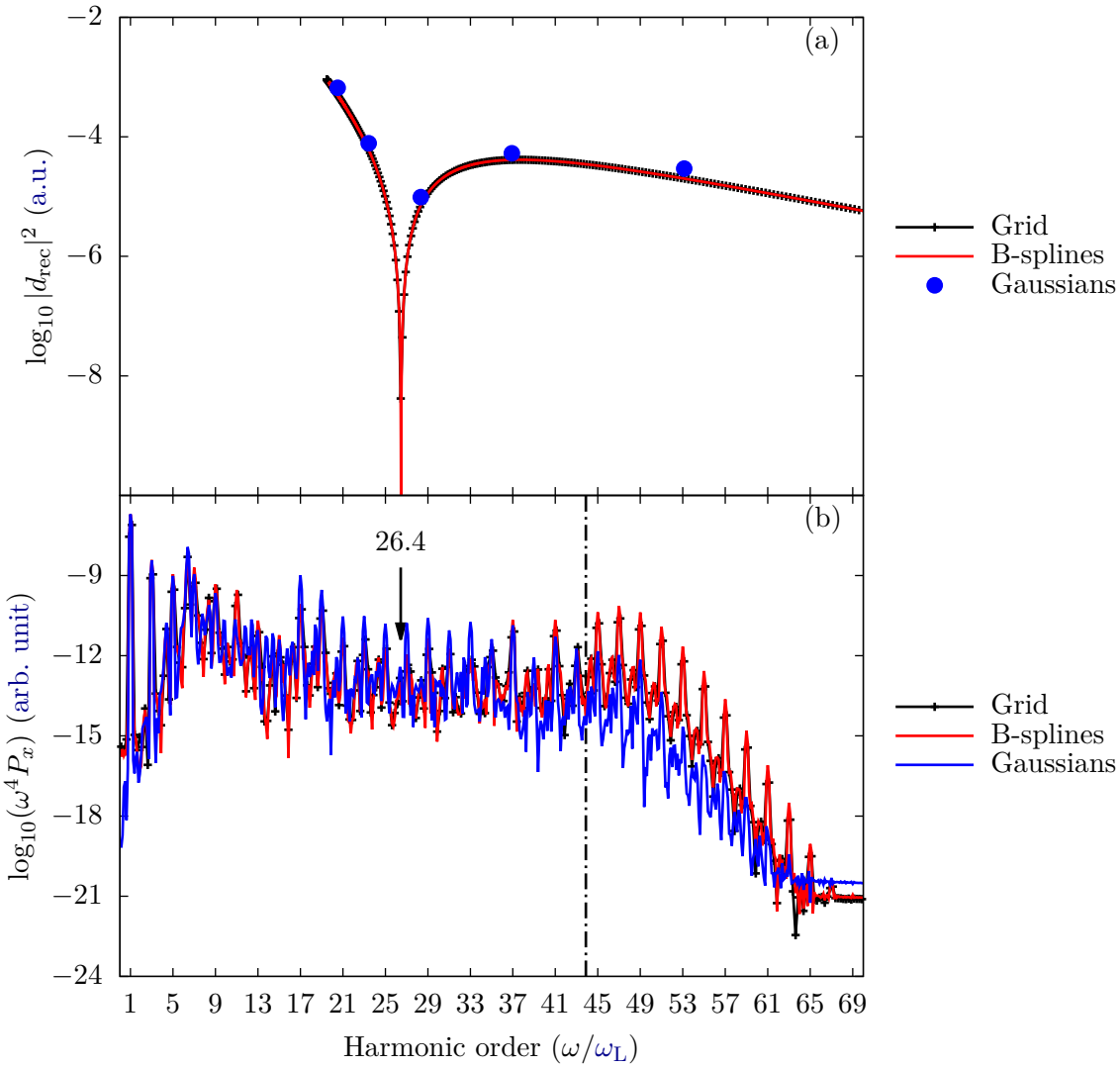

Figure VI.9 *Two center interferences at $R = 2.0$ a.u. : (a) recombination dipole and (b) HHG spectrum at $I_{\rm L} = 2 \times 10^{14}$ W.cm^{-2}. The arrow points to the expected position of the two center interference minimum extracted from the recombination dipole. The dot dashed line is the cutoff energy $E_{cutoff} = 43.9\omega_{\rm L}$.*

independent on the laser intensity and can be extracted from the analysis of the recombination dipole $d_{\rm rec}(E) = \langle\varphi_0|\hat{x}|\varphi_E\rangle$ [211] where φ_0 is the ground state and φ_E is a continuum state at energy E of $\hat{H}_0$. This quantity is plotted in panel (a) of Figure VI.8 for $R = 1.8$ a.u., in panel (a) of Figure VI.9 for $R = 2.0$ a.u. and in panel (a) of Figure VI.10 for $R = 2.2$ a.u.. We observe that, as in section IV.2.3, the position of the minimum in the HHG spectrum is well predicted by the first zero of the recombination dipole in the considered energy range. We found that this corresponds to $\omega_{\rm min} = 34.0\omega_{\rm L}$ for $R = 1.8$ a.u., $26.4\omega_{\rm L}$ for $R = 2.0$ a.u. and $20.8\omega_{\rm L}$ for $R = 2.2$ a.u.. We would like to note that the extraction of the minimum from the recombination dipole is straightforward for Grid and B-splines, while in the case of Gaussians the density of "continuum"

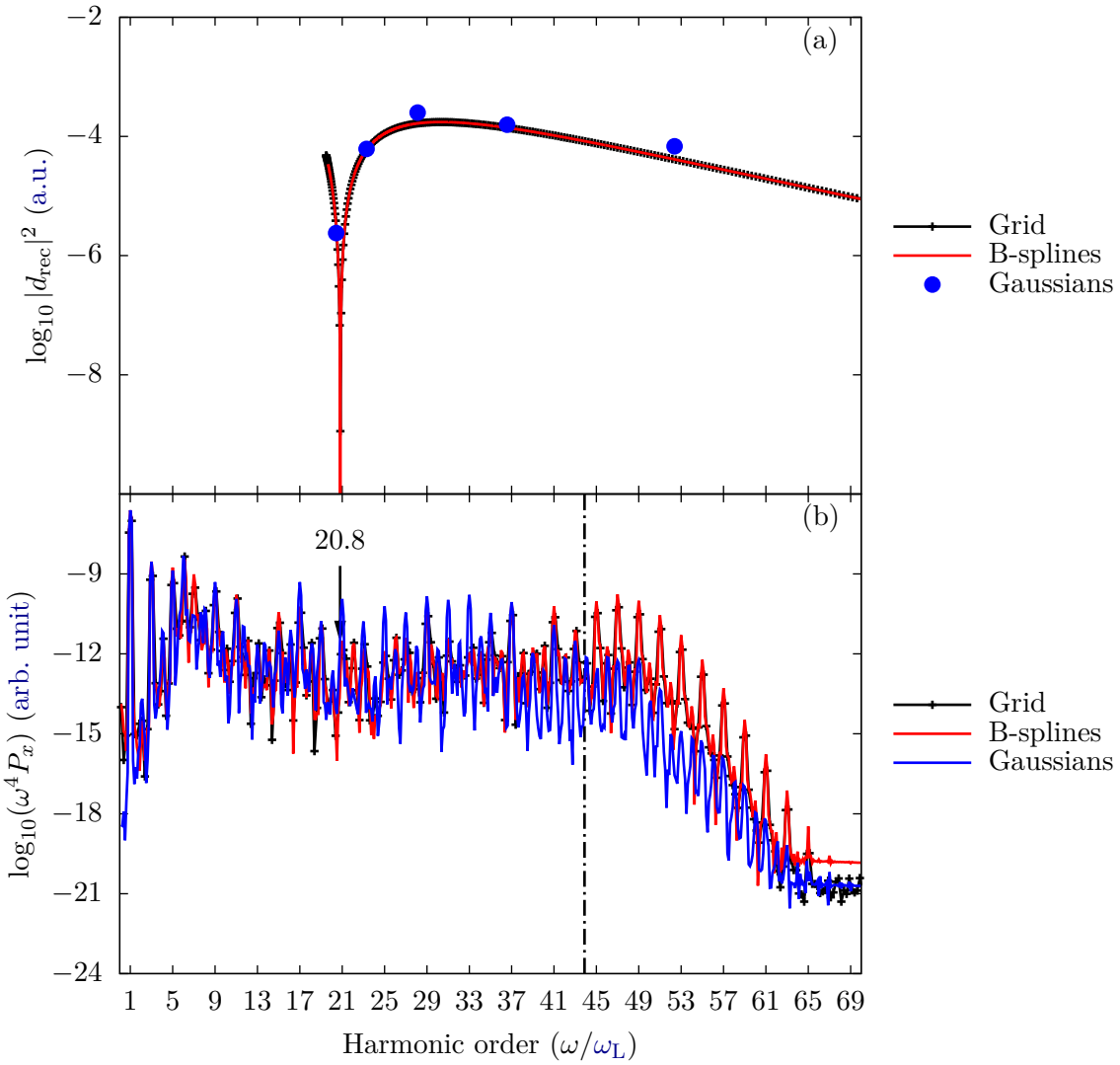

Figure VI.10 *Two center interferences at $R = 2.2$ a.u. : (a) recombination dipole and (b) HHG spectrum at $I_{\rm L} = 2 \times 10^{14}$ W.cm^{-2}. The arrow points to the expected position of the two center interference minimum extracted from the recombination dipole. The dot dashed line is the cutoff energy $E_{cutoff} = 43.9\omega_{\rm L}$.*

state is much too low to observe precisely the position of the zero, and only a frequency window can be given. The molecular SFA model predicts the position of the minimum at $\omega_{\rm min} = \frac{\pi^2}{2R^2\omega_{\rm L}}$ [211] which gives $\omega_{\rm min} = 26.7\omega_{\rm L}$ for $R = 1.8$ a.u., $21.6\omega_{\rm L}$ for $R = 2.0$ a.u. and $17.9\omega_{\rm L}$ for $R = 2.2$ a.u.. We find again that the molecular SFA underestimates the position of the minimum. As analyzed in Chapter IV, this is caused by the two main approximations of this model: the Linear Combination of Atomic Orbitals (LCAO) and the Plane Wave Approximation (PWA).

We report in panel (b) of Figures VI.8, VI.9 and VI.10 the HHG spectra for respectively $R = 1.8$ a.u., 2.0 a.u. and 2.2 a.u. with $I_{\rm L} = 2 \times 10^{14}$ W.cm^{-2}. We observe that all the basis sets reproduce the position of the minimum of the two-center interference. For

$R = 2.0$ a.u., we confirm that the position of the minimum does not depend on the laser intensity. Indeed, we observe it at $\omega_{\min} = 26.4\omega_L$, for all the intensities that we have used in this work, as can be seen on Figures VI.4 and VI.9. As analyzed in Chapter IV, we find that this minimum appears more or less sharply depending on the laser intensity and on the internuclear distance. More details on these features may be found in Chapter IV.

From these studies we deduced that all the basis sets are capable to accurately reproduce the two-center interference.

VI.2.5 Energy distribution

We studied ATI spectra for a Ti:Sapphire laser with a carrier frequency $\omega_L = 0.057$ a.u. (1.55 eV, 800 nm), intensity $I_L = 10^{14}$ W.cm^{-2} and a duration of 10 optical cycles. The results are shown on panel (a) of Figure VI.11.

The energy spectrum of Figure VI.11 has positive energy peaks (bound-continuum transitions) corresponding to the electron density ionized during the propagation, i.e. the photoelectron spectrum, while the peaks in the negative region (bound-bound transitions) represent the electron density that remains in the ground state, and that has been transferred to excited states. We recall that only the positive energy region of an ATI spectrum is experimentally measurable.

As already seen for HHG, Grid and B-splines describe with the same accuracy both bound-bound and bound-continuum transitions. Their ATI spectra coincide and correctly reproduce the expected features of an ATI spectrum: the distance between two consecutive ATI peaks (in the positive energy region) is constant and equal to the energy of a photon, i.e. 0.057 a.u..

On the other hand, Gaussians are only able to reproduce bound-bound transitions. The negative energy part of the spectrum is quite close to the one obtained with the Grid and B-splines, while bound-continuum transitions are out of reach for the Gaussian basis set. This limitation is due to the low density of states in the "continuum". Indeed, with the basis set parameters used here, only six "continuum" states are reproduced in the energy region between 0 and 1 a.u., as we can see in the bottom panel in Figure VI.2. This low density of states is far from enough to reproduce the correct ATI energy distribution and explains why no more than six peaks are observed in the positive energy region of Gaussians spectrum. The energy of the six ATI peaks correspond to the energy of the six "continuum" states presented in Figure VI.2.

To detail this feature, we plot in panel (b) of Figure VI.11 the photoelectron spectrum, computed with Gaussians, after absorption of one photon and for three different photon energies $\omega_L = 1.34$ a.u., 1.47 a.u. and 1.61 a.u.. In all three cases the photon energy is larger that the ionization potential $I_p = 1.11$ a.u.. We should thus see a photoelectron peak at a positive energy $E_p = \omega_L - I_p$. Indeed, this is what we observe when $\omega_L = 1.34$ a.u. and when $\omega_L = 1.61$ a.u.. It is however striking that in the case when $\omega_L = 1.47$ a.u. we do not see any peak. To understand why, we also show on Figure VI.11 the energy position of the ground state -1.11 a.u. and of the first "continuum" energies 0.06 a.u., 0.22 a.u. and 0.50 a.u. which corresponds to symmetry allowed transitions. One clearly sees that if the photon energy matches the energy of a transition from the ground state to one of the "continuum" states then we get a photoelectron peak. However, if the photon energy does not match any transition then no ionization is observed. This

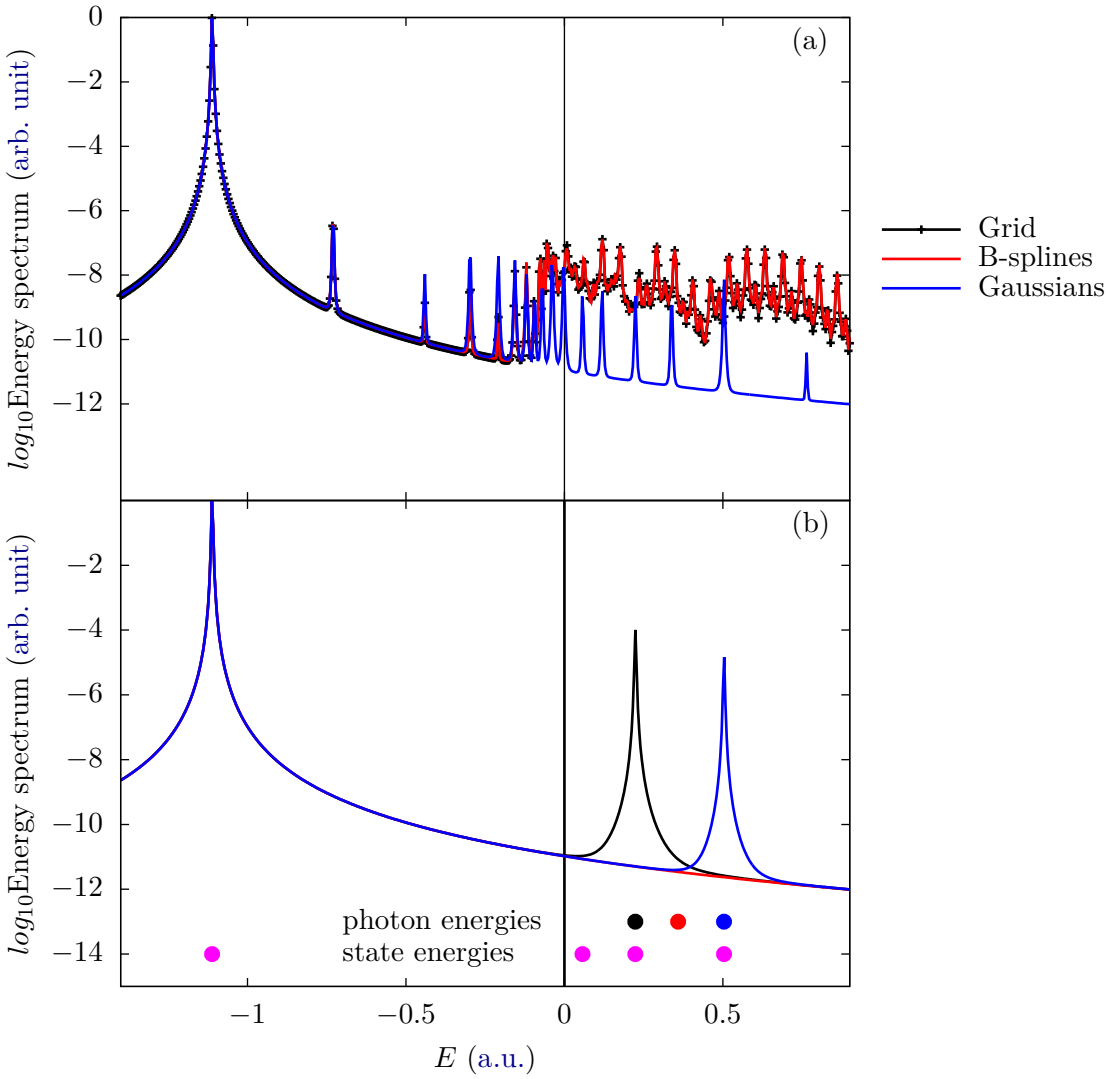

Figure VI.11 *(a) ATI spectrum calculated at the equilibrium interatomic distance* $R = 2.0$ a.u.*. (b) Photoelectron spectrum computed with the Gaussian basis set at the equilibrium distance* $R = 2.0$ a.u. *with* $I_L = 10^{14}$ W.cm^{-2} *and* $\omega_L = 1.34$ a.u. *(black),* $\omega_L = 1.47$ a.u. *(red) and* $\omega_L = 1.61$ a.u. *(blue). The ground state energy (-1.11* a.u.*) and the continuum energy states (0.06* a.u.*, 0.22* a.u. *and 0.50* a.u.*) which corresponds to transitions allowed by symmetry are displayed (magenta dots).*

crucial feature forbids the computation of a correct photoelectron or ATI spectrum with the Gaussians basis set used here. We believe that larger basis sets can in principle describe ATI, however linear dependencies of Gaussians can limit their applicability for such non-linear processes.

VI.3 One dimensional bielectronic models

We now generalize the use of the Grid and Gaussian basis sets to multi-electron species. In this section we consider bielectronic model systems, with one dimension for each electron. The advantage of such systems is that we can perform accurate simulations on bidimensional grid, and thus have a deep comparison of the methods.

We define a one dimensional bielectronic model for H_2 with the field-free Hamiltonian:

$$\hat{H}_0 = -\frac{1}{2}\frac{\partial^2}{\partial x_1^2} - \frac{1}{2}\frac{\partial^2}{\partial x_2^2} + V_0(x_1) + V_0(x_2) + V_{ee}(x_1, x_2), \tag{VI.10}$$

where the nuclei-electron interaction potential V_0 is a one dimensional molecular Soft-Coulomb potential (II.2) with regularization parameter a_{H_2}, and where the interelectronic repulsion V_{ee} is a Soft-Coulomb potential (II.1) with regularization parameter b_{H_2}. The parameters a_{H_2} and b_{H_2} are chosen to reproduce the ground state energy and vertical ionization potential of H_2 at a given internuclear distance. We did the simulations at the equilibrium distance $R = 1.408$ a.u., with $a_{H_2} = 1.991$ a.u. and $b_{H_2} = 5.345$ a.u., which reproduces $E_0 = -1.384$ a.u. and $I_p = 0.604$ a.u..

For comparison purposes we also investigated a one dimensional bielectronic model for the Helium atom. In this case the regularization parameter are $a_{He} = 0.707$ a.u. and $b_{He} = 0.582$ a.u., which reproduces $E_0 = -1.91$ a.u. and $I_p = 0.91$ a.u..

We chose exactly the same laser parameters as for the 1D simulations of H_2^+ (see section VI.1.4).

VI.3.1 Real-space bidimensional grid

As described in section II.2.1, the time-dependent wave function is discretized on a real-space bidimensional square grid of $N \times N$ points (x_i, y_j). It is thus represented by the vector

$$|\psi(t)\rangle \equiv (\psi(x_1, y_1, t), \ldots, \psi(x_i, y_j, t), \ldots, \psi(x_N, y_N, t)). \tag{VI.11}$$

The TDSE is solved by means of the split-operator algorithm (see section II.2.2). The H_2^+ ground state computed by imaginary time propagation (see section II.2.3) is taken as the initial state in the propagation. In addition, to avoid unphysical reflections at the boundaries of the simulation grid, a mask-type absorber function [143] was implemented with a spatial extension of $h_{abs} = 100$ a.u. (see section II.1.1 c)) at each boundary of the 2D box.

VI.3.2 Gaussian-based TDCI

The time-dependent wave function is expanded on the basis of the eigenvectors of the field-free Hamiltonian $\hat{H}_0$:

$$\psi(x_1, x_2, t) = \sum_i c_i(t)\varphi_i(x_1, x_2). \tag{VI.12}$$

These eigenvectors are themselves computed with a Gaussian-based Configuration Interaction (CI) algorithm [270]. They are expressed in the basis of the two electron spin

adapted Slater determinants $\Psi_{k,l}$:

$$\varphi_i(x_1, x_2) = \sum_{k,l} d_{k,l}^{(i)} \Psi_{k,l}(x_1, x_2), \tag{VI.13}$$

where k and l label the two orbitals that enters each Slater determinant. Note that, since the electric field does not affect the spin of the system, we will restrict our active space to Slater determinant with a total spin equal to zero. The orbitals χ_k entering the Slater determinants are computed with a Self Consistent Field (SCF) restricted Hartree-Fock (HF) algorithm. They are expressed on the same Gaussian basis set ($\phi_j(x)$) as we did for the 1D H_2^+ model system (see section VI.1.3)

$$\chi_k(x) = \sum_j \alpha_{k,j} \phi_j(x). \tag{VI.14}$$

For H_2 we use exactly the same Gaussian basis set as we did for H_2^+, while for the Helium atom, we only have one center on which all the Gaussians are localized. We thus have half as many basis functions, and thus less linear dependencies. We could thus use 8K functions (see section VI.1.3) for each angular momentum without having any linear dependencies, which gives a total of 22 basis functions.

We performed simulations both at a Configuration Interaction with Single excitations (CIS) and at a Configuration Interaction with Single and Double excitations (CISD) level of description. The CISD simulations are equivalent to *full*-CI simulations for systems with only two electrons. In this case, the active space thus contains all the Slater determinants formed with all possible pairs of HF orbitals. For Gaussian basis sets containing N_g basis functions, we thus get N_g^2 determinants in the active space. For the CIS simulations, the active space is restricted to *singly* excited Slater determinants, i.e. determinants composed of one occupied orbital ϕ_α and of one virtual orbital ϕ_v. Note that there is only one occupied orbital ϕ_0 for 2-electron systems described with a restricted HF. We thus get only N_g determinants in the active space.

The TDSE is solved with the split-operator method, exactly like for the 1D H_2^+ model system (see section VI.1.3).

VI.4 Bielectronic results and discussion

VI.4.1 Spectrum of the field-free Hamiltonian

As we did for H_2^+, to better understand the time-dependent results, we start by analyzing the spectrum of the field free Hamiltonian. We first compare the ground state of our one dimensional bielectronic H_2 that was computed either with the 2D grid or by the Gaussian-based CIS and CISD. We plot a cut of the ground state at $x_2 = 0$ on Figure VI.12. As for H_2^+ we observe that the Gaussians are perfectly able to reproduce the ground state. Both the CIS and CISD results match perfectly the grid results. We show on Figure VI.13 two "continuum" states, computed with the same three methods: one just above the first ionization threshold of H_2 (left panels), and one just above the second ionization threshold (right panels). Note that it is more difficult to directly compare "continuum" states computed with different methods in the case of a bielectronic system. Indeed, our

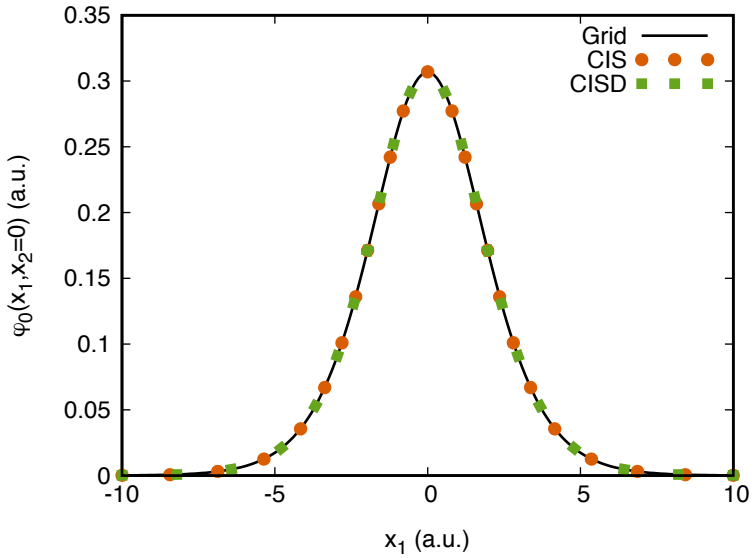

Figure VI.12 *Cut at $x_2 = 0$ of the ground state of H_2 calculated with the 2D grid, and with the Gaussian-based CIS and CISD.*

H_2 system displays several ionization thresholds for each excited state of the H_2^+ molecular ion, and a double ionization threshold above which both electron may be ionized. The positive energy levels may thus be several times, or even infinitely, degenerated. This is why we limit ourselves to the comparison of "continuum" states close to the first ionization thresholds, i.e. corresponding to the ground state or first excited state of the H_2^+ molecular ion.

We observe on Figure VI.13 the same trend than for the "continuum" states H_2^+ (see section VI.2.1): the 2D grid allows to reproduce the oscillatory behavior of the "continuum" states. On the contrary, the Gaussian-based methods are only able to get the first few of these oscillations. For the "continuum" state just above the first ionization threshold (left panels), it is striking that the CIS method (panel (e)) already gives a good approximation of the wave function near the nuclei. The CISD slightly improves the quality of the state. This is actually expected since this "continuum" state corresponds to the ground state of the ion. It should thus be predominantly represented by singly excited Slater determinants, where one electron is in the ground state orbital, and another is in a virtual orbital. The other "continuum" state, shown on the right panels of Figure VI.13, corresponds to the first excited state of H_2^+. It is thus impossible to compute such a state with the CIS method.

We display on Figure VI.14 the energy and density of states for the first few eigenstates of the field-free Hamiltonian $\hat{H}_0$. We could only compute it with the CIS and CISD methods. Indeed and as already mentioned in section II.2.1, for bidimensional grids the size of the Hamiltonian gets quite large, so that the computational cost to diagonalize it with the QL algorithm is prohibitive. As expected from the size of the active space, we get a lot more states with the CISD than with the CIS. The density of states decreases as $1/E$ with the CIS. On the contrary it is almost constant, and always much higher, with the CISD.

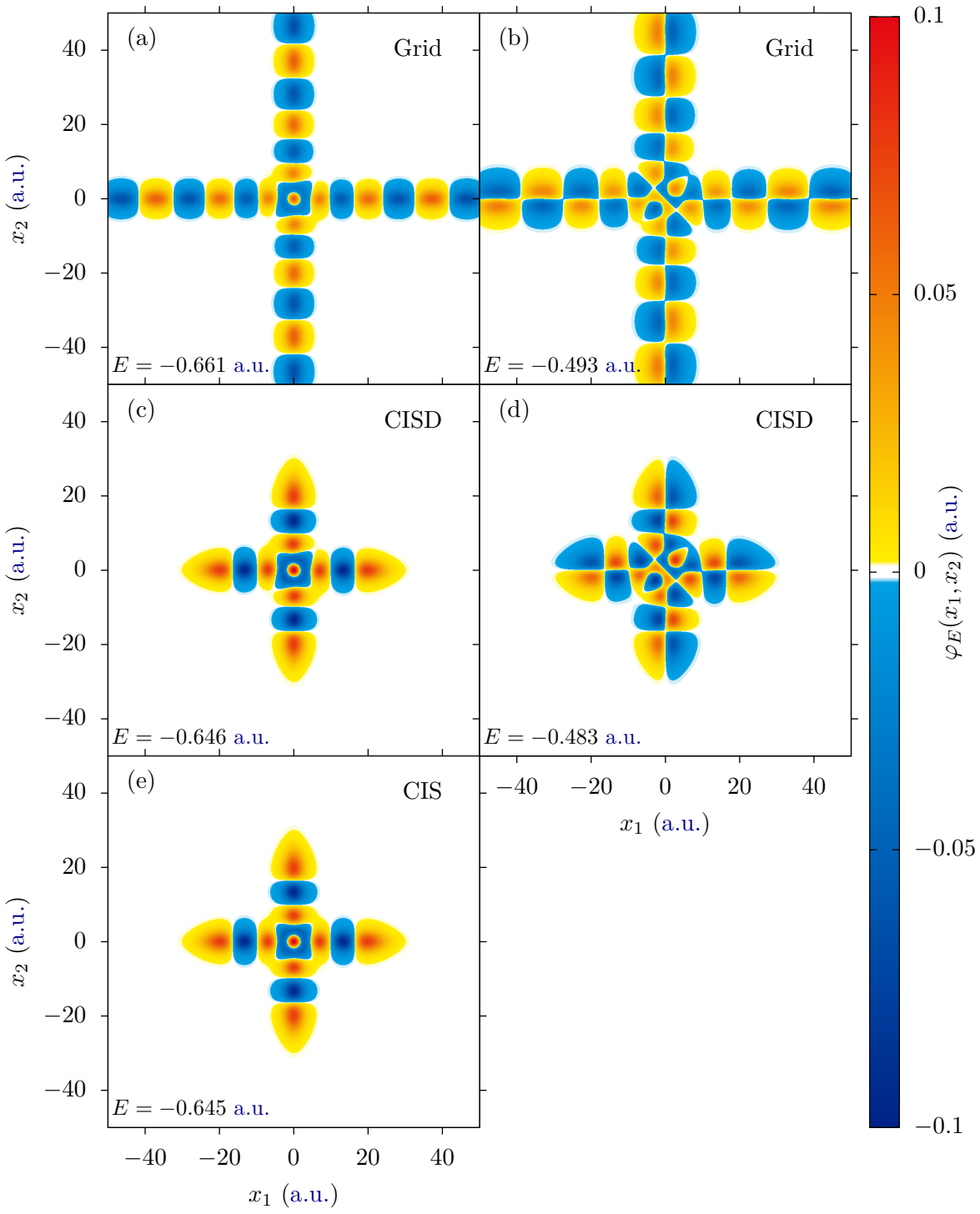

Figure VI.13 *Singly ionized continuum state $\varphi_E(x_1, x_2)$ normalized with th L_2 norm, computed (a)-(b) by inverse iteration on the 2D grid or with the Gaussian-based (c)-(d) CISD or (e) CIS methods. Left panels: 1st ionization threshold, right panels: 2nd ionization threshold.*

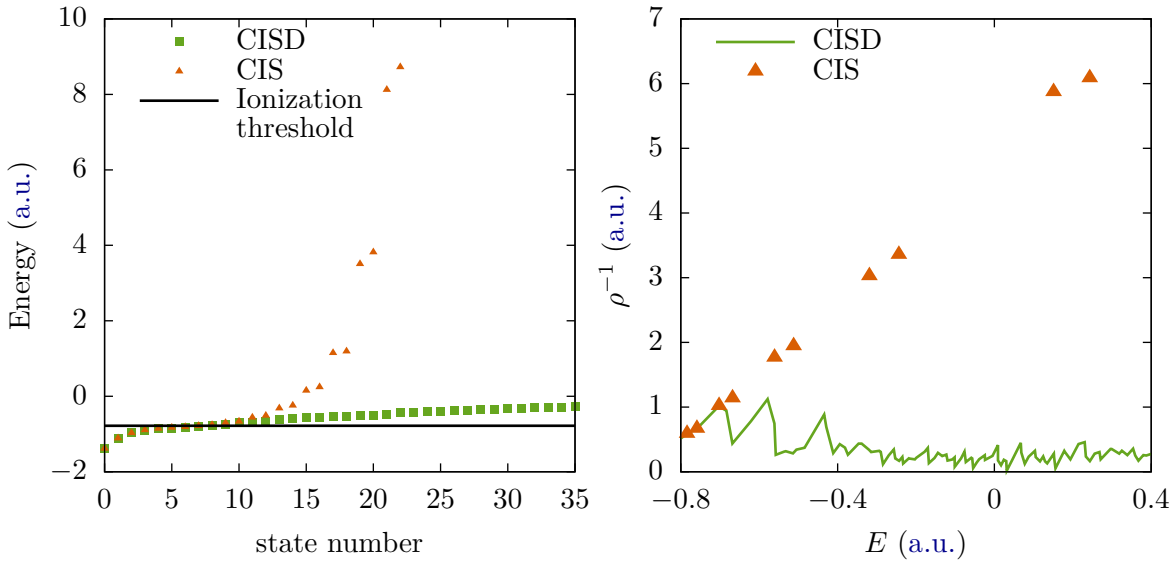

Figure VI.14 *(a) Eigenvalues up to the* 35^{th} *eigenstate. (b) Inverse of the density of continuum states normalized with the same arbitrary constants as the Gaussian results in Figure VI.2.*

Since we get more states when we use the CISD algorithm, we might think that it enhances the representation of the continuum, and thus systematically improves the dynamics. However we point out the fact that, since we have more than one electron, we actually have *several* continua, one for each state of the ion. When going from the CIS to the CISD description, we add *doubly* excited Slater determinants, thus states where *both* electrons are excited with respect to the HF determinant. But these states are not necessarily important to describe the system dynamics. For example, in the case of HHG, the ionization channels that will predominantly contribute to the optical response are the channels where only one electron is ionized from one of the highest occupied orbitals of the HF Slater determinant. These ionization channels are already included in the CIS level of theory, so that we do not expect the CISD to substantially improve the results. Of course, if one wants to describe situations where both electrons are excited during the propagation, e.g. double ionization, then it is mandatory to use at least the CISD method.

Note that an advantage of the CI methods is that it provides a natural, intuitive, basis to disentangle the contributions of the different ionization channels that we just mention, when analyzing the wave function. This partitioning is more delicate with the grid representation of the wave function. Of course, the grid method contains all these contributions, and gives a priori more accurate results. Hence, these two methods may be seen as complementary, the grid brings precise numerical results, while CI allows to develop physical insights and interpretations.

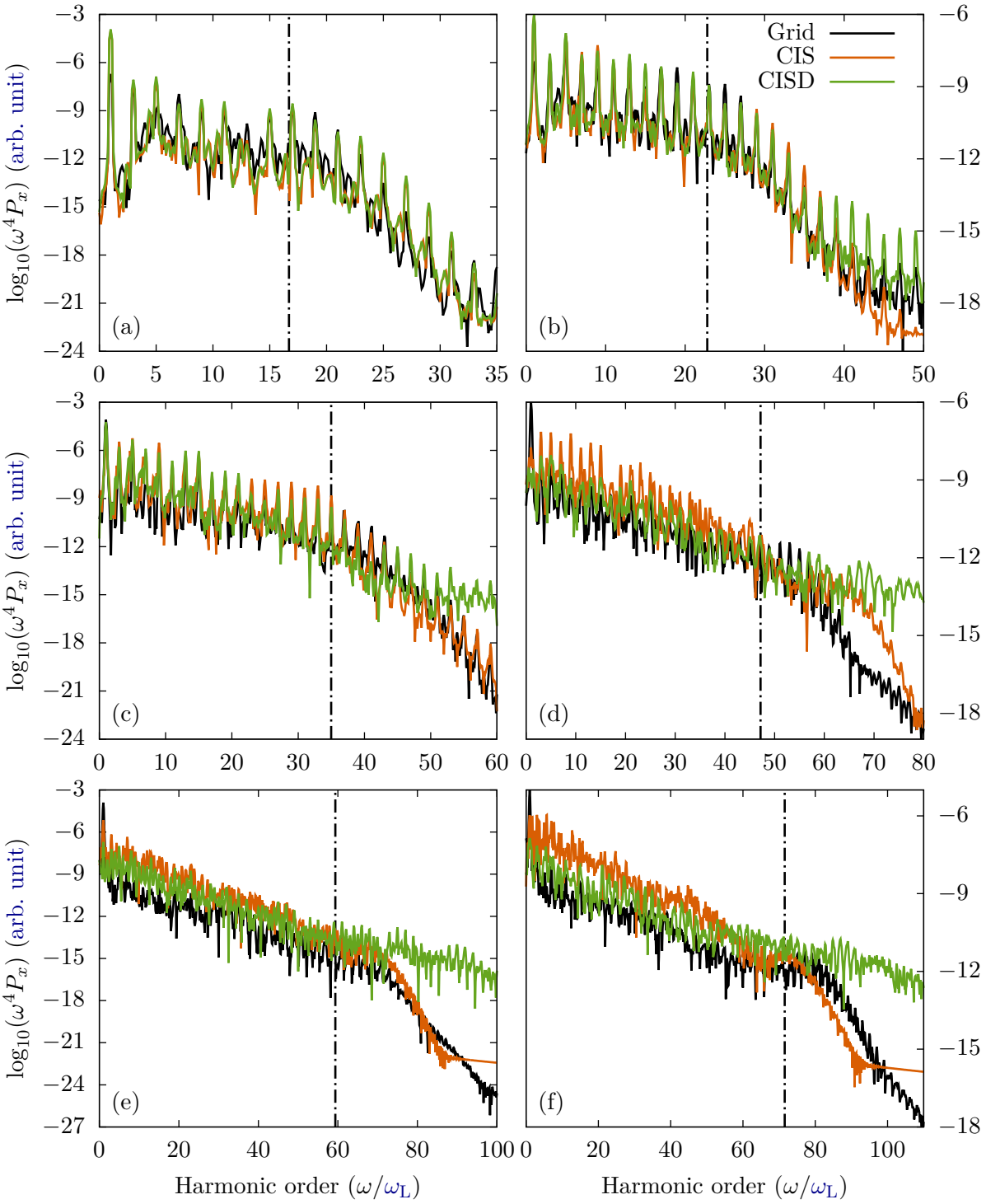

Figure VI.15 *HHG spectra of our H_2 model system in the acceleration form with laser intensities: (a) $I_L = 5 \times 10^{13}$ W.cm^{-2}, (b) $I_L = 10^{14}$ W.cm^{-2}, (c) $I_L = 2 \times 10^{14}$ W.cm^{-2}, (d) $I_L = 3 \times 10^{14}$ W.cm^{-2}, (e) $I_L = 4 \times 10^{14}$ W.cm^{-2} and (f) $I_L = 5 \times 10^{14}$ W.cm^{-2}. The dot-dashed line reproduce the cutoff energy: (a) $E_{cutoff} = 16.7\omega_L$, (b) $E_{cutoff} = 22.8\omega_L$, (c) $E_{cutoff} = 35.0\omega_L$, (d) $E_{cutoff} = 47.2\omega_L$, (e) $E_{cutoff} = 59.4\omega_L$ and (f) $E_{cutoff} = 71.6\omega_L$.*

VI.4.2 HHG

We studied the HHG spectrum of our H_2 model system upon irradiation by a Ti:Sa laser with carrier frequency $\omega_L = 0.057$ a.u. (1.55 eV, 800 nm) and intensities $I_L = 5\times10^{13}$ W.cm^{-2}, 10^{14} W.cm^{-2}, 2×10^{14} W.cm^{-2}, 3×10^{14} W.cm^{-2}, 4×10^{14} W.cm^{-2} and 5×10^{14} W.cm^{-2}. As for H_2^+ the pulse has a trapezoidal envelope of 10 optical cycles in total, with linear ramps of 1 optical cycle.

Once again, all the methods reproduce well the expected features of a HHG spectrum, regardless of the applied field intensity: the intensity of the low-order harmonics decreases rapidly, then a plateau region follows where the intensity remains nearly constant, and at high frequencies the harmonic intensity decreases again. Here again, the system has inversion symmetry so that only the odd harmonics are emitted. We also observe the same general trend: the Gaussian-based numerical methods reproduce well the emitted HHG spectrum for low intensities, here for $I_L \lesssim 3\times10^{14}$ W.cm^{-2}. The accuracy of the computed spectra then quickly deteriorates for higher field intensities. These observations are almost identical whether we look at the CIS or CISD results, which is in agreement with our previous remarks (see section VI.4.1).

We also computed the HHG spectrum for a one dimensional bielectronic He model atom, and for the same laser parameters. The results are shown on Figure VI.16. The observations are similar to the ones we just gave for H_2, but the agreement between the two basis sets is poorer. This indicates that the use of several centers for the Gaussians improves the quality of the basis, and its ability to correctly represent continuum states. This is in agreement with previous results of Coccia and Luppi who proposed in [261] to use "multicentered" Gaussian basis sets to improve the quality of the Gaussian basis set. This involves defining "ghost" atoms, on which to put more Gaussians and thus increase the size of the basis set without adding too much linear dependencies. Accordingly, the quality of the Gaussian basis set should actually improve for bigger molecules. This is thus promising for the generalization of the method to larger systems.

VI.5 Conclusion

We explicitly solved the 1D TDSE for H_2^+ in presence of an intense electric field and we systematically explored the numerical performance of real-space Grid, B-splines and Gaussian basis sets optimized for the continuum. We analyzed the performance of the three basis sets for HHG and ATI in the case of H_2^+. In particular, for HHG, the capability of the basis set to reproduce the "two-center interferences" was investigated. We obtained that Grid and B-splines representations of the time-dependent wave function give equivalent results for both HHG and ATI. On the contrary, the behaviour of Gaussians is more complicated and it depends on the intensity of the laser. In fact, it is possible to optimize Gaussians to describe continuum and therefore multiphoton process such as HHG. However, this optimization is limited by the linear dependencies issue. In practice, for HHG we found that Gaussians can perform well up to $I_L = 5\times10^{14}$ W.cm^{-2}. For higher intensity only low energy harmonics are still correct, and only if one uses the acceleration form of the dipole to compute the spectrum. Despite their limitations, Gaussians basis sets can reproduce intricate features of the HHG spectrum, such as hyper-Raman like resonances and two-center interferences. However, in the case of ATI, Gaussians basis

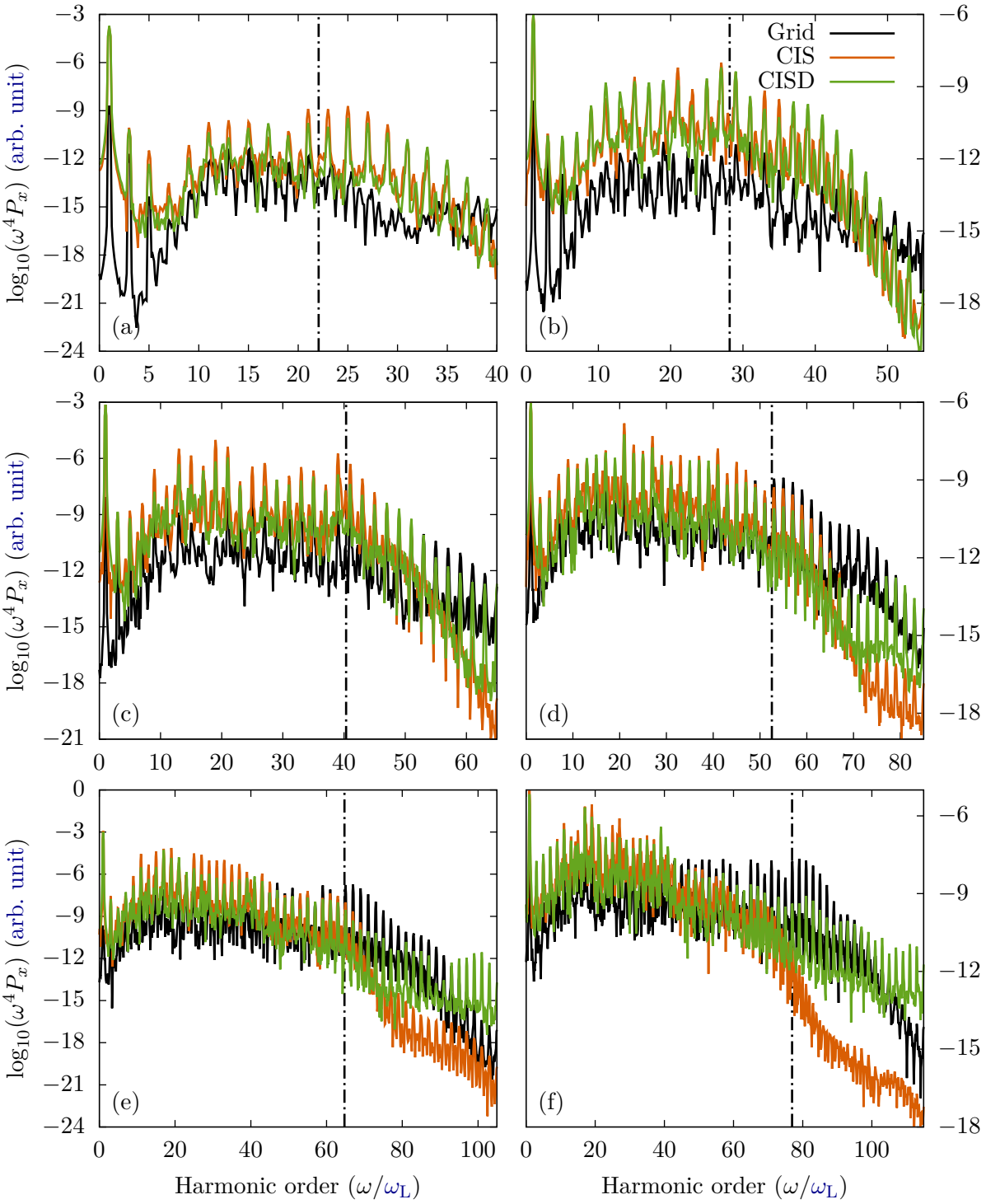

Figure VI.16 *HHG spectra of our Helium model system in the acceleration form with laser intensities: (a)* $I_L = 5 \times 10^{13}$ W.cm^{-2}, *(b)* $I_L = 10^{14}$ W.cm^{-2}, *(c)* $I_L = 2 \times 10^{14}$ W.cm^{-2}, *(d)* $I_L = 3 \times 10^{14}$ W.cm^{-2}, *(e)* $I_L = 4 \times 10^{14}$ W.cm^{-2} *and (f)* $I_L = 5 \times 10^{14}$ W.cm^{-2}. *The dot-dashed line reproduce the cutoff energy: (a)* $E_{cutoff} = 22.1\omega_L$, *(b)* $E_{cutoff} = 28.2\omega_L$, *(c)* $E_{cutoff} = 40.4\omega_L$, *(d)* $E_{cutoff} = 52.5\omega_L$, *(e)* $E_{cutoff} = 64.7\omega_L$ *and (f)* $E_{cutoff} = 76.9\omega_L$.

sets cannot possibly describe a correct spectrum.

We then assessed the accuracy of the TDCI method to reproduce the HHG spectra of bielectronic model systems for H_2 and for the Helium atom. We found that already for such small systems bidimensional grid are numerically demanding, while the TDCI method remains very cheap, even at the CISD level of description. Moreover, we saw that the Gaussian-based TDCI is actually able to reproduce correctly the HHG spectrum of both bielectronic systems as long as the intensity is not too high, i.e. up to $I_L \sim 5\times 10^{13}$ W.cm^{-2} for our 1D Helium atom and up to $I_L \sim 2 \times 10^{14}$ W.cm^{-2} for our 1D H_2 molecule. For higher intensities only the low energy harmonics are reproduced. The Gaussian-based TDCI performed much better on the H_2 molecule than it did for the Helium atom. We strongly believe that it is related to the number of centers on which we place the Gaussians of the basis. Indeed, multicentered Gaussian basis sets are numerically more efficient because they generate less linear dependencies. This feature gives promising perspectives for the description of larger molecules. Finally, we showed that the double excitations contribute almost nothing to the HHG emission, so that the CIS level of description is sufficient. For systems with more than two electrons, this can save a lot of computational resources, and would thus allow to generalize the method to larger species very easily.

Conclusion

During my PhD I studied different aspects of the interaction of atoms and molecules with strong laser fields. I developed analytical models to understand the mechanisms at the basis of the correlated and highly non-linear processes that are observed in strong field physics. The strength of these approximate models lies in their ability to reach interpretations and insight on physical phenomena. To support my interpretations, I combined this approach with the results of accurate numerical simulations performed on toy model systems. These simple models actually present many advantages. On the one hand they allow to tune all their fundamental parameters, and thus to concentrate on one of several particular physical issues. Moreover their low dimensionality enables to perform extensive numerical treatments. In particular I solved both the Time-Dependent Schrödinger Equation (TDSE) and the Time-Independent Schrödinger Equation (TISE) to extract as many information as possible from the resulting time-dependent wave function. I also exploited these numerical simulations to meticulously test the underlying approximations of the developed analytical models.

More precisely, I investigated the electronic and nuclear dynamics of atoms and diatomic molecules in intense femtosecond laser pulses. I first concentrated on the highly non-linear electronic processes that are triggered by such laser pulses, like ATI, HHG or non sequential multiple ionization. In Chapter III, I studied the common first step of all these processes, the archetype of the quantum effect with no classical equivalent whatsoever, namely tunnel ionization. In an infrared laser field, the time variations of the electric field are very slow with respect to the natural electronic time scales, so that the ionization yield can be directly deduced from the time-independent problem in a static electric field. I studied this ionization yield for several atomic and molecular model systems. I showed the importance of the DC Stark shift, both for quantitative and qualitative descriptions of tunnel ionization, and I derived an analytical expression in the semi-classical approximation that takes this effect into account. I showed that the Stark shift is the dominant contribution to the anisotropy of the tunnel emission in asymmetric molecules. I demonstrated how crucial the accurate calculation of this Stark shift can be, especially for highly polarizable molecules for which second order perturbation theory breaks down. What is more, I analyzed the reasons that causes discrepancies between the asymptotic analytical formula and the numerically exact simulations. I could disentangle the error induced by the different approximations used in the asymptotic derivation, and I found that some of these approximations are actually severally unjustified at working laser intensities, but that, thanks to a fortunate error compensation, the final results were still reasonable.

One of the direct applications of strong field physics is High order Harmonic generation Spectroscopy (HHS), where the light emitted by HHG is analyzed to extract structural

and dynamical information on the emitter. In the particular case of two center interferences in diatomic molecules, I questioned in Chapter IV the circumstances where this information may be either blurred or, on the contrary, contrasted and thus more easily accessible experimentally. I completed the analytical work performed in the aligned case in [129]. I gave it a more rigorous ground by properly defining a parameter, i.e. the internuclear distance R, for the expansion of the molecular SFA. I also obtained the complete expansion of the expression of the HHG spectrum, and extended it to the general case of any molecular and field orientations. I assessed the conclusions of this analytical model by solving the TDSE for several model systems. By comparing the results obtained in one and two dimensions, I concluded that the transverse spreading of the electron wave packet during its propagation after tunnel ionization did have some impact on the two center interferences. Finally I performed a detailed analysis of the two major approximations of the molecular SFA: the Linear Combination of Atomic Orbitals (LCAO) and the Plane Wave Approximation (PWA). I demonstrated that both approximations induce a relatively large error, but that they conveniently compensate each other. The simple, commonly used, formula (IV.41) thus allows to predict the position of the interference minimum with a reasonable accuracy. However this error compensation implies that this agreement of the molecular SFA with exact results is not robust at all. Instead it will be highly sensitive to the system and laser parameters. This drastically restricts the predictive abilities of the model and limits the possibility to improve it by correcting for either one of these approximations separately. It is important to realize that the conclusions obtained here greatly benefited from the numerical separation of the contributions of the short and long trajectories to the final HHG spectrum. The method that we used involved an absorber that had a finite width and imperfect absorbing performances. We would get more reliable results and thus improve our understanding of two center interferences by implementing a better separation method. It would be interesting to consider the infinite-range exterior complex scaling absorber proposed by Scrinzi [142]. Moreover, we could not explain the interesting features that appeared in 2D with respect to the 1D case. The computation of 2D continuum states, as is done by Basile Wurmser who is currently doing his PhD in the group, could thus be of great help in this respect.

These electronic dynamics were investigated and simulated in the frozen nuclei approximation. However for very light molecules such as H_2, the nuclei may have enough time to move during short laser pulses of a few fs, so that the dynamics may be affected by vibronic couplings between the electronic and nuclear degrees of freedom. In Chapter V, I investigated these couplings, and their effects on the nuclear dynamics of model systems for homonuclear diatomic molecules. I questioned the ability of a Born-Oppenheimer (BO) theoretical method to model these couplings through the inclusion of an R-dependent ionization rate and of an R-dependent Stark shift [222, 223, 227]. I showed the inconsistency of previous approaches where the R-dependent ionization rate, leading to the Lochfraß mechanism, and the R-dependent Stark shift, leading to the Bond-Softening mechanism, were included separately. Indeed I demonstrated that since both mechanisms may actually interfere, they have to be included simultaneously in the model. Or, to put it briefly, the effect of both Lochfraß and Bond-Softening put together is not equal to the sum of their individual effects. With this in mind, I also put into question the claim that the phase of the nuclear wave packet oscillations after interaction could be related to the slope of the R-dependent ionization rate near the equilibrium

distance at early times. Finally, I found circumstances where the nuclear dynamics could not be reproduced by this BO model. In these cases the nuclear dynamics is strongly affected by vibronic correlations that cannot be included in a BO representation of the wave function. I showed that the signature of these correlations causes a strong dependence of the nuclear wave packet oscillations on the Carrier Envelope Phase (CEP) of the incident laser pulses, giving a possibility to access these correlations experimentally. Besides, I proposed an analytical model based on the Wigner-Weisskopf approach to give a more rigorous theoretical framework for the Bond-Softening mechanism. Using this model I could find a correction to the BO model that might take into account some of the vibronic correlation effects. It might be interesting to investigate the influence of this correction on the dynamics, and to see if it indeed allows to reproduce the CEP effects that we just mention. The extension of this model to the Lochfraß mechanism still needs to be done.

Finally, in Chapter VI, I investigated various numerical methods to solve the TDSE of larger and more complex systems for which electronic correlations influence the strong field dynamics. In collaboration with the Laboratoire de Chimie Théorique at Sorbonne Université, we investigated three different basis sets to represent the time-dependent wave function. We showed that grid and B-splines are equally able to accurately reproduce the electronic dynamics of H_2^+. However, their high computational cost makes it difficult to generalize them to larger systems. We found that Gaussians were actually able, as long as the laser intensity is not too high, to reproduce the HHG spectrum of H_2^+, including fine structures caused by so-called hyper-Raman resonances or two-center interferences. This was somewhat unexpected since the spectrum of the Gaussian-based Hamiltonian only contained a few (less than 15) "continuum" states in the relevant energy region, which prevents them to correctly reproduce e.g. ATI spectra. Taking advantage of the affordable numerical cost of the Gaussians, we developed a Gaussian-based Time-Dependent Configuration Interaction (TDCI) method to solve the TDSE for multielectronic systems. I tested the agreement of this method with accurate results that I obtained by solving the TDSE on a bidimensional grid for 1D bielectronic model systems. As for the monoelectronic case, I found that the Gaussian-based TDCI method performed well for relatively low intensities, but that the agreement with the grid results quickly deteriorates for stronger laser fields. The multicentered characteristic of the Gaussian basis sets seemed to have a particular importance for the correct representation of continuum states, suggesting that the method might actually show better performance for larger molecules. Importantly the CIS level of description appeared sufficient for a correct computation of HHG spectra, which is promising for a generalization to larger systems with more than two electrons. An interesting improvement would be to extend the TDCI method to other basis sets such as real space grid or B-splines functions. This might imply a larger computation cost, and would require to develop parallel computational strategies. Another possibility would be to consider mixed basis sets that would combine the performances of the gaussians for the bound states and of the grid or B-splines for the continuum part.

The full understanding of the dynamics of atoms and molecules triggered by strong laser fields still has a long way to go. I hope I showed that simple toy models, combined with approximate analytical reasoning could be of invaluable help in this respect. We can never know where the next revolutionary ideas will emerge from, but I am convinced that these simple intuitive systems do help to stir our physicists' imagination.

Appendix A
Saddle Point Approximation in SFA

This appendix has been written with the invaluable help of Antoine Fermé, who is currently doing his PhD at the Laboratoire de Mathématiques d'Orsay at Université Paris-Sud.

The steepest-descents, saddle-point, and stationary-phase methods are closely related techniques of asymptotic computation of integrals based on Laplace's method. They are ubiquitous in mathematics and physics, because they are used to compute approximations of Fourier and Laplace transforms, and to solve asymptotically many partial differential equations, thus allowing the evaluation of e.g. the semiclassical limit of quantum theories (be it via the Wentzel–Kramers–Brillouin method, or Feynman path integrals), the ray limit of wave optics (e.g. to describe caustics [277]), or the boundary layer limit of hydrodynamics. An archetypal application is the approximation of Airy functions at infinity.

A.1 Method of stationary phase

Possible references (arbitrarily chosen among the likely hundreds) for the material in this section are chapter 6 of [123] for the one dimensional case, appendix D of [278] for a short exposition of the multidimensional case, and section 7.7 of [279] for the full mathematical proofs.

The method of stationary phase allows to compute asymptotic expansions of integrals with a parameter u:

$$I(u) = \int_{\mathcal{K}} \mathrm{d}x\, f(x)\, \mathrm{e}^{\mathrm{i}u\phi(x)}, \tag{A.1}$$

when $u \to +\infty$, and where the prefactor f, and the (reduced) phase ϕ are smooth functions, with ϕ real, and $\mathcal{K} \subset \mathbb{R}^n$ is a bounded domain of integration. Note that f, ϕ, and $\mathcal{K}$ do not depend on the parameter u, so that $I(u)$ is bounded independently of u:

$$|I(u)| \leq \int_{\mathcal{K}} \mathrm{d}x\, |f(x)| < \infty. \tag{A.2}$$

The idea behind the method of stationary phase is that, for large values of u, the prefactor $f(x)$ can be considered constant compared to the rapidly oscillating exponential term $\mathrm{e}^{\mathrm{i}u\phi(x)}$. Consequently the integrand is approximately a sinusoid whose positive and

negative contributions almost cancel each other. The main contributions to the integral thus come from the points where this cancellation does not work, i.e. points where $u\phi(x)$ varies too slowly. This will be the case near points x_0 in $\mathcal{K}$ where the phase ϕ is *stationary*:

$$\boldsymbol{\nabla}\phi(x_0) = \phi'(x_0) = 0. \tag{A.3}$$

To get the correct asymptotic behavior of $I(u)$ we will thus have to distinguish between two possible cases: whether the phase has any such stationary points, or not.

a) Non-stationary phase theorem

Turning this intuition into something precise, we have, if the phase ϕ has no stationary point on the integration region, the *non-stationary phase theorem*:

$$\boxed{I(u) = O(1/u^N), \text{ for all } N \in \mathbb{N}.} \tag{A.4}$$

To prove this we will proceed in two steps.

We first assume that a partial derivative of the phase never vanish:

$$\partial_{x_i}\phi(x) \neq 0 \text{ for all } x \text{ in } \mathcal{K}. \tag{A.5}$$

Then, writing

$$\mathrm{e}^{\mathrm{i}u\phi(x)} = \frac{1}{\mathrm{i}u\partial_{x_i}\phi(x)}\partial_{x_i}(\mathrm{e}^{\mathrm{i}u\phi(x)}), \tag{A.6}$$

we can make an integration by parts and obtain

$$I(u) = \underbrace{\int_{\partial\mathcal{K}} \frac{\partial}{\partial x_i}\cdot\nu(x)\widehat{\mathrm{d}x_i}\,\frac{f(x)}{\mathrm{i}u\partial_{x_i}\phi(x)}\,\mathrm{e}^{\mathrm{i}u\phi(x)}}_{\text{boundary term}} - \int_{\mathcal{K}}\mathrm{d}x\,\partial_{x_i}\left(\frac{f}{\mathrm{i}u\partial_{x_i}\phi}\right)(x)\,\mathrm{e}^{\mathrm{i}u\phi(x)}, \tag{A.7}$$

where $\partial\mathcal{K}$ is the boundary of the integration domain, $\widehat{\mathrm{d}x_i}$ indicates integration on all coordinates except x_i, and $\frac{\partial}{\partial x_i}\cdot\nu$ is the scalar product of the i-th basis vector $\frac{\partial}{\partial x_i}$ with the unit normal vector of $\partial\mathcal{K}$ pointing outwards. As f vanish on $\partial\mathcal{K}$ the boundary term is zero, and we are left with

$$I(u) = -\frac{1}{u}\int_{\mathcal{K}}\mathrm{d}x\,\partial_{x_i}\left(\frac{f}{\mathrm{i}\partial_{x_i}\phi}\right)(x)\,\mathrm{e}^{\mathrm{i}u\phi(x)} = \frac{1}{u}\tilde{I}(u), \tag{A.8}$$

where the new integral $\tilde{I}(u)$ is of the kind (A.1). In particular $\tilde{I}(u)$ is bounded, i.e. at most of order $O(1)$, so that

$$I(u) = O(1/u). \tag{A.9}$$

Moreover, the phase of the integrand in $\tilde{I}(u)$ is still ϕ and thus has no stationary points. Consequently, by the previous argument, it is also of order $O(1/u)$. Putting this back in (A.8), we conclude that $I(u)$ is $O(1/u^2)$. By simple iteration, we get (A.4).

Now we turn to the general case, i.e. we do not assume (A.5). In this case, we can still decompose $\mathcal{K}$ in regions $\mathcal{U}_j$ where for each $\mathcal{U}_j$ there is an i_j such that

$$\partial_{x_{i_j}}\phi(x) \neq 0 \text{ for all } x \text{ in } \mathcal{U}_j. \tag{A.10}$$

Because $\mathcal{K}$ is bounded, we can take only a **finite** number of such regions $\mathcal{U}_j$. Applying the integration by parts argument to the integral over $\mathcal{U}_j$ and summing over j, all the boundary integrals will cancel with each other except on the boundary of $\mathcal{K}$. In the end we are back to (A.7) and thus (A.8). This completes the proof of the *non-stationary phase theorem*.

b) Stationary phase theorem

Now, if ϕ has a unique stationary point x_0 in K, assumed to be non degenerate i.e. such that $\det \mathcal{H}_\phi(x_0) \neq 0$ where $\mathcal{H}_\phi(x_0) = \phi''(x_0)$ is the Hessian matrix of ϕ at x_0, the first term of the asymptotic expansion reads

$$I(u) = \Big(\frac{2\pi}{u}\Big)^{n/2} e^{\mathrm{i}\phi(x_0)} \frac{f(x_0)}{\sqrt{\det(-\mathrm{i}\phi''(x_0))}} + O(1/u^{n/2+1}) \tag{A.11}$$

with the square root branch given explicitly by

$$\sqrt{\det(-\mathrm{i}\phi''(x_0))} = \sqrt{|\phi''(x_0)|} e^{-\mathrm{i}\frac{\pi}{4}\mathbf{sign}(\phi''(x_0))} \tag{A.12}$$

where $\mathbf{sign}(\phi''(x_0))$ is the sum of the signs of the eigenvalues of $\phi''(x_0)$.

This formula is obtained separating the integration domain into two regions, a small ball around the stationary point and its complement:

$$\int_{\mathcal{K}} \mathrm{d}x\, f(x)\, \mathrm{e}^{\mathrm{i}u\phi(x)} = \int_{B(x_0,\epsilon)} \mathrm{d}x\, f(x)\, \mathrm{e}^{\mathrm{i}u\phi(x)} + \underbrace{\int_{\mathcal{K}\setminus B(x_0,\epsilon)} \mathrm{d}x\, f(x)\, \mathrm{e}^{\mathrm{i}u\phi(x)}}_{=O(1/u^\infty)}. \tag{A.13}$$

Since there are no stationary points on the complement, the second term is $O(1/u^\infty)$, by (A.4).

We can now Taylor expand f at zeroth order and ϕ at second order around x_0:

$$f(x)\, \mathrm{e}^{\mathrm{i}u\phi(x)} = \big(f(x_0) + O(|x-x_0|)\big)\, \mathrm{e}^{\mathrm{i}u\left[\phi(x_0)+\frac{1}{2}(x-x_0)^T\phi''(x_0)(x-x_0)+O\left(|x-x_0|^3\right)\right]}. \tag{A.14}$$

and the integral on the small ball is almost equal to the integral of the Taylor expansion. Indeed the rest can be shown to be $O(1/u)$, so that we get

$$I(u) = \int_{B(x_0,\epsilon)} \mathrm{d}x\, f(x_0)\, \mathrm{e}^{\mathrm{i}u(\phi(x_0)+\frac{1}{2}(x-x_0)^T\phi''(x_0)(x-x_0))}(1+O(1/u)). \tag{A.15}$$

The phase of this new integrand has no stationary point outside of $B(x_0,\epsilon)$, so that we can extend the domain of integration on all $\mathbb{R}^n$ adding only a $O(1/u^\infty)$ error (again by (A.4)). Finally, remembering the formula for the Fourier transform of a multidimensional Gaussian function, we get the formula (A.11)[1].

Now in the case of multiple stationary points in $\mathcal{K}$, we decompose the integration region into small balls around each stationary point, plus the remaining region where there is no stationary points. The latter region contributes $O(1/u^\infty)$, whereas the contributions of each ball add together, so that we simply have to sum the formula (A.11) for all stationary points.

[1] If the stationary point is degenerate, we Taylor expand ϕ till the first nonzero order p, and get a first asymptotic term of order $O(1/u^{n/p})$.

A.2 Application to the approximate computation of the dipole

We have to approximate

$$\widetilde{\mathbf{D}}_{\pm}(\omega) = \int \mathrm{d}t \int_0^t \mathrm{d}t' \int \mathrm{d}\mathbf{p}\, \mathbf{d}_{\mathrm{rec}}(\mathbf{p} + \mathbf{A}_{\mathrm{L}}(t)) d_{\mathrm{ion}}(\mathbf{p} + \mathbf{A}_{\mathrm{L}}(t'), t')\, \mathrm{e}^{-\mathrm{i}[S(\mathbf{p},t,t') \pm \omega t]} \tag{A.16}$$

with

$$S(p,t,t') = \int_{t'}^{t} \mathrm{d}\tau \left(\frac{[\mathbf{p} + \mathbf{A}_{\mathrm{L}}(\tau)]^2}{2} + I_{\mathrm{p}} \right), \tag{A.17}$$

and where $\mathbf{p}$ is a 3-dimensional variable.

To justify applying the formula (A.11), we must put this integral in the form (A.1) i.e. find an asymptotic parameter $u \gg 1$ so that the integrand reads $f(x)\, \mathrm{e}^{\mathrm{i}u\phi(x)}$ with x representing integration variables, and a corresponding integration region $\mathcal{K}$. It implies extracting the implicit dependence on physical parameters to ensure that the new prefactor f, phase ϕ, and integration region $\mathcal{K}$ do not depend on this parameter u. This assumption of independence will impose constraints on the physical parameters, whose practical compliance will control the accuracy of the approximation. In short, we will find **when** the saddle point approximation can be trusted or not.

Concretely it boils down to recast (A.16) in terms of dimensionless quantities. The good change of variables is the following :

$$\mathcal{R} = \mathbf{r}\sqrt{2I_{\mathrm{p}}} \tag{A.18a}$$

$$\mathcal{P} = \frac{\mathbf{p}}{\sqrt{2I_{\mathrm{p}}}} \tag{A.18b}$$

$$\mathcal{T} = \omega_{\mathrm{L}} t \tag{A.18c}$$

where the position/velocity commutation relations are preserved.

The dimensionless parameters that will appear are as follows :

$$u = \frac{I_{\mathrm{p}}}{\omega_{\mathrm{L}}} \tag{A.19}$$

$$\gamma = \sqrt{\frac{I_{\mathrm{p}}}{2U_{\mathrm{p}}}} \tag{A.20}$$

$$\overline{\omega} = \frac{\omega}{I_{\mathrm{p}}} \tag{A.21}$$

Note that the expected cutoff formula for the HHG spectra becomes

$$\overline{\omega}_c = 1 + 1.58\, \gamma^{-2}. \tag{A.22}$$

These parameters are not independent of each other, indeed we have $U_{\mathrm{p}} = {F_0}^2/4{\omega_{\mathrm{L}}}^2$ so that

$$\gamma^2 = 2u\frac{{\omega_{\mathrm{L}}}^3}{{F_0}^2} \tag{A.23}$$

or

$$\gamma^2 = 2\frac{{I_{\mathrm{p}}}^3}{{F_0}^2} u^{-2} \tag{A.24}$$

and

$$\overline{\omega} = Ku^{-1} \tag{A.25}$$

where $K = \omega/\omega_{\mathrm{L}}$ is the harmonic order of emission.

The intensity F_0 of the field writes

$$F_0 = \frac{\omega_{\mathrm{L}}\sqrt{2I_{\mathrm{p}}}}{\gamma} \tag{A.26}$$

so that

$$\mathbf{F}_{\mathrm{L}}(t) = \frac{\omega_{\mathrm{L}}\sqrt{2I_{\mathrm{p}}}}{\gamma}\mathcal{F}(\mathcal{T}) \tag{A.27}$$

and

$$\mathbf{A}_{\mathrm{L}}(t) = \frac{\sqrt{2I_{\mathrm{p}}}}{\gamma}\mathcal{A}(\mathcal{T}) \tag{A.28}$$

where $\mathcal{A}(\mathcal{T})$ and $\mathcal{F}(\mathcal{T})$ are respectively a cosine and a sine function of period 2π, multiplied by an envelope beginning at $\mathcal{T} = 0$ and ending at $\mathcal{T} =$ number of cycles $\times\, 2\pi$.

With these dimensionless quantities the phase reads

$$S(\mathbf{p}, t, t') + \omega t = \frac{I_{\mathrm{p}}}{\omega_{\mathrm{L}}}\left[\int_{\mathcal{T}'}^{\mathcal{T}} \mathrm{d}\tau \left(\left[\mathcal{P} + \frac{\mathcal{A}(\tau)}{\gamma}\right]^2 + 1\right) \pm \overline{\omega}\mathcal{T}\right] = u\phi(\mathcal{P}, \mathcal{T}, \mathcal{T}') \tag{A.29}$$

where we have changed the variable of integration in accordance with (A.18). Now the reduced phase $\phi(\mathcal{P}, \mathcal{T}, \mathcal{T}')$ implicitly depends only on γ and $\overline{\omega}$.

Recall that the dipoles are given by

$$d_{\mathrm{ion}}(\mathbf{p} + \mathbf{A}_{\mathrm{L}}(t'), t') = F_{\mathrm{L}}(t') \left\langle \mathbf{p} + \mathbf{A}_{\mathrm{L}}(t') \right| x \left| \varphi_0 \right\rangle \tag{A.30}$$

$$\mathbf{d}_{\mathrm{rec}}(\mathbf{p} + \mathbf{A}_{\mathrm{L}}(t)) = \left\langle \varphi_0 \right| \hat{\mathbf{D}} \left| \mathbf{p} + \mathbf{A}_{\mathrm{L}}(t) \right\rangle . \tag{A.31}$$

We now make the observables x and D dimensionless, in line with (A.18), by the expressions $\mathcal{X} = x\sqrt{2I_{\mathrm{p}}}$ and $\mathcal{D} = (2I_{\mathrm{p}})^{\mp 1/2}\hat{\mathbf{D}}$ where the exponent depends on the form of the dipole (velocity or position):

$$d_{\mathrm{ion}}(\mathbf{p} + \mathbf{A}_{\mathrm{L}}(t'), t') = \frac{\omega_{\mathrm{L}}}{\gamma}\mathcal{F}(\mathcal{T}') \left\langle \mathcal{P} + \frac{\mathcal{A}(\mathcal{T}')}{\gamma} \middle| \mathcal{X} \middle| \phi_0 \right\rangle \tag{A.32}$$

$$\mathbf{d}_{\mathrm{rec}}(\mathbf{p} + \mathbf{A}_{\mathrm{L}}(t)) = (2I_{\mathrm{p}})^{\pm 1/2} \left\langle \phi_0 \middle| \mathcal{D} \middle| \mathcal{P} + \frac{\mathcal{A}(\mathcal{T})}{\gamma} \right\rangle . \tag{A.33}$$

The prefactor is thus

$$(2I_{\mathrm{p}})^{\pm 1/2}\omega_{\mathrm{L}} f(\mathcal{P}, \mathcal{T}, \mathcal{T}') \tag{A.34}$$

where f's only implicit dependence is on γ.

In the end the integral writes :

$$\frac{(2I_{\mathrm{p}})^{\frac{3\pm 1}{2}}}{\omega_{\mathrm{L}}} \int \mathrm{d}\mathcal{T} \int_0^{\mathcal{T}} \mathrm{d}\mathcal{T}' \int \mathrm{d}\mathcal{P}\, f(\mathcal{P}, \mathcal{T}, \mathcal{T}') e^{-\mathrm{i}u\phi(\mathcal{P}, \mathcal{T}, \mathcal{T}')}, \tag{A.35}$$

after changing integration variables from $(\mathbf{p}, t, t')$ to $(\mathcal{P}, \mathcal{T}, \mathcal{T}')$.

Now let us review the assumptions that would guarantee the validity of the saddle point approximation.

- $u \gg 1$ i.e. the ionization potential must be large compared to the frequency of the electric field.
- $\gamma \sim 1 \iff {F_0}^2/(2{I_\mathrm{p}}^3) \sim u^2$ i.e. the intensity of the electric field must be large compared to the cube of the ionization potential (but recall that we need $\gamma \leq 1$ for tunnelling to dominate).
- $\overline{\omega} \sim 1 \iff K \sim u$ i.e. the formula will only be valid for high harmonic orders of the emitted spectrum.

So we are looking at the limit of low frequency $\omega_\mathrm{L} << I_\mathrm{p}$, for a strong field $\gamma \leq 1$, and only at the high frequency part of the emitted spectra, where K scales as u^{-1}.

The dimensionless saddle point equation $\boldsymbol{\nabla}\phi(\mathcal{P},\mathcal{T},\mathcal{T}') = 0$ reads

$$\boldsymbol{\nabla}_{\mathcal{P}}\phi = \int_{\mathcal{T}'}^{\mathcal{T}} \mathrm{d}\tau \left(\mathcal{P} + \frac{\mathcal{A}(\tau)}{\gamma}\right) = 0 \tag{A.36}$$

$$\frac{\partial\phi}{\partial\mathcal{T}'} = -(\mathcal{P} + \frac{\mathcal{A}(\mathcal{T}')}{\gamma})^2 - 1 = 0 \tag{A.37}$$

$$\frac{\partial\phi}{\partial\mathcal{T}} = (\mathcal{P} + \frac{\mathcal{A}(\mathcal{T})}{\gamma})^2 + 1 \pm \overline{\omega} = 0. \tag{A.38}$$

This is simply the dimensionless counterpart of the atomic saddle equations (I.104).

We can easily solve the first equation and plug it in the other two:

$$\mathcal{P}(\mathcal{T},\mathcal{T}') = -\gamma^{-1}\frac{1}{(\mathcal{T}-\mathcal{T}')}\int_{\mathcal{T}'}^{\mathcal{T}} \mathrm{d}\tau\, \mathcal{A}(\tau) \tag{A.39}$$

$$\left[\mathcal{A}(\mathcal{T}') - \frac{1}{(\mathcal{T}-\mathcal{T}')}\int_{\mathcal{T}'}^{\mathcal{T}} \mathrm{d}\tau\, \mathcal{A}(\tau)\right]^2 = -\gamma^2 \tag{A.40}$$

$$\left[\mathcal{A}(\mathcal{T}) - \frac{1}{(\mathcal{T}-\mathcal{T}')}\int_{\mathcal{T}'}^{\mathcal{T}} \mathrm{d}\tau\, \mathcal{A}(\tau)\right]^2 = -\gamma^2(1 \pm \overline{\omega}). \tag{A.41}$$

It is clear that equation (A.40) has no real solution $\mathcal{T}'$. Given that the region of integration $\mathcal{K}$ is real, we conclude from (A.4) that the integral is $O(1/u^\infty)$. This is coherent with the fact that this phenomena relies on tunnelling, which is an exponentially small effect (see chapter III).

Nevertheless we can still compute the first non zero order of the prefactor of this exponential. The general way is to deform the domain of integration in complex coordinates $(\mathcal{P},\mathcal{T},\mathcal{T}')$, while keeping the integral convergent, so that it passes through a **complex** saddle point z_0. As the value of a complex analytic integral does not vary when the contour is deformed, as long as it does not cross singular points of the integrand, this deformation process preserves the value of the integral. If the new domain of integration is chosen carefully, in practice it has to cross the saddle points in directions where the phase has a constant imaginary part, then the integral can be handled by the method of stationary phase. Indeed close to the saddle points, this constant imaginary part in the phase will result in a real attenuated exponential term (as expected from the previous consideration) that we can factor out of the integral, and thus be left with an integral of the form (A.1).

Note that the *saddle* point z_0 will correspond to a *stationary* point of the real part of the phase $\mathrm{Re}(\phi)$. Indeed, as hinted by the change of terminology, a stationary point of a real function corresponds to a saddle point of its complex analytic extension.

So the question becomes : find the complex solutions of (A.36), find the appropriate directions, then try deforming the contour to make it pass through one or several of these solutions. Note that the integration domain cannot be deformed at its boundaries so finding a deformation is not trivial.

Remark that we need to find, among all the saddle points, the ones through which the deformed integration domain has to pass, i.e. we need to determine which of the saddle points contribute to the integral. In general this turns out to be very difficult, especially for multidimensional integrals. More explicitly we need to compute the curves coming from a saddle point z_0 on which the phase stays real. These curves (the so-called *curves of steepest descents*) are of two kinds. The first kind over which the phase has a maximum at z_0, and the second kind over which the phase has a minimum at z_0. The union of the minimum curves is called a ascending disk (or *Lefschetz thimble* as in the introduction of [280]), while the union of the maximum curves is an descending disk. Indeed both are deformed copies of a disk $\mathbb{R}^n$ in $\mathbb{C}^n$. Then, the rule reads : a saddle point contributes if and only if its descending disk intersects the original integration region $\mathcal{K}$.

Here we are in the case $\mathcal{K} \subset \mathbb{R}^{n+2} \subset \mathbb{C}^{n+2}$ i.e. in real dimension $2(n+2)$, so it is not generally easy to compute these ascending disks - even with computers. We were not able to do it here.

A more empirical approach is to apply the method of stationary phase first to the $\mathcal{P}$-integral, considering it as an integral with fixed parameters $(\mathcal{T}, \mathcal{T}')$. Since we find only one saddle point $\mathcal{P}(\mathcal{T}, \mathcal{T}')$ (A.39), we know that is has to contribute to the $\mathcal{P}$-integral. Then we plug the result in the $(\mathcal{T}, \mathcal{T}')$-integral and apply again the method of stationary phase.

We compute numerically the complex saddle points $(\mathcal{T}, \mathcal{T}')$ solutions of (A.41),(A.40). They are two of them $(\mathcal{T}_S, \mathcal{T}'_S)$ and $(\mathcal{T}_L, \mathcal{T}'_L)$, corresponding respectively to the small and long trajectories. Assuming both these saddle points contribute, we apply twice the formula (A.11) and sum the two terms. Eventually - changing back variables - we get the formula (I.107) with the prefactor (I.109).

Appendix B

Free particle in a grid

We want to find the expression of the energies of a free particle in a grid. The grid is defined as in section II.1.1: it is composed of N_x points $(x_j)_{j=1,N_x}$ ranging from $-L$ to $+L$ and separated by a constant step Δx. The eigenstates Ψ are solution of

$$-\frac{1}{2\Delta x^2}\Psi(x_{j-1}) + \frac{1}{\Delta x^2}\Psi(x_j) - \frac{1}{2\Delta x^2}\Psi(x_{j+1}) = E\Psi(x_j). \tag{B.1}$$

As in the case of a free particle in a box [135], the solutions takes the form of plane waves:

$$\Psi(x_j) = A\,\mathrm{e}^{\mathrm{i}kx_j} + B\,\mathrm{e}^{-\mathrm{i}kx_j}\,. \tag{B.2}$$

This function has to satisfy continuity conditions at borders of the box. The condition $\Psi(-L) = 0$ forces

$$A\,\mathrm{e}^{-\mathrm{i}kL} + B\,\mathrm{e}^{\mathrm{i}kL} = 0, \tag{B.3}$$

which gives

$$\Psi(x_j) = 2\mathrm{i}A\,\mathrm{e}^{-\mathrm{i}kL}\sin(kx_j + kL). \tag{B.4}$$

The condition $\Psi(L) = 0$ imposes

$$k = \frac{n\pi}{2L}, \quad n \in \{0, .., N_x\}. \tag{B.5}$$

Inserting (B.4) into (B.1) gives:

$$E\Delta x^2 \sin(kx + kL) = -\frac{1}{2}\sin(kx + kL - k\Delta x) + \sin(kx + kL) - \frac{1}{2}\sin(kx + kL + k\Delta x) \tag{B.6}$$

$$= -\frac{1}{2}\sin(kx + kL)\cos(k\Delta x) + \cancel{\frac{1}{2}\cos(kx + kL)\sin(k\Delta x)} + \sin(kx + kL) - \frac{1}{2}\sin(kx + kL)\cos(k\Delta x) - \cancel{\frac{1}{2}\cos(kx + kL)\sin(k\Delta x)} \tag{B.7}$$

$$= \sin(kx + kL)\,[1 - \cos(k\Delta x)] \tag{B.8}$$

$$= 2\sin(kx + kL)\sin^2\left(\frac{k\Delta x}{2}\right). \tag{B.9}$$

Using (B.5), we get the final expression for energies:

$$E_n = \frac{2}{\Delta x^2} \sin^2 \left(\frac{n\pi \Delta x}{4L} \right). \tag{B.10}$$

We immediately see that the energies do not span all values between 0 and $+\infty$, but reach a maximum at $E_{\max} = 2/\Delta x^2$. We also see that, when $\Delta x \to 0$ we recover the free particle in a box formula:

$$E_n \underset{\Delta x \to 0}{\longrightarrow} \frac{n^2 \pi^2}{2(2L)^2} = \frac{k^2}{2}, \tag{B.11}$$

from which we can compute the density of states:

$$\rho(E) = \frac{\mathrm{d}n}{\mathrm{d}E} = \frac{2L}{\pi \sqrt{2E}}, \tag{B.12}$$

where the 2 comes from the degeneracy of the $\pm n$ states.

Appendix C

Strömgren normalization method

In this appendix we explain, following [271, 281], the Strömgren procedure to normalize on the energy scale the one dimensional continuum states of an arbitrary even potential V that vanishes at infinity:

$$V(x) \underset{x\pm\to\infty}{\longrightarrow} 0. \tag{C.1}$$

These continuum states φ_E are solution of the linear differential equation:

$$\varphi_E''(x) = -2\,(E - V(x))\,\varphi_E(x), \tag{C.2}$$

with positive energy E. Since the potential vanishes at infinity, we can define an "asymptotic region" beyond some limit x_a, where the normalized continuum states χ_E take the general asymptotic form:

$$\chi_E(x) = \frac{1}{\sqrt{\pi k(x)}}\sin(\theta(x)), \quad \text{if} \quad |x| \gg x_a \tag{C.3}$$

where

$$k(x) = \frac{\mathrm{d}\theta}{\mathrm{d}x} \tag{C.4}$$

$$k \underset{x\to\pm\infty}{\longrightarrow} \sqrt{2E}. \tag{C.5}$$

In practice, we will compute a solution φ_E of the TISE (C.2) with the RK4 algorithm using the arbitrary initial conditions given in section II.1.3 c). We then want to determine the normalization constant C that relates this solution φ_E to the normalized solution χ_E:

$$\varphi_E(x) = \frac{1}{C}\chi_E(x). \tag{C.6}$$

For this we fit the numeric solution to the asymptotic form (C.3), via the determination of the function $k(x)$ and $\theta(x)$.

We choose in the asymptotic region an interval $[x_0, x_1]$ on which we know the wave function φ_E and define:

$$a_0 = \sqrt{\pi k(x_0)}\varphi_E(x_0) = \frac{1}{C}\sin(\theta(x_0)) \tag{C.7}$$

$$a_1 = \sqrt{\pi k(x_1)}\varphi_E(x_1) = \frac{1}{C}\sin(\theta(x_1)) \tag{C.8}$$

$$\alpha = \int_{x_0}^{x_1} k(x)\,\mathrm{d}x \qquad = \theta(x_1) - \theta(x_0). \tag{C.9}$$

We can express the normalization constant C with these three quantities:

$$\begin{cases} \sin(\alpha) = \sin(\theta(x_1))\cos(\theta(x_0)) - \sin(\theta(x_0))\cos(\theta(x_1)) \\ \cos(\alpha) = \cos(\theta(x_0))\cos(\theta(x_1)) + \sin(\theta(x_0))\sin(\theta(x_1)) \end{cases} \tag{C.10}$$

$$\Rightarrow \begin{cases} \sin(\alpha) = Ca_1\sqrt{1-C^2a_0^2} - Ca_0\sqrt{1-C^2a_1^2} \\ \cos(\alpha) = \sqrt{1-C^2a_0^2}\sqrt{1-C^2a_1^2} + C^2a_0a_1 \end{cases} \tag{C.11}$$

$$\Rightarrow \begin{cases} \sin^2(\alpha) = C^2\left[a_1^2\left(1-C^2a_0^2\right) + a_0^2\left(1-C^2a_1^2\right) - 2a_0a_2\sqrt{1-C^2a_0^2}\sqrt{1-C^2a_1^2}\right] \\ \cos(\alpha) = \sqrt{1-C^2a_0^2}\sqrt{1-C^2a_1^2} + C^2a_0a_1 \end{cases} \tag{C.12}$$

$$\Rightarrow \sin^2(\alpha) = C^2\left[a_0^2 + a_1^2 - 2a_0a_1\cos(\alpha)\right]. \tag{C.13}$$

Which finally gives:

$$\boxed{C = \sqrt{\frac{\sin^2(\alpha)}{a_0^2 + a_1^2 - 2a_0a_1\cos(\alpha)}}}. \tag{C.14}$$

To evaluate C, we thus need to compute a_0, a_1 and α, i.e. evaluate $k(x)$ in the asymptotic region.

To determine $k(x)$ in the asymptotic region, we insert the normalized wave function $\chi_E(x)$ in the TISE (C.2). Let us start by the expression of the second derivative:

$$\chi_E'(x) = \frac{1}{\sqrt{\pi}}\left[\frac{\mathrm{d}k^{-\frac{1}{2}}}{\mathrm{d}x}\sin(\theta) + k^{-\frac{1}{2}}\cos(\theta)\frac{\mathrm{d}\theta}{\mathrm{d}x}\right] \tag{C.15}$$

$$= \frac{1}{\sqrt{\pi}}\left[\frac{\mathrm{d}k^{-\frac{1}{2}}}{\mathrm{d}x}\sin(\theta) + k^{\frac{1}{2}}\cos(\theta)\right] \tag{C.16}$$

$$\chi_E''(x) = \frac{1}{\sqrt{\pi}}\left[\frac{\mathrm{d}^2k^{-\frac{1}{2}}}{\mathrm{d}x^2}\sin(\theta) + \cancel{\frac{\mathrm{d}k^{-\frac{1}{2}}}{\mathrm{d}x}k\cos(\theta)} + \cancel{\frac{\mathrm{d}k^{\frac{1}{2}}}{\mathrm{d}x}\cos(\theta)} - k^{\frac{3}{2}}\sin(\theta)\right] \tag{C.17}$$

$$= \left[\frac{\mathrm{d}^2k^{-\frac{1}{2}}}{\mathrm{d}x^2}k^{\frac{1}{2}} - k^2\right]\chi_E(x) \tag{C.18}$$

$$= -2\left(E - V(x)\right)\varphi_E(x) \quad (\text{using}(\text{C.2})) \tag{C.19}$$

We thus end up with a new differential equation on k:

$$\frac{\mathrm{d}^2k^{-\frac{1}{2}}}{\mathrm{d}x^2}k^{\frac{1}{2}} - k^2 + A = 0, \tag{C.20}$$

where $A = 2\left(E - V(x)\right)$. We find an approximate solution of this equation in the asymptotic region, where k varies slowly, by writing:

$$k^2 = A + \frac{\mathrm{d}^2k^{-\frac{1}{2}}}{\mathrm{d}x^2}k^{\frac{1}{2}} \simeq A + \frac{\mathrm{d}^2\kappa^{-\frac{1}{2}}}{\mathrm{d}x^2}\kappa^{\frac{1}{2}}, \tag{C.21}$$

with

$$\kappa = A^{\frac{1}{2}} \tag{C.22}$$

$$\frac{\mathrm{d}\kappa^{-\frac{1}{2}}}{\mathrm{d}x} = -\frac{1}{4}\frac{\mathrm{d}A}{\mathrm{d}x}A^{-\frac{5}{4}} \tag{C.23}$$

$$\frac{\mathrm{d}^2\kappa^{-\frac{1}{2}}}{\mathrm{d}x^2} = -\frac{1}{4}\frac{\mathrm{d}^2A}{\mathrm{d}x^2}A^{-\frac{5}{4}} + \frac{5}{16}\left(\frac{\mathrm{d}A}{\mathrm{d}x}\right)^2 A^{-\frac{9}{4}}. \tag{C.24}$$

With this we can express k only as a function of A and its derivatives, or only as a function of the potential V and its derivatives:

$$\boxed{k \simeq \sqrt{A - \frac{1}{A}\frac{\mathrm{d}^2V}{\mathrm{d}x^2} + \frac{5}{16}\left(\frac{1}{A}\frac{\mathrm{d}V}{\mathrm{d}x}\right)^2}.} \tag{C.25}$$

This last equation allows us to compute k on the interval $[x_0; x_1]$. We will then deduce the quantities a_0, a_1 and α, and finally the normalization constant C. Moreover we will assess the validity of the different approximations by checking the convergence of C for different intervals $[x_0; x_1]$ further and further away from the origin.

Appendix D

Split-operator algorithm

In this appendix we establish the expression of the error that is made at each time step by the split-operator algorithm. This error comes from the approximation of the evolution operator:

$$U = \mathrm{e}^{-\mathrm{i}\hat{H}\Delta t} = \mathrm{e}^{-\mathrm{i}\left(\hat{T}+\hat{V}\right)\Delta t}\,. \tag{D.1}$$

First we consider the case of the simple decomposition:

$$\begin{aligned}
U_{2\mathrm{nd}} &= \mathrm{e}^{-\mathrm{i}\hat{T}\Delta t}\,\mathrm{e}^{-\mathrm{i}\hat{V}\Delta t} && \text{(D.2)}\\
&= \left(\mathbb{1} - \mathrm{i}\hat{T}\Delta t - \hat{T}^2\frac{\Delta t^2}{2} + O\left(\Delta t^3\right)\right)\left(\mathbb{1} - \mathrm{i}\hat{V}\Delta t - \hat{V}^2\frac{\Delta t^2}{2} + O\left(\Delta t^3\right)\right) && \text{(D.3)}\\
&= \mathbb{1} - \mathrm{i}\left(\hat{T}+\hat{V}\right)\Delta t - \left(2\hat{T}\hat{V} + \hat{T}^2 + \hat{V}^2\right)\frac{\Delta t^2}{2} + O\left(\Delta t^3\right) && \text{(D.4)}\\
&= \mathbb{1} - \mathrm{i}\hat{H}\Delta t - \hat{H}^2\frac{\Delta t^2}{2} + \left[\hat{V},\hat{T}\right]\frac{\Delta t^2}{2} + O\left(\Delta t^3\right) && \text{(D.5)}\\
&= \mathrm{e}^{-\mathrm{i}\hat{H}\Delta t} + O\left(\Delta t^2\right). && \text{(D.6)}
\end{aligned}$$

As $\left[\hat{V},\hat{T}\right] \neq 0$ we get an error proportional to Δt^2.

On the contrary, for the split-operator algorithm, we use the symmetric decomposition:

$$U_{\mathrm{SO}} = \mathrm{e}^{-\mathrm{i}\hat{V}\Delta t/2}\,\mathrm{e}^{-\mathrm{i}\hat{T}\Delta t}\,\mathrm{e}^{-\mathrm{i}\hat{V}\Delta t/2} \tag{D.7}$$

$$\begin{aligned}
&= \left(\mathbb{1} - \mathrm{i}\hat{V}\frac{\Delta t}{2} - \hat{V}^2\frac{\Delta t^2}{8} + \mathrm{i}\hat{V}^3\frac{\Delta t^3}{48} + O\left(\Delta t^4\right)\right) \\
&\times \left(\mathbb{1} - \mathrm{i}\hat{T}\Delta t - \hat{T}^2\frac{\Delta t^2}{2} + \mathrm{i}\hat{T}^3\frac{\Delta t^3}{6} + O\left(\Delta t^4\right)\right) \qquad \text{(D.8)} \\
&\times \left(\mathbb{1} - \mathrm{i}\hat{V}\frac{\Delta t}{2} - \hat{V}^2\frac{\Delta t^2}{8} + \mathrm{i}\hat{V}^3\frac{\Delta t^3}{48} + O\left(\Delta t^4\right)\right) \\
&= \mathbb{1} - \mathrm{i}\left(\hat{T} + \hat{V}\right)\Delta t - \left(\hat{T}^2 + \hat{T}\hat{V} + \hat{V}\hat{T} + \hat{V}^2\right)\frac{\Delta t^2}{2} \\
&+ \mathrm{i}\left(\frac{1}{6}\hat{T}^3 + \frac{1}{4}\hat{T}^2\hat{V} + \frac{1}{4}\hat{V}\hat{T}^2 + \frac{1}{8}\hat{T}\hat{V}^2 + \frac{1}{4}\hat{V}\hat{T}\hat{V} + \frac{1}{8}\hat{V}^2\hat{T} + \frac{1}{6}\hat{V}^3\right)\Delta t^3 \qquad \text{(D.9)} \\
&+ O\left(\Delta t^4\right) \\
&= \mathbb{1} - \mathrm{i}\hat{H}\Delta t - \hat{H}^2\frac{\Delta t^2}{2} + \mathrm{i}\hat{H}^3\frac{\Delta t^3}{6} \\
&+ \mathrm{i}\left(\frac{1}{12}\hat{T}^2\hat{V} - \frac{1}{6}\hat{T}\hat{V}\hat{T} + \frac{1}{12}\hat{V}\hat{T}^2 - \frac{1}{24}\hat{T}\hat{V}^2 + \frac{1}{12}\hat{V}\hat{T}\hat{V} - \frac{1}{24}\hat{V}^2\hat{T}\right)\Delta t^3 \qquad \text{(D.10)} \\
&+ O\left(\Delta t^4\right) \\
&= \mathrm{e}^{-\mathrm{i}\hat{H}\Delta t} + \left(2\Big[[V,T],T\Big] - \Big[V,[V,T]\Big]\right)\frac{\Delta t^3}{6} + O\left(\Delta t^4\right) \qquad \text{(D.11)} \\
&= \mathrm{e}^{-\mathrm{i}\hat{H}\Delta t} + O\left(\Delta t^3\right) \qquad \text{(D.12)}
\end{aligned}$$

and get an error proportional to Δt^3.

Appendix E

Simulation parameters

The parameters used for the different numerical simulations presented in this thesis are listed here.

n_t	Number of time steps per laser cycle.
ω_{L}	Laser pulsation.
I_{L}	Laser field intensity.
F_0	Laser field amplitude.
N_{c}	Number of optical cycles in the laser pulse. When one number is given, the pulse envelope is a sine square function, while when 3 numbers $N_{\mathrm{ramp}} - N_{\mathrm{plat}} - N_{\mathrm{ramp}}$ are given, the pulse envelope has a trapezoidal shape with ramps of N_{ramp} optical cycles and a plateau of N_{plat} optical cycles.
ζ	Exponent used for the absorbing boundary conditions (see section II.1.2 c)).
h_{abs}	Width of the absorber (see section II.1.2 c)), the eventual subscript refer to the dimension.
L	Size of the simulation box, the eventual subscript refer to the dimension.
N_x	Number of grid points, the subscript refer to the dimension.
γ_W	Half width of the window operator (see section II.3.4 b)).
L_W	Size of the box used for the window method (see section II.3.4 d)).
h_{sep}	Width of the absorber used for trajectory separation (see section II.3.3). In 2D simulations, this absorber is chosen circular (we replace x by $r = \sqrt{x^2 + y^2}$ in (II.32)), we thus only have one value for h_{sep}.
L_{sep}	Size of the "small" box from which we get the wave function corresponding to the short trajectories. It also corresponds to the end of the absorber used for the trajectory separation (we replace L by L_{sep} in (II.32)). In 2D simulations, the small box is also chosen circular, we thus only have one value for L_{sep}.

	n_t	ω_{L}	I_{L}	N_{c}	ζ	h_{abs}	L	N_x	γ_W	L_W	h_{sep}	L_{sep}
Fig. I.1	131 072	0.057	10^{14}	1-8-1	0.125	100	2 000	200 001	0.02	2 500	-	-
	8 192	0.057	10^{14}	1-8-1	0.125	100	2 000	200 001	0.02	2 500	-	-
Fig. I.2	8 192	0.057	10^{14}	1-8-1	0.125	100	2 000	200 001	0.02	2 500	-	-
Fig. I.3 Fig. I.4	$\max\left(200, \frac{2\pi}{0.1\omega_{\mathrm{L}}}\right)$	-	3.51×10^{12}	200	0.125	200	500	20 001	-	-	-	-
Fig. I.5	4 096	0.057	3×10^{14}	1-8-1	0.125	400	500	20 001	-	-	-	-
Fig. I.6	100	1	3.51×10^{12}	30	0.125	100	1 000	200 001	-	-	-	-
Fig. I.8	50 000	0.019	8.77×10^{13}	8	0.125	100	1 000	200 001	-	-	-	-
Fig. II.6 Fig. II.8 Fig. II.9	8 192	0.057	2×10^{14}	2	0.03125	70	300	6 001	-	-	20	$\frac{F_0}{{\omega_{\mathrm{L}}}^2} + 15 \simeq 38.2$
Fig. II.7	8 192	0.057	2×10^{14}	1-8-1	0.03125	70	300	6 001	-	-	-	-
Fig. II.11	512	1.5	3.51×10^{12}	20	0.125	50	500	10 001	-	50 500	-	-
Fig. II.12	512	1.5	3.51×10^{12}	20	0.125	50	500	10 001	0.001	-	-	-
Fig. III.2	$\Delta t = 0.1$	0.001	-	-	0.125	200	500	20 001	-	-	-	-
Fig. III.5	$\Delta t = 0.1$	0.001	-	-	0.125	200	500	20 001	-	-	-	-
Fig. III.6	$\Delta t = 0.1$	0.001	-	-	0.125	200	500	20 001	-	-	-	-
Fig. III.7	$\Delta t = 0.1$	0.001	-	-	0.125	100	500	20 001	-	-	-	-
	$\Delta t = 0.1$	0.005	-	-	0.125	100	500	20 001	-	-	-	-
Fig. III.9	$\Delta t = 0.1$	0.001	-	-	0.125	100	500	20 001	-	-	-	-
	$\Delta t = 0.1$	0.005	-	-	0.125	100	500	20 001	-	-	-	-

	n_t	ω_L	F_0	N_c	ζ	$h_{\mathrm{abs},x}$	$h_{\mathrm{abs},y}$	L_x	L_y	N_x	N_y	h_sep	L_sep
Fig. IV.1 Fig. IV.3 (b) Fig. IV.7	8 192	0.057	0.1	2	0.015625	70	-	300	-	6 001	-	25	$\frac{F_0}{{\omega_\mathrm{L}}^2} + 15 \simeq 45.8$
Fig. IV.2 Fig. IV.3 (a) Fig. IV.8	1 024	0.057	0.1	2	0.125	50	50	204.8	204.8	4 096	4 096	25	$\frac{F_0}{{\omega_\mathrm{L}}^2} + 15 \simeq 45.8$
Fig. IV.4	2 048	0.057	0.1	2	0.125	50	50	204.8	204.8	4 096	4 096	25	$\frac{F_0}{{\omega_\mathrm{L}}^2} + 15 \simeq 45.8$
Fig. IV.5	2 048	0.057	0.1	2	0.125	50	50	204.8	204.8	4 096	4 096	25	$\frac{F_0}{{\omega_\mathrm{L}}^2} + 15 \simeq 45.8$
Fig. IV.6 Fig. IV.8	1 024	0.057	0.1	2	0.125	50	50	204.8	204.8	4 096	4 096	25	$\frac{F_0}{{\omega_\mathrm{L}}^2} + 15 \simeq 45.8$

	n_t	ω_L	I_L	N_c	ζ	$h_{\mathrm{abs},x}$	$h_{\mathrm{abs},R}$	L_x	L_R	N_x	N_R
Fig. V.2 H_2	8 192	7.5×10^{-2}	-	-	0.125	20	-	100	-	2 001	-
Fig. V.2 A_2	8 192	7.5×10^{-2}	-	-	0.125	20	-	100	-	4 001	-
Fig. V.2 G_2	8 192	10^{-4}	-	-	0.125	20	-	100	-	4 001	-
Simulations BS, LF	8 192	0.057	-	-	-	0	-	-	20	-	8 000
Fig. V.6 (a),(c),(e) Fig. V.8 (a) XR	1 024	0.057	10^{14}	8	0.125	100	0	204.8	10.24	4 096	1 024
Fig. V.7 (a),(c),(e) Fig. V.8 (c) XR Fig. V.9 (c) XR	1 024	0.057	4×10^{14}	8	0.125	100	0	204.8	10.24	4 096	1 024
Fig. V.8 (a) XR	1 024	0.057	4×10^{14}	4	0.125	100	0	204.8	10.24	4 096	1 024
Fig. V.8 (b) XR	1 024	0.057	4×10^{14}	6	0.125	100	0	204.8	10.24	4 096	1 024
Fig. V.10 (a) XR	1 024	0.057	4×10^{14}	8	0.125	150	0	204.8	10.24	4 096	1 024
Fig. V.10 (b) XR	1 024	0.057	4×10^{14}	8	0.125	170	0	204.8	10.24	4 096	1 024
Fig. V.10 (c) XR	1 024	0.057	4×10^{14}	8	0.125	190	0	204.8	10.24	4 096	1 024
Fig. V.11 XR	1 024	0.057	10^{15}	8	0.125	100	0	204.8	10.24	4 096	1 024

	n_t	ω_{L}	I_{L}	N_{c}	ζ	h_{abs,x_1}	h_{abs,x_2}	L_{x_1}	L_{x_2}	N_{x_1}	N_{x_2}
Fig. VI.4 Grid	8 192	0.057	-	1-8-1	1.5625×10^{-2}	100	-	800	-	20 001	-
	16 384	0.057	$7 \times 10^{‘14}$	1-8-1	7.8125×10^{-3}	100	-	800	-	20 001	-
Fig. VI.5 Grid											
Fig. VI.6 (a)	8 192	0.057	-	1-8-1	1.5625×10^{-2}	100	-	800	-	20 001	-
Fig. VI.7 Grid											
Fig. VI.9 Grid											
Fig. VI.8 Grid	8 192	0.057	$2 \times 10^{‘14}$	1-8-1	1.5625×10^{-2}	100	-	800	-	20 001	-
Fig. VI.10 Grid	8 192	0.057	$2 \times 10^{‘14}$	1-8-1	1.5625×10^{-2}	100	-	800	-	20 001	-
Fig. VI.11 (a) Grid	131 072	0.057	10^{14}	1-8-1	0.125	100	-	2 000	-	200 001	-
Fig. VI.15 Grid	1 024	0.057	-	1-8-1	0.125	100	100	409.6	409.6	8 192	8 192
Fig. VI.16 Grid	1 024	0.057	-	1-8-1	0.125	100	100	204.8	204.8	4 096	4 096

French Summary

S.1 Introduction

La lumière et la matière sont parmi les objets les plus étudiés par les physiciens. Ils peuvent interagir de tant de façons différentes qu'ils ouvrent des possibilités pour ainsi dire infinies. Ces interactions sont à l'origine d'un des domaines les plus riches et les plus actifs de la physique, mais présentent également un nombre toujours croissant d'applications en permettant de développer des techniques expérimentales toujours plus poussées. Un des exemples les plus marquants est l'utilisation de l'*émission stimulée*, qui provient de l'interaction d'un atome avec un photon, et qui est à la base du laser (Light Amplification by Stimulated Emission of Radiation, i.e. amplification de lumière par émission stimulée de rayonnement) que l'on retrouve désormais dans tous les laboratoires, des tables optiques jusque dans les salles de conférences.

L'incroyable succès du laser en tant qu'outil universel pour un large éventail d'applications expérimentales provient de ses propriétés fondamentales. C'est une source de lumière monochromatique, intense, mais surtout *cohérente*. Cette dernière particularité en fait l'outil idéal pour étudier les propriétés quantiques fondamentales de la matière. Depuis l'invention pionnière du maser (Microwave Amplification by Stimulated Emission of Radiation, i.e. Amplification de micro-ondes par émission stimulée de rayonnement) dans les années 1950, suivie du développement du laser dans les années 1960, d'importants efforts ont permis d'améliorer les différentes caractéristiques de cette célèbre source lumineuse. De nouvelles bandes de longueur d'onde peuvent désormais être émises, et certains lasers peuvent même accorder leur longueur d'onde sur certaines plages spectrales. L'intensité émise a été augmentée de plusieurs ordres de grandeur, ce qui a ouvert la voie à la physique des champs forts [1]. En particulier, l'invention de l'amplification par dérive de fréquence (Chirped Pulse Amplification) [2] a été une incroyable percée pour la génération d'impulsion laser de forte intensité. Les impulsions lasers ont également vu leur durée réduite jusqu'aux limites de la transformée de Fourier. Ces impulsions qui ne dure pas plus d'un cycle laser peuvent atteindre quelques femtosecondes seulement (1 fs $= 10^{-15}$ s). Cet incroyable réussite est à l'origine de la *femtochimie*, dont les expériences pionnières de Zewail [3, 4] ont permis d'étudier à des échelles de temps aussi rapides des dynamiques moléculaires, c'est à dire des réactions chimiques.

Ces avancées techniques, et en particulier la possibilité d'atteindre des champs lasers très intenses (de 10^{14} W.cm^{-2} à 10^{22} W.cm^{-2}) ont conduit à la découverte de processus physiques fortement non linéaires comme l'ionisation au dessus du seuil (ATI) en 1979 [5], l'ionisation multiple non séquentielle en 1982 [6], ou la génération d'harmoniques d'ordre

élevé (HHG) par deux groupes différents en 1987 [7] et en 1988 [8]. Ces découvertes ont induit un fort développement de travaux théoriques pour construire des modèles et mettre au point des mécanismes pour expliquer ces processus [9–11], ce qui reste encore aujourd'hui un domaine de recherche très actif. Mais au delà de son intérêt physique fondamental, la génération d'harmonique a engendré une véritable révolution. Elle a permis de générer des impulsions lumineuses cohérentes dans le domaine des extrêmes ultra-violets (XUV), ce qui reste impossible pour les lasers optiques actuels, avec les durées d'impulsion les plus courtes jamais produites. Ces impulsions peuvent durer seulement quelques dizaines d'attosecondes (1 as $= 10^{-18}$ s) [12–14], le record mondial actuel étant de 43 as [15], et offrent donc la possibilité d'étudier des dynamiques *électroniques* à leurs échelles de temps naturelles.

Cette nouvelle source lumineuse est à l'origine d'un tout nouveau domaine de la science : la physique attoseconde [16–19]. Elle a été utilisée pour mesurer des délais attosecondes de photoionisation dans des gaz rare comme le Néon [20] et l'argon [21], mais aussi dans des systèmes plus complexes comme des molécules chirales [22] et des solides [23, 24]. La dynamique de processus fondamentaux comme le déclin Auger [25] ou l'ionisation tunnel [26] a pu être étudiée expérimentalement. Des dynamiques électroniques ont pu être reconstruite avec une résolution attoseconde dans des atomes [27], des molécules [28] et des solides [29–31]. Des corrélations électroniques dynamiques ont été observées par la dynamique attoseconde d'une résonance de Fano dans l'hélium [32, 33]. Des dynamiques nucléaire sub-femtosecondes ont pu être mesurées dans des molécules [34]. La physique attoseconde s'étend même aujourd'hui aux nano-structures [35–37], pour lesquelles les champs proches, qui proviennent de leur interaction avec le champ incident, ont pu être utilisés pour mesurer et contrôler la dynamique et la diffusion d'électrons à l'échelle attoseconde [38–40].

En plus de ses propriétés remarquables qui en ont fait une source lumineuse incontournable, la lumière émise par la génération d'harmoniques contient aussi énormément d'informations sur le système qui a lui-même émit cette lumière. Cela a contribué au développement d'un nouveau type de spectroscopie qui repose sur la génération d'harmoniques en tant qu'*auto-sonde* [41]. Cette technique permet de mesurer des dynamiques nucléaires attosecondes [42–44], d'imager des paquets d'onde électroniques dépendants du temps [45], de reconstruire les orbitales du système par tomographie [46–48], de suivre des dynamiques poly-électroniques dans des atomes [49], des molécules [50] et des solides [51], de distinguer les énantiomères d'une molécule chirale [55], ou de révéler des symétries dynamiques dans des atomes et des molécules [56].

Ces avancées passionnantes poussent au développement de méthodes théoriques et numériques poussées pour analyser, interpréter, et préparer toutes ces expériences. En effet l'interaction entre atomes et photons est souvent comprise par l'intermédiaire de la très puissante théorie des perturbations dépendante du temps. Cependant cette méthode ne permet de modéliser que les processus linéaires, ou modérément non linéaire, que l'on observe en présence de champs relativement peu intenses. Dans le cas de la génération d'harmoniques, ou d'autre processus fortement non linéaires, l'intensité du laser incident est comparable au potentiel d'interaction entre les électrons et les noyaux. Celui-ci ne peux donc pas être considéré comme une perturbation. La description théorique de la dynamiques électroniques en présence de tels champs lasers nécessite donc de résoudre

l'équation de Schrödinger dépendante du temps (TDSE) :

$$\mathrm{i}\hbar\frac{\mathrm{d}\,|\Psi(t)\rangle}{\mathrm{d}t} = \hat{H}(t)\,|\Psi(t)\rangle$$

qui fait intervenir la fonction d'onde dépendante du temps $|\Psi(t)\rangle$ qui décrit intégralement l'état du système, et le Hamiltonien dépendant du temps $\hat{H}(t)$ qui gouverne sa dynamique. Néanmoins cette approche ne permet d'acquérir que peu de compréhension physique des processus physique en jeu. En effet, comme la fonction d'onde n'est pas une observable physique, elle n'est pas directement accessible expérimentalement, et reste donc très difficile à interpréter en tant que telle.

Au cours de ma thèse, j'ai utilisé deux stratégies différentes pour construire des modèles physiques sur des processus en champs forts. D'une part j'ai considéré des système modèles simplifiés en dimensions réduites pour lesquels j'ai pu réaliser des simulations numériques approfondies. J'ai ainsi pu résoudre la TDSE pour un grand nombre de paramètres tant pour le champ laser que pour les systèmes modèles, et par la suite analyser de diverses façons la fonction d'onde obtenue. D'autre part, j'ai construit des modèles analytiques approchés pur décrire la dynamiques de ces systèmes. Ces deux approches sont extrêmement complémentaires, et leur juxtaposition permet analyse fine des approximations à la bases de ces modèles.

Le but de cette thèse et d'explorer différents aspects de la dynamique d'atomes et de molécules lorsqu'elle est déclenchée par des champs lasers intenses. Dans un premier chapitre j'explique les différents modèles couramment invoqués pour comprendre l'interaction entre matière et rayonnement. En particulier je détaille le célèbre modèle en trois étapes, qui est à l'origine de la plupart des interprétations physiques dont nous disposons aujourd'hui sur les processus en champs intenses. Un deuxième chapitre est consacré à la présentation des systèmes modèles pour lesquels j'ai résolu la TDSE et des différentes méthodes numériques employées pour simuler et analyser la dynamique de ces systèmes en présence d'un champ laser intense. Dans les chapitres III, IV et V je présente mes résultats sur l'ionisation tunnel, des interférences à deux centres dans des molécules diatomiques révélée par la génération d'harmoniques, et sur les corrélations électrons-noyaux observées dans des dynamiques vibroniques dans H_2. Dans un dernier chapitre, réalisé en grande partie avec Felipe Zapata Abellán, Emanuele Coccia, Julien Toulouse, Valérie Véniard et Eleonora Luppi du Laboratoire de Chimie Théorique à Sorbonne Université, j'explore la possibilité de résoudre la TDSE pour des systèmes plus complexes où les corrélations électroniques jouent un rôle fondamental dans la dynamique.

S.2 Atomes et molécules en champ intense

L'interaction d'un atome avec un champ laser peut donner lieu à des phénomènes très différents suivant les gammes de temps, et d'énergie considérées. On distingue couramment deux principaux régimes d'interaction : le régime multiphotonique et le régime tunnel. La limite entre les deux est mesurée avec le paramètre de Keldysh [113] :

$$\gamma = \sqrt{\frac{I_\mathrm{p}}{2U_\mathrm{p}}}, \tag{S.1}$$

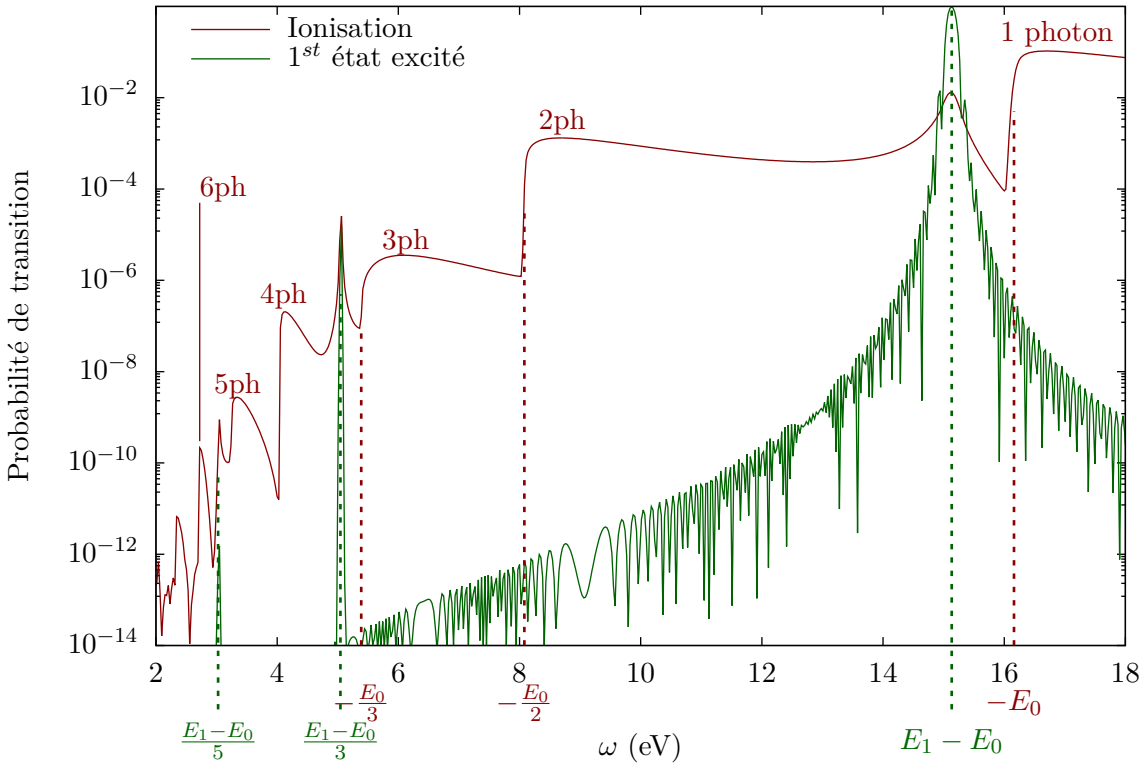

Figure S.1 *Spectre d'absorption d'un électron dans un potentiel gaussien* $V(x) = -\mathrm{e}^{-x^2/2}$*, soumis à une impulsion laser à enveloppe sinus carré de 200 cycles et d'intensité* $I_\mathrm{L} = 3.5 \times 10^{12}$ W.cm^{-2}*. Le nombre de photons correspondant à chaque seuil d'ionisation est indiqué.*

où I_p est le potentiel d'ionisation du système et $U_\mathrm{p} = F_0^2/(4\omega_\mathrm{L}^2)$ est le potentiel pondéromoteur du champ, avec F_0 l'amplitude du champ au maximum de l'impulsion laser et ω_L sa pulsation.

Lorsque le paramètre de Keldysh est grand $\gamma \gg 1$, c'est à dire pour des hautes fréquences, et des champs peu intenses, on est en régime multiphotonique. Dans ce cas, l'interaction avec le champ peut être efficacement traitée par la théorie des perturbations dépendantes du temps [86]. Ce modèle approché permet de calculer la probabilité de transition depuis un état propre du système sans champ vers un autre état propre, qu'il soit lié ou qu'il appartiennent au continuum. Après un temps d'interaction suffisamment long devant la période du laser, on trouve que cette probabilité présente des résonances si la fréquence du laser correspond à la différence d'énergie entre l'état final et l'état initial. En développant à des ordres supérieurs, on trouve également d'autres résonances, d'intensité moindre, lorsque cette différence d'énergie est un multiple entier de la fréquence du laser, correspondant au nombre de photons échangés (absorbés ou émis) lors de la transition.

Pour illustrer ces caractéristiques fondamentales, nous représentons en Figure S.1 les probabilités de transition pour un système modèle possédant deux états liés soumis à une impulsion laser relativement longue et de faible intensité. Les résonances prévues par la

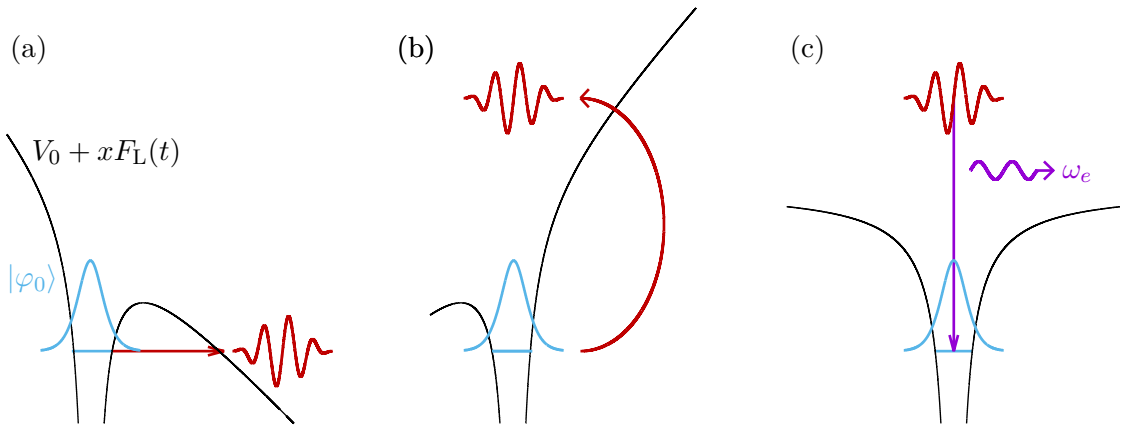

Figure S.2 *Représentation schématique du modèle en trois étapes : (a) ionisation tunnel, (b) accélération par le champ et retour à proximité des noyaux, (c) recombinaison et émission d'un photon XUV.*

théorie des perturbations dépendante du temps sont indiquées sur la figure. Certaines transitions sont cependant absentes : par exemple on n'observe aucune résonance pour un photon d'énergie $\omega_L = (E_1 - E_0)/2$. Ceci est du à des règles de sélections imposées par la symétrie des états initiaux et finaux et par le nombre de photons mis en jeu dans la transition.

Au contraire dans le cas où le paramètre de Keldysh est petit $\gamma \ll 1$, c'est à dire pour des faibles fréquences, et en champ intense, on est en régime tunnel. Dans ce cas le champ laser intense ne peut pas être considéré comme une perturbation. Néanmoins comme la fréquence du laser est faible comparée aux échelles de temps caractéristiques de la dynamique électronique, on peut considérer que l'électron suit *adiabatiquement* le champ électrique. C'est à dire qu'on suppose que l'électron réagit instantanément à la valeur que prend le champ à chaque instant. On peut donc regarder le potentiel effectif, constitué du potentiel d'interaction avec les noyaux et de l'interaction avec le champ, que ressent l'électron à un temps t. Ceci est représenté schématiquement en Figure S.2 (a) : on voit apparaître une barrière de potentiel au travers de laquelle l'électron va pouvoir s'échapper par effet tunnel, créant un paquet d'onde électronique dans le continuum. À un instant ultérieur, lorsque la valeur instantanée du champ a changé de signe, ce paquet d'onde est ramené proche du cœur ionique dont il est parti, comme illustré en Figure S.2 (b). Lorsque ce paquet d'onde se retrouve à proximité des noyaux, il y a une probabilité non nulle pour qu'il se *recombine* avec l'état fondamental, comme schématisé en Figure S.2 (c), et qu'il libère ainsi toute l'énergie cinétique accumulée lors de son trajet dans le continuum en émettant un photon. Ces trois processus (a) ionisation tunnel, (b) propagation dans le continuum et accélération par le champ et (c) recombinaison constituent le fameux modèle en trois étapes [9, 10, 91, 11]. Le processus dans son ensemble est appelé la génération d'harmoniques d'ordre élevé (HHG). Il se répète à chaque demi cycle laser de part et d'autres des noyaux. Le rayonnement émis présente des caractéristiques très spécifiques. Il présent un spectre très large constitué des harmoniques du rayonnement laser incident,

et, dans le cas où le système présente un centre d'inversion, uniquement des harmoniques impaires. Dans le domaine temporel, il prend la forme d'un train d'impulsions lasers pouvant durer chacune quelques dizaines d'attosecondes seulement. De plus, comme les électrons ayant suivis différentes trajectoires lors de la seconde étape (b) ont tous le même état final et initial, il peuvent interférer entre eux. Ces interférences encodent beaucoup d'informations sur le système et apparaissent également dans le spectre de la lumière émise.

S.3 Ionisation tunnel

L'ionisation tunnel fut en premier lieu modélisée par Keldysh [113], et a depuis fait l'attention d'un grand nombre de travaux théoriques. Comme pour beaucoup de processus fortement non linéaire, la seule manière de décrire précisément l'ionisation tunnel est de résoudre la TDSE. Comme cela nécessite d'importantes ressources numériques, les théoriciens ont souvent recours à différentes approximations pour simplifier les systèmes traités, ou à des méthodes analytiques approchées. Parmi ces méthodes analytiques, les plus couramment utilisées sont les formules obtenues par Ammosov, Delone et Krainov [177] et par Perelomov, Popov et Terent'ev [174] pour les atomes, et étendues aux molécules par Tong et al. [178, 179] et Kjeldsen et Madsen [180]. Ces formules reposent toutes sur l'approximation adiabatique et sont donc déduites de la formule en champ statique obtenue par Landau et Lifshitz pour l'atome d'hydrogène [132] et généralisée par Smirnov et Chibisov (SC) [184].

Cependant ces formules sont uniquement valides pour un champ asymptotiquement faible $F \to 0$ et ont donc une précision limitée pour des champs non nuls. En comparant les résultats données par la formule de Smirnov et Chibisov et des résultats "exacts", à la précision numérique près, j'ai montré dans ma thèse que la compensation d'erreur jouait un rôle fondamental dans l'accord résultats analytiques et numériques. J'ai également établi une formule *corrigée* qui tient compte de l'effet du champ laser sur les niveaux d'énergies dy système, ce qui est couramment appelé l'effet Stark. Correction permet d'améliorer considérablement la précision de la formule SC. La contribution de l'effet Stark est même indispensable pour reproduire le comportement qualitatif de l'ionisation de molécules polaires. Pour les atomes et pour certaines molécules peu polaires l'effet Stark peut être calculé par la théorie des perturbations indépendantes du temps au deuxième ordre (2PT). Ceci est illustré en Figure S.3 (a) : l'accord entre la formule SC et les calculs numérique "TDSE" se détériore quand le champ s'intensifie. Pour cette petite molécule, la théorie des perturbations au second ordre (2PT) permet de corriger la formule et d'améliorer l'accord. Néanmoins dans le cas de molécules très polarisable, comme celle présentée en Figure S.3 (b) il est nécessaire d'utiliser la théorie des perturbations indépendante du temps *dégénérée* pour obtenir un accord acceptable.

S.4 Interférences à deux centres observées par la génération d'harmoniques d'ordres élevés

La génération d'harmoniques n'est pas qu'une source lumineuse. Elle permet également d'avoir accès à nombre d'informations tant structurelles que dynamiques sur le système

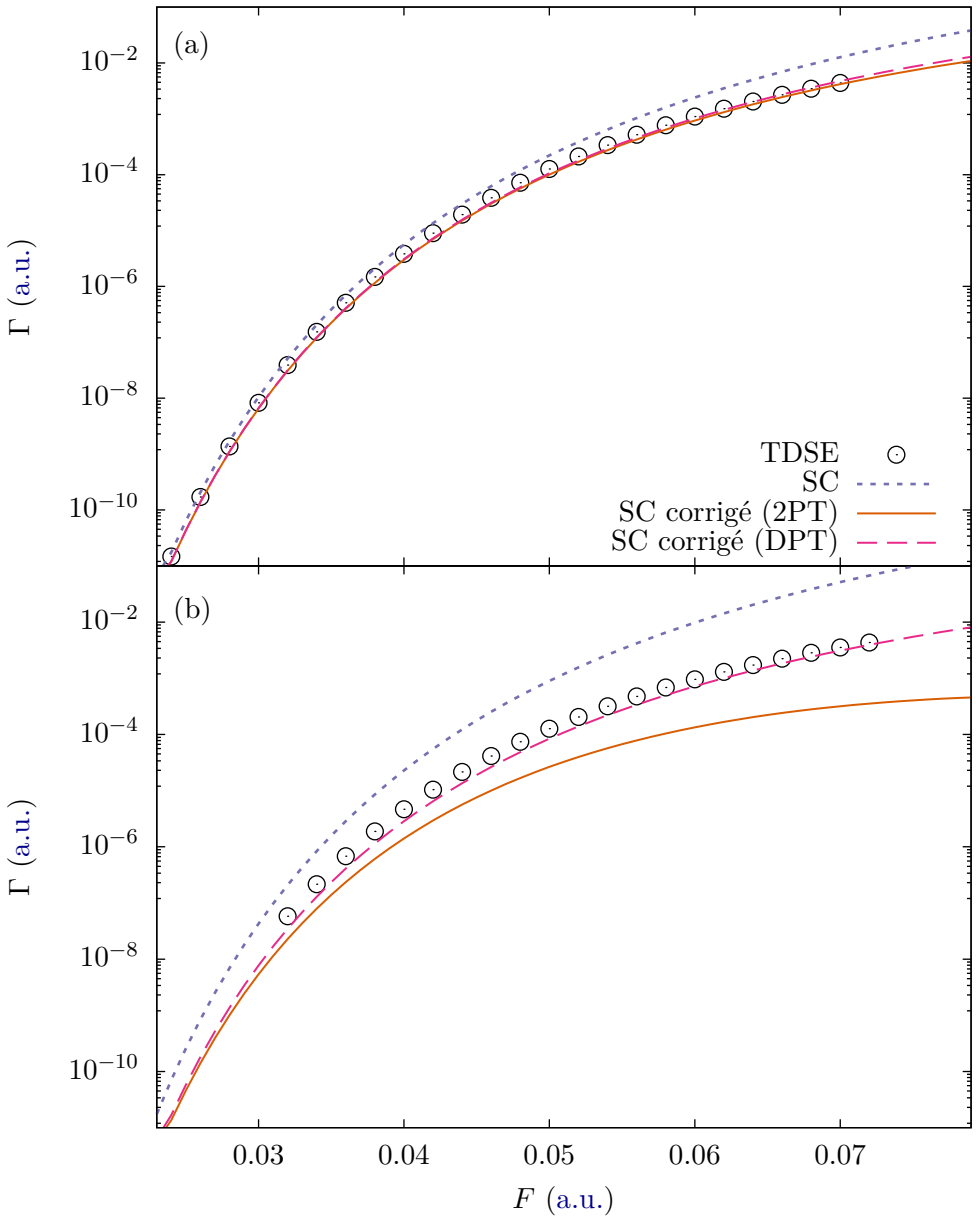

Figure S.3 *Rendement d'ionisation tunnel de systèmes modèles à une dimension représentant des molécules diatomiques homonucléaires alignées avec le champ définis par un potentiel Soft-Coulomb*(II.2) *avec les paramètres (a)* $a = 1$ *u.a. et* $R = 2.2$ *u.a. (b)* $a = 0.6925$ *u.a. et* $R = 4$ *u.a..*

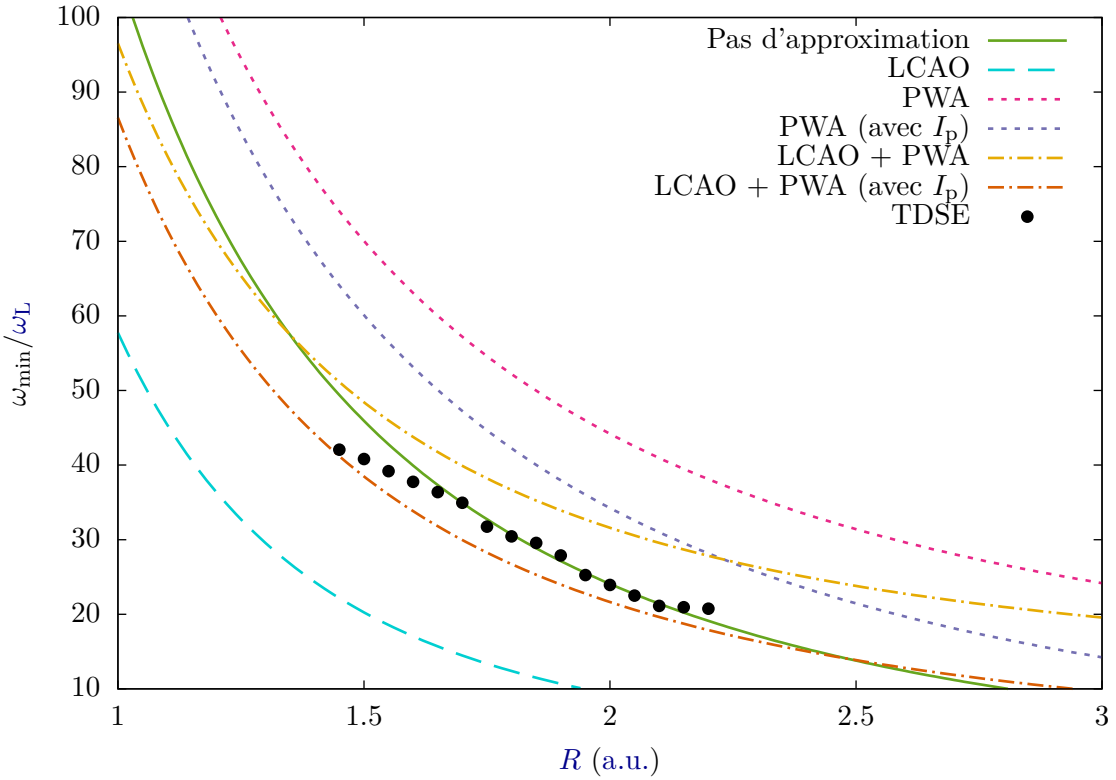

Figure S.4 *Position du minimum d'interférence dans le spectre harmonique (TDSE) et position du premier zéro du dipôle de recombinaison calculé avec différents niveaux d'approximations pour un système modèle à une dimension représentant une molécule de H_2 alignée avec le champ.*

qui émet le rayonnement harmonique. Dans le cas des molécules diatomiques, la troisième et dernière étape du modèle en trois étapes peut avoir lieu à chacun des deux noyaux. Ils se comportent alors comme deux points sources cohérents qui peuvent interférer, à la façon des deux trous d'Young. La figure d'interférence obtenue se superpose alors au spectre harmonique émis. En particulier le premier minimum d'interférence apparait comme un minimum dans le spectre, ce qui a pu être observé expérimentalement dans CO_2 [203–208], N_2O [99, 209] et N_2 [210]. Ces interférences à deux centres ont été modélisées par Lein [200] en adaptant au molécules diatomiques le modèle communément utilisé pour décrire la génération d'harmonique : l'approximation du champ fort (SFA).

J'ai confronté les prédictions de ce modèle analytique avec les résultats de simulations numériques à une et deux dimensions. J'ai notamment cherché à identifier les paramètres régissant le contraste de ces interférences, et les conditions où l'ont pouvait les observer avec le plus de netteté. En particulier j'ai étudié l'influence de l'orientation entre la molécule et le champ sur la position et la forme du minimum dans le spectre harmonique. Pour mieux comprendre les résultats donnés par le SFA moléculaires, j'ai voulu tester deux des principales approximations sous-jacentes à ce modèle : la combinaison linéaire d'orbitales atomiques (LCAO) et l'approximation des ondes planes (PWA). À cette fin, j'ai comparé la position du minimum d'interférences prédite par le SFA moléculaires à celle extraite

des simulations numériques. Ces résultats sont montrés en Figure S.4 : les prédictions du SFA moléculaire (en traits brisés jaunes) surestiment de quelques harmoniques la position du minimum extraite du spectre des simulations numériques "TDSE" (en points noirs). Une correction empirique impliquant un décalage des énergies du continuum de I_p (en traits brisés oranges) semble améliorer légèrement l'accord entre les deux. Cependant si l'on regarde les prédictions du même modèle, avec la PWA mais sans faire l'approximation LCAO (pointillés roses) on voit que, paradoxalement, les prédictions du modèles se dégradent. De même, si on garde l'approximation LCAO, mais qu'on s'affranchit de la PWA (pointillés bleus), le SFA moléculaire donne de très mauvais résultats. Lorsqu'on ne fait aucune des deux approximations, ni la PWA ni la LCAO, (en ligne pleine verte) on retrouve un très bon accord avec les simulations numériques. Cela indique que les erreurs causées par chacune de ces deux approximations se compensent presque parfaitement, donnant l'illusion d'un bon accord entre modèle analytique et simulations numériques. Néanmoins, aucune des deux approximations sous-jacente à ce modèle n'est véritablement justifiée Cela montre donc que les prédictions du SFA moléculaire, bien qu'apparemment raisonnables, sont en réalité à prendre avec beaucoup de précautions, surtout à des fin quantitatives.

S.5 Dynamiques vibroniques de molécules en champ intense

Lorsque les noyaux de la molécule considérée sont suffisamment légers, alors leur dynamique ne peut être négligée même durant les impulsions extrêmement courtes, de quelques femtosecondes, que nous avons considérées jusqu'alors. Récemment, ces dynamiques nucléaires femtosecondes ont été observées expérimentalement dans D_2 [222]. Sous l'effet d'une impulsion laser femtoseconde infrarouge, un paquet d'onde vibrationnel cohérent a pu être créé dans l'état électronique fondamental de D_2 dont les vibrations ont ensuite pu être mesurées. Toutefois, cette expérience pose la question du mécanisme physique ayant créé ce paquet d'onde. En effet, pour une molécule diatomique homonocléaire, le champ laser ne couple pas les différents niveaux vibrationnels d'un état électronique donné. L'absorption d'un ou plusieurs photons est donc interdite par symétrie.

Deux mécanismes ont été proposés pour expliquer ce processus d'excitation vibrationnelle [223] : le Bond-Softening qui peut se traduire de l'anglais par "affaiblissement de la liaison", et le Lochfraß qui veut dire "manger ou creuser un trou" en allemand. Ces mécanismes sont tous deux issus d'un modèle qui repose sur deux approximations : l'approximation adiabatique et l'approximation de Born-Oppenheimer (BO). L'approximation adiabatique suppose que les électrons s'adaptent instantanément aux variations du champ laser, et l'approximation de BO suppose qu'ils s'adaptent également instantanément aux mouvements des noyaux. Cette seconde hypothèse permet de factoriser la fonction d'onde en deux termes : une fonction d'onde électronique pour laquelle les coordonnées nucléaires ne sont plus des variables mais des paramètres, et une fonction d'onde nucléaire qui dépend uniquement des coordonnées nucléaires. Une partie des corrélations entre les degrés de liberté électroniques et nucléaires est donc négligée par cette approximation. Ceci est illustré en Figure S.5 (a) : les dynamiques purement nucléaires (i) ou électroniques (ii) sont parfaitement décrites par ce modèle. De plus, les corrélations (iii) qui impliquent des termes où le paquet d'onde quitte le fondamental, mais

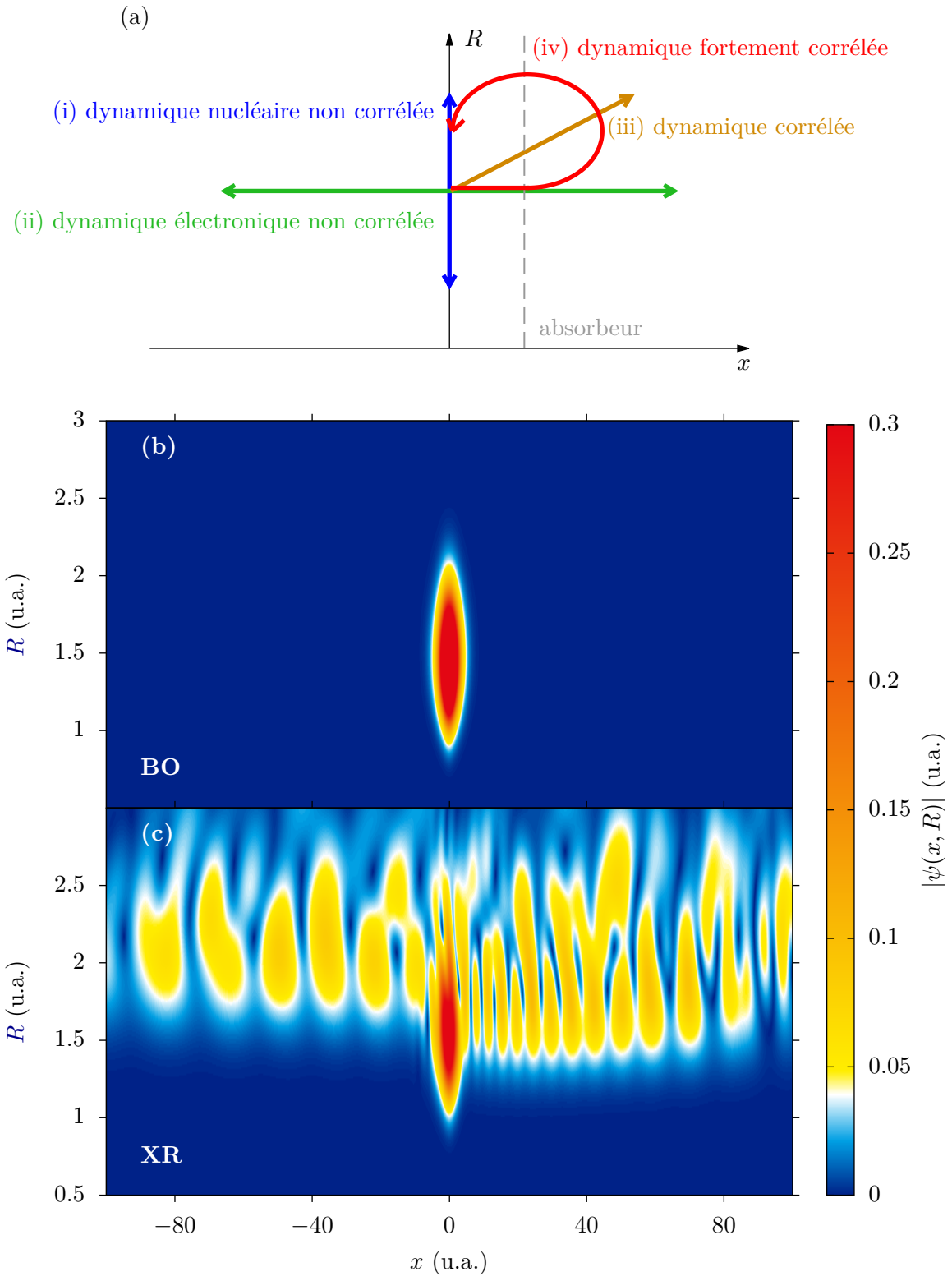

Figure S.5 *Corrélations vibroniques. (a) Représentation schématique des différentes contributions aux corrélations vibroniques affectant la dynamique. Module de la fonction d'onde au cours d'une impulsion laser de 8 cycles d'intensité* $I_{\mathrm{L}} = 3 \times 10^{14}$ W.cm^{-2} *et de phase* $\phi_{\mathrm{cep}} = \pi/2$ *calculé avec (b) une représentation BO de la fonction d'ode et avec (c) une simulation numérique entièrement corrélée (XR).*

ne revient plus interférer avec le reste de la dynamique seront également décrites. Ces corrélations sont actuellement absentes de la fonction d'onde BO en elle-même comme cela peut se voir en Figure S.5 (b) qui ne présente aucuns termes diagonaux, mais leur effet sur la dynamique nucléaire sera bien pris en compte par le modèle. Cependant, les corrélations (iv) impliquant des termes où le paquet d'onde quitte le fondamental et *revient* influer sur la dynamique à un temps ultérieur dans l'impulsion seront complètement absentes du modèle BO. Pour évaluer l'influence de ces corrélations j'ai comparé les résultats donnés par le modèle BO avec des simulations numériques entièrement corrélées dont une fonction d'onde est montrée sur Figure S.5 (c). Ces calculs montrent que ces corrélations vibroniques influent de façon non négligeable sur le paquet d'onde vibrationnel créé, non seulement sur l'amplitude et la phase de ses oscillations, mais également sur ses composantes vibrationnelles. Ceci dépend de la phase du laser incident (la dénommée *carrier-envelope phase*) et serait donc directement accessible expérimentalement.

S.6 Interaction de configuration dépendante du temps

Afin de pouvoir modéliser la dynamique en champ fort de systèmes plus complexes, avec plus de degrés de liberté, il est nécessaire de développer des méthodes numériques spécifiques. En effet, les méthodes couramment employées pour résoudre l'équation de Schrödinger dépendante du temps deviennent très couteuses, d'un point de vue des ressources numériques, dès lors que le système possède plus d'un électron. En collaboration avec le Laboratoire de Chimie Théorique à Sorbonne Université nous avons étudié la possibilité d'étendre les méthodes de chimie quantique, en particulier l'interaction de configuration, aux problèmes dépendants du temps. Au cours des dernières années ces méthodes ont été optimisées pour calculer les états liés de plusieurs types de systèmes, dont des molécules relativement grosses. Cependant la description des états du continuum reste encore un défi théorique pour ces méthodes, notamment pour celles qui utilisent des fonctions de bases gaussiennes. Or les états du continuum jouent un rôle central pour la modélisation de la génération d'harmoniques et pour les dynamiques électroniques en champ fort en général. Nous avons donc dans un premier temps analysé les performances de trois différents types de fonctions de bases, grille, B-splines et gaussiennes, pour représenter ces états du continuum et pour reproduire le spectre harmonique d'un système à un électron : H_2^+. Nous avons réalisé des simulations à une et à trois dimensions.

Un spectre harmonique est présenté en Figure S.6 (b), où on voit que les trois bases donnent des résultats très proches, tant que l'intensité du laser n'est pas trop élevée. En particulier le minimum d'interférence est parfaitement prédit dans les trois cas. Ceci est d'autant plus impressionnant pour les gaussiennes que cette base ne contient en tout que 24 fonctions, dont seulement 5 états d'énergie positive (correspondant au "continuum") dans la gamme d'énergie concernée. Le dipôle de recombinaison est également présenté en Figure S.6 (a). Le calcul de cette grandeur suppose de calculer avec précision à la fois le fondamental et les états d'énergie positive. Dans le cas des gaussiennes, comme il n'y a que 5 états dans la gamme d'énergie considérée, on ne peut le calculer que pour ces 5 valeurs. On observe néanmoins un bon accord des trois méthodes.

Le faible nombre de fonctions dans la base gaussienne est à la fois un avantage et un inconvénient. D'une part cela implique d'avoir très peu d'états d'énergie positive, et

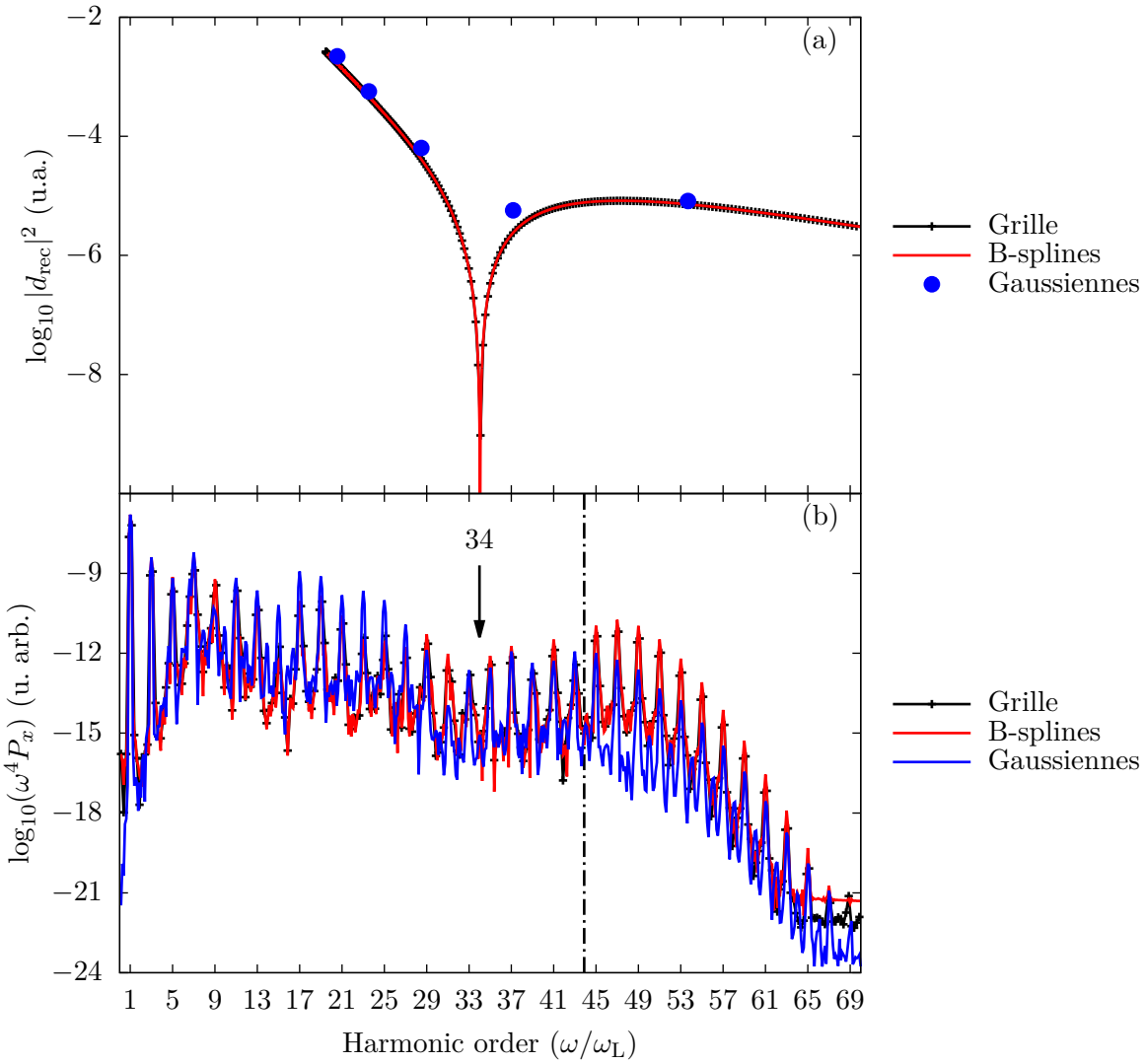

Figure S.6 *Interférences à deux centres dans un système modèle à une dimension représentant H_2^+ à $R = 1.8$ a.u. : (a) dipôle de recombinaison et (b) spectre harmonique pour un laser titane saphir à $I_{\mathrm{L}} = 2 \times 10^{14}$ W.cm^{-2}. La flèche indique la position du zéro du dipôle de recombinaison, les traits brisés indique la position du cut-off prédite par le modèle de en trois étapes.*

donc d'avoir très peu d'information sur le vrai continuum du système. En contrepartie cela permet de considérablement réduire les temps de calculs, et donc de modéliser des système plus gros. J'ai donc étudié la possibilité d'utiliser ces bases gaussiennes pour des systèmes à plusieurs électrons en utilisant la méthode d'interaction de configuration dépendante (TDCI) du temps développée en collaboration avec le LCT [235]. J'ai comparé les résultats donnés par cette méthode TDCI avec des résultats "exacts", à l'erreur numérique près, obtenus par des simulations sur des grilles bidimensionnelles pour des systèmes modèles à deux électrons, avec une dimension d'espace pour chaque électron, représentant le dihydrogène et l'hélium Les résultats sont prometteurs, surtout lorsque

l'on utilise des bases avec des gaussiennes multi-centrées comme conseillé dans [261].

S.7 Conclusion

Au cours de ma thèse j'ai étudié différents aspects de l'interaction d'atomes et de molécules avec des champs lasers intenses. J'ai développé des modèles analytiques pour comprendre les mécanismes derrière les processus corrélés et fortement non linéaires que l'on observe en physique des champs forts. La force de ces modèles approchés repose sur leur capacité à construire des interprétations physiques à ces phénomènes. Pour soutenir mes interprétations, j'ai combiné cette approche avec les résultats de simulations numériques précises réalisées pour des systèmes modèles. Ces systèmes simples présentent beaucoup d'avantages. D'un côté ils permettent de changer à volonté leurs propriétés fondamentales et donc de se concentrer sur un ou plusieurs problèmes physiques particuliers. De plus leur dimension réduite permet de réaliser un traitement numérique approfondi. En pratique j'ai résolu l'équation de Schrödinger dépendante du temps et l'équation de Schrödinger indépendante du temps pour extraire autant d'informations que possible de la fonction d'onde dépendante du temps. J'ai également mis à profit ces simulations numériques pour tester les approximations sous-jacentes au modèles analytiques.

Plus précisément j'ai étudié les dynamiques électroniques et nucléaires d'atomes et de molécules diatomiques en présence d'impulsions lasers infrarouges femtosecondes. Je me suis d'abord concentrée sur les processus électroniques fortement non linéaires qui sont déclenchés par de telles impulsions lasers comme la génération d'harmoniques, dont j'ai étudié la première étape, c'est à dire l'ionisation tunnel, au chapitre III. Pour un laser infrarouge, les variations temporelles du champ électrique sont très lentes comparées aux échelles de temps électroniques. On peut donc déduire le rendement d'ionisation tunnel directement du problème en champ statique. J'ai calculé ce rendement d'ionisation pour différents systèmes modèles atomiques et moléculaires. J'ai montré l'importance de l'effet Stark, à la fois pour une description quantitative et qualitative de l'ionisation tunnel, et j'ai obtenu une expression analytique dans l'approximation quasi-classique qui prend cet effet en compte. J'ai également montré que l'effet Stark représente la contribution dominante à l'anisotropie de l'émission tunnel pour des molécules polaires. J'ai démontré à quel point le calcul précis de l'effet Stark était important, tout particulièrement pour des molécules très polarisables pour lesquelles la théorie des perturbations au second ordre ne permet pas d'obtenir un résultat satisfaisant. De plus, j'ai analysé les raisons à la bases des désaccords entre formule analytique et simulations numériques. J'ai pu désintriquer les erreurs induites par les différentes approximations utilisées dans le développement analytique, et j'ai trouvé que certaines approximations n'étaient en réalité pas justifiées, mais qu'une compensation d'erreur permettant d'obtenir néanmoins des résultats raisonnables.

Une des applications directes de la physique des champs fort est la spectroscopie de hautes harmoniques (HHS), où la lumière émise par la génération d'harmoniques est analysée pour extraire des informations structurelles et dynamiques sur le système émetteur. Dans le cas particulier des interférences à deux centres dans des molécules diatomiques homonucléaires j'ai cherché à comprendre, au chapitre IV, les conditions dans lesquelles cet interférences pouvaient présenter le meilleur contraste, et donc être plus facilement mesurables expérimentalement. J'ai complété le développement analytique réalisé pour

des molécules alignées avec le laser [129]. Je lui ai donné un fondement plus rigoureux en définissant un paramètre, i.e. la distance internucléaire R, pour le développement de type Taylor du SFA moléculaire. J'ai aussi obtenu l'expression complète du spectre harmonique au premier ordre de ce développement et je l'ai étendu au cas d'une orientation quelconque de la molécule et du champ électrique. J'ai évalué les prédictions de ce modèle analytique en les confrontant à des simulations numériques pour différents systèmes. En comparant les résultats obtenus à une et à deux dimensions, j'ai conclu que l'étalement transverse du paquet d'onde électronique au cours de la propagation après l'ionisation tunnel avait en réalité un impact sur les interférences à deux centres. Finalement, j'ai réalisé une analyse détaillée de l'erreur induite par les deux approximations sous-jacentes au SFA moléculaire : la LCAO et la PWA. J'ai démontré que chacune de ces deux approximations induisait en réalité des erreurs non négligeables mais qui ont la chance de se compenser, ce qui permet au SFA moléculaire de prédire la position du minimum d'interférence avec une précision raisonnable.

Pour des molécules très légères comme H_2 l'approximation qui consiste à geler les degrés de liberté nucléaires n'est en réalité pas valable, même pour des impulsions très courtes de quelques femtosecondes. Au chapitre V, j'ai étudié les couplages entre degrés de liberté électroniques et nucléaires pour des systèmes modèles représentant des molécules diatomiques homonucléaires. J'ai évalué la capacité du modèle BO à modéliser ces couplages à travers l'introduction d'un rendement d'ionisation et d'un effet Stark dépendant de la distance internucléaire R. J'ai montré la nécessité de considérer les deux mécanismes du Lochfraß et du Bond-Softening comme un tout cohérent, et non comme deux mécanismes indépendants et décorrélés comme cela est souvent fait [222, 223, 227]. J'ai également trouvé des conditions pour pouvoir observer expérimentalement l'effet de couplages vibroniques sur la dynamique nucléaire qui ne sont pas pris en compte par ce modèle de BO, et qui vont donc plus loin que ce qui peut être décrit par le Lochfraß et le Bond-Softening. Finalement, j'ai proposé un modèle analytique basé sur l'approche Wigner-Weisskopf pour donner un cadre plus rigoureux au mécanisme du Bond-Softening. Cela m'a permis d'obtenir un terme correctif qui pourrait tenir compte d'une partie des corrélations négligées par le modèle de BO, mais qui reste à évaluer. Ce modèle pourrait être étendu au cas du Lochfraß, mais cela reste à faire.

Dans un dernier chapitre, j'ai étudié différentes méthodes numériques pour résoudre la TDSE de systèmes plus gros et plus complexes pour lesquels les corrélations électroniques jouent un rôle dans la dynamique en champ fort. En collaboration avec le LCT, nous avons étudié trois différentes bases pour représenter la fonction d'onde dépendante du temps. Nous avons montré que les grilles et les B-splines étaient toutes deux capables de reproduire efficacement la dynamique électronique de H_2^+ tant à une qu'à trois dimensions. Cependant les ressources numériques importantes qu'elles nécessitent les rendent difficiles à envisager pour de plus gros systèmes. Nous avons trouvé que les gaussiennes étaient en réalité capables, tant que l'intensité du laser n'est pas trop élevée, de reproduire le spectre harmonique de H_2^+, y compris des effets fins tels que les interférences à deux centres et les résonances de types hyper-Raman. Ceci était d'autant plus inattendu qu'elle ne permettent d'obtenir que quelques états d'énergie positive, ce qui les empêche de décrire correctement des phénomènes tels que l'ionisation au dessus du seuil. En mettant à profit les faibles ressources numériques nécessaires au gaussiennes, nous avons développé un TDCI basées sur des gaussiennes, pour résoudre la TDSE de systèmes poly-électroniques.

J'ai testé les performances de cette méthode en la comparant à des simulations numériques "exactes", à l'erreur numérique près, réalisées sur des grilles bidimensionnelles. J'ai trouvé que cette méthode était prometteuse pour le calcul de spectres harmonique de grosses molécules.

La complète compréhension des phénomènes physiques en champs fort n'est pas pour demain. J'espère avoir réussi à montrer que des petits modèles simples, combinés à des raisonnements analytiques approchés, pouvaient apporter une aide précieuse dans ce domaine. Personne ne peut savoir d'où viendront les prochaines idées révolutionnaires, mais je suis convaincue que ces systèmes modèles intuitifs aident en tout cas à alimenter notre imagination de physiciens.

Bibliography

[1] **P. Mulser & D. Bauer**. *High power laser-matter interaction*. No. 238 in Springer tracts in modern physics (Springer, Heidelberg) (2010). OCLC: 699733993. 1, 205

[2] **D. Strickland & G. Mourou**. Compression of amplified chirped optical pulses. *Optics Communications* **56**, 219 (1985). URL http://dx.doi.org/10.1016/0030-4018(85)90120-8. 1, 205

[3] **A. H. Zewail**. Laser Femtochemistry. *Science* **242**, 1645 (1988). URL http://dx.doi.org/10.1126/science.242.4886.1645. 1, 205

[4] **A. H. Zewail**. Femtochemistry: Atomic-Scale Dynamics of the Chemical Bond. *J. Phys. Chem. A* **104**, 5660 (2000). URL http://dx.doi.org/10.1021/jp001460h. 1, 205

[5] **P. Agostini, F. Fabre, G. Mainfray, G. Petite & N. K. Rahman**. Free-Free Transitions Following Six-Photon Ionization of Xenon Atoms. *Physical Review Letters* **42**, 1127 (1979). URL http://dx.doi.org/10.1103/PhysRevLett.42.1127. 1, 205

[6] **A. L'Huillier, L. A. Lompre, G. Mainfray & C. Manus**. Multiply Charged Ions Formed by Multiphoton Absorption Processes in the Continuum. *Phys. Rev. Lett.* **48**, 1814 (1982). URL http://dx.doi.org/10.1103/PhysRevLett.48.1814. 1, 205

[7] **A. McPherson, G. Gibson, H. Jara, U. Johann, T. S. Luk, I. A. McIntyre, K. Boyer & C. K. Rhodes**. Studies of multiphoton production of vacuum-ultraviolet radiation in the rare gases. *J. Opt. Soc. Am. B, JOSAB* **4**, 595 (1987). URL http://dx.doi.org/10.1364/JOSAB.4.000595. 1, 21, 206

[8] **M. Ferray, A. L'Huillier, X. F. Li, L. A. Lompre, G. Mainfray & C. Manus**. Multiple-harmonic conversion of 1064 nm radiation in rare gases. *J. Phys. B: At. Mol. Opt. Phys.* **21**, L31 (1988). URL http://dx.doi.org/10.1088/0953-4075/21/3/001. 1, 21, 206

[9] **M. Y. Kuchiev**. Atomic antenna. *JETP Lett.* **45**, 404 (1987). URL http://www.jetpletters.ac.ru/ps/1241/article_18763.shtml. 1, 26, 75, 206, 209

[10] **J. L. Krause, K. J. Schafer & K. C. Kulander**. High-order harmonic generation from atoms and ions in the high intensity regime. *Physical Review Letters* **68**,

3535 (1992). URL http://dx.doi.org/10.1103/PhysRevLett.68.3535. 26, 150, 209

[11] **M. Lewenstein, P. Balcou, M. Y. Ivanov, A. L'huillier & P. B. Corkum**. Theory of high-harmonic generation by low-frequency laser fields. *Phys. Rev. A* **49**, 2117 (1994). URL http://journals.aps.org/pra/abstract/10.1103/PhysRevA.49.2117. 1, 21, 32, 34, 36, 66, 75, 154, 158, 159, 206, 209

[12] **M. Hentschel, R. Kienberger, C. Spielmann, G. A. Reider, N. Milosevic, T. Brabec, P. Corkum, U. Heinzmann, M. Drescher & F. Krausz**. Attosecond metrology. *Nature* **414**, 509 (2001). URL http://dx.doi.org/10.1038/35107000. 1, 5, 67, 206

[13] **R. López-Martens et al.** Amplitude and Phase Control of Attosecond Light Pulses. *Physical Review Letters* **94** (2005). URL http://dx.doi.org/10.1103/PhysRevLett.94.033001.

[14] **D. H. Ko, K. T. Kim, J. Park, J.-h. Lee & C. H. Nam**. Attosecond chirp compensation over broadband high-order harmonics to generate near transform-limited 63 as pulses. *New J. Phys.* **12**, 063008 (2010). URL http://dx.doi.org/10.1088/1367-2630/12/6/063008. 1, 206

[15] **T. Gaumnitz, A. Jain, Y. Pertot, M. Huppert, I. Jordan, F. Ardana-Lamas & H. J. Wörner**. Streaking of 43-attosecond soft-X-ray pulses generated by a passively CEP-stable mid-infrared driver. *Opt. Express, OE* **25**, 27506 (2017). URL http://dx.doi.org/10.1364/OE.25.027506. 1, 206

[16] **A. Scrinzi, M. Y. Ivanov, R. Kienberger & D. M. Villeneuve**. Attosecond physics. *J. Phys. B: At. Mol. Opt. Phys.* **39**, R1 (2006). URL http://dx.doi.org/10.1088/0953-4075/39/1/R01. 2, 206

[17] **P. B. Corkum & F. Krausz**. Attosecond science. *Nature Physics* **3**, 381 (2007). URL http://dx.doi.org/10.1038/nphys620.

[18] **F. Calegari, G. Sansone, S. Stagira, C. Vozzi & M. Nisoli**. Advances in attosecond science. *J. Phys. B: At. Mol. Opt. Phys.* **49**, 062001 (2016). URL http://dx.doi.org/10.1088/0953-4075/49/6/062001.

[19] **F. Krausz**. The birth of attosecond physics and its coming of age. *Phys. Scr.* **91**, 063011 (2016). URL http://dx.doi.org/10.1088/0031-8949/91/6/063011. 2, 206

[20] **M. Schultze et al.** Delay in Photoemission. *Science* **328**, 1658 (2010). URL http://dx.doi.org/10.1126/science.1189401. 2, 206

[21] **K. Klünder et al.** Probing Single-Photon Ionization on the Attosecond Time Scale. *Physical Review Letters* **106** (2011). URL http://dx.doi.org/10.1103/PhysRevLett.106.143002. 2, 206

[22] **S. Beaulieu et al.** Attosecond-resolved photoionization of chiral molecules. *Science* **358**, 1288 (2017). URL http://dx.doi.org/10.1126/science.aao5624. 2, 20, 206

[23] **A. L. Cavalieri et al.** Attosecond spectroscopy in condensed matter. *Nature* **449**, 1029 (2007). URL http://dx.doi.org/10.1038/nature06229. 2, 206

[24] **S. Neppl, R. Ernstorfer, E. M. Bothschafter, A. L. Cavalieri, D. Menzel, J. V. Barth, F. Krausz, R. Kienberger & P. Feulner**. Attosecond Time-Resolved Photoemission from Core and Valence States of Magnesium. *Physical Review Letters* **109** (2012). URL http://dx.doi.org/10.1103/PhysRevLett.109.087401. 2, 206

[25] **M. Drescher, M. Hentschel, R. Kienberger, M. Uiberacker, V. Yakovlev, A. Scrinzi, T. Westerwalbesloh, U. Kleineberg, U. Heinzmann & F. Krausz**. Time-resolved atomic inner-shell spectroscopy. *Nature* **419**, 803 (2002). URL http://dx.doi.org/10.1038/nature01143. 2, 206

[26] **M. Uiberacker et al.** Attosecond real-time observation of electron tunnelling in atoms. *Nature* **446**, 627 (2007). URL http://dx.doi.org/10.1038/nature05648. 2, 206

[27] **D. M. Villeneuve, P. Hockett, M. J. J. Vrakking & H. Niikura**. Coherent imaging of an attosecond electron wave packet. *Science* **356**, 1150 (2017). URL http://dx.doi.org/10.1126/science.aam8393. 2, 20, 206

[28] **F. Calegari et al.** Ultrafast electron dynamics in phenylalanine initiated by attosecond pulses. *Science* **346**, 336 (2014). URL http://dx.doi.org/10.1126/science.1254061. 2, 206

[29] **M. Schultze et al.** Attosecond band-gap dynamics in silicon. *Science* **346**, 1348 (2014). URL http://dx.doi.org/10.1126/science.1260311. 2, 20, 30, 206

[30] **S. Neppl et al.** Direct observation of electron propagation and dielectric screening on the atomic length scale. *Nature* **517**, 342 (2015). URL http://dx.doi.org/10.1038/nature14094.

[31] **C. Lemell, S. Neppl, G. Wachter, K. Tőkési, R. Ernstorfer, P. Feulner, R. Kienberger & J. Burgdörfer**. Real-time observation of collective excitations in photoemission. *Physical Review B* **91** (2015). URL http://dx.doi.org/10.1103/PhysRevB.91.241101. 2, 206

[32] **V. Gruson et al.** Attosecond dynamics through a fano resonance: Monitoring the birth of a photoelectron. *Science* **354**, 734 (2016). URL http://science.sciencemag.org/content/354/6313/734.abstract. 2, 5, 20, 67, 206

[33] **A. Kaldun et al.** Observing the ultrafast buildup of a Fano resonance in the time domain. *Science* **354**, 738 (2016). URL http://dx.doi.org/10.1126/science.aah6972. 2, 20, 206

[34] **A. S. Alnaser et al.** Subfemtosecond steering of hydrocarbon deprotonation through superposition of vibrational modes. *Nature Communications* **5**, 3800 (2014). URL http://dx.doi.org/10.1038/ncomms4800. 2, 206

[35] **P. Hommelhoff & M. F. Kling**. *Attosecond Nanophysics: From Basic Science to Applications* (Wiley-VCH) (2015). 2, 206

[36] **M. F. Ciappina et al.** Attosecond physics at the nanoscale. *Rep. Prog. Phys.* **80**, 054401 (2017). URL http://dx.doi.org/10.1088/1361-6633/aa574e.

[37] **M. I. Stockman et al.** Roadmap on plasmonics. *J. Opt.* **20**, 043001 (2018). URL http://dx.doi.org/10.1088/2040-8986/aaa114. 2, 206

[38] **F. Süßmann et al.** Field propagation-induced directionality of carrier-envelope phase-controlled photoemission from nanospheres. *Nature Communications* **6**, 7944 (2015). URL http://dx.doi.org/10.1038/ncomms8944. 2, 206

[39] **B. Förg et al.** Attosecond nanoscale near-field sampling. *Nature Communications* **7**, 11717 (2016). URL http://dx.doi.org/10.1038/ncomms11717.

[40] **L. Seiffert et al.** Attosecond chronoscopy of electron scattering in dielectric nanoparticles. *Nature Physics* **13**, 766 (2017). URL http://dx.doi.org/10.1038/nphys4129. 2, 206

[41] **S. Haessler, J. Caillat & P. Salières**. Self-probing of molecules with high harmonic generation. *J. Phys. B: At. Mol. Opt. Phys.* **44**, 203001 (2011). URL http://dx.doi.org/10.1088/0953-4075/44/20/203001. 2, 20, 206

[42] **M. Lein**. Attosecond Probing of Vibrational Dynamics with High-Harmonic Generation. *Physical Review Letters* **94** (2005). URL http://dx.doi.org/10.1103/PhysRevLett.94.053004. 2, 206

[43] **S. Baker, J. S. Robinson, C. A. Haworth, H. Teng, R. A. Smith, C. C. Chirilă, M. Lein, J. W. G. Tisch & J. P. Marangos**. Probing Proton Dynamics in Molecules on an Attosecond Time Scale. *Science* **312**, 424 (2006). URL http://dx.doi.org/10.1126/science.1123904.

[44] **S. Baker et al.** Dynamic Two-Center Interference in High-Order Harmonic Generation from Molecules with Attosecond Nuclear Motion. *Phys. Rev. Lett.* **101**, 053901 (2008). URL http://dx.doi.org/10.1103/PhysRevLett.101.053901. 2, 206

[45] **S. Haessler et al.** Attosecond imaging of molecular electronic wavepackets. *Nat. Phys.* **6**, 200 (2010). URL http://dx.doi.org/10.1038/nphys1511. 2, 20, 206

[46] **J. Itatani, J. Levesque, D. Zeidler, H. Niikura, H. Pépin, J. C. Kieffer, P. B. Corkum & D. M. Villeneuve**. Tomographic imaging of molecular orbitals. *Nature* **432**, 867 (2004). URL http://dx.doi.org/10.1038/nature03183. 2, 164, 206

[47] **C. Vozzi, M. Negro, F. Calegari, G. Sansone, M. Nisoli, S. D. Silvestri & S. Stagira**. Generalized molecular orbital tomography. *Nature Physics* **7**, 822 (2011). URL http://dx.doi.org/10.1038/nphys2029.

[48] **P. Salières, A. Maquet, S. Haessler, J. Caillat & R. Taïeb**. Imaging orbitals with attosecond and Ångström resolutions: toward attochemistry? *Rep. Prog. Phys.* **75**, 062401 (2012). URL http://dx.doi.org/10.1088/0034-4885/75/6/062401. 2, 206

[49] **A. D. Shiner, B. E. Schmidt, C. Trallero-Herrero, H. J. Wörner, S. Patchkovskii, P. B. Corkum, J.-C. Kieffer, F. Légaré & D. M. Villeneuve**. Probing collective multi-electron dynamics in xenon with high-harmonic spectroscopy. *Nature Physics* **7**, 464 (2011). URL http://dx.doi.org/10.1038/nphys1940. 2, 149, 206

[50] **O. Smirnova, Y. Mairesse, S. Patchkovskii, N. Dudovich, D. Villeneuve, P. Corkum & M. Y. Ivanov**. High harmonic interferometry of multi-electron dynamics in molecules. *Nature* **460**, 972 (2009). URL http://dx.doi.org/10.1038/nature08253. 2, 5, 20, 150, 164, 206

[51] **R. E. F. Silva, I. V. Blinov, A. N. Rubtsov, O. Smirnova & M. Ivanov**. High-harmonic spectroscopy of ultrafast many-body dynamics in strongly correlated systems. *Nature Photonics* **12**, 266 (2018). URL http://dx.doi.org/10.1038/s41566-018-0129-0. 2, 206

[52] **O. Smirnova, Y. Mairesse & S. Patchkovskii**. Opportunities for chiral discrimination using high harmonic generation in tailored laser fields. *J. Phys. B: At. Mol. Opt. Phys.* **48**, 234005 (2015). URL http://dx.doi.org/10.1088/0953-4075/48/23/234005. 2

[53] **D. Ayuso, P. Decleva, S. Patchkovskii & O. Smirnova**. Chiral dichroism in bi-elliptical high-order harmonic generation. *J. Phys. B: At. Mol. Opt. Phys.* **51**, 06LT01 (2018). URL http://dx.doi.org/10.1088/1361-6455/aaae5e.

[54] **D. Ayuso, P. Decleva, S. Patchkovskii & O. Smirnova**. Strong-field control and enhancement of chiral response in bi-elliptical high-order harmonic generation: an analytical model. *J. Phys. B: At. Mol. Opt. Phys.* **51**, 124002 (2018). URL http://dx.doi.org/10.1088/1361-6455/aabc95. 2

[55] **R. Cireasa et al.** Probing molecular chirality on a sub-femtosecond timescale. *Nature Physics* **11**, 654 (2015). URL http://dx.doi.org/10.1038/nphys3369. 2, 206

[56] **D. Baykusheva, M. S. Ahsan, N. Lin & H. J. Wörner**. Bicircular High-Harmonic Spectroscopy Reveals Dynamical Symmetries of Atoms and Molecules. *Physical Review Letters* **116** (2016). URL http://dx.doi.org/10.1103/PhysRevLett.116.123001. 2, 206

[57] **S. Choi & B. Sundaram**. Bose-Einstein condensate as a nonlinear Ramsey interferometer operating beyond the Heisenberg limit. *Physical Review A* **77** (2008). URL http://dx.doi.org/10.1103/PhysRevA.77.053613. 5

[58] **A. Widera, O. Mandel, M. Greiner, S. Kreim, T. W. Hänsch & I. Bloch**. Entanglement Interferometry for Precision Measurement of Atomic Scattering Properties. *Physical Review Letters* **92** (2004). URL http://dx.doi.org/10.1103/PhysRevLett.92.160406. 5

[59] **C. D. Lin, A.-T. Le, Z. Chen, T. Morishita & R. Lucchese**. Strong-field rescattering physics—self-imaging of a molecule by its own electrons. *J. Phys. B: At. Mol. Opt. Phys.* **43**, 122001 (2010). URL http://dx.doi.org/10.1088/0953-4075/43/12/122001. 5, 20, 75

[60] **C. Zhai, X. Zhu, P. Lan, F. Wang, L. He, W. Shi, Y. Li, M. Li, Q. Zhang & P. Lu**. Diffractive molecular-orbital tomography. *Phys. Rev. A* **95**, 033420 (2017). URL http://dx.doi.org/10.1103/PhysRevA.95.033420. 5

[61] **M. Vacher, R. Gaillac, A. Maquet, R. Taïeb & J. Caillat**. Transition dynamics in two-photon ionisation. *Journal of Optics* **19**, 114011 (2017). URL http://dx.doi.org/10.1088/2040-8986/aa8f56. 5

[62] **Y.-L. Cao et al.** MFN1 structures reveal nucleotide-triggered dimerization critical for mitochondrial fusion. *Nature* **542**, 372 (2017). URL http://dx.doi.org/10.1038/nature21077. 5

[63] **Y. Yuan et al.** Cryo-EM structures of MERS-CoV and SARS-CoV spike glycoproteins reveal the dynamic receptor binding domains. *Nature Comm.* **8**, 15092 (2017). URL http://dx.doi.org/10.1038/ncomms15092.

[64] **H. N. Chapman et al.** Femtosecond diffractive imaging with a soft-X-ray free-electron laser. *Nature Phys.* **2**, 839 (2006). URL http://dx.doi.org/10.1038/nphys461.

[65] **J. Kern et al.** Simultaneous Femtosecond X-ray Spectroscopy and Diffraction of Photosystem II at Room Temperature. *Science* **340**, 491 (2013). URL http://dx.doi.org/10.1126/science.1234273.

[66] **T. Ekeberg et al.** Three-Dimensional Reconstruction of the Giant Mimivirus Particle with an X-Ray Free-Electron Laser. *Phys. Rev. Lett.* **114** (2015). URL http://dx.doi.org/10.1103/PhysRevLett.114.098102. 5

[67] **A. Ashkin**. Acceleration and trapping of particles by radiation pressure. *Physical review letters* **24**, 156 (1970). 5

[68] **S. Bennetts, C.-C. Chen, B. Pasquiou & F. Schreck**. Steady-State Magneto-Optical Trap with 100-Fold Improved Phase-Space Density. *Phys. Rev. Lett.* **119** (2017). URL http://dx.doi.org/10.1103/PhysRevLett.119.223202. 5

[69] **D. Meschede, T. Udem & T. Esslinger**. *Exploring the World with the Laser* (Springer) (2018). 5

[70] **T. Peyronel, O. Firstenberg, Q.-Y. Liang, S. Hofferberth, A. V. Gorshkov, T. Pohl, M. D. Lukin & V. Vuletić**. Quantum nonlinear optics with single photons enabled by strongly interacting atoms. *Nature* **488**, 57 (2012). URL http://dx.doi.org/10.1038/nature11361. 5

[71] **C. Sayrin et al.** Real-time quantum feedback prepares and stabilizes photon number states. *Nature* **477**, 73 (2011). URL http://dx.doi.org/10.1038/nature10376. 5

[72] **M. M. Kash, V. A. Sautenkov, A. S. Zibrov, L. Hollberg, G. R. Welch, M. D. Lukin, Y. Rostovtsev, E. S. Fry & M. O. Scully**. Ultraslow group velocity and enhanced nonlinear optical effects in a coherently driven hot atomic gas. *Physical Review Letters* **82**, 5229 (1999). 5

[73] **D. F. Phillips, A. Fleischhauer, A. Mair, R. L. Walsworth & M. D. Lukin**. Storage of Light in Atomic Vapor. *Physical Review Letters* **86**, 783 (2001). URL http://dx.doi.org/10.1103/PhysRevLett.86.783.

[74] **P. Vernaz-Gris, K. Huang, M. Cao, A. S. Sheremet & J. Laurat**. Highly-efficient quantum memory for polarization qubits in a spatially-multiplexed cold atomic ensemble. *Nature Communications* **9**, 363 (2018). URL http://dx.doi.org/10.1038/s41467-017-02775-8. 5

[75] **H. G. Muller**. Reconstruction of attosecond harmonic beating by interference of two-photon transitions. *Appl Phys B* **74**, s17 (2002). URL http://dx.doi.org/10.1007/s00340-002-0894-8. 5

[76] **Y. Mairesse & F. Quéré**. Frequency-resolved optical gating for complete reconstruction of attosecond bursts. *Physical Review A* **71** (2005). URL http://dx.doi.org/10.1103/PhysRevA.71.011401.

[77] **V. S. Yakovlev, F. Bammer & A. Scrinzi**. Attosecond streaking measurements. *Journal of Modern Optics* **52**, 395 (2005). URL http://dx.doi.org/10.1080/09500340412331283642. 5

[78] **J.-M. Raimond**. Atoms and photons. http://www.lkb.upmc.fr/cqed/teaching/teachingjmr/ (2016). 6, 62, 142

[79] **J. D. Jackson**. *Classical Electrodynamics* (John Wiley & Sons, Inc.), third edn. (1998). 7

[80] **E. Cormier & P. Lambropoulos**. Optimal gauge and gauge invariance in non-perturbative time-dependent calculation of above-threshold ionization. *J. Phys. B: At. Mol. Opt. Phys.* **29**, 1667 (1996). URL http://dx.doi.org/10.1088/0953-4075/29/9/013. 10

[81] **M. Baghery, U. Saalmann & J. M. Rost**. Essential Conditions for Dynamic Interference. *Physical Review Letters* **118** (2017). URL http://dx.doi.org/10.1103/PhysRevLett.118.143202. 10

[82] **K. J. Schafer & K. C. Kulander**. Energy analysis of time-dependent wave functions: Application to above-threshold ionization. *Phys. Rev. A* **42**, 5794 (1990). URL http://dx.doi.org/10.1103/PhysRevA.42.5794. 11, 68, 71

[83] **J. Crank, P. Nicolson & D. R. Hartree**. A practical method for numerical evaluation of solutions of partial differential equations of the heat-conduction type. *Math. Proc. Cambridge* **43**, 50 (1947). URL http://dx.doi.org/10.1017/S0305004100023197. 11, 47, 152, 153

[84] **C. C. Chirilă & M. Lein**. Strong-field approximation for harmonic generation in diatomic molecules. *Phys. Rev. A* **73**, 023410 (2006). URL http://dx.doi.org/10.1103/PhysRevA.73.023410. 12, 35, 37, 39, 98, 117, 120, 164

[85] **A. Galstyan, O. Chuluunbaatar, A. Hamido, Y. V. Popov, F. Mota-Furtado, P. F. O'Mahony, N. Janssens, F. Catoire & B. Piraux**. Reformulation of the strong-field approximation for light-matter interactions. *Physical Review A* **93** (2016). URL http://dx.doi.org/10.1103/PhysRevA.93.023422. 12

[86] **C. Cohen-Tannoudji, B. Diu & F. Laloë**. *Mécanique quantique*, vol. 2 (Hermann) (1973). 12, 208

[87] **K. W. D. Ledingham & R. P. Singhal**. High intensity laser mass spectrometry — a review. *International Journal of Mass Spectrometry and Ion Processes* **163**, 149 (1997). URL http://dx.doi.org/10.1016/S0168-1176(97)00015-3. 17

[88] **K. Kimura**. Development of laser photoelectron spectroscopy based on resonantly enhanced multiphoton ionization. *Journal of Electron Spectroscopy and Related Phenomena* **100**, 273 (1999). URL http://dx.doi.org/10.1016/S0368-2048(99)00051-1.

[89] **K. Kimura**. Very-High-Resolution Laser Photoelectron Spectroscopy of Molecules. In *Very High Resolution Photoelectron Spectroscopy*, Lecture Notes in Physics, pp. 215–239 (Springer, Berlin, Heidelberg) (2007). URL http://dx.doi.org/10.1007/3-540-68133-7_8. 17

[90] **P. Salières, A. L'Huillier & M. Lewenstein**. Coherence Control of High-Order Harmonics. *Phys. Rev. Lett.* **74**, 3776 (1995). URL http://dx.doi.org/10.1103/PhysRevLett.74.3776. 20, 21, 30

[91] **P. B. Corkum**. Plasma perspective on strong field multiphoton ionization. *Phys. Rev. Lett.* **71**, 1994 (1993). URL http://dx.doi.org/10.1103/PhysRevLett.71.1994. 20, 26, 30, 75, 154, 158, 159, 209

[92] **K. J. Schafer, B. Yang, L. F. DiMauro & K. C. Kulander**. Above threshold ionization beyond the high harmonic cutoff. *Physical Review Letters* **70**, 1599 (1993). URL http://dx.doi.org/10.1103/PhysRevLett.70.1599. 20, 26

[93] **D. B. Milošević, G. G. Paulus, D. Bauer & W. Becker**. Above-threshold ionization by few-cycle pulses. *J. Phys. B: At. Mol. Opt. Phys.* **39**, R203 (2006). URL http://dx.doi.org/10.1088/0953-4075/39/14/R01. 20

[94] **A. Becker, R. Dörner & R. Moshammer**. Multiple fragmentation of atoms in femtosecond laser pulses. *J. Phys. B: At. Mol. Opt. Phys.* **38**, S753 (2005). URL http://dx.doi.org/10.1088/0953-4075/38/9/021. 20, 75

[95] **P. Antoine, A. L'Huillier & M. Lewenstein**. Attosecond Pulse Trains Using High–Order Harmonics. *Phys. Rev. Lett.* **77**, 1234 (1996). URL http://dx.doi.org/10.1103/PhysRevLett.77.1234. 20, 21, 65

[96] **P. Salières, A. L'Huillier, P. Antoine & M. Lewenstein**. Study of the spatial and temporal coherence of high order harmonics. *arXiv:quant-ph/9710060* (1997). URL http://arxiv.org/abs/quant-ph/9710060. ArXiv: quant-ph/9710060. 21, 30, 65, 75

[97] **Y. Mairesse**. Attosecond Synchronization of High-Harmonic Soft X-rays. *Science* **302**, 1540 (2003). URL http://dx.doi.org/10.1126/science.1090277. 20

[98] **P. M. Kraus, A. Rupenyan & H. J. Wörner**. High-Harmonic Spectroscopy of Oriented OCS Molecules: Emission of Even and Odd Harmonics. *Phys. Rev. Lett.* **109** (2012). URL http://dx.doi.org/10.1103/PhysRevLett.109.233903. 20, 32

[99] **A. Rupenyan, P. Kraus, J. Schneider & H. Wörner**. High-harmonic spectroscopy of isoelectronic molecules: Wavelength scaling of electronic-structure and multielectron effects. *Phys. Rev. A* **87** (2013). URL http://dx.doi.org/10.1103/PhysRevA.87.033409. 20, 76, 77, 97, 212

[100] **S. Ghimire, A. D. DiChiara, E. Sistrunk, P. Agostini, L. F. DiMauro & D. A. Reis**. Observation of high-order harmonic generation in a bulk crystal. *Nature Physics* **7**, 138 (2011). URL http://dx.doi.org/10.1038/nphys1847. 21

[101] **S. Ghimire, G. Ndabashimiye, A. D. DiChiara, E. Sistrunk, M. I. Stockman, Pierre Agostini, L. F. DiMauro & D. A. Reis**. Strong-field and attosecond physics in solids. *J. Phys. B: At. Mol. Opt. Phys.* **47**, 204030 (2014). URL http://dx.doi.org/10.1088/0953-4075/47/20/204030.

[102] **G. Ndabashimiye, S. Ghimire, M. Wu, D. A. Browne, K. J. Schafer, M. B. Gaarde & D. A. Reis**. Solid-state harmonics beyond the atomic limit. *Nature* **534**, 520 (2016). URL http://dx.doi.org/10.1038/nature17660. 21

[103] **M. Sivis, M. Taucer, G. Vampa, K. Johnston, A. Staudte, A. Y. Naumov, D. M. Villeneuve, C. Ropers & P. B. Corkum**. Tailored semiconductors for high-harmonic optoelectronics. *Science* **357**, 303 (2017). URL http://dx.doi.org/10.1126/science.aan2395. 21

[104] **G. Vampa et al.** Plasmon-enhanced high-harmonic generation from silicon. *Nature Physics* **13**, 659 (2017). URL http://dx.doi.org/10.1038/nphys4087. 21

[105] **A. D. DiChiara, E. Sistrunk, T. A. Miller, P. Agostini & L. F. DiMauro**. An investigation of harmonic generation in liquid media with a mid-infrared laser. *Opt. Express, OE* **17**, 20959 (2009). URL http://dx.doi.org/10.1364/OE.17.020959. 21

[106] **A. L'Huillier, K. J. Schafer & K. C. Kulander**. Theoretical aspects of intense field harmonic generation. *J. Phys. B: At. Mol. Opt. Phys.* **24**, 3315 (1991). URL http://dx.doi.org/10.1088/0953-4075/24/15/004. 21, 30

[107] **I. P. Christov, M. M. Murnane & H. C. Kapteyn**. Generation and propagation of attosecond x-ray pulses in gaseous media. *Physical Review A* **57**, R2285 (1998). URL http://dx.doi.org/10.1103/PhysRevA.57.R2285. 21

[108] **M. B. Gaarde, J. L. Tate & K. J. Schafer**. Macroscopic aspects of attosecond pulse generation. *J. Phys. B: At. Mol. Opt. Phys.* **41**, 132001 (2008). URL http://dx.doi.org/10.1088/0953-4075/41/13/132001. 21, 30

[109] **X. F. Li, A. L'Huillier, M. Ferray, L. A. Lompre & G. Mainfray**. Multiple-harmonic generation in rare gases at high laser intensity. *Physical Review A* **39**, 5751 (1989). URL http://dx.doi.org/10.1103/PhysRevA.39.5751. 21

[110] **G. Farkas & C. Tóth**. Proposal for attosecond light pulse generation using laser induced multiple-harmonic conversion processes in rare gases. *Physics Letters A* **168**, 447 (1992). URL http://dx.doi.org/10.1016/0375-9601(92)90534-S.

[111] **J. J. Macklin, J. D. Kmetec & C. L. Gordon**. High-order harmonic generation using intense femtosecond pulses. *Physical Review Letters* **70**, 766 (1993). URL http://dx.doi.org/10.1103/PhysRevLett.70.766. 21

[112] **P. M. Paul, E. S. Toma, P. Breger, G. Mullot, F. Augé, P. Balcou, H. G. Muller & P. Agostini**. Observation of a Train of Attosecond Pulses from High Harmonic Generation. *Science* **292**, 1689 (2001). URL http://dx.doi.org/10.1126/science.1059413. 21, 67

[113] **L. V. Keldysh**. Ionization in the field of a strong electromagnetic wave. *Sov. Phys. JETP* **20**, 1307 (1965). URL http://jetp.ac.ru/cgi-bin/dn/e_020_05_1307.pdf. 21, 75, 207, 210

[114] **M. V. Frolov, N. L. Manakov, A. M. Popov, O. V. Tikhonova, E. A. Volkova, A. A. Silaev, N. V. Vvedenskii & A. F. Starace**. Analytic theory of high-order-harmonic generation by an intense few-cycle laser pulse. *Physical Review A* **85** (2012). URL http://dx.doi.org/10.1103/PhysRevA.85.033416. 24, 142

[115] **M. Y. Ivanov, T. Brabec & N. Burnett**. Coulomb corrections and polarization effects in high-intensity high-harmonic emission. *Physical Review A* **54**, 742 (1996). URL http://dx.doi.org/10.1103/PhysRevA.54.742. 28

[116] **M. B. Gaarde, F. Salin, E. Constant, P. Balcou, K. J. Schafer, K. C. Kulander & A. L'Huillier**. Spatiotemporal separation of high harmonic radiation into two quantum path components. *Phys. Rev. A* **59**, 1367 (1999). URL https://journals.aps.org/pra/abstract/10.1103/PhysRevA.59.1367. 30

[117] **M. Bellini, C. Lyngtextbackslasha a, A. Tozzi, M. B. Gaarde, T. W. Hänsch, A. L'Huillier & C.-G. Wahlström**. Temporal coherence of ultrashort high-order harmonic pulses. *Phys. Rev. Lett.* **81**, 297 (1998). 30

[118] **L. Medišauskas, J. Wragg, H. van der Hart & M. Y. Ivanov**. Generating Isolated Elliptically Polarized Attosecond Pulses Using Bichromatic Counterrotating Circularly Polarized Laser Fields. *Physical Review Letters* **115** (2015). URL http://dx.doi.org/10.1103/PhysRevLett.115.153001. 32

[119] **C. A. Mancuso et al.** Strong-field ionization with two-color circularly polarized laser fields. *Physical Review A* **91** (2015). URL http://dx.doi.org/10.1103/PhysRevA.91.031402.

[120] **D. B. Milošević**. High-order harmonic generation by a bichromatic elliptically polarized field: conservation of angular momentum. *J. Phys. B: At. Mol. Opt. Phys.* **48**, 171001 (2015). URL http://dx.doi.org/10.1088/0953-4075/48/17/171001.

[121] **A. Fleischer, O. Kfir, T. Diskin, P. Sidorenko & O. Cohen**. Spin angular momentum and tunable polarization in high-harmonic generation. *Nature Photonics* **8**, 543 (2014). URL http://dx.doi.org/10.1038/nphoton.2014.108. 32

[122] **M. Ivanov & K. Rzążewski**. Are Free-free Transitions a Good Basis for Nonlinear Optics? *J. Mod. Opt.* **39**, 2377 (1992). URL http://dx.doi.org/10.1080/09500349214552421. 34

[123] **C. M. Bender & S. A. Orszag**. *Advanced mathematical methods for scientists and engineers* (International Student Edition) (1978). 35, 183

[124] **J. J. Duistermaat**. *Fourier Integral Operators* (Springer) (2011). 35

[125] **E. H. Hauge & J. A. Stovneng**. Tunneling times: a critical review. *Rev. Mod. Phys.* **61**, 20 (1989). 36

[126] **A. Maquet, J. Caillat & R. Taïeb**. Attosecond delays in photoionization: time and quantum mechanics. *J. Phys. B: At. Mol. Opt. Phys.* **47**, 204004 (2014). URL http://dx.doi.org/10.1088/0953-4075/47/20/204004. 36

[127] **L. E. Chipperfield**. *High Harmonic Generation with Few-Cycle Pulses*. Ph.D. thesis, Imperial College, University of London (2007). 37

[128] **C. F. d. M. Faria**. High-order harmonic generation in diatomic molecules: A quantum-orbit analysis of the interference patterns. *Phys. Rev. A* **76**, 043407 (2007). URL http://dx.doi.org/10.1103/PhysRevA.76.043407. 37, 39, 97, 98, 101

[129] **F. Risoud**. *Theoretical study of attosecond dynamics in atoms and molecules using high-order harmonic generation as a self-probe*. Ph.D. thesis, Université Pierre et Marie Curie, Paris VI (2016). 37, 65, 98, 101, 104, 106, 107, 108, 109, 110, 112, 115, 117, 118, 120, 180, 218

[130] **C. C. Chirilă & M. Lein**. Assessing different forms of the strong-field approximation for harmonic generation in molecules. *Journal of Modern Optics* **54**, 1039 (2007). URL http://dx.doi.org/10.1080/09500340601043447. 38

[131] **J. C. Baggesen & L. B. Madsen**. On the dipole, velocity and acceleration forms in high-order harmonic generation from a single atom or molecule. *J. Phys. B: At. Mol. Opt. Phys.* **44**, 115601 (2011). URL http://dx.doi.org/10.1088/0953-4075/44/11/115601. 38, 62

[132] **L. D. Landau & E. M. Lifshitz**. *Quantum mechanics: non-relativistic theory*, vol. 3 of *Course of Theoretical Physics* (Pergamon Press), 2 edn. (1965). 42, 76, 77, 78, 79, 90, 91, 92, 210

[133] **Q. Su & J. H. Eberly**. Model atom for multiphoton physics. *Phys. Rev. A* **44**, 5997 (1991). URL http://dx.doi.org/10.1103/PhysRevA.44.5997. 42

[134] **M. Reed & B. Simon**. *IV: Analysis of Operators*, vol. 4 (Elsevier) (1978). 43

[135] **C. Cohen-Tannoudji, B. Diu & F. Laloë**. *Mécanique quantique*, vol. 1 (Hermann) (1973). 45, 61, 146, 191

[136] **W. H. Press, S. A. Teukolsky, W. T. Vetterling & B. P. Flannery**. *Numerical Recipes in Fortran 77*, vol. 1 of *Fortran Numerical Recipes* (Cambridge University Press), 2 edn. (1992). 48, 72

[137] **W. H. Press, S. A. Teukolsky, W. T. Vetterling & B. P. Flannery**. *Numerical Recipes in Fortran 90*, vol. 2 of *Fortran Numerical Recipes* (Cambridge University Press), 2 edn. (1996). 48, 50, 77, 91, 152, 153, 157

[138] **R. Campargue**. Progress in overexpanded supersonic jets and skimmed molecular beams in free-jet zones of silence. *J. Phys. Chem.* **88**, 4466 (1984). URL http://dx.doi.org/10.1021/j150664a004. 49

[139] **U. V. Riss & H.-D. Meyer**. *J. Chem. Phys.* **105**, 1409 (1996). 49

[140] **F. He, C. Ruiz & A. Becker**. Absorbing boundaries in numerical solutions of the time-dependent Schrödinger equation on a grid using exterior complex scaling. *Phys. Rev. A* **75** (2007). URL http://dx.doi.org/10.1103/PhysRevA.75.053407.

[141] **L. Tao, W. Vanroose, B. Reps, T. N. Rescigno & C. W. McCurdy**. Long-time solution of the time-dependent Schrödinger equation for an atom in an electromagnetic field using complex coordinate contours. *Phys. Rev. A* **80** (2009). URL http://dx.doi.org/10.1103/PhysRevA.80.063419. 150

[142] **A. Scrinzi**. Infinite-range exterior complex scaling as a perfect absorber in time-dependent problems. *Phys. Rev. A* **81**, 053845 (2010). URL http://dx.doi.org/10.1103/PhysRevA.81.053845. 49, 180

[143] **J. L. Krause, K. J. Schafer & K. C. Kulander**. Calculation of photoemission from atoms subject to intense laser fields. *Phys. Rev. A* **45**, 4998 (1992). 49, 152, 169

[144] **B. N. Parlett**. *The Symmetric Eigenvalue Problem*. No. 20 in Classics in applied mathematics (Society for Industrial and Applied Mathematics) (1998). 50

[145] **J. C. Butcher**. *Numerical methods for ordinary differential equations* (John Wiley & Sons, Inc.) (2016). 51

[146] **N. Moiseyev**. *Non-Hermitian quantum mechanics* (Cambridge University Press, Cambridge) (2011). OCLC: 707100447. 52, 60

[147] **C. H. Maier, L. S. Cederbaum & W. Domcke**. A spherical-box approach to resonances. *J. Phys. B: At. Mol. Phys.* **13**, L119 (1980). URL http://dx.doi.org/10.1088/0022-3700/13/4/001. 53

[148] **V. A. Mandelshtam, T. R. Ravuri & H. S. Taylor**. Calculation of the density of resonance states using the stabilization method. *Physical Review Letters* **70**, 1932 (1993). URL http://dx.doi.org/10.1103/PhysRevLett.70.1932. 53

[149] **H. Bachau, E. Cormier, P. Decleva, J. E. Hansen & F. Martín**. Applications of B -splines in atomic and molecular physics. *Rep. Prog. Phys.* **64**, 1815 (2001). URL http://dx.doi.org/10.1088/0034-4885/64/12/205. 53, 150, 152

[150] **M. Frigo & S. G. Johnson**. The Design and Implementation of FFTW3. *Proceedings of the IEEE* **93**, 216 (2005). URL http://dx.doi.org/10.1109/JPROC.2004.840301. 57

[151] **K. Burnett, V. C. Reed, J. Cooper & P. L. Knight**. Calculation of the background emitted during high-harmonic generation. *Phys. Rev. A* **45**, 3347 (1992). 61

[152] **A. D. Bandrauk, S. Chelkowski, D. J. Diestler, J. Manz & K.-J. Yuan**. Quantum simulation of high-order harmonic spectra of the hydrogen atom. *Physical Review A* **79** (2009). URL http://dx.doi.org/10.1103/PhysRevA.79.023403. 62

[153] **K. Varjú et al.** Frequency chirp of harmonic and attosecond pulses. *Journal of Modern Optics* **52**, 379 (2005). URL http://dx.doi.org/10.1080/09500340412331301542. 62, 109

[154] **Y. Nomura et al.** Attosecond phase locking of harmonics emitted from laser-produced plasmas. *Nature Physics* **5**, 124 (2009). URL http://dx.doi.org/10.1038/nphys1155.

[155] **G. Doumy, J. Wheeler, C. Roedig, R. Chirla, P. Agostini & L. F. DiMauro**. Attosecond Synchronization of High-Order Harmonics from Midinfrared Drivers. *Physical Review Letters* **102** (2009). URL http://dx.doi.org/10.1103/PhysRevLett.102.093002. 109

[156] **M. C. Kohler, C. H. Keitel & K. Z. Hatsagortsyan**. Attochirp-free high-order harmonic generation. *Opt. Express, OE* **19**, 4411 (2011). URL http://dx.doi.org/10.1364/OE.19.004411. 62

[157] **F. Risoud, C. Lévêque, M. Labeye, J. Caillat, A. Maquet, P. Salières, R. Taïeb & T. Shaaran**. Laser-induced blurring of molecular structure information in high harmonic spectroscopy. *Scientific Reports* **7**, 17302 (2017). URL http://dx.doi.org/10.1038/s41598-017-17416-9. 65, 98, 107, 108, 109, 117

[158] **P. Kruit & F. H. Read**. Magnetic field paralleliser for 2π electron-spectrometer and electron-image magnifier. *J. Phys. E: Sci. Instrum.* **16**, 313 (1983). URL http://dx.doi.org/10.1088/0022-3735/16/4/016. 67

[159] **T. Tsuboi, E. Y. Xu, Y. K. Bae & K. T. Gillen**. Magnetic bottle electron spectrometer using permanent magnets. *Review of Scientific Instruments* **59**, 1357 (1988). URL http://dx.doi.org/10.1063/1.1139722.

[160] **I. Jordan, A. Jain, T. Gaumnitz, J. Ma & H. J. Wörner**. Photoelectron spectrometer for liquid and gas-phase attosecond spectroscopy with field-free and magnetic bottle operation modes. *Review of Scientific Instruments* **89**, 053103 (2018). URL http://dx.doi.org/10.1063/1.5011657. 67

[161] **M. A. Khalal et al.** Multielectron spectroscopy: energy levels of K n + and Rb n + ions (n = 2, 3, 4). *J. Phys. B: At. Mol. Opt. Phys.* **50**, 225003 (2017). URL http://dx.doi.org/10.1088/1361-6455/aa90d6. 67

[162] **P. Lablanquie et al.** Multi-electron coincidence spectroscopy: Triple Auger decay of Ar 2p and 2s holes. *Journal of Electron Spectroscopy and Related Phenomena* **220**, 125 (2017). URL http://dx.doi.org/10.1016/j.elspec.2017.04.003. 67

[163] **R. Forbes, A. E. Boguslavskiy, I. Wilkinson, J. G. Underwood & A. Stolow**. Excited state wavepacket dynamics in NO2 probed by strong-field ionization. *The Journal of Chemical Physics* **147**, 054305 (2017). URL http://dx.doi.org/10.1063/1.4996461. 67

[164] **M. Nisoli, P. Decleva, F. Calegari, A. Palacios & F. Martín**. Attosecond Electron Dynamics in Molecules. *Chem. Rev.* **117**, 10760 (2017). URL http://dx.doi.org/10.1021/acs.chemrev.6b00453. 149, 150

[165] **D. Kiesewetter, R. R. Jones, A. Camper, S. B. Schoun, P. Agostini & L. F. DiMauro**. Probing electronic binding potentials with attosecond photoelectron wavepackets. *Nature Physics* **14**, 68 (2018). URL http://dx.doi.org/10.1038/nphys4279. 67

[166] **S. Petretti, Y. V. Vanne, A. Saenz, A. Castro & P. Decleva**. Alignment-Dependent Ionization of $textbackslashmathbf{N_2}$, $textbackslashmathbf{O_2}$, and $textbackslashmathrm{CO_2}$ in Intense Laser Fields. *Phys. Rev. Lett.* **104**, 223001 (2010). URL http://dx.doi.org/10.1103/PhysRevLett.104.223001. 75

[167] **M. Abu-samha & L. B. Madsen**. Photoelectron angular distributions from polar molecules probed by intense femtosecond lasers. *Physical Review A* **82** (2010). URL http://dx.doi.org/10.1103/PhysRevA.82.043413. 76, 77, 90

[168] **M. Awasthi, Y. V. Vanne, A. Saenz & P. Decleva**. Single-active-electron approximation for describing molecules in ultrashort laser pulses and its application to molecular hydrogen. *Physical Review A* **77** (2008). URL http://dx.doi.org/10.1103/PhysRevA.77.063403. 75

[169] **D. B. Milošević**. Strong-field approximation for ionization of a diatomic molecule by a strong laser field. *Physical Review A* **74** (2006). URL http://dx.doi.org/10.1103/PhysRevA.74.063404. 75

[170] **T. Kjeldsen & L. Madsen**. Strong-field ionization of diatomic molecules and companion atoms: Strong-field approximation and tunneling theory including nuclear motion. *Physical Review A* **71** (2005). URL http://dx.doi.org/10.1103/PhysRevA.71.023411. 75

[171] **J. Svensmark, O. I. Tolstikhin & L. B. Madsen**. Coulomb and dipole effects in tunneling ionization of molecules including nuclear motion. *Physical Review A* **91** (2015). URL http://dx.doi.org/10.1103/PhysRevA.91.013408. 75, 76

[172] **S. V Popruzhenko**. Keldysh theory of strong field ionization: history, applications, difficulties and perspectives. *Journal of Physics B: Atomic, Molecular and Optical Physics* **47**, 204001 (2014). URL http://dx.doi.org/10.1088/0953-4075/47/20/204001. 75

[173] **V. S. Popov**. Tunnel and multiphoton ionization of atoms and ions in a strong laser field (Keldysh theory). *Physics-Uspekhi* **47**, 855 (2004). URL http://dx.doi.org/10.1070/PU2004v047n09ABEH001812. 75

[174] **A. M. Perelomov, V. S. Popov & M. V. Terent'ev**. Ionization of atoms in an alternating electric field. *Sov. Phys. JETP* **23**, 924 (1966). URL http://www.jetp.ac.ru/cgi-bin/dn/e_023_05_0924.pdf. 75, 94, 95, 210

[175] **A. M. Perelomov, V. S. Popov & M. V. Terent'ev**. Ionization of atoms in an alternating electric field: II. *Sov. Phys. JETP* **24**, 207 (1967). URL http://www.jetp.ac.ru/cgi-bin/dn/e_024_01_0207.pdf.

[176] **A. M. Perelomov & V. S. Popov**. IONIZATION OF ATOMS IN AN ALTERNATING ELECTRICAL FIELD. Ill. *Soviet Physics JETP* **25** (1967). URL http://www.jetp.ac.ru/cgi-bin/dn/e_025_02_0336.pdf. 75

[177] **M. V. Ammosov, N. B. Delone & V. P. Krainov**. Tunnel Ionization Of Complex Atoms And Atomic Ions In Electromagnetic Field. vol. 0664, pp. 138–141 (1986). URL http://dx.doi.org/10.1117/12.938695. 75, 210

[178] **X. M. Tong, Z. X. Zhao & C. D. Lin**. Theory of molecular tunneling ionization. *Physical Review A* **66** (2002). URL http://dx.doi.org/10.1103/PhysRevA.66.033402. 75, 210

[179] **Z. X. Zhao, X. M. Tong & C. D. Lin**. Alignment-dependent ionization probability of molecules in a double-pulse laser field. *Phys. Rev. A* **67**, 043404 (2003). URL http://dx.doi.org/10.1103/PhysRevA.67.043404. 75, 210

[180] **T. K. Kjeldsen & L. B. Madsen**. Strong-field ionization of N 2 : length and velocity gauge strong-field approximation and tunnelling theory. *J. Phys. B: At. Mol. Opt. Phys.* **37**, 2033 (2004). URL http://dx.doi.org/10.1088/0953-4075/37/10/003. 75, 210

[181] **O. I. Tolstikhin, T. Morishita & S. Watanabe**. Adiabatic theory of ionization of atoms by intense laser pulses: One-dimensional zero-range-potential model. *Phys. Rev. A* **81**, 033415 (2010). URL http://dx.doi.org/10.1103/PhysRevA.81.033415. 75

[182] **O. I. Tolstikhin & T. Morishita**. Adiabatic theory of ionization by intense laser pulses: Finite-range potentials. *Physical Review A* **86** (2012). URL http://dx.doi.org/10.1103/PhysRevA.86.043417. 75

[183] **Y. H. Lai et al.** Experimental investigation of strong-field-ionization theories for laser fields from visible to midinfrared frequencies. *Phys. Rev. A* **96**, 063417 (2017). URL http://dx.doi.org/10.1103/PhysRevA.96.063417. 76, 81

[184] **B. M. Smirnov & M. I. Chibisov**. The breaking up of atomic particles by an electric field and by electron collisions. *Sov. Phys. JETP* **22**, 585 (1966). URL http://www.jetp.ac.ru/cgi-bin/dn/e_022_03_0585.pdf. 76, 77, 78, 79, 91, 92, 94, 95, 210

[185] **P. A. Batishchev, O. I. Tolstikhin & T. Morishita**. Atomic Siegert states in an electric field: Transverse momentum distribution of the ionized electrons. *Physical Review A* **82** (2010). URL http://dx.doi.org/10.1103/PhysRevA.82.023416. 76, 91

[186] **V. H. Trinh, O. I. Tolstikhin, L. B. Madsen & T. Morishita**. First-order correction terms in the weak-field asymptotic theory of tunneling ionization. *Physical Review A* **87** (2013). URL http://dx.doi.org/10.1103/PhysRevA.87.043426.

[187] **S. Ohgoda, O. I. Tolstikhin & T. Morishita**. Photoionization of hydrogen in a strong static electric field. *Phys. Rev. A* **95**, 043417 (2017). URL http://dx.doi.org/10.1103/PhysRevA.95.043417. 76

[188] **O. I. Tolstikhin, T. Morishita & L. B. Madsen**. Theory of tunneling ionization of molecules: Weak-field asymptotics including dipole effects. *Physical Review A* **84** (2011). URL http://dx.doi.org/10.1103/PhysRevA.84.053423. 76, 88

[189] **L. Hamonou, T. Morishita & O. I. Tolstikhin**. Molecular Siegert states in an electric field. *Physical Review A* **86** (2012). URL http://dx.doi.org/10.1103/PhysRevA.86.013412.

[190] **V. H. Trinh, V. N. T. Pham, O. I. Tolstikhin & T. Morishita**. Weak-field asymptotic theory of tunneling ionization including the first-order correction terms: Application to molecules. *Physical Review A* **91** (2015). URL http://dx.doi.org/10.1103/PhysRevA.91.063410. 76

[191] **O. I. Tolstikhin & T. Morishita**. Weak-field versus Born-Oppenheimer asymptotics in the theory of tunneling ionization of molecules. *Phys. Rev. A* **95**, 033410 (2017). URL http://dx.doi.org/10.1103/PhysRevA.95.033410. 76

[192] **N. L. Manakov, M. V. Frolov, A. F. Starace & I. I. Fabrikant**. Interaction of laser radiation with a negative ion in the presence of a strong static electric field.

Journal of Physics B: Atomic, Molecular and Optical Physics **33**, R141 (2000). URL http://iopscience.iop.org/0953-4075/33/15/201. 76

[193] **S. V. Borzunov, N. L. Manakov, A. F. Starace & M. V. Frolov**. Decay of a negative molecular ion in a constant electric field. *Journal of Experimental and Theoretical Physics* **112**, 725 (2011). URL http://dx.doi.org/10.1134/S1063776111030095. 76

[194] **B. Zhang, J. Yuan & Z. Zhao**. Dynamic Core Polarization in Strong-Field Ionization of CO Molecules. *Physical Review Letters* **111** (2013). URL http://dx.doi.org/10.1103/PhysRevLett.111.163001. 76

[195] **V. P. Majety & A. Scrinzi**. Static field ionization rates for multi-electron atoms and small molecules. *Journal of Physics B: Atomic, Molecular and Optical Physics* **48**, 245603 (2015). URL http://dx.doi.org/10.1088/0953-4075/48/24/245603. 76

[196] **V.-H. Hoang, S.-F. Zhao, V.-H. Le & A.-T. Le**. Influence of permanent dipole and dynamic core-electron polarization on tunneling ionization of polar molecules. *Physical Review A* **95** (2017). URL http://dx.doi.org/10.1103/PhysRevA.95.023407. 76, 80, 90

[197] **L. Holmegaard et al.** Photoelectron angular distributions from strong-field ionization of oriented molecules. *Nature Physics* **6**, 428 (2010). URL http://dx.doi.org/10.1038/nphys1666. 76, 77, 80, 90

[198] **H. Li, D. Ray, S. De, I. Znakovskaya, W. Cao, G. Laurent, Z. Wang, M. F. Kling, A. T. Le & C. L. Cocke**. Orientation dependence of the ionization of CO and NO in an intense femtosecond two-color laser field. *Physical Review A* **84** (2011). URL http://dx.doi.org/10.1103/PhysRevA.84.043429. 76, 80, 90

[199] **M. Labeye, F. Risoud, A. Maquet, J. Caillat & R. Taieb**. Tunnel ionization of atoms and molecules: How accurate are the weak-field asymptotic formulas? *Journal of Physics B: Atomic, Molecular and Optical Physics* (2018). URL http://dx.doi.org/10.1088/1361-6455/aab6de. 76

[200] **M. Lein, N. Hay, R. Velotta, J. P. Marangos & P. L. Knight**. Interference effects in high-order harmonic generation with molecules. *Phys. Rev. A* **66**, 023805 (2002). URL http://dx.doi.org/10.1103/PhysRevA.66.023805. 97, 106, 107, 108, 109, 115, 117, 119, 151, 164, 212

[201] **Y. Chen & B. Zhang**. Tracing the structure of asymmetric molecules from high-order harmonic generation. *Physical Review A* **84** (2011). URL http://dx.doi.org/10.1103/PhysRevA.84.053402. 97

[202] **B. Zhang, Y. Chen, X. Jiang & X. Sun**. Identifying the interference effect in different harmonic-emission channels from oriented asymmetric molecules. *Physical Review A* **88** (2013). URL http://dx.doi.org/10.1103/PhysRevA.88.053428. 97

[203] **A.-T. Le, X.-M. Tong & C. D. Lin**. Evidence of two-center interference in high-order harmonic generation from C O 2. *Physical Review A* **73** (2006). URL http://dx.doi.org/10.1103/PhysRevA.73.041402. 97, 212

[204] **N. Wagner, X. Zhou, R. Lock, W. Li, A. Wüest, M. Murnane & H. Kapteyn**. Extracting the phase of high-order harmonic emission from a molecule using transient alignment in mixed samples. *Physical Review A* **76** (2007). URL http://dx.doi.org/10.1103/PhysRevA.76.061403. 97

[205] **W. Boutu et al.** Coherent control of attosecond emission from aligned molecules. *Nature Physics* **4**, 545 (2008). URL http://dx.doi.org/10.1038/nphys964. 97

[206] **X. Zhou, R. Lock, W. Li, N. Wagner, M. M. Murnane & H. C. Kapteyn**. Molecular Recollision Interferometry in High Harmonic Generation. *Physical Review Letters* **100** (2008). URL http://dx.doi.org/10.1103/PhysRevLett.100.073902.

[207] **T. Kanai, E. J. Takahashi, Y. Nabekawa & K. Midorikawa**. Observing molecular structures by using high-order harmonic generation in mixed gases. *Physical Review A* **77** (2008). URL http://dx.doi.org/10.1103/PhysRevA.77.041402.

[208] **R. Torres et al.** Revealing molecular structure and dynamics through high-order harmonic generation driven by mid-IR fields. *Physical Review A* **81** (2010). URL http://dx.doi.org/10.1103/PhysRevA.81.051802. 97, 212

[209] **A. Rupenyan, P. Kraus, J. Schneider & H. Wörner**. Quantum interference and multielectron effects in high-harmonic spectra of polar molecules. *Physical Review A* **87** (2013). URL http://dx.doi.org/10.1103/PhysRevA.87.031401. 97, 212

[210] **B. K. McFarland, J. P. Farrell, P. H. Bucksbaum & M. Gühr**. High-order harmonic phase in molecular nitrogen. *Physical Review A* **80** (2009). URL http://dx.doi.org/10.1103/PhysRevA.80.033412. 97, 212

[211] **M. Lein, N. Hay, R. Velotta, J. P. Marangos & P. L. Knight**. Role of the Intramolecular Phase in High-Harmonic Generation. *Physical Review Letters* **88** (2002). URL http://dx.doi.org/10.1103/PhysRevLett.88.183903. 97, 152, 163, 165, 166

[212] **E. V. van der Zwan & M. Lein**. Two-center interference and ellipticity in high-order harmonic generation from H 2 +. *Physical Review A* **82** (2010). URL http://dx.doi.org/10.1103/PhysRevA.82.033405. 97

[213] **O. Smirnova, M. Spanner & M. Ivanov**. Anatomy of strong field ionization II: to dress or not to dress? *Journal of Modern Optics* **54**, 1019 (2007). URL http://dx.doi.org/10.1080/09500340701234656. 98

[214] **M. D. Śpiewanowski, A. Etches & L. B. Madsen**. High-order-harmonic generation from field-distorted orbitals. *Physical Review A* **87** (2013). URL http://dx.doi.org/10.1103/PhysRevA.87.043424. 110

[215] **M. D. Śpiewanowski & L. B. Madsen**. Field-induced orbital distortion in high-order-harmonic generation from aligned and oriented molecules within adiabatic strong-field approximation. *Physical Review A* **89** (2014). URL http://dx.doi.org/10.1103/PhysRevA.89.043407. 98, 110

[216] **G. L. Kamta & A. D. Bandrauk**. Three-dimensional time-profile analysis of high-order harmonic generation in molecules: Nuclear interferences in H 2 +. *Physical Review A* **71** (2005). URL http://dx.doi.org/10.1103/PhysRevA.71.053407. 107, 117, 164

[217] **Y.-C. Han & L. B. Madsen**. Internuclear-distance dependence of the role of excited states in high-order-harmonic generation of $H_2 textasciicircum +$. *Phys. Rev. A* **87**, 043404 (2013). URL http://dx.doi.org/10.1103/PhysRevA.87.043404. 107, 117, 164

[218] **S. Odžak & D. B. Milošević**. Molecular high-order harmonic generation: analysis of a destructive interference condition. *J. Phys. B: At. Mol. Opt. Phys.* **42**, 071001 (2009). URL http://dx.doi.org/10.1088/0953-4075/42/7/071001.

[219] **S. Odžak & D. B. Milošević**. Interference effects in high-order harmonic generation by homonuclear diatomic molecules. *Physical Review A* **79** (2009). URL http://dx.doi.org/10.1103/PhysRevA.79.023414. 107

[220] **J. H. Posthumus**. The dynamics of small molecules in intense laser fields. *Rep. Prog. Phys.* **67**, 623 (2004). URL http://dx.doi.org/10.1088/0034-4885/67/5/R01. 121

[221] **H. Ibrahim, C. Lefebvre, A. D. Bandrauk, A. Staudte & F. Légaré**. H 2 : the benchmark molecule for ultrafast science and technologies. *J. Phys. B: At. Mol. Opt. Phys.* **51**, 042002 (2018). URL http://dx.doi.org/10.1088/1361-6455/aaa192. 121, 128

[222] **T. Ergler, B. Feuerstein, A. Rudenko, K. Zrost, C. D. Schröter, R. Moshammer & J. Ullrich**. Quantum-Phase Resolved Mapping of Ground-State Vibrational D_2 Wave Packets via Selective Depletion in Intense Laser Pulses. *Phys. Rev. Lett.* **97**, 103004 (2006). URL http://dx.doi.org/10.1103/PhysRevLett.97.103004. 121, 122, 123, 124, 128, 130, 132, 148, 180, 213, 218

[223] **E. Goll, G. Wunner & A. Saenz**. Formation of Ground-State Vibrational Wave Packets in Intense Ultrashort Laser Pulses. *Phys. Rev. Lett.* **97**, 103003 (2006). URL http://dx.doi.org/10.1103/PhysRevLett.97.103003. 121, 122, 123, 128, 130, 132, 148, 180, 213, 218

[224] **A. Saenz**. Enhanced ionization of molecular hydrogen in very strong fields. *Phys. Rev. A* **61**, 051402 (2000). URL http://dx.doi.org/10.1103/PhysRevA.61.051402. 121, 128

[225] **A. Saenz**. Behavior of molecular hydrogen exposed to strong dc, ac, or low-frequency laser fields. II. Comparison of ab initio and Ammosov-Delone-Krainov

rates. *Physical Review A* **66** (2002). URL http://dx.doi.org/10.1103/PhysRevA.66.063408. 121

[226] **L. Fang & G. N. Gibson**. Comparison of R-Dependent Ionization and Bond-Softening as Mechanisms for Creating Vibrational Coherence in Hot Molecules. p. JThD4 (OSA) (2009). URL http://dx.doi.org/10.1364/CLEO.2009.JThD4. 122, 123

[227] **L. Fang & G. N. Gibson**. Strong-field induced vibrational coherence in the ground electronic state of hot I2. pp. 1–2 (IEEE) (2008). URL http://dx.doi.org/10.1109/CLEO.2008.4552398. 122, 124, 128, 130, 132, 148, 180, 218

[228] **A. Palacios, J. L. Sanz-Vicario & F. Martín**. Theoretical methods for attosecond electron and nuclear dynamics: applications to the H 2 molecule. *J. Phys. B: At. Mol. Opt. Phys.* **48**, 242001 (2015). URL http://dx.doi.org/10.1088/0953-4075/48/24/242001. 149

[229] **D. A. Telnov & S.-I. Chu**. textitAb initio study of the orientation effects in multiphoton ionization and high-order harmonic generation from the ground and excited electronic states of H 2 +. *Physical Review A* **76** (2007). URL http://dx.doi.org/10.1103/PhysRevA.76.043412.

[230] **Y.-M. Lee, J.-S. Wu, T.-F. Jiang & Y.-S. Chen**. Parallel solver for the three-dimensional Cartesian-grid-based time-dependent Schrtextbackslash"odinger equation and its applications in laser-$textbackslashmathrm{H_2}textasciicircum+$ interaction studies. *Phys. Rev. A* **77**, 013414 (2008). URL http://dx.doi.org/10.1103/PhysRevA.77.013414.

[231] **C. B. Madsen & L. B. Madsen**. Theoretical studies of high-order harmonic generation: Effects of symmetry, degeneracy, and orientation. *Phys. Rev. A* **76**, 043419 (2007). URL http://dx.doi.org/10.1103/PhysRevA.76.043419. 149, 164

[232] **S. Pabst & R. Santra**. Strong-Field Many-Body Physics and the Giant Enhancement in the High-Harmonic Spectrum of Xenon. *Physical Review Letters* **111** (2013). URL http://dx.doi.org/10.1103/PhysRevLett.111.233005. 149

[233] **A. Chacón, M. F. Ciappina & M. Lewenstein**. Signatures of double-electron re-combination in high-order harmonic generation driven by spatially inhomogeneous fields. *arXiv:1511.01792 [physics]* (2015). URL http://arxiv.org/abs/1511.01792. ArXiv: 1511.01792. 149

[234] **B. D. Bruner et al.** Multidimensional high harmonic spectroscopy of polyatomic molecules: detecting sub-cycle laser-driven hole dynamics upon ionization in strong mid-IR laser fields. *Faraday Discuss.* **194**, 369 (2016). URL http://dx.doi.org/10.1039/C6FD00130K. 150

[235] **E. Coccia, B. Mussard, M. Labeye, J. Caillat, R. Taïeb, J. Toulouse & E. Luppi**. Gaussian continuum basis functions for calculating high-harmonic

generation spectra. *Int. J. Quantum Chem.* **116**, 1120 (2016). URL http://dx.doi.org/10.1002/qua.25146. 150, 151, 153, 154, 216

[236] **C.-Z. Gao, P. M. Dinh, P.-G. Reinhard & E. Suraud**. Towards the analysis of attosecond dynamics in complex systems. *Phys. Chem. Chem. Phys.* **19**, 19784 (2017). URL http://dx.doi.org/10.1039/C7CP00995J.

[237] **X. Liu, X. Zhu, L. Li, Y. Li, Q. Zhang, P. Lan & P. Lu**. Selection rules of high-order-harmonic generation: Symmetries of molecules and laser fields. *Phys. Rev. A* **94**, 033410 (2016). URL http://dx.doi.org/10.1103/PhysRevA.94.033410.

[238] **I. S. Ulusoy & M. Nest**. Correlated Electron Dynamics: How Aromaticity Can Be Controlled. *J. Am. Chem. Soc.* **133**, 20230 (2011). URL http://dx.doi.org/10.1021/ja206193t.

[239] **S.-I. Chu**. Recent development of self-interaction-free time-dependent density-functional theory for nonperturbative treatment of atomic and molecular multiphoton processes in intense laser fields. *The Journal of Chemical Physics* **123**, 062207 (2005). URL http://dx.doi.org/10.1063/1.1904587. 150

[240] **J. Wassaf, V. Véniard, R. Taïeb & A. Maquet**. Strong Field Atomic Ionization: Origin of High-Energy Structures in Photoelectron Spectra. *Phys. Rev. Lett.* **90**, 013003 (2003). URL http://dx.doi.org/10.1103/PhysRevLett.90.013003. 150

[241] **C. Ruiz, L. Plaja, R. Taïeb, V. Véniard & A. Maquet**. Quantum and semiclassical simulations in intense laser-*textbackslashmathrmH*$_2$*textasciicircum*+ interactions. *Phys. Rev. A* **73**, 063411 (2006). URL http://dx.doi.org/10.1103/PhysRevA.73.063411.

[242] **R. Sawada, T. Sato & K. L. Ishikawa**. Implementation of the multiconfiguration time-dependent Hatree-Fock method for general molecules on a multiresolution Cartesian grid. *Phys. Rev. A* **93**, 023434 (2016). URL http://dx.doi.org/10.1103/PhysRevA.93.023434. 150

[243] **S. Pabst, A. Sytcheva, O. Geffert & R. Santra**. Stability of the time-dependent configuration-interaction-singles method in the attosecond and strong-field regimes: A study of basis sets and absorption methods. *Phys. Rev. A* **94**, 033421 (2016). URL http://dx.doi.org/10.1103/PhysRevA.94.033421. 150

[244] **U. De Giovannini, D. Varsano, M. A. L. Marques, H. Appel, E. K. U. Gross & A. Rubio**. Ab initio angle- and energy-resolved photoelectron spectroscopy with time-dependent density-functional theory. *Phys. Rev. A* **85**, 062515 (2012). URL http://dx.doi.org/10.1103/PhysRevA.85.062515. 150

[245] **X. Chu & G. C. Groenenboom**. Contributions of inner-valence molecular orbitals and multiphoton resonances to high-order-harmonic generation of *textbackslashmathrmN*$_2$: A time-dependent density-functional-theory study. *Phys. Rev. A* **93**, 013422 (2016). URL http://dx.doi.org/10.1103/PhysRevA.93.013422. 150

[246] **D. Wang, X. Zhu, X. Liu, L. Li, X. Zhang, P. Lan & P. Lu**. High harmonic generation from axial chiral molecules. *Opt. Express, OE* **25**, 23502 (2017). URL http://dx.doi.org/10.1364/OE.25.023502. 150

[247] **X. Andrade et al.** Real-space grids and the Octopus code as tools for the development of new simulation approaches for electronic systems. *Phys. Chem. Chem. Phys.* **17**, 31371 (2015). URL http://dx.doi.org/10.1039/C5CP00351B. 150

[248] **C. d. Boor**. *A Practical Guide to Splines*. Applied Mathematical Sciences (Springer-Verlag, New York) (1978). URL //www.springer.com/gp/book/9780387953663. 150

[249] **B. W. Shore**. Solving the radial Schrödinger equation by using cubic-spline basis functions. *The Journal of Chemical Physics* **58**, 3855 (1973). URL http://dx.doi.org/10.1063/1.1679740. 150

[250] **C. Froese Fischer & M. Idrees**. Spline algorithms for continuum functions. *Computers in Physics* **3**, 53 (1989). URL http://dx.doi.org/10.1063/1.168325. 150

[251] **C. F. Fischer & M. Idrees**. Spline methods for resonances in photoionisation cross sections. *J. Phys. B: At. Mol. Opt. Phys.* **23**, 679 (1990). URL http://dx.doi.org/10.1088/0953-4075/23/4/002. 150

[252] **F. Martín**. Ionization and dissociation using B-splines: photoionization of the hydrogen molecule. *J. Phys. B: At. Mol. Opt. Phys.* **32**, R197 (1999). URL http://dx.doi.org/10.1088/0953-4075/32/16/201. 150

[253] **E. Cormier & P. Lambropoulos**. Above-threshold ionization spectrum of hydrogen using B-spline functions. *J. Phys. B: At. Mol. Opt. Phys.* **30**, 77 (1997). URL http://dx.doi.org/10.1088/0953-4075/30/1/010. 150

[254] **M. Stener, D. Toffoli, G. Fronzoni & P. Decleva**. Recent advances in molecular photoionization by density functional theory based approaches. *Theor Chem Account* **117**, 943 (2007). URL http://dx.doi.org/10.1007/s00214-006-0212-3. 150

[255] **L. Argenti & R. Colle**. On the B-splines effective completeness. *Computer Physics Communications* **180**, 1442 (2009). URL http://dx.doi.org/10.1016/j.cpc.2009.03.002. 150

[256] **C. Froese Fischer**. A B-spline Hartree–Fock program. *Computer Physics Communications* **182**, 1315 (2011). URL http://dx.doi.org/10.1016/j.cpc.2011.01.012. 150

[257] **L. A. A. Nikolopoulos**. A package for the ab-initio calculation of one- and two-photon cross sections of two-electron atoms, using a CI B-splines method. *Computer Physics Communications* **150**, 140 (2003). URL http://dx.doi.org/10.1016/S0010-4655(02)00684-7.

[258] **R. Nepstad, T. Birkeland & M. Førre**. Numerical study of two-photon ionization of helium using an textitab initio numerical framework. *Physical Review A* **81** (2010). URL http://dx.doi.org/10.1103/PhysRevA.81.063402. 150

[259] **B. Fetić & D. B. Milošević**. Numerical solution of the time-dependent Schrtextbackslash"odinger equation for $textbackslashmathrmH_2textasciicircum+$ ion with application to high-harmonic generation and above-threshold ionization. *Phys. Rev. E* **95**, 053309 (2017). URL http://dx.doi.org/10.1103/PhysRevE.95.053309. 150

[260] **A. F. White, C. J. Heide, P. Saalfrank, M. Head-Gordon & E. Luppi**. Computation of high-harmonic generation spectra of the hydrogen molecule using time-dependent configuration-interaction. *Molecular Physics* **114**, 947 (2016). URL http://dx.doi.org/10.1080/00268976.2015.1119900. 151

[261] **E. Coccia & E. Luppi**. Optimal-continuum and multicentered Gaussian basis sets for high-harmonic generation spectroscopy. *Theor Chem Acc* **135**, 43 (2016). URL http://dx.doi.org/10.1007/s00214-015-1770-z. 151, 157, 175, 217

[262] **E. Luppi & M. Head-Gordon**. Computation of high-harmonic generation spectra of H2 and N2 in intense laser pulses using quantum chemistry methods and time-dependent density functional theory. *Molecular Physics* **110**, 909 (2012). URL http://dx.doi.org/10.1080/00268976.2012.675448. 151

[263] **E. Coccia, R. Assaraf, E. Luppi & J. Toulouse**. Ab initio lifetime correction to scattering states for time-dependent electronic-structure calculations with incomplete basis sets. *The Journal of Chemical Physics* **147**, 014106 (2017). URL http://dx.doi.org/10.1063/1.4991563. 151

[264] **F. L. Yip, C. W. McCurdy & T. N. Rescigno**. Hybrid Gaussian–discrete-variable representation for one- and two-active-electron continuum calculations in molecules. *Physical Review A* **90** (2014). URL http://dx.doi.org/10.1103/PhysRevA.90.063421. 151

[265] **C. Marante, L. Argenti & F. Martín**. Hybrid Gaussian–B-spline basis for the electronic continuum: Photoionization of atomic hydrogen. *Phys. Rev. A* **90**, 012506 (2014). URL http://dx.doi.org/10.1103/PhysRevA.90.012506. 151

[266] **C. Marante, M. Klinker, I. Corral, J. González-Vázquez, L. Argenti & F. Martín**. Hybrid-Basis Close-Coupling Interface to Quantum Chemistry Packages for the Treatment of Ionization Problems. *J. Chem. Theory Comput.* **13**, 499 (2017). URL http://dx.doi.org/10.1021/acs.jctc.6b00907. 151

[267] **H. J. Wörner, J. B. Bertrand, P. Hockett, P. B. Corkum & D. M. Villeneuve**. Controlling the Interference of Multiple Molecular Orbitals in High-Harmonic Generation. *Phys. Rev. Lett.* **104**, 233904 (2010). URL http://dx.doi.org/10.1103/PhysRevLett.104.233904. 151, 164

[268] **A. Picón, A. Bahabad, H. C. Kapteyn, M. M. Murnane & A. Becker**. Two-center interferences in photoionization of a dissociating H 2 + molecule. *Physical*

Review A **83** (2011). URL http://dx.doi.org/10.1103/PhysRevA.83.013414. 151

[269] **K. Kaufmann, W. Baumeister & M. Jungen**. Universal Gaussian basis sets for an optimum representation of Rydberg and continuum wavefunctions. *J. Phys. B: At. Mol. Opt. Phys.* **22**, 2223 (1989). URL http://dx.doi.org/10.1088/0953-4075/22/14/007. 153

[270] **A. Szabo & N. S. Ostlund**. *Modern Quantum Chemistry: Introduction to advanced electronic structure theory* (Dover Publications, Inc.) (1996). 153, 169

[271] **M. J. Seaton & G. Peach**. The Determination of Phases of Wave Functions. *Proc. Phys. Soc.* **79**, 1296 (1962). URL http://dx.doi.org/10.1088/0370-1328/79/6/127. 157, 193

[272] **A. Macías, F. Martín, A. Riera & M. Yáañez**. A practical solution to the "unknown normalization" problem. *International Journal of Quantum Chemistry* **33**, 279 (1988). URL http://dx.doi.org/10.1002/qua.560330404. 157

[273] **F. I. Gauthey, C. H. Keitel, P. L. Knight & A. Maquet**. Role of initial coherence in the generation of harmonics and sidebands from a strongly driven two-level atom. *Physical Review A* **52**, 525 (1995). URL http://dx.doi.org/10.1103/PhysRevA.52.525. 162

[274] **N. Suárez, A. Chacón, J. A. Pérez-Hernández, J. Biegert, M. Lewenstein & M. F. Ciappina**. High-order-harmonic generation in atomic and molecular systems. *Phys. Rev. A* **95**, 033415 (2017). URL http://dx.doi.org/10.1103/PhysRevA.95.033415. 164

[275] **Y. J. Chen & J. Liu**. High-order harmonic generation from diatomic molecules with large internuclear distance: The effect of two-center interference. *Physical Review A* **77** (2008). URL http://dx.doi.org/10.1103/PhysRevA.77.013410. 164

[276] **C. Vozzi et al.** Controlling Two-Center Interference in Molecular High Harmonic Generation. *Physical Review Letters* **95** (2005). URL http://dx.doi.org/10.1103/PhysRevLett.95.153902. 164

[277] **M. Berry**. Rays, wavefronts and phase: a picture book of cusps. *Huygens' principle* pp. 1690–1990 (1992). 183

[278] **R. Schubert**. *Semiclassical localization in phase space*. Ph.D. thesis, Universitat Ulm (2001). URL https://people.maths.bris.ac.uk/~marcvs/publications/my_papers/thesis.pdf. 183

[279] **L. Hörmander**. *The Analysis of Linear Partial Differential Operators I: Distribution Theory and Fourier Analysis*. Classics in Mathematics (Springer Berlin Heidelberg) (1964-2015). URL https://books.google.fr/books?id=aaLrCAAAQBAJ. 183

[280] **L. Scorzato**. The Lefschetz thimble and the sign problem. *PoS* **LATTICE2015**, 016 (2016). URL https://arxiv.org/abs/1512.08039. 189

[281] **D. R. Bates & M. J. Seaton**. The quantal theory of continuous absorption of radiation by various atoms in their ground states: Ii. further calculations on oxygen, nitrogen and carbon. *Monthly Notices of the Royal Astronomical Society* **109**, 698 (1949). URL http://dx.doi.org/10.1093/mnras/109.6.698. 193

Marie Labeye **19 juillet 2018**

Sujet : Molécules soumises à des impulsions laser intenses et courtes : Simulations de dynamiques ultrarapides corrélées.

Résumé : Cette thèse porte sur différents aspects des dynamiques ultra-rapides d'atomes et de molécules soumises à des impulsions laser infrarouges courtes et intenses. Nous étudions des processus fortement non linéaires tels que l'ionisation tunnel, la génération d'harmoniques d'ordre élevé ou l'ionisation au-dessus du seuil. Deux approches différentes sont utilisées. D'un côté nous mettons au point des modèles analytiques approchés qui nous permettent de construire des interprétations physiques de ces processus. D'autre part nous appuyons les interprétations données par ces modèles avec les résultats obtenus par des simulations numériques qui résolvent explicitement l'équation de Schrödinger dépendante du temps en dimension réduite. Nous étudions également une méthode numérique basée sur l'interaction de configuration dépendante du temps afin de pouvoir des décrire des systèmes à plusieurs électrons plus gros et plus complexes.

Mots clés : physique des champs forts, physique attoseconde, génération d'harmoniques d'ordre élevé, ionisation tunnel, dynamiques corrélées, simulations numériques

Subject: Molecules interacting with short and intense laser pulses: Simulations of correlated ultrafast dynamics.

Abstract: In this thesis we study different aspects of the ultrafast dynamics of atoms and molecules triggered by intense and short infrared laser pulses. Highly non-linear processes like tunnel ionization, high order harmonic generation and above threshold ionization are investigated. Two different and complementary approaches are used. On the one hand we construct approximate analytical models to get physical insight on these processes. On the other hand, these models are supported by the results of accurate numerical simulations that explicitly solve the time dependent Schrödinger equation for simple benchmark models in reduced dimensions. A numerical method based on time dependent configuration interaction is investigated to describe larger and more more complex systems with several electrons.

Keywords: strong field physics, attosecond physics, high order harmonic generation, tunnel ionization, correlated dynamics, numerical simulations